PROTON-PROTON CORRELATION FUNCTIONS AS A PROBE TO REACTION DYNAMICS

By

Micha A. Kilburn

A DISSERTATION

Submitted to
Michigan State University
in partial fulfillment of the requirements
for the degree of

DOCTOR OF PHILOSOPHY

Physics

2011

ABSTRACT

PROTON-PROTON CORRELATION FUNCTIONS AS A PROBE TO REACTION DYNAMICS

By

Micha A. Kilburn

In an experiment at NSCL, proton-proton (p-p) correlation functions were measured in ^{40}Ca+^{40}Ca and ^{48}Ca+^{48}Ca reactions, both at E/A = 80 MeV. The High Resolution Array (HiRA) detected light particles with excellent energy ($\leq$200 keV) and angular ($\approx 0.2^{\circ}$) resolution. The MSU 4π Array covered 77% of the total 4π solid angle and was used to determine the impact parameter for collisions using transverse energy (E_t) as the relevant observable.

Two-particle correlation functions are employed in this work to measure the space-time extent of the source. A transport model previously predicted that the p-p correlation functions would be sensitive to the density dependence of the symmetry energy, while other work had already shown the p-p correlation functions to be sensitive to nucleon-nucleon (NN) in-medium cross sections.

More detailed calculations performed in this dissertation indicate that that sensitivity to the symmetry energy is subtle. Much less subtle is the dependence of the p-p correlation functions on the laboratory angle of the total momentum vector of the two protons. At forward angles, where the correlation function is sensitive to the projectile spectator, the measured correlation functions appear consistent with sources that are very extended in space-time. The space-time extent of these sources exceed the predictions of BUU transport calculations, which are the main tool for probing the symmetry energy via correlation functions. At backward angles, where it is sensitive to the expanding participant source,

the observed sources are more compact; there the trends can be reproduced by the BUU calculations.

At the most forward angles, we note that the qualitative trends of the correlation function with angle and energy run counter to the qualitative trends of smaller sources for particles with higher momentum typically reported by published work in this incident energy domain. While we observe this latter trend at backward angles, the momentum dependence in the source size observed at forward angles is comparatively weak and trends in the opposite direction, with the most energetic protons displaying the weakest correlation functions. These energetic protons are closer to the expected velocity for projectile spectator remnants, suggesting their origins in the decay of these remnants.

Further analysis of the correlation functions with gates on rapidity and transverse momentum allowed a clean exclusion of projectile decay. After excluding this kinematic domain, it was possible to obtain data that can be compared to a BUU transport model. This model, however, predicted a weak sensitivity to the density dependence of the symmetry energy that is too small to be experimentally probed. Consistent with prior work, we find a strong sensitivity to the *NN* in-medium cross section reduction as well as a strong previously unobserved sensitivity to the production of light clusters. Comparisons between the BUU calculations establish the sensitivity of data to these transport quantities as well as the range of values for these transport quantities that may be consistent with the present measurements.

To the women behind the scenes: Debbie, Kim and Shari

ACKNOWLEDGMENT

This dissertation and the work within could not have been completed without the help of many advisers, colleagues and friends. To not acknowledge them at the beginning would be a crime on par with excluding the bibliography at the end, for without them there would be nothing to read in between.

I would like to thank my adviser, Bill Lynch, for his guidance, knowledgeable mind, and faith in me. When we had a similar vision, the course was clear. When our views differed, the result was clarity in my own thoughts and conceptions. In addition, I thank Pawel Danielewicz for advising me as a theorist for two years. He was understanding when I switched to an experimental group, and continued to provide guidance as a committee member. I also thank the rest of the members on my guidance committee: Betty Tsang, for her "get it done" attitude and useful suggestions; Piotr Piecuch for providing another theoretical eye; and Norman Birge, for advising me as a TA and asking probing questions.

The analysis for this thesis work was a joint effort between myself and two postdocs: Vlad and Daniela. Without their efforts, the experiment would not have ran, and it certainly would have taken me longer to graduate. Without their friendship, it would have felt like an eternity. I will never forget Vlad's persistence and Daniela's patience during the late nights working with them before, throughout, and after the experiment.

The analysis would have taken much longer to complete if Zibi had not joined our group as a postdoc, after the Henzl's departure, and helped with the finishing touches. His work on extracting source sizes from the correlations was pivotal and his advice was most useful. He was diligent and thoughtful while we worked on a paper together, and he is also a mean

poker player.

I must thank the rest of the HiRA family, the other siblings, uncles, and cousins in addition to the parents and older siblings mentioned above. The cooperation of the entire family is necessary in any successful HiRA experiment. I am grateful for my big brothers: Mark and Andy. I thank Mark for being my mentor, getting me on the Art's softball team, and convincing me to make the switch from theory to join HiRA. I thank Andy for being my officemate and patiently answering my numerous questions about HiRA, ROOT and C++ in general. I want to thank my little brothers, Dan and Mike for keeping it real and fun, my other siblings Ali and Jenny for all their help, and cousin Clemens for all of his hard work and attention to meticulous details. A special thanks to Dan for all of those morning conversations and his helpful descriptions. I am immensely appreciative to the stepson, Brent, for his friendship and help with BUU. Hats off to my uncles: Sergei for rolling the calcium target and teaching me words in Russian, Bob who taught me more about programming in a couple of hours than I had learned in months, and Lee for reminding me why to use "Do not use" tags. Uncle Mike was also pivotal in the experimental setup. His work ethic and humor are to be admired. Most thanks to my godfather, Giuseppe, for his questions and ideas pertaining to BUU, correlation functions and the imaging technique.

I also want to give a shout out to members of the 4π family: Skip Vander Molen for his extensive help with the experimental setup and his masterful control of Freddie; Gary Westfall for answering all of my questions during analysis about what they did many moons ago; and Dan Brown for his cheerful outlook and friendship during the experimental setup. Although only vaguely related to the family, Scott Pratt has also been very patient and helpful, providing advice and codes to help with the analysis.

I am indebted to various staff around the lab. I thank Renan Fontus for his extensive help with the laser system analysis, and always being friendly. I thank Len Morris for all of his patience and work designing parts for the experiment. I thank Dave Sanderson and Andy Thulin for teaching me everything I wanted to know about vacuum systems, and more. I thank John Yurkon for his extensive knowledge, and help with targets and flanges. I thank Hang Lui for his help getting running on the HPCC, where most of the simulations were performed. My most sincere thanks go to Shari Conroy. She not only helped me with travel arrangements, and kept me caffeinated, but she was a friend, and hooked me up with hockey tickets even after she retired.

Other professors at the lab also made my stay here more welcoming. Filomena made me feel at home immediately, and always asked how things were going when we passed in the hallways. Remco and I also chatted often, usually outside, but he has opened some doors that I didn't know could be opened. His friendship has also been invaluable. Thomas was only here briefly, but I won't forget how he rooted for me during my last subject exam. The first time I met Michael, he stole the basketball from me during the annual REU/faculty game. Throughout my time here, he's helped keep me on track by providing a voice of reason when it was needed most. His humor hasn't hurt either.

Throughout my years at the lab, I became more and more interested in explaining nuclear science to the public. After all, it's their money funding us, and they should know what they are paying for. For that I thank Geoff Koch for exposing me to the publicity side of science, and getting me involved in numerous projects which gave me a voice. Perhaps one of my greatest mentors during grad school came from the most unlikely of places: the outreach coordinator, Zach Constan. He arrived at the lab two years after me, shortly after I had

began giving tours of the lab. He completely revamped the tour program and added many other outreach programs. His enthusiasm was contagious and I somehow caught the outreach bug. His ideas are infectious and his advice has been curing. I am glad to be following in his footsteps.

During my time here, I wasn't just a part of the NSCL, I was also a part of the Physics department. I will look back on my time with the recruiting committee with fondness, and thank them all for treating me as an equal colleague. I also thank Wolfgang for listening when we asked him to, and letting me take over the grad section of the website. My most sincere thanks go to Kim and Debbie, for providing answers, advice, and their friendship.

I wouldn't have made it through graduate school without the camaraderie of the original posse: Dan, Jon, Josh V, and Josh S. Those late night homework sessions would have been all-nighters without their help and those first few years would have been disastrous without their companionship. There are many more friends and family I should thank for their support over the last seven years. They are too many to name, but they are not forgotten.

The most pivotal years for me were the first and the last. While the posse got me through the first, Samantha got me through the last. I thank her for all of her support and motivation in getting through the final push. She was the light at the end of the tunnel.

PREFACE

In nuclear science, we build large detectors to measure tiny particles with the goal of understanding giant astronomical objects. To "understand" we must solve a puzzle that has had us scratching our heads since the beginning of humanity: Where did we, and everything around us, come from? Carl Sagan wrote "We are made of star stuff," but a puzzle remains: How did the stars make all of the elements? People in nuclear science, particle physics, and astrophysics each work on a different piece of the puzzle, and over time, the solution to it is starting to take shape. In this way, nuclear scientists are like detectives, piecing together bits of information to unravel the mystery of existence.

The tiny particles that we study are atomic nuclei comprised of nucleons (protons and neutrons) at the center of the atom. These nuclei have sizes that are smaller than that of atomic physics and yet larger than that of high energy physics studies. Because nuclei are too small to be seen with the most powerful microscope, we must develop not only the macroscopic detectors needed to study these submicroscopic objects, but we must also be creative in how we "measure" properties of nuclei. We can't put a single nucleus on a bathroom scale, but we can deduce its mass. We can't look at a single nucleus, but we can determine its shape. There is not a physical ruler small enough to measure the size of a nucleus, however, we can not only determine its matter radius, but also the radius of the charge distribution (due largely to protons). For nuclei with many more neutrons than protons, nuclear scientists can also detect a neutron skin or a halo neutron around the outer edges of the nucleus if they exist. In this way, nuclear scientists are like biologists, dissecting the details of how nuclei are built and how their internal dynamics work.

The properties mentioned thus far only deal with the structure of the nucleus. However, there are questions concerning what can take place during nuclear collisions in general, and complex central collisions in particular. What fragments are created after a central collision? How many neutrons will pass from a neutron-rich nucleus to a neutron-poor nucleus during a collision? If we regard nuclei as droplets of nuclear matter, what is the nuclear equation of state? Complicating this task is the fact that just as you can't measure size with a ruler, you can't put a probe in the middle of the reaction. Instead, we detect nuclei produced from a nuclear collision far away from the actual collision, and long after the collision is over. From these measurements, we then infer what happened in the past. In this way, nuclear scientists are like archaeologists, reconstructing the collision dynamics from the events that occurred in the past.

In both nuclear structure and nuclear reaction studies, the data often is not enough on its own to give a complete representation: It must be compared to a theoretical model. In nuclear structure, one might compare data to predictions from shell model theory, while in the case of reactions, one might compare data to transport models that simulate nuclear collisions. The knowledge gained from both structure and reactions can be used as input into astrophysical models that simulate processes such as stellar nucleosynthesis or supernovae explosions, resulting in predictions for elemental abundances. In this way, nuclear scientists are like architects, designing a construct from abstract ideas.

Nuclear science is all of this and more. While this dissertation focuses on only one small piece of the puzzle, it's an important piece necessary for tying together what we learn from nuclear structure, nuclear reactions, and nuclear astrophysics. As you read on, remember that this isn't the beginning or the end, but merely a step in the right direction.

TABLE OF CONTENTS

LIST OF TABLES

LIST OF FIGURES

Chapter 1

Introduction

All matter is made of atoms, each of which is comprised of a nucleus and electrons. The nucleus, the core of the atom, consists of nucleons: Neutrons(n) and protons(p). Nuclear science, at the interface between chemistry and physics, is the study of this nucleus. The nucleus is bound together by nuclear forces. Its binding energy can be described by a complicated relationship involving its mass number and charge. The mass number, denoted as $A = N + Z$, is the number of nucleons, where Z denotes the charge number and represents the number of protons, and the difference between mass number and charge number is denoted by N, which represents the number of neutrons. One term in the parametrization of the nuclear contribution to the binding energy depends upon the asymmetry, $N - Z$, between the number of neutrons and protons. This asymmetry term plays an important role not only in nuclear science, but also in nuclear astrophysics, for when this difference between neutron and proton number is extrapolated to the extremum, pure neutron matter is obtained, similar to that found in the interior of a neutron star. One original goal of this dissertation work was to study nuclei with an excess of neutrons to extract parameters that

affect the properties of neutron stars.

This introductory chapter will first provide a historical motivation, listing previous studies this dissertation is built upon in section 1.1. Next, the main experimental observable, proton-proton (p-p) correlation functions are introduced in section 1.2, with an explanation of how they are measured, a description of their features, and an explanation of their relation to the space-time extent of the emitting source during a nuclear collision. In section 1.3, background information on the transport simulation used in this work is provided, and two of the physics inputs, the density dependence of the symmetry energy and nucleon-nucleon (NN) in-medium cross sections, are explained. Finally, the organization of the remainder of the dissertation is outlined.

1.1 Motivation

The three main areas of nuclear physics: structure, reactions, and astrophysics, are sometimes viewed as discrete entities with only the atomic nucleus to tie them together. One common thread between them is the equation of state (EOS) of nuclear matter. An equation of state is a relationship between pressure, temperature, and density. One well known equation of state is the ideal gas law

$$pV = nRT. \tag{1.1}$$

The ideal gas law can be used to describe nuclei, but only at very high temperatures and at a low phase space density where the Pauli principle and nuclear interactions can be neglected. In reality, a different EOS is required for many of the important systems that are at a higher

density where NN interactions and the Pauli exclusion principle are important.

The EOS is important for describing the bulk and thermodynamic properties of macroscopic nuclear systems [9]. Consequently, aspects of the EOS are essential to the description of astrophysical phenomena such as the evolution of the universe after the Big Bang [10], supernovae [11], and the structure of a neutron star [12]. For the latter it is useful to distinguish between the symmetric matter EOS, which is the limiting form of the EOS that applies to nuclei and nuclear systems with $N \approx Z$, and the symmetry energy, which can be thought of as a correction term to the symmetric matter EOS for nuclei and nuclear systems with $N - Z > 0$.

Since the turn of the millennium, it has appeared that heavy-ion collisions had provided some constraints on the isospin symmetric matter EOS [13], however, the symmetry energy is still widely unconstrained. Attention has been turned towards constraining the symmetry energy with the increasing availability of neutron rich radioactive beams with large asymmetries in N-Z.

The symmetry energy is important for neutron rich nuclei, and the structure of the nucleus is governed by the symmetry energy in many aspects. While the most direct connection is through the binding energy (see subsection 1.3.1), the symmetry energy also influences other aspects such as neutron skin thickness [14], pygmy dipole resonance [15, 16], giant monopole resonance [17], and isobaric analog states [18].

Many properties of neutron stars are governed by the symmetry energy, including their maximum mass [19], and the relation between the mass and radius [20]. While it is known that a neutron star cools by neutrino emission, it is unknown whether it occurs via the direct or modified Urca process (named after the Cassino da Urca in Rio de Janeiro). The direct

Urca process may be possible. Whether this occurs or not depends in part on the density dependence of the symmetry energy [12, 21].

The dynamics of nuclear reactions have been predicted to be sensitive to the symmetry energy, and many observables have been developed to explore this relationship. Based on theoretical calculations, for example, one may expect that two-particle correlation functions [8], single and double ratios of free neutrons and protons [22], isoscaling [23], isotopic distributions [24], and isospin diffusion [25] among others [26, 27] should be sensitive to the symmetry energy. An overview of some of the current constraints on the symmetry energy can be found in Ref. [28].

In order to constrain the symmetry energy from a heavy-ion collision (HIC), a comparison to a theoretical model is needed. Hydrodynamic models were one of the first used, but they assumed a zero mean free path for nucleons inside the nuclear medium. In its place, theorists have developed transport theories for use at intermediate energies, many of which can be understood from the point of the semiclassical Thomas Fermi (TF) model. The TF model, applied first to the description of atoms, describes nucleons as a semiclassical Fermi gas interacting by a self consistent mean field. Like the TF model, the BUU (Boltzmann-Uehling-Uhlenbeck) equation models the nucleus as a semiclassical distribution of nucleons interacting by a self consistent mean field. In addition to the mean field potential, *NN* collisions via the residual interaction are calculated in a collision term that enforces the Pauli exclusion principle by incorporating Pauli blocking factors, discussed in section 1.3. Ambiguities arose in the transport calculations due the treatment of the mean field potential. There may be different physical origins for momentum dependence in the mean field such as momentum dependence of the *NN* effective interaction, similar to that of the free-space

NN scattering matrix. In addition, the fact that nucleons are identical particles, leads to momentum dependencies from the Fock or exchange term. The inclusion of a mean field potential modifies the EOS from the Fermi gas EOS that would result in the limit of a vanishing mean field potential.

Current BUU transport models used to study nuclear reactions have many unconstrained physics inputs, only one of which is the symmetry energy. In order to constrain the symmetry energy using any observable from heavy-ion collisions, one must also constrain other inputs such as the *NN* in-medium cross section (described in Subsection 1.3.2). It turns out that the *p*-*p* correlation function is not as sensitive to the density dependence of the symmetry energy as it is to the in-medium cross section. In addition, there are other features of reaction dynamics in transport models that also affect *p*-*p* correlation functions such as momentum dependence of the mean field potential and cluster production, which will be addressed in section 4.5. While constraining the density dependence of the symmetry energy was the original motivation for this work, this motivation has evolved to focus on the other unconstrained inputs in transport theory because the theoretical predictions have evolved.

1.2 Introduction to *p*-*p* Correlation Functions

For uncorrelated events, $P(A(1), B(2)) = P(A(1)) \cdot P(B(2))$, that is the probability of an observable taking a value of A(1) for particle 1 and B(2) for particle 2 in an event can be described by the product of observing A(1) for particle 1 times the probability of observing B(2) for particle 2 independently. If the observables are correlated, this is no longer true. Correlation functions are one way to describe how the correlated two particle distributions differ from the product of the uncorrelated single particle distributions. These difference

can arise from final state interactions (FSI) between the two particles during a HIC and, in the case of identical Fermions, from the anti-symmetrization required for the relative wavefunctions. Due to FSI and identical particle effects, correlation functions reflect the size of the source from which the particles are emitted. For pairs of photons, the symmetry of the relative wavefunction of two photons can be used to measure the radii of stars, while for pairs of protons, the combination of anti-symmetrization of the relative wavefunction and FSI can be used to measure the space-time extent of the emitting nuclear source. The source is the region of the nuclear reaction which emits particles. Not all particles emitted from a HIC are correlated however. A simple illustration of how correlations can be large or small depending on the source of the nucleons is provided in Figs. 1.1 and 1.2 in the context of the participant-spectator model. In the participant spectator model, when a nucleus strikes another nucleus, the overlap region along the beam axis is called the participant zone. The part of the projectile which does not overlap with the target is "sheared off" and is called the projectile spectator. Likewise, the part of the target which does not overlap is called the target spectator zone. Figs. 1.1 and 1.2 provide crude representations of particles which may or may not be correlated. Fig. 1.1 gives an example of momentum vectors for emitted particles which are likely to be strongly correlated while Fig. 1.2 is an example of emitted particles which are likely to be weakly correlated. While the participant-spectator description is not as precise at intermediate energies as it is at relativistic energies, it remains, nevertheless, qualitatively correct and provides a useful terminology for describing the various sources of particles produced in a collision.

In this dissertation, correlations are measured via intensity interferometry. Such correlations are sometimes called HBT correlations, named after Hanbury-Brown and Twiss [29].

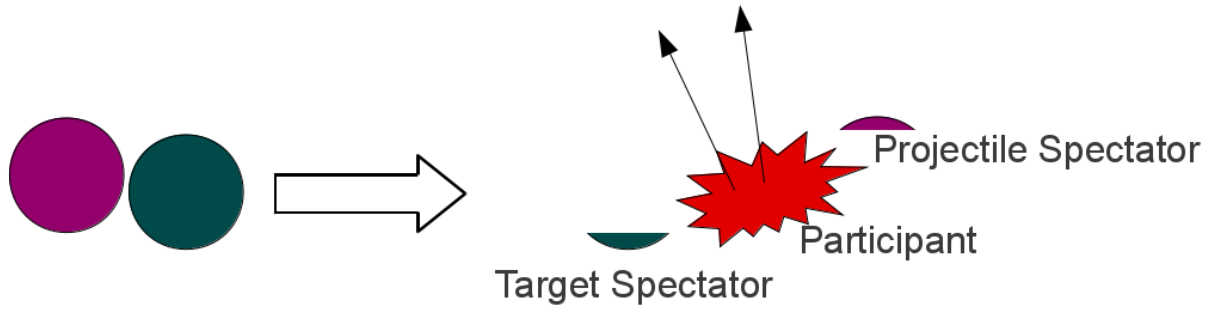

Figure 1.1: Before and after cartoon of a heavy-ion collision. The black arrows represent momentum vectors for two particles which are strongly correlated. For interpretation of the references to color in this and all other figures, the reader is referred to the electronic version of this dissertation.

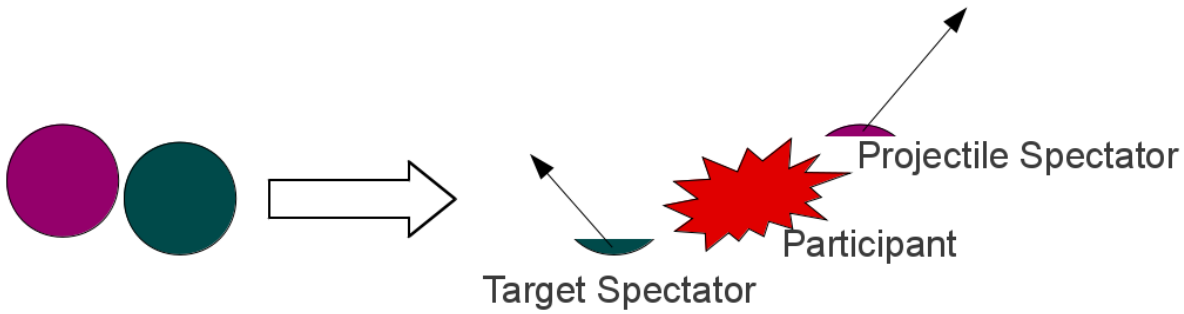

Figure 1.2: Same cartoon as above, however, here the black arrows represent momentum vectors for two particles which are weakly correlated.

The HBT correlation technique was invented to measure the size of radio sources in the galaxies Cygnus and Cassiopeia, and then used to measure the angular radius of the star Sirius. In these early studies, the relevant correlations were between two photons and the main effect was caused by the fact that the two photons are bosons and their relative wavefunction must be symmetric. Since then, HBT has also been used to measure femtoscale sources by measuring correlations between pairs of pions or pairs of protons [30]. This method has been subsequently used successfully to study the size of the source for a wide range of particle types and colliding nuclei at a wide range of collision energies. [31–35].

In this dissertation, the primary concern is of p-p correlations, $C(\vec{q})$. Experimentally, this observable is calculated by

$$C(\vec{q}) = 1 + R(\vec{q}) \equiv \aleph \frac{\sum Y_{12}(\vec{p_1}, \vec{p_2})}{\sum Y_1(\vec{p_1}) Y_2(\vec{p_2})} \tag{1.2}$$

the ratio of correlated to uncorrelated events, where the relative momentum, $\vec{q}$, is calculated in the center of mass of the proton pair and is defined by

$$\vec{q} = \frac{1}{2}(\vec{p_1} - \vec{p_2}). \tag{1.3}$$

In Eq. 1.2, $C(\vec{q}) = 1$ for particles which are uncorrelated. Consequently, $R(\vec{q})$ describes the degree of correlation, and should be 0, in the absence of collective effects, at large $\vec{q}$ where the effect of final state interactions and identical particle effects are vanishing small. In Eq. 1.2, the numerator, $Y_{1,2}$ is the yield of events where two protons are detected with p_1 and p_2 respectively. The denominator mixes protons with momenta p_1 and p_2 from different events with the same impact parameter and calculates q as if the two protons were emitted from

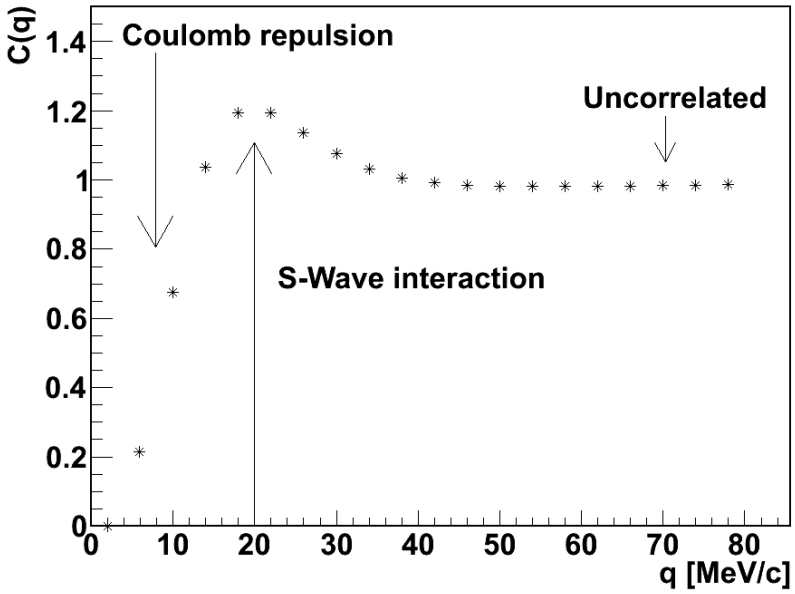

Figure 1.3: A p-p correlation function constructed from a Gaussian source with $r_{1/2} = 6$ fm. Important features are labeled.

the same event. Both numerator and denominator must be summed over the same range of measured particle momenta and over the same range of impact parameters.

An example of a p-p correlation function, as a function of relative momentum, is shown in Fig. 1.3. The peak at 20 MeV/c is due to the attractive $^1S_0$ potential and the anticorrelation at low relative momentum is due to Coulomb repulsion and Pauli blocking. It is clear at high relative momentum, there is no correlation between proton pairs.

The peak of the correlation function includes contributions from both early, fast emission protons, and late, slower protons from secondary decays and evaporation. Many transport models, such as BUU, do not adequately account for protons emitted from secondary decays and evaporation and thus comparing the height of the correlation between experiment and theory is difficult. The shape, ie. width, of the correlation function is a better indicator for comparison. Experimental correlation functions are often "imaged" to produce source

functions which are compared to source functions from transport theory.

Imaging is a term that refers to the process of extracting a source function from a correlation function. Correlation functions are related to the space-time extent of the source by the angle-averaged Koonin-Pratt [36,37] equation

$$C(q) = 1 + 4\pi \int K(q,r)S(r)r^2 dr \tag{1.4}$$

where the kernel, K, given by

$$K(q,r) = |\phi_q(r)|^2 - 1 \tag{1.5}$$

is the relative two proton wavefunction squared minus one. The relative wavefunction describes the propagation of two protons separated by distance, r, in the pair's center of mass frame, traveling to a detector at infinity with asymptotic relative momentum q. The source function, *S(r)*, is the probability of two protons being separated by a distance, r, at the time the second proton is emitted.

Source functions for two protons typically peak at $r = 0$ fm and often have a Gaussian-like shape. For a purely Gaussian source, the half width half maximum, $r_{1/2}$, has a negative linear correlation with the full width half maximum (FWHM) of the correlation function [38], as shown in Fig. 1.4. That is, the wider the correlation function, the smaller the source size.

To interpret *p-p* correlation functions from the data, it is instructive to compare them to transport models that simulate nuclear reactions in order to learn how the experimental observables can be related to reaction dynamics and to theoretical quantities such as the EOS, the momentum dependence of the mean field and the *NN* in-medium cross sections.

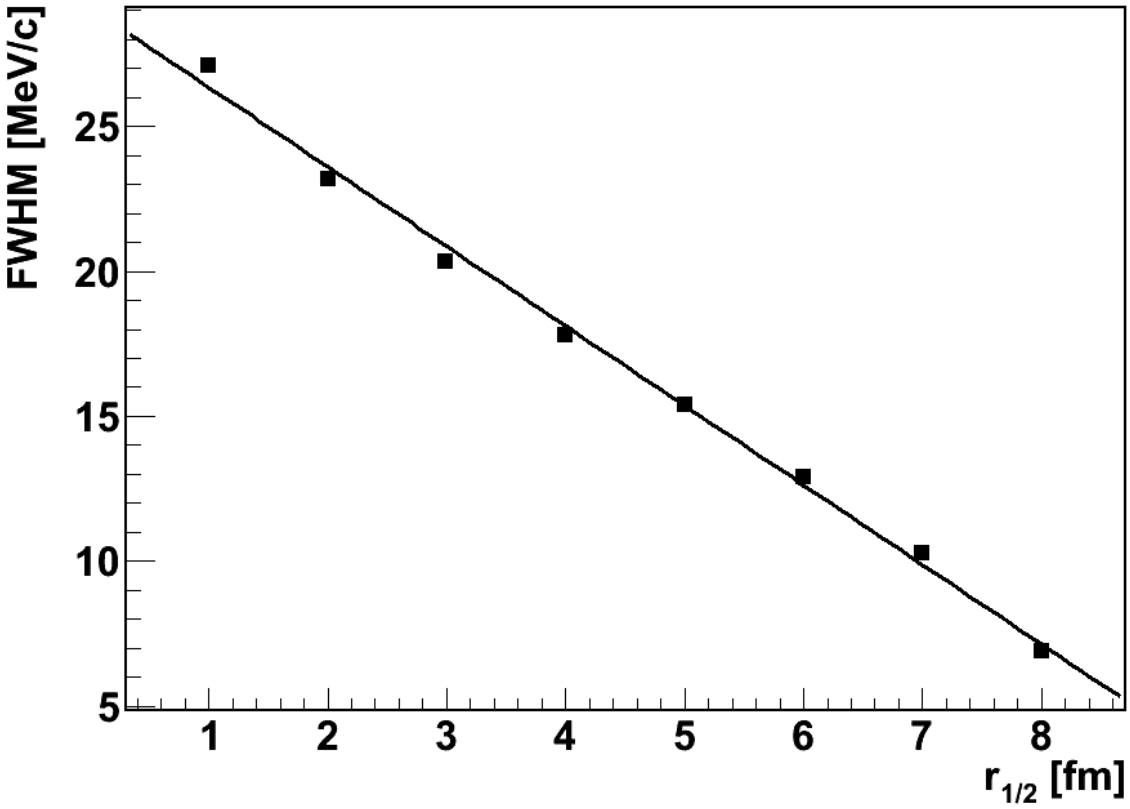

Figure 1.4: *FWHM* of a *p*-*p* correlation as a function of $r_{1/2}$ of a Gaussian source function.

1.3 Introduction to the BUU Transport Model

The Boltzmann-Uehling-Uhlenbeck (BUU) transport equation was developed and applied to nuclear collisions in Ref. [39] where it was initially applied to relativistic heavy ion collisions. A useful review of transport models, including the BUU equation can be found in Ref. [40]. While there are many programs that solve the BUU equation in use currently, we have performed most of our calculations using the BUU transport model developed by Danielewicz and collaborators [41–43]. The following description adopts the notation of this version. BUU transport models simulate heavy-ion collisions by self-consistently solving the modified Boltzmann equation

$$\frac{\partial f}{\partial t}+\frac{\partial \epsilon_{\mathbf{p}}}{\partial \mathbf{p}}\frac{\partial f}{\partial \mathbf{r}}-\frac{\partial \epsilon_{\mathbf{p}}}{\partial \mathbf{r}}\frac{\partial f}{\partial \mathbf{p}}=\int d\mathbf{p}_2\int d\Omega' v_{12}\frac{d\sigma}{d\Omega'}((1\mp f_1)(1\mp f_2)f_1'f_2'-(1\mp f_1')(1\mp f_2')f_1f_2) \tag{1.6}$$

where Uehling and Uhlenbeck introduced the quantum statistical factors [44] involving f_1 and f_2 that are found in the collision integral on the right hand side of the equation. The terms on the left hand side of Eq. 1.6 describe the changes in Wigner transform of the one particle density matrix, f, due to the motion of particles in the mean field, while the terms on the right hand side describe changes in f due to collisions between particles, scattering into or out of various momentum states, and include Pauli-blocking [43]. The minus signs are for fermions and the plus signs are for bosons on the right hand side. The mean field potential is created by all other nucleons and ϵ is the single particle energy.

When the right hand side of the equation is set to 0, the Boltzmann equation reduces to the Vlasov equation which describes the evolution of a single particle under the influence of the mean field potential. By Liouville's theorem, the phase space density will not change

as a result of the mean field potential, but the inclusion of the statistical collision term on the right hand side can cause a modification of the phase-space density and a corresponding violation of the Pauli principal. The blocking factors f_1 and f_2 on the right hand side prevent that.

While Eq. (1.6) is derived as a semi-classical limit of the quantum mechanical Hartree-Fock equation, it can be solved classically by a test particle approach. To accurately determine the mean field, and to provide the accurate phase space density needed for the Pauli blocking factors, the phase space density for each nucleon is represented by many test particles [39, 45]. The test particles evolve through the mean field by Hamilton's equations [46]

$$\dot{\vec{p}} = -\nabla_{\vec{r}} H \tag{1.7}$$

and

$$\dot{\vec{r}} = \nabla_{\vec{p}} H. \tag{1.8}$$

The stability of the transport code with respect to test particle number is explored in section 4.3.

The colliding nuclei are initialized using Thomas-Fermi equations which find the density configuration of nucleons which results in the lowest ground state energy for the nucleus. The surfaces of the nuclei are nearly touching at time = 0 fm/c. The test particles collide on a computational grid of variable size, and the dependence on this size is investigated in section 4.2. The Coulomb force affects charged particles at a larger range than can be accounted for in this model, so when particles leave the grid, they are boosted to infinity where the Coulomb force becomes negligible. Any free particles remaining on the grid at the

end of the simulation are also boosted to infinity.

In this work, only particles emitted from reactions are important, so it is important to define what constitutes emission within the BUU transport code. First, "bound" and "free" must be defined. Physically, particles are considered free when they are decoupled from the mean field and no longer collide. At each time step, particles are checked to see whether or not they are bound. If the local density is greater than $\rho_0/15$, where $\rho_0 = 0.16$ fm^{-3} is the saturation density, the particle is bound. If the density is less than $\rho_0/15$, the particle is temporarily boosted to the rest frame of the projectile. If the particle's energy in this rest frame is less than the rest mass minus the binding energy, it is bound. If not, it is boosted to the rest frame of the target to see if it is bound within that residue by the same energy criteria. If it is not bound in either residue, it is marked as unbound. A collision resets this process. If the particle is unbound when it exits the computational grid, or at the end of the simulation, it is considered emitted. If it emitted, its position, momentum, and density at the time of last collision are written to a file to calculate source functions.

The source function, and thus *p*-*p* correlation function, can depend on many inputs in the BUU transport model. Two inputs, the symmetry energy and *NN* in-medium cross section reduction, are introduced in detail below.

1.3.1 Defining the Symmetry Energy Parametrization

One of the original goals of this dissertation work was to constrain the density dependence of the symmetry energy. The symmetry energy is the difference in binding energy between pure neutron matter, $A=N$, and symmetric matter, $Z=N$. A simple parametrization of the

binding energy of a nucleus is given by the Bethe-Weizaecker formula

$$E_B = a_v A - a_s A^{2/3} - a_c \frac{Z(Z-1)}{A^{1/3}} - a_A \frac{(N-Z)^2}{A} + \delta_0(A,Z)\frac{a_P}{A^{1/2}} \tag{1.9}$$

in the liquid drop model. This binding energy assumes a density independent form of the asymmetry term. In this parametrization, the first term is the volume term, proportional to the volume of the nucleus, and based on the strong nuclear force. The second term is the surface term, also based on the strong force, however, similar to surface tension in liquids. The third term is due to Coulomb force, taking into account electrostatic repulsion between protons. The fourth term is the asymmetry term, (also called the Pauli energy) which shows that when the number of neutrons is much greater than the number of protons, the energy is different than it would be for a system with the same number of nucleons but equal neutrons and protons. The last term is the pairing term, where $\delta_0 = 1$ for Z,N both even, $\delta_0 = -1$ for Z,N both odd, and $\delta_0 = 0$ for A odd.

A phenomenological parametrization of the energy as a function of density and isospin can be written as follows

$$E/A(\rho,\delta) = E/A(\rho,0) + (E_{kin}(\rho/\rho_0)^{2/3} + E_{int}(\rho/\rho_0)^{\gamma})\delta^2 \tag{1.10}$$

where $\delta = (\rho_n - \rho_p)/\rho$. This is an expansion in δ where only even terms are kept due to charge exchange parity. Fourth order and higher terms are small enough to be negligible. The first term, where $\delta = 0$, is the symmetric matter EOS and has been fairly well constrained over the past few decades. The second term, is a correction for the asymmetry. The constant, E_{kin}, which governs the size of the kinetic contribution is on average about 12.5 MeV/A

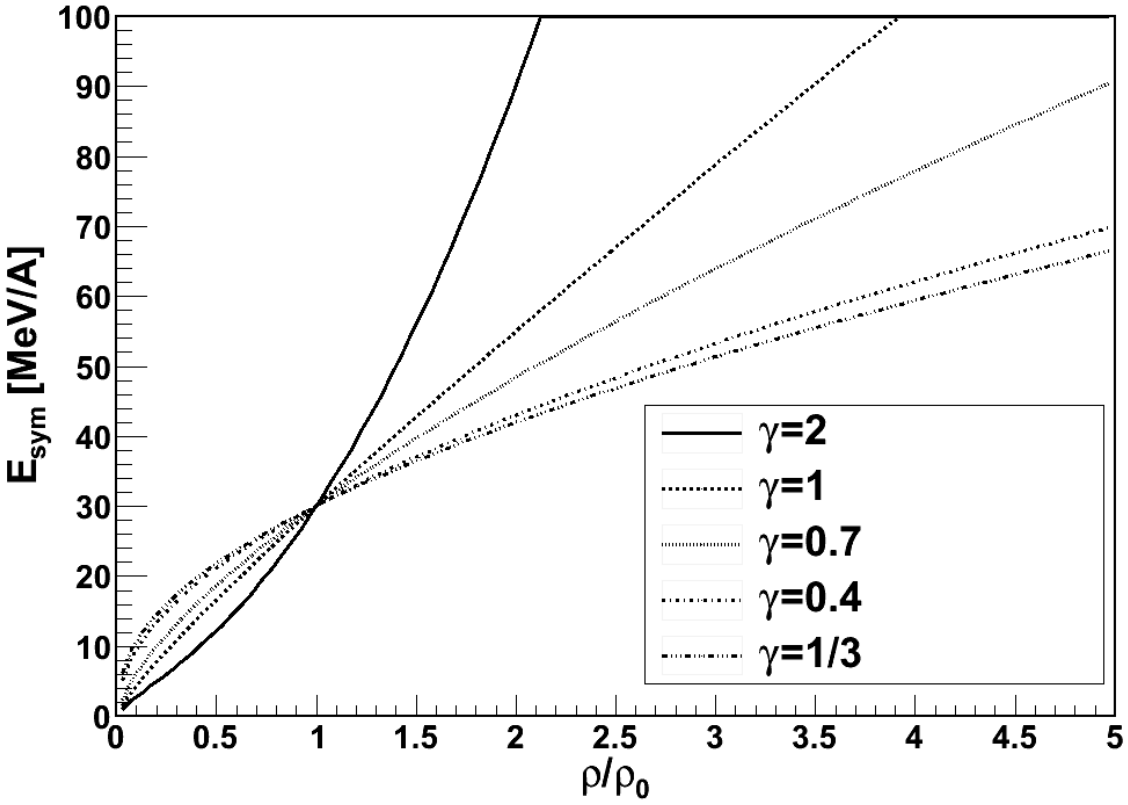

Figure 1.5: Different density dependencies of the symmetry energy.

for a free fermi gas [47] and the constant for the interaction contribution, E_{int}, was chosen to be 17.6 MeV/A so that results are consistent with Ref. [26]. Values of the exponent for the density dependence, γ, explored were 1/3, 0.4, 0.7, 1, and 2 as shown in Fig. 1.5 where the density dependence of the symmetry energy for pure neutron matter is shown. Smaller values of $\gamma < 1$ have a weakened density dependence which is called soft. Larger values with $\gamma > 1$ have a stronger density dependence and are referred to as stiff or hard.

1.3.2 Defining the Nucleon-Nucleon Cross Section Parametrization

One can obtain information about the symmetry energy from heavy-ion collisions, but these collisions are influenced by other transport quantities as well. One of these quantities is the

nucleon-nucleon cross section, σ_{NN}. The baryon scattering cross section may be modified in the nuclear medium, but this modification is poorly constrained [8,48,49]. Three different σ_{NN} parametrizations were explored for this work. The first were free cross sections, that is, with no in-medium modification, determined by fitting to tables of data. The second, referred to as Rostock, was an energy dependent in-medium reduction, which is a parametrization of that given by Brueckner-Hartree-Fock microscopic calculations [50], described by

$$\sigma(\rho) = \sigma_{free} exp\Big(-0.6 \frac{\rho}{\rho_0} \frac{1}{1 + (KE_{cm}/150MeV)^2} \Big). \tag{1.11}$$

The last was a strongly density dependent in-medium reduction [43], referred to as screened, and described by

$$\sigma_\eta(\rho) = \sigma_0 tanh[\sigma_{free}/\sigma_0] \tag{1.12}$$

where $\sigma_0 = \eta\rho^{-2/3}$. The screened in-medium cross section reduction ensures that the geometric cross section radius does not exceed the interparticle distance. This is similar to requiring that the mean free path is not much less than one mono-layer of nucleons at normal nuclear density.

1.4 Organization of Thesis

The remainder of the thesis is organized as follows: Chapter 2 characterizes the experimental setup, both mechanical and electronic. A detailed description of the targets is also given. Then, chapter 3 chronicles the calibration procedures for all detectors and describes how events are selected based on the centrality of the reaction. It also describes how target oxidation is quantified. Next, chapter 4 explores many inputs of the BUU transport simulation

code such as momentum dependence of the mean field potential, light cluster production, and NN in-medium cross section reduction. Chapter 5 provides experimental data in the form of two and three-particle correlation functions. There, the dependence of p-p correlation functions on laboratory momentum, both in angle and magnitude is examined, as is the dependence on transverse momentum and center of mass rapidity. This chapter also includes corresponding source functions, and comparisons to BUU theory. Finally, chapter 6 summarizes the results and conclusions of this work. It also provides an outlook for the future. Appendices include a description of the precise laser measurements of detector positions, a description of the analysis packaged used, and an explanation of how to quantify the space-time extent of the source.

Chapter 2

Experimental Setup

The "4π+HiRA" experiment (NSCL-PAC number 03045 [51]) was performed in the fall of 2006 using stable beams from the National Superconducting Cyclotron Laboratory (NSCL) Coupled Cyclotron Facility (CCF) at Michigan State University. The experiment was named after the two detection systems, the soccer ball shaped NSCL 4π Array [52] and the High Resolution Array (HiRA) [53], used in the experiment. The experiment was located in the N2 vault, as shown in Fig. 2.1, which shows the layout of the experimental area at NSCL in 2006. Immediately after the experiment, the NSCL experimental area underwent major reconfiguration and the N2 and N3 vaults were combined into one vault. The 4π was decommissioned and its frame was placed in the Biomedical and Physical Sciences building on MSU campus as an exhibit, marking the end of an era of experiments with this device.

This chapter begins with a brief description of the reaction systems studied. It continues with a description of the purpose of each of the two detector arrays and a description of their layout. Next, the components of HiRA are explored in detail. This is followed by specifics of the 4π detector array. Then, a description of the targets is given. Finally, descriptions of

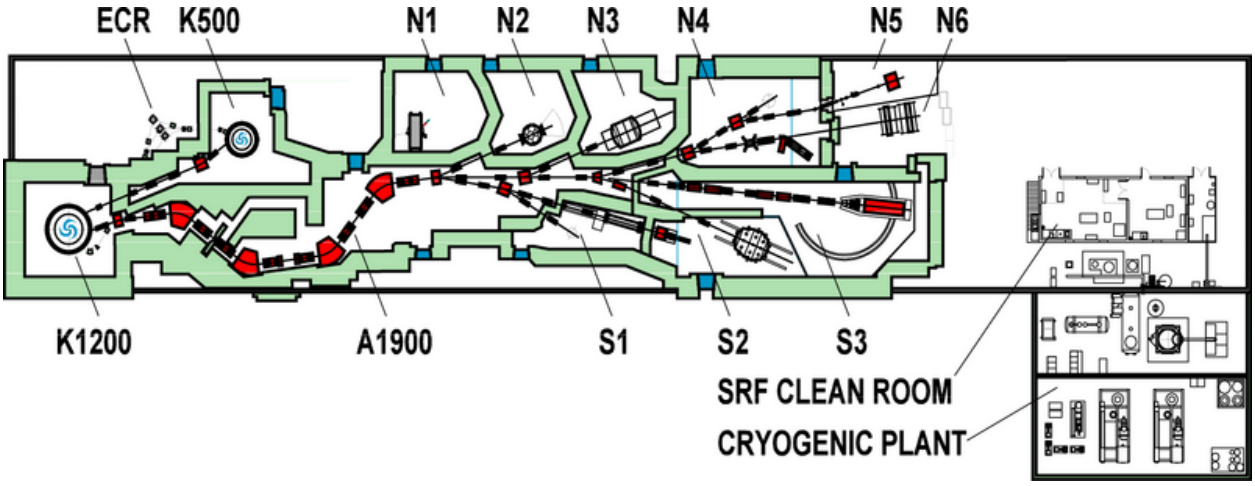

Figure 2.1: Layout of the CCF, from above, in early fall of 2006.

the electronics for HiRA, the 4π, and the trigger logic are provided.

2.1 Reaction Systems

^{40}Ca+^{40}Ca, ^{48}Ca+^{48}Ca, and ^{48}Ca+^{40}Ca reaction systems were studied at E/A = 80 MeV. This dissertation will focus on the two symmetric reactions for constructing correlation functions. While rare, unstable, neutron-rich beams would have been ideal for the studies in question, stable beams were employed to achieve the statistics needed for p-p correlation functions.

In addition, the ^{40}Ca+CH_2 at E/A = 25 MeV reaction was used. The hydrogen in the polyethylene (plastic) target was scattered into HiRA for calibration of the CsI crystals, as explained in section 3.1.2.

Both beams of ^{40}Ca and ^{48}Ca at E/A = 80 MeV impinged on a mylar foil target to monitor the calcium targets for oxidation, which is discussed more in section 3.3.

2.2 Experimental Layout

Two detector arrays were used in this dissertation experiment: The 4π detector array, which is comprised of the "ball" (shaped like a soccer ball) and a forward array[1] (FA), and a High Resolution Array (HiRA) [54]. The 4π array is a truncated icosahedron with 20 hexagonal modules, 10 pentagonal modules, and 2 pentagonal faces that serve as the beam entrance and exit. Each module in the ball houses 6 (hexagonal) or 5 (pentagonal) logarithmic detectors to be described in section 2.4. In addition, the forward array contains 45 phoswich detectors and is mounted on the exit pentagon. The 4π was used to determine the impact parameter using transverse energy. Nuclei with Z$\leq$3 could be identified in the ball and nuclei with Z$\leq$7 could be identified in the forward array. Individual isotopes could not be resolved in the 4π array.

HiRA, described in greater detail in section 2.3, consists of a variable number of telescopes. Each telescope is comprised of a single sided silicon strip detector, a double sided silicon strip detector and four CsI(TI) crystals. HiRA was used to identify Z$\leq$3 isotopes with good energy resolution for correlation functions. The excellent angular resolution of HiRA allows us to identify pairs of nuclei with a relative angle of less than 1°.

Seventeen telescopes of HiRA, arranged in five towers, were mounted on a custom made vacuum flange, shown in Figs. 2.2 and 2.3, replacing one hexagonal module of the 4π detector. The towers of telescopes were mounted on rails to easily separate them during assembly. The rectangular holes in the flange, seen in Fig. 2.2, were necessary for electrical feedthroughs. There were also water feedthroughs to allow for cooling of the detectors. The sides of each telescope canisters were mechanically modified to allow for close packing. The telescopes

[1] Referred to as the high rate array (HRA) in references [1, 5, 52].

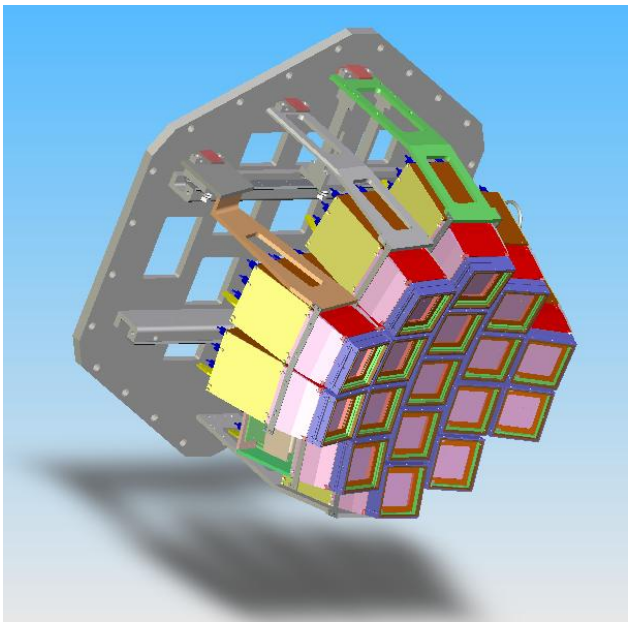

Figure 2.2: Drawing of the HiRA Array mounted on a modified 4π flange.

were angled so that the center of the front face of each telescope pointed to a common point 60 cm away, which was roughly the target position. From laser position measurements (see App. A), it was determined that the middle of the thick silicon detectors of the HiRA array were at an average distance of 61.9 cm from the target.

Fig. 2.3 shows HiRA just before insertion into the 4π and Fig. 2.4 shows most of the detector system with HiRA inserted. On the left of Fig. 2.4 is the side of the HiRA array and just left of center one can see the reflective faces of part of the forward array. The rest of the detectors are elements of the 4π ball. In this photograph, the beam comes in from the right and the forward array is downstream. Two more hexagonal modules were removed from the 4π for access to HiRA and the installation of a cryogenic vacuum pump.

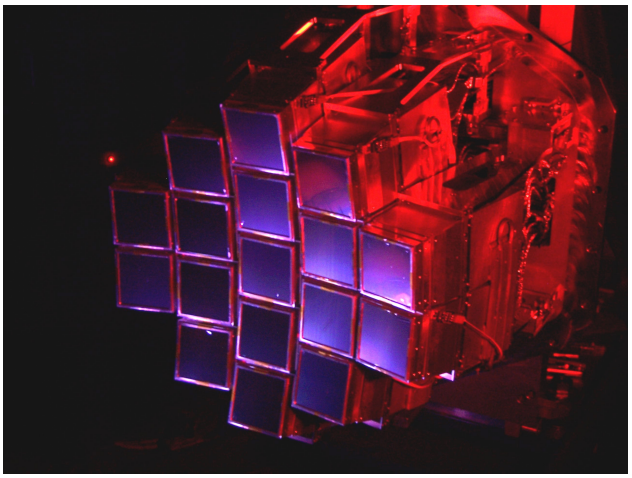

Figure 2.3: Photograph of the HiRA Array with special lighting.

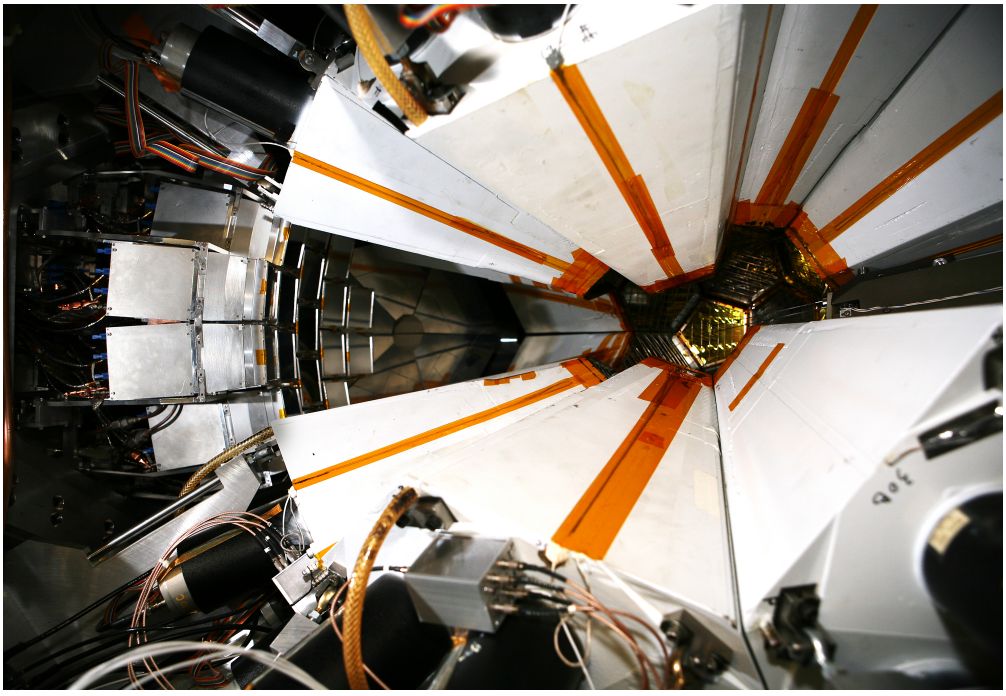

Figure 2.4: Photograph of the HiRA Array inside the 4π Array.

2.3 The High Resolution Array, HiRA

Each HiRA telescope, a schematic of which is shown in Fig. 2.5, is equipped with a thin 65 μm silicon detector, DE, with 32 vertical strips on the front and a thick 500 μm double sided strip detector, E, with 32 vertical strips on the front and 32 horizontal strips on the back. The E detector will be referred to as EF for the energy detected by the front strip and EB for the energy detected by the back strip. The double sided strips on the E detector provide 1024 pixels, each 1.95 mm by 1.95 mm for an angular width of $\sim 0.18^{\circ}$ at 62 cm. The silicon detectors are backed by four CsI crystals which are 39 mm in length on average. An excellent description of the HiRA telescopes is given by Rogers and Wallace [2, 3, 54]. Particles which stop in the E can be identified using DE vs E energy plots. Particles which stop in the CsI crystals can be identified using E vs CsI energy plots. In this dissertation, particles stopping in the E detectors are not analyzed.

Seventeen telescopes, arranged as in Fig. 2.6 and labeled by their number, were used in the experiment. Telescopes 4 and 17 did not have the DE installed since most protons at forward angles would have high enough energy to punch through the E detector into the CsI crystals. Telescopes 2, 7 and 9 have been excluded from this analysis due to malfunctioning electronics.

The HiRA array spanned roughly 18°-57° theta in the lab. The optimal angular coverage for the array is shown in Fig. 2.7. In reality, most detectors had some EF and EB strips which were not working throughout the experiment. The actual HiRA coverage can be seen in Fig. 2.8. Many channels of the chip electronics did not work properly. Also, the middle strips from each silicon detector are removed from analysis because particles hitting these strips will often pass in between two CsI crystals.

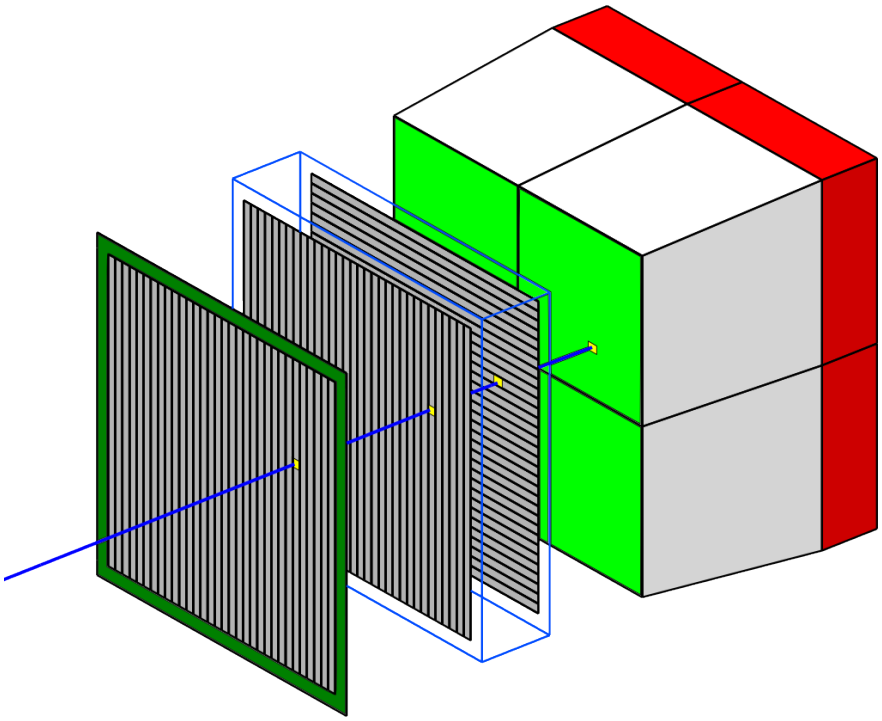

Figure 2.5: Drawing of HiRA telescope components [2].

During the experiment, all components of the telescopes had bias applied to them. All CsI crystals were biased to 80 V. The EBs were biased to 100 V. The biases for DEs and EFs are given in Table 2.1. The net bias across the 1.5 mm thick double sided silicon strip detector is the difference between the EF and EB bias values. Also in the table are sample leakage currents, which drifted during the experiment. These were monitored regularly during the experiment to ensure that there was no discharge on the silicon surfaces, or breakdown of the detectors. The telescopes are listed from top to bottom, and from forward to backward angles from the beam axis.

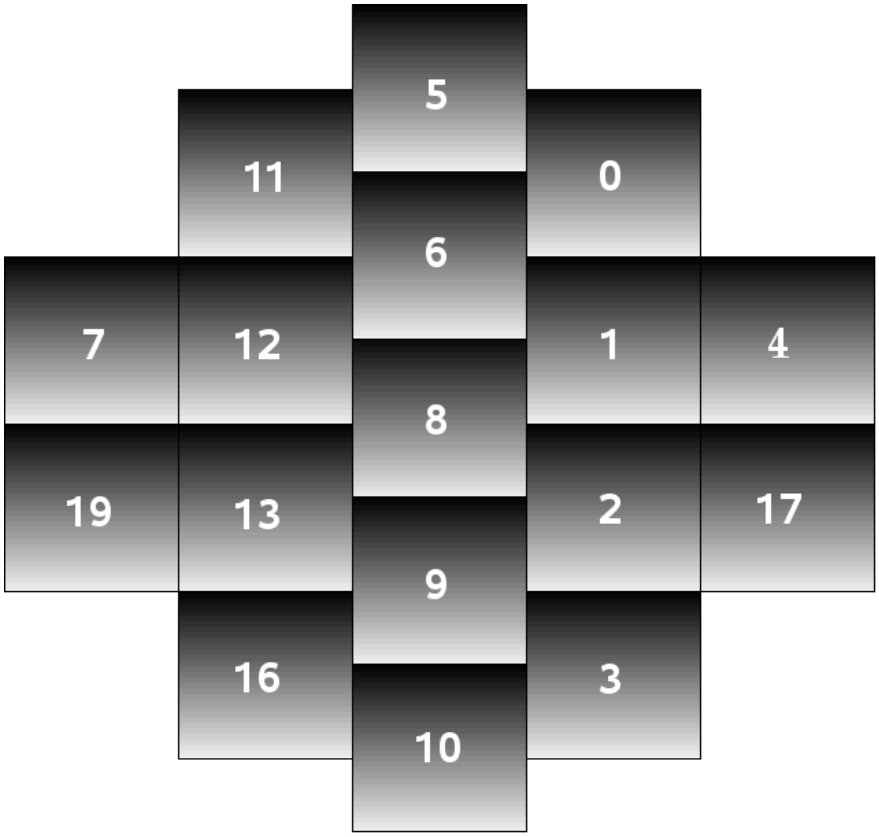

Figure 2.6: The HiRA array, labeled with telescope numbers, as viewed from the target. In this diagram the beam travels from left to right so that telescopes 4 and 17 are the most forward.

Tele #	EF Bias [V]	E Current [μA]	DE Bias [V]	DE Current [μA]
4	-200	1.64	-9	0.16
17	-200	1.90	-8	0.06
0	-190	0.70	-7	0.108
1	-250	1.60	-9	0.27
3	-315	1.34	-7	0.171
5	-240	2.38	-11	0.11
6	-340	1.78	-7	0.21
8	-360	1.80	-8	0.057
10	-150	1.58	-8	0.033
11	-250	1.36	-7	0.015
12	-340	1.72	-7	0.038
13	-310	1.48	-8	0.27
16	-160	1.76	-7	0.03
19	-210	1.04	-6	0.081

Table 2.1: Biases applied to E and DE detectors and corresponding sample leakage currents.

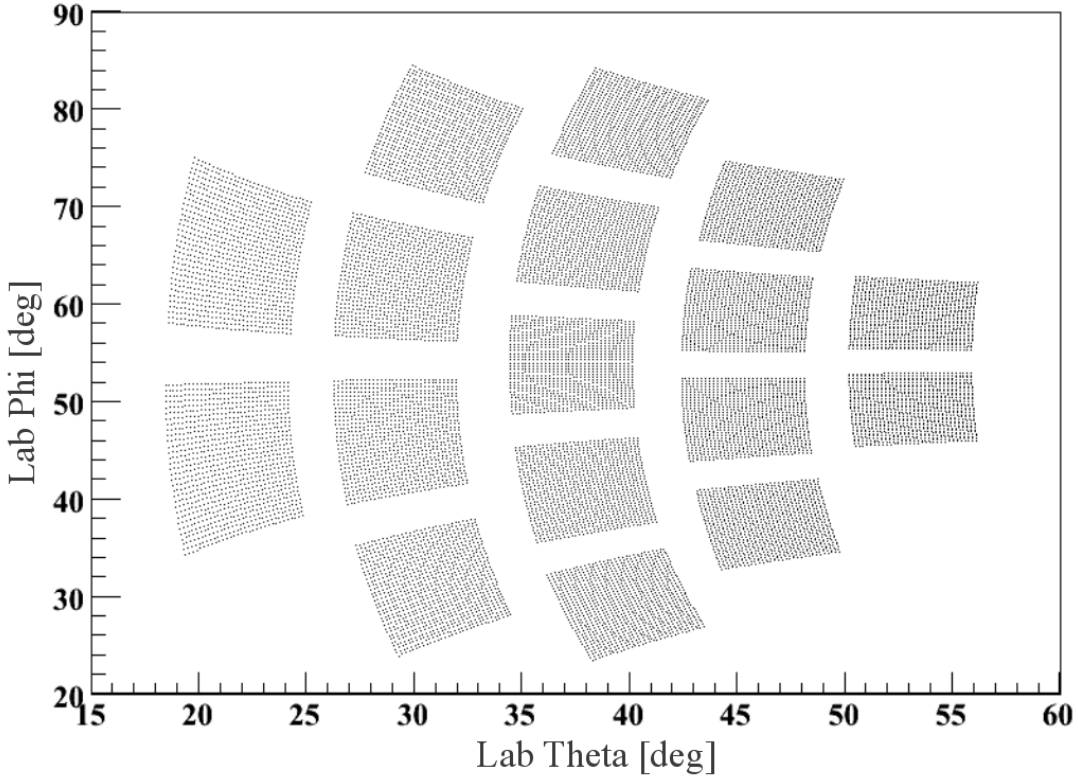

Figure 2.7: Angular coverage of the entire HiRA array.

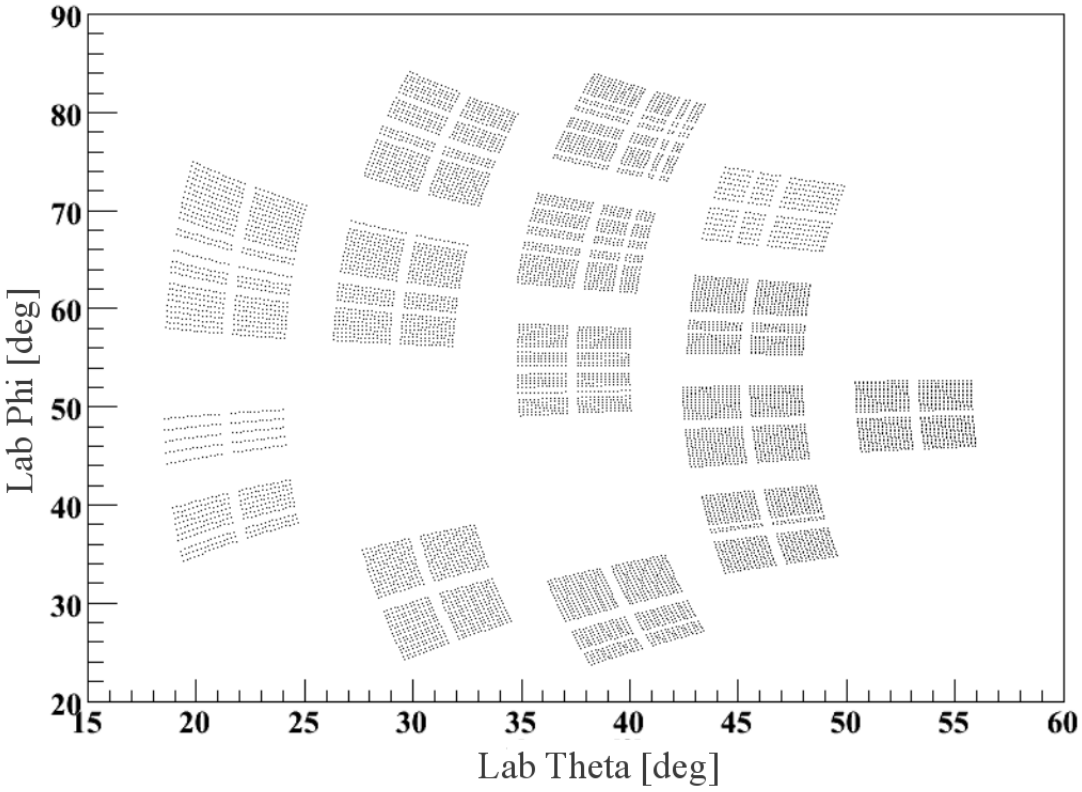

Figure 2.8: Actual angular coverage of the HiRA array.

2.4 4π Detector Array

The 4π Detector Array was a logarithmic detector system covering 3/4 of the total 4π solid angle. It was designed in late 1982 to detect all charged particles from intermediate energy collisions of nuclei. The detector system consisted of multi-wire proportional counters, Bragg curve counters, and fast and slow phoswiches. In addition there was a zero degree detector that was removed prior to this work. Only the phoswiches were used in this experiment.

The ball has an inside diameter of $70^{"}$, and is $101^{"}$ long, resulting in a volume of 3400 liters^3. RTV was used to seal the aluminum pieces of the framework, nicknamed the "soccer ball" for its shape. $145'$ of rubber O-rings were used to seal the modules and feedthrough plates [52].

Before this experiment, the 4π had sat dormant for a number of years. One of the first tasks was to make the chamber vacuum tight. After two weeks of leak testing, fixing leaks, and the installation of a cryogenics pump, a reasonable vacuum could be attained. During the experiment, the vacuum averaged 5x10^{-5} Torr and broke the 10^{-6} Torr mark just hours before the end of beam time.

Each hexagonal module in the 4π contained six phoswiches and each pentagonal module contained five phoswiches, whose front and rear surfaces were triangular in shape. The polar angle, with respect to the beam line, of the midpoint of each module in the array is given in Table 2.2 [52]. Each hexagonal module subtended a solid angle of 6 x 65.96 msr and each pentagonal module subtended a solid angle of 5 x 49.92 msr [52]. Module 5 was removed for the insertion of HiRA, module 15 was removed to have access to HiRA, and module 29 was removed to install a cryogenics pump to help obtain a better vacuum. After removing these modules, the ball covered 9.37 sr. The FA covered 280 msr giving a total of 9.65 steradians

Mod	A	B	C	D	E	F
	θ (°)	θ (°)	θ (°)	θ (°)	θ (°)	θ (°)
1-5	23.1	32.3	46.0	51.7	46.0	32.3
6-10	54.7	54.7	67.3	74.6	67.3	
11-15	64.9	72.4	86.5	93.5	86.5	72.4
16-20	86.5	93.5	107.6	115.1	107.6	93.5
21-25	105.4	112.7	125.3	125.3	112.7	
26-30	128.3	134.0	147.7	156.9	147.7	134.0

Table 2.2: Mean polar angles of the ball phoswiches.

Element	Thickness [mm]	Bicron plastic	Rise Time [ns]	Fall Time [ns]
Ball Fast ΔE	3	BC-412	1	3.3
Ball Slow E	250	BC-444	20	180
FA Fast ΔE	1.7	NE-110	1.1	3.3
FA Slow E	194	NE-115	8	320

Table 2.3: Thicknesses and composition of the phoswiches in the ball and FA. Rise and fall times are also given, although the signal from the photomultiplier tube for the thin scintillator will have much long rise and fall times.

or roughly 77% of total 4π solid angle.

Each phoswich was comprised of a thin wafer of fast plastic scintillator to detect the initial rate of energy loss as it entered the 4π module, and a thick slow plastic scintillator to stop the charged particle and detect the total energy deposited. Some specifications of the phoswiches in the ball and FA are given in Table 2.3 [52].

The forward array was comprised of 45 closely packed phoswich detectors, surrounding the exit beam line as shown in Fig. 2.9. Also shown in the figure is the relationship to the first ring of modules [5] and the HiRA array. While the θ angle can be conveniently defined with respect to the beam axis, the reference for ϕ is arbitrary. In Fig. 2.9 you can see the reference for ϕ, with 0° defined as the center of FA element 1. The polar and azimuthal angle for the center of each FA element is given in Table 2.4 [5].

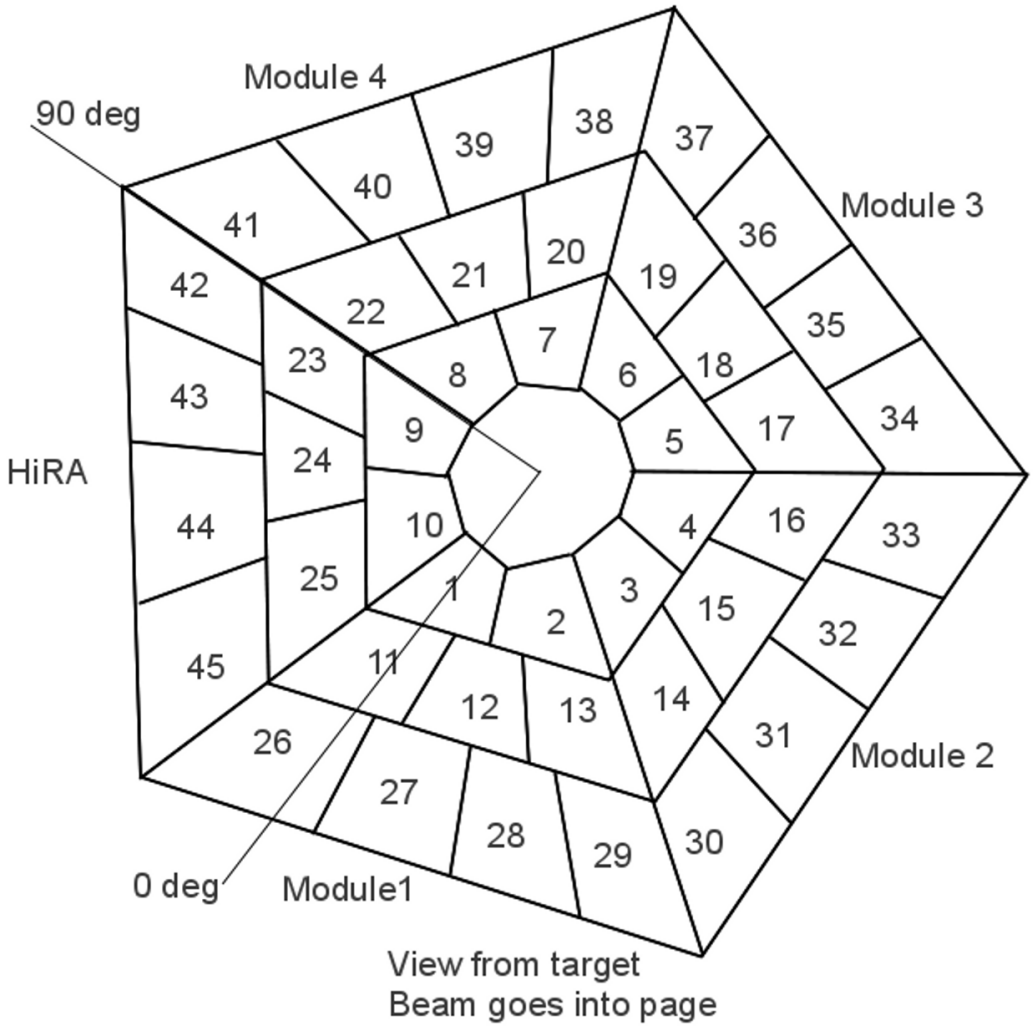

Figure 2.9: Schematic diagram of the forward array. Also shown is the lab reference for the azimuthal angle.

Detector	θ (°)	ϕ (°)	Detector	θ (°)	ϕ (°)	Detector	θ (°)	ϕ (°)
1	5.4	0.0	16	10.6	246.0	31	14.3	279.0
2	5.4	324.0	17	10.6	222.0	32	14.3	261.0
3	5.4	288.0	18	9.6	198.0	33	15.9	243.0
4	5.4	252.0	19	10.6	174.0	34	15.9	225.0
5	5.4	216.0	20	10.6	150.0	35	14.3	207.0
6	5.4	180.0	21	9.6	126.0	36	14.3	189.0
7	5.4	144.0	22	10.6	102.0	37	15.9	171.0
8	5.4	108.0	23	10.6	78.0	38	15.9	153.0
9	5.4	72.0	24	9.6	54.0	39	14.3	135.0
10	5.4	36.0	25	1-.6	30.0	40	14.3	117.0
11	10.6	6.0	26	15.9	9.0	41	15.9	99.0
12	9.6	342.0	27	14.3	351.0	42	15.9	81.0
13	10.6	318.0	28	14.3	333.0	43	14.3	63.0
14	10.6	294.0	29	15.9	315.0	44	14.3	45.0
15	9.6	270.0	30	15.9	297.0	45	15.9	27.0

Table 2.4: Mean angles of the FA phoswiches.

2.5 Target Details

A nuclear reaction occurs when a projectile nucleus strikes a nucleus in a target, which is a thin metal foil. The composition and thicknesses of targets used in this experiment are summarized in Table 2.5. Calcium targets were used for the nuclear reactions of interest.

Target	Thickness [mg/cm^2]
^{40}Ca	2.2
^{48}Ca	5.1
CH_2	2.95
mylar	0.9
scintillator	N/A
Natural Ni	4.6
empty frame	N/A

Table 2.5: List of targets used with their respective thickness.

A polyethylene target was used to elastically scatter protons for CsI calibration described in section 3.1.2. A mylar target was used to monitor the oxidation of the ^{40}Ca and ^{48}Ca targets, described in section 3.3. A scintillator target was used for initial beam tuning. A

natural nickle target was used for "target in" measurements and debugging procedures, while an empty frame was used for "target out" measurements to assess the amount of beam hitting the target frame. The particle rates in the FA of the MSU 4π Array were monitored during this process. The rates should be negligible when using a blank frame as a target, unless the beam is hitting the frame. During beam tuning, the "target in" to "target out" ratio was minimized to reduce the amount of beam on frame. This was especially important for the E/A = 25 MeV ^{40}Ca beam which was degraded significantly from E/A = 140 MeV and had a relatively large beam spot.

The calcium targets were rolled at the NSCL in a glove box filled with argon because calcium is highly reactive with oxygen. Most adhesives either require oxygen to cure or contain oxygen in them, therefore vacuum grease was used to "glue" the calcium targets to the aluminum frames. All frames used in the experiment were oblong shaped and rotated 37.5° so that the beam impinged on a circular target while the targets actually faced the center of the HiRA array. This had a dual advantage: The operators were able to tune on a circular target and the difference in energy loss of particles leaving the target was minimized. Had the target been perpendicular to the beam, it would have significantly degraded the energy resolution of the unbound resonances detected with the HiRA detectors.

The frames were connected to a base using carbon fiber rods, which are lightweight enough that the target would not sag appreciably, and yet flexible enough to be navigated by the target driver, "Freddy", into the cylindrical carousel shown in Fig. 2.10. "Freddy Krueger" was the nickname "fondly" given to the system of stepping motors and machinery used to move a target, by its base, from the carousel to the center of the ball. Freddy earned its nickname for its predilection of shredding targets and for its longevity.

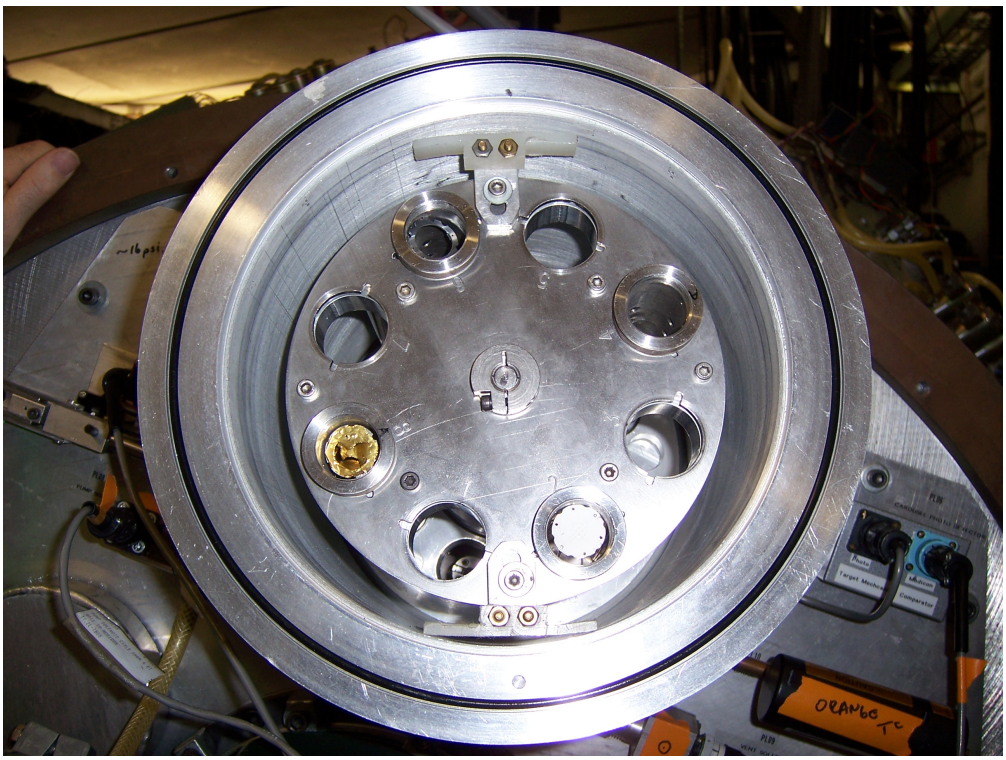

Figure 2.10: Photograph of target carousel which housed all targets used. Pictured, clockwise, are an old scintillator target at 5 o'clock, an old broken gold target at 8 o'clock, and a new empty oblong frame at 11 o'clock.

2.6 Electronics

2.6.1 HiRA

The electronics for the HiRA silicon detectors were housed outside of the vacuum chamber due to lack of space inside the chamber. There are 100 channels per telescope that need to be processed. All of these signals were routed through a vacuum tight flange using 32 pin individually shielded ribbon cables. Each detector required three cables, one for the DE, one for the EF, and one for the EB. Outside of the chamber, each cable was connected to a chipboard housing 2 Application Specific Integrated Circuit (ASIC) chips, where each chip can process 16 channels. A photograph of a chipboard with a prototype chip is shown in Fig. 2.11 with a quarter to provide a scale. In the case of the DE detectors, due to the high capacitance of the thin silicon, external pre-amplifiers were used to reduce noise on the onboard pre-amplifiers. The E detectors are thicker, and not as sensitive to electronic noise, thus the onboard pre-amplifiers were sufficient.

A maximum of 15 chipboards in principal can be connected to a single motherboard, shown in Fig. 2.12. Each motherboard distributes power for the chipboards, distributes high voltage for the detectors, and reads out all signals. In the version at the time of this dissertation experiment, each motherboard could only supply current to ten chipboards. The copper bars seen in Fig. 2.12 were necessary for cooling the chips which operate at $\sim 30^{\circ}$ C. Six motherboards were used in this experiment, two for DEs and four for Es.

The signal from the silicon is processed in the ASIC chip, which contains the preamplifier, shaper and discriminator circuitry, shown in Fig. 2.13 for a single channel. The chip itself provides several inspection channels for the user to inspect the preamplifier, shaper

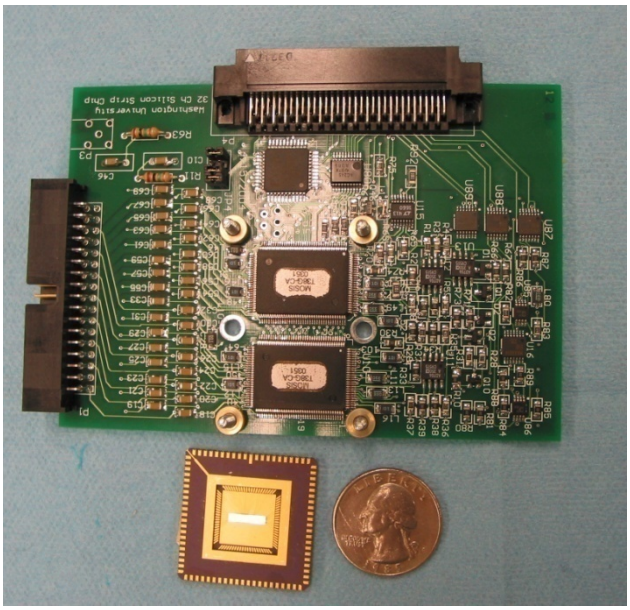

Figure 2.11: Photograph of chipboard with quarter for size comparison.

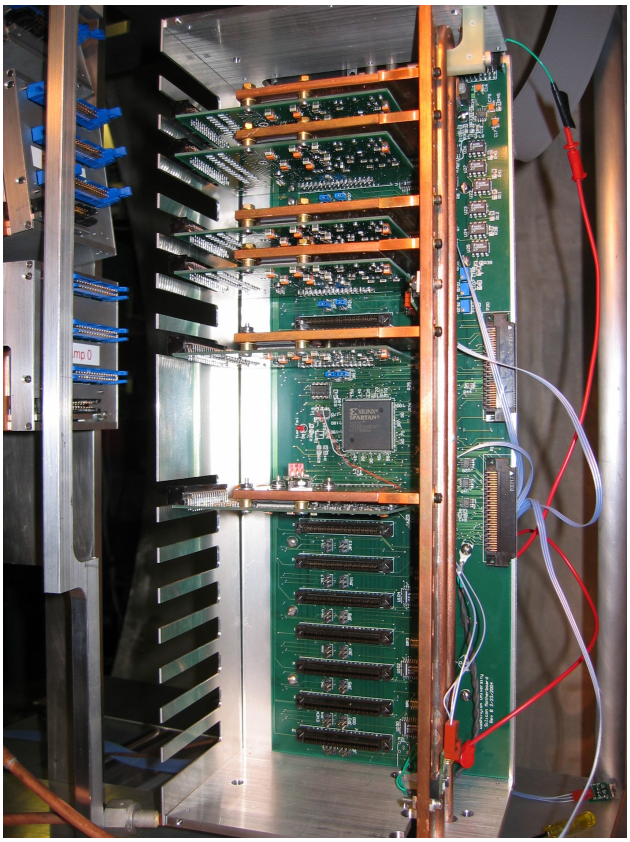

Figure 2.12: Photograph of HiRA motherboard with six chipboards installed.

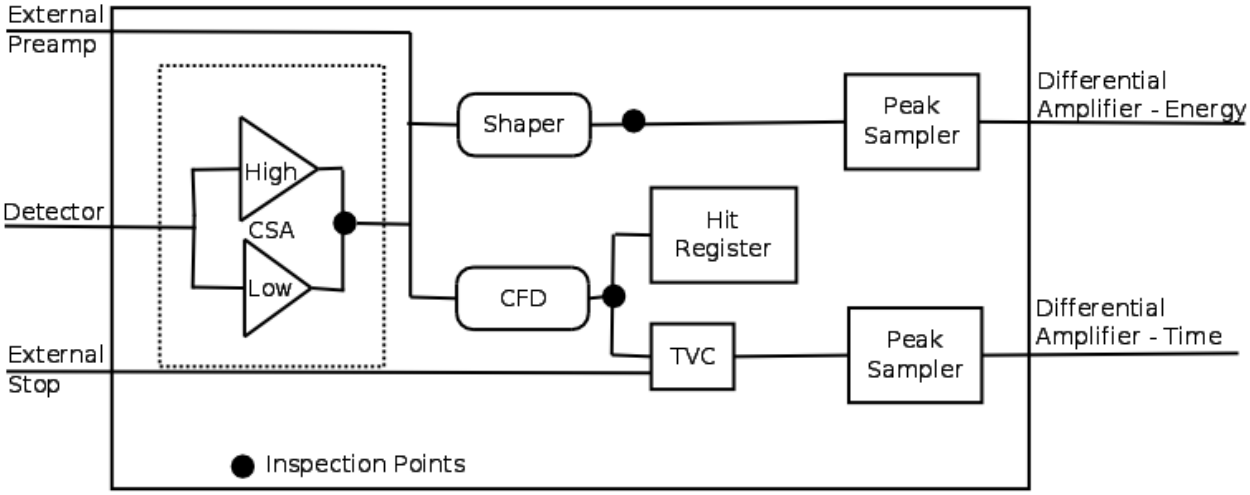

Figure 2.13: Diagram of the ASIC electronics logic. [2, 3]

and discriminator outputs. The settings of the ASIC chip, such as discriminator threshold and preamplifier gain, are controlled using an external program and set through an XLM (universal logic module). In the ASIC, the detector signal is split into time (not used in this experiment) and energy branches, which enter the Flash ADC (FADC) on a pair of double-lemo cables. This strategy reduces the number of electronic modules needed, as well as the number of cables, which is important when considering the high number of channels in HiRA.

The schematics of the HiRA silicon electronics is shown at the top of Fig. 2.14. The data were read out from the motherboard using an XLM. To start the XLM data acquisition, the XLM needed to be triggered. The XLM trigger in this experiment was generated based on signals in CsI exceeding multiplicity of one or two (HiRA trigger) in coincidence with a 4π signal exceeding a multiplicity of four.

When triggered, the XLM read in channel information from a motherboard and then sent a clock signal to the FADC to digitize the energy each time it had a trigger. The XLM generated a complete signal once it was finished acquiring data from the motherboard. In

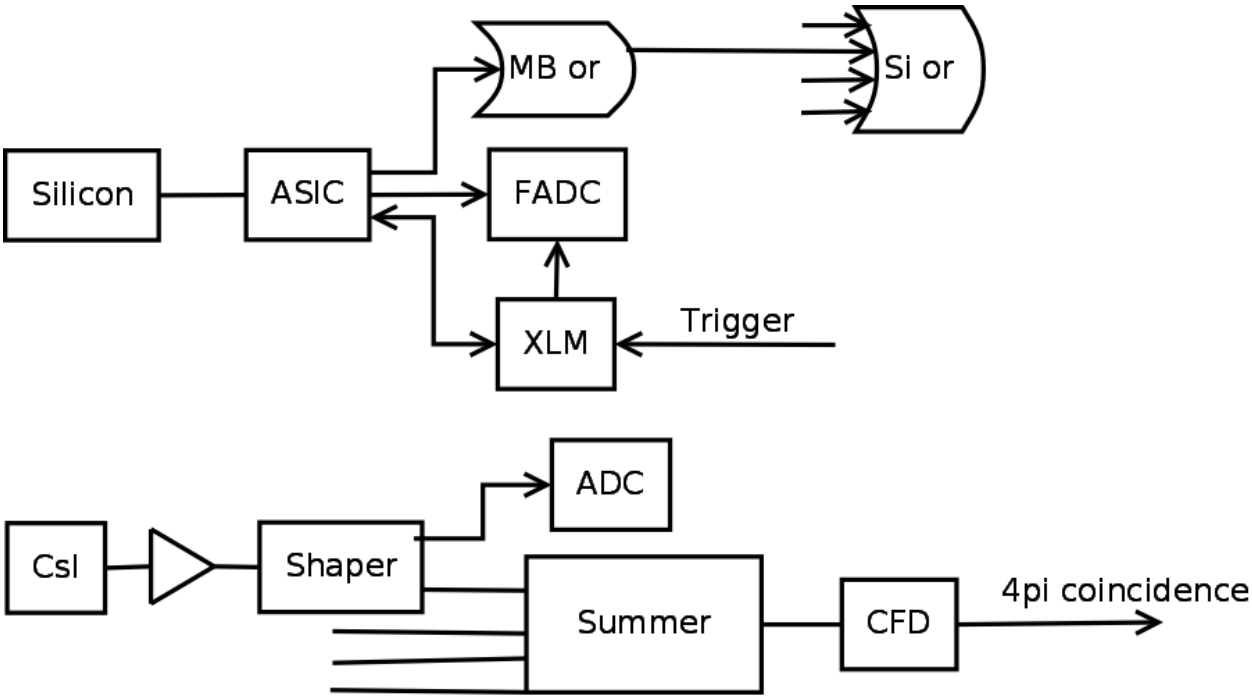

Figure 2.14: Diagram of the HiRA electronics logic. [2, 4]

the case of HiRA singles, the complete signal was used as a computer trigger. During regular data taking, it was the HiRA trigger in coincidence with the 4π that triggered the computer.

For the CsI crystals, shown at the bottom of Fig. 2.14, the pulses were processed in a preamplifier located inside of the HiRA telescope can. The signal was then routed into a CAMAC Pico System shaper/discriminator module before being routed to the ADC (CAEN V785). The sum output from Pico shaper/discriminator was used to generate total sum of all CsI signals in order to generate a multiplicity based HiRA trigger. This signal was sent in coincidence with 4π to generate XLM trigger and other important logic signals.

2.6.2 4π Array

An idealized current pulse from a phoswich detector can be seen in Fig. 2.15 where the solid line is the total signal, the dashed line is the fast component and the dotted line is the slow

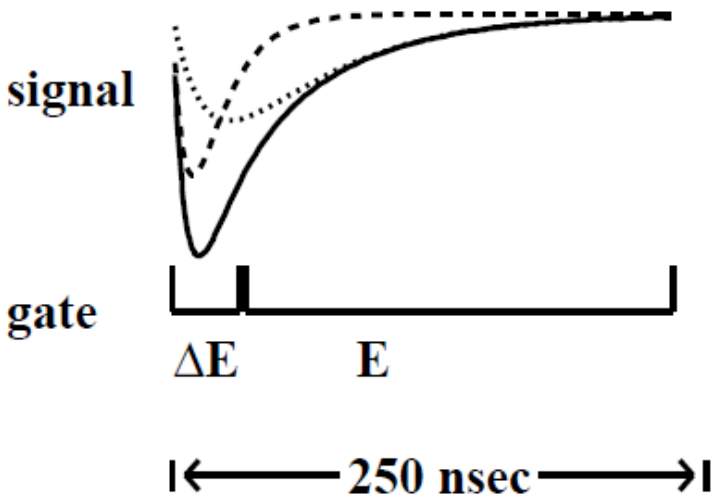

Figure 2.15: Idealized signal from a phoswich detector. [5]

component. The ΔE and E gates are shown to separate the fast and slow components. It can be seen that the signals overlap, and each is contaminated by the other. The method of disentangling them is necessary for generating accurate calibrations and that method is described in subsection 3.2.1.

Two independent and fairly similar electronic branches have been employed for the FA and ball, as shown in Figs. 2.16 and 2.17. The phoswich, photomultiplier tube (PMT), PMT base and voltage divider are housed inside of the vacuum chamber of the 4π. The PMTs serve to amplify the light created by the scintillator plastic. The bias for the PMT and the signal from it are transmitted over a single SHV cable for each detector. This cable is connected to a splitter where the signal is separated from the high voltage and split into fast (ΔE), slow (E), and time components.

The ΔE subbranch entered through a 100 ns passive delay before entering a V862 Caen QDC, which was used in a common gated mode by supplying a logical yes level to the individual gate inputs. Each ΔE had its own corresponding common gate corresponding

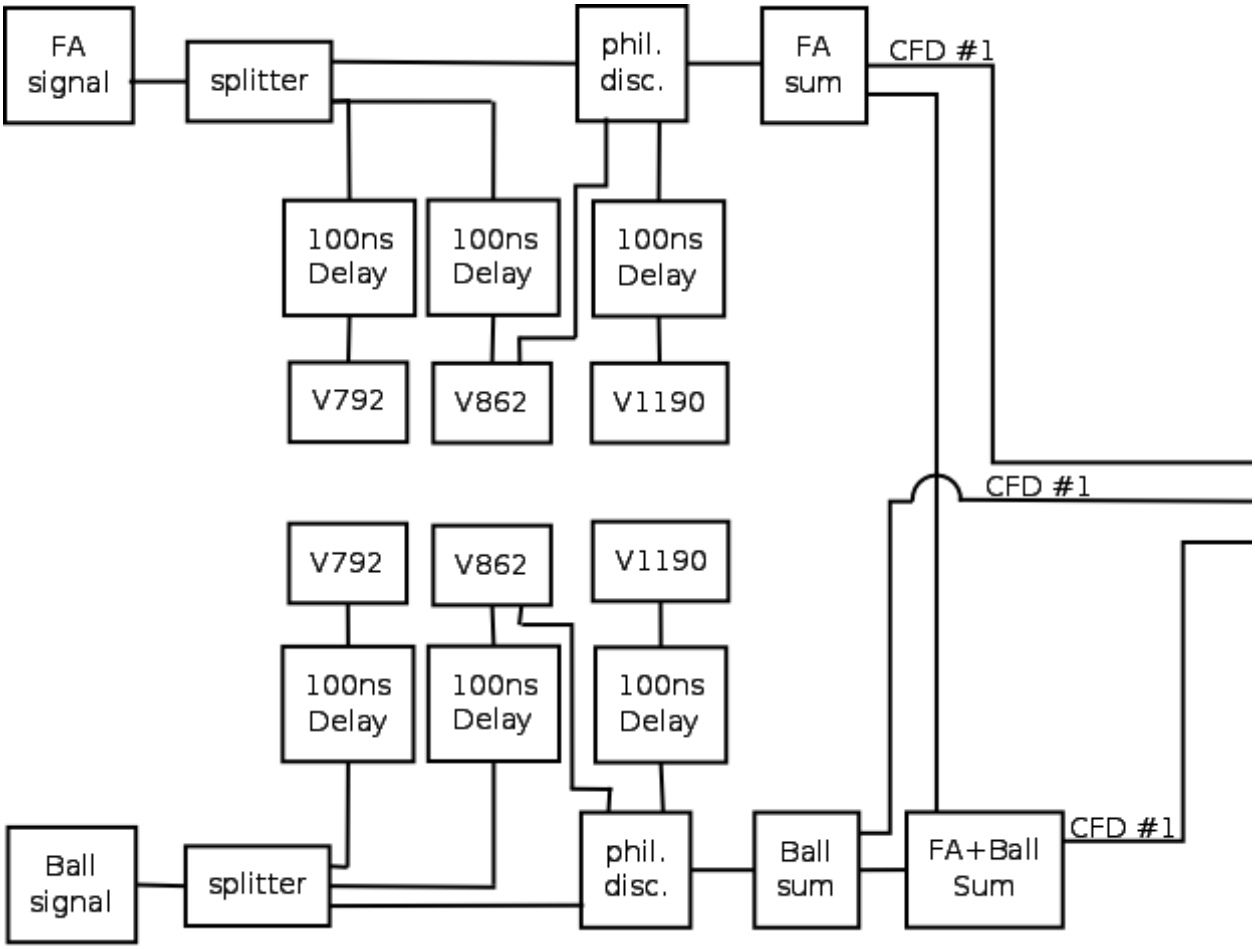

Figure 2.16: Diagram of the 4π electronics logic, part (a).

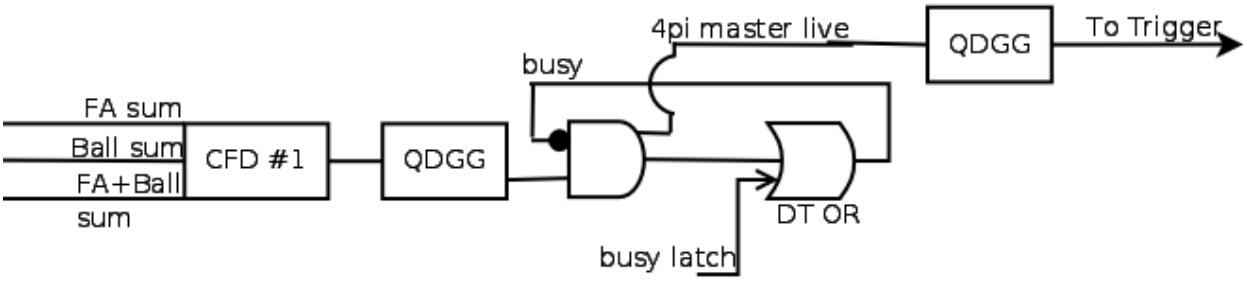

Figure 2.17: Diagram of the 4π electronics logic, part(b).

to an OR of the discriminators for the signal input to the QDC. The E subbranch entered through a 100 ns passive delay before entering a V792 Caen QDC which was used in common gate mode. Both of these modules were fast cleared if there were no valid HiRA data in coincidence with the 4π.

The time subbranch is processed in a Phillips 7106 discriminator. The sum output of the discriminator was used to enter summers to generate total, ball or FA+ball sum signal. Each Phillips discriminator preamplifier output corresponds to $\sim$50mV per channel fired. The total sum of the FA+ball can thus be used to generate multiplicity based 4π trigger signal. In this experiment a multiplicity at least four in the FA+ball was required to reject the most peripheral events. The sum signal was processed in a constant fraction discriminator to the master live signal, which was the 4π trigger signal, also used to generate the slow E gate. To generate time information, time signals from the Phillips discriminator are also sent to V1190 TDC as individual start signals. Stop for the TDC is provided by the 4π master live plus HiRA coincidence. This was a substitute for a fast clear since this module did not have one.

2.6.3 Trigger Logic

For the purpose of taking regular data, data events were only recorded if there was a HiRA event in coincidence with an event in the 4π. The coincidence trigger logic is shown in Fig. 2.18. For the data acquisition to trigger, a multiplicity greater than one (or two) in the CsI crystals was required, fulfilled by setting a threshold on sum of CsI discriminator signals. This signal entered a coincidence with 4π master, which was selected based on FA+ball multiplicity above four. The lower portion of Fig. 2.18 shows the busy logic, which was used

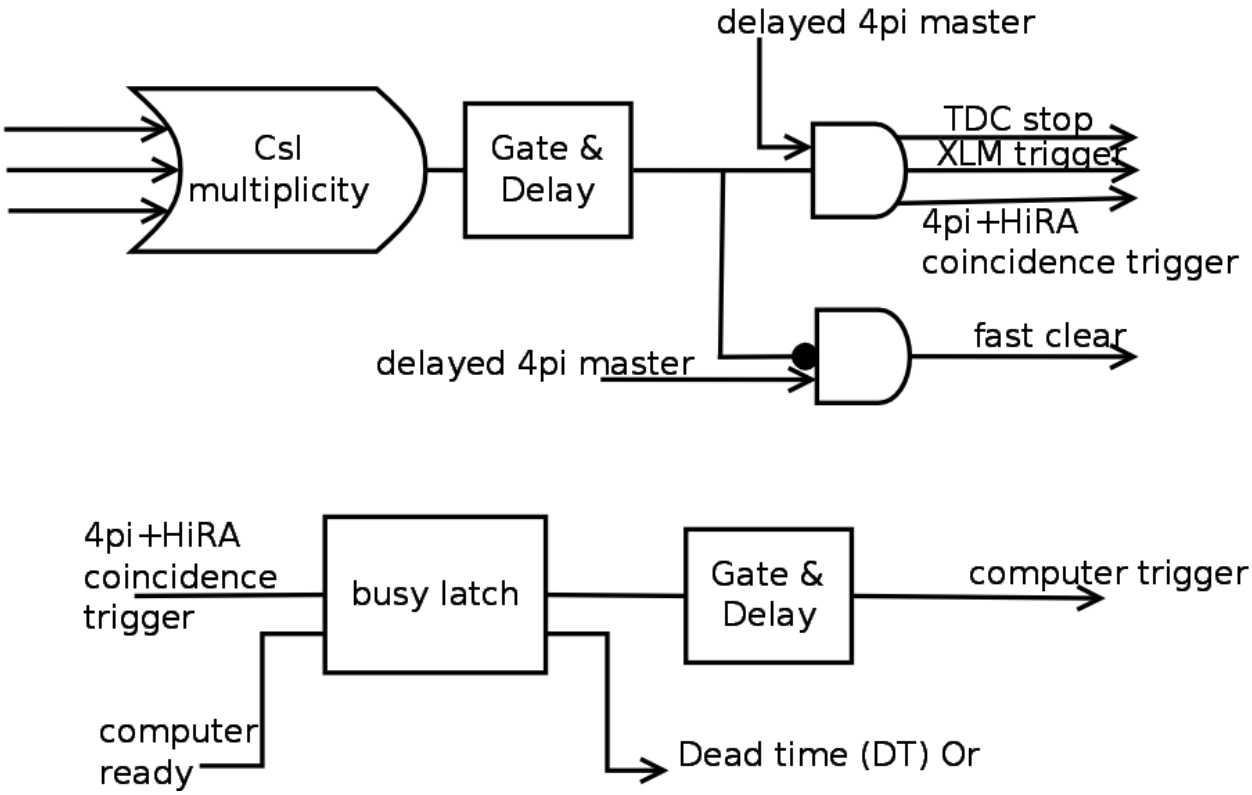

Figure 2.18: Diagram of the coincidence trigger logic. [6]

to generate the computer trigger. If a HiRA and 4π coincidence signal was generated and the computer was ready to acquire the data, the computer trigger signal was issued. CsI multiplicity two events were recorded to construct the numerator of the correlation functions while multiplicity one events were recorded to construct the denominator of the correlation functions.

A variety of other triggers were also needed and employed. An FA singles trigger was used for target in, target out measurements. An FA+ball singles trigger was used for debugging and minimum bias runs used for impact parameter selection. A HiRA singles trigger was used for debugging HiRA and setting thresholds. For the CsI calibration runs the data was triggered by multiplicity one in the CsI crystals, while vetoing events with any data in the 4π.

Chapter 3

Data Analysis

Detectors do not immediately provide the energy of particles detected. They provide a signal which is digitized, processed by various electronics modules, and encoded before being written to a computer file. In this thesis experiment, one hundred hours of experimental data corresponds roughly to one hundred gigabytes of raw computer data. This data must be transformed, processed, and condensed into meaningful physics quantities. Detailed information about the nature of this processing can be found in Appendix B.

This chapter explains preliminary analysis, including the method with which the raw electronic channels were converted into energies for each detector component. HiRA calibrations are described first, beginning with a discussion of silicon strip calibrations and finishing with the CsI crystal calibrations. The 4π section is next, starting with the calibration of the phoswiches and ending with a detailed description of the selection of central events. The final section in this chapter quantifies any oxidation of the calcium targets during the experiment.

3.1 HiRA

Each component of HiRA, (DE, EF/EB, and CsI) was calibrated separately. However, the same basic procedures were followed for both silicon detectors and will only be described once. Any differences in the calibrations for the silicons will be highlighted. The CsI calibration will then be described in depth.

3.1.1 Silicon Calibration

There are two stages in calibrating a silicon strip detector. The first step is to test the linearity of the electronics with a pulser, and the second step is to calibrate each strip with an α source. It was discovered that an additional correction step was needed, and this is discussed in Subsection 3.1.1.1.

A precision BNC PB-5 pulser was used to send specific voltages to the test input of the Si detectors, mimicking a real signal from a particle. A pulser ramp was performed, with 21 steps at 0.25 V intervals. There were no significant non-linearities found on any of the channels.

The second stage of silicon calibration involves exposing all strips to an α source. At the end of the experiment, a ^{228}Th α source was employed to calibrate the DEs and the Es on the two most forward telescopes, 4 and 17, which had no DE installed. However, the α particles stopped in the DE detectors in the other telescopes. Thus, these DE detectors were removed to calibrate the E detectors. Fig. 3.1 shows the decay chain of ^{228}Th with prominent energies for the α source listed in red. These five energies are used for calibration purposes. Fig 3.2 shows an example of an α energy spectrum for one single strip in an E detector. The five most prominent peaks are those used for calibration purposes.

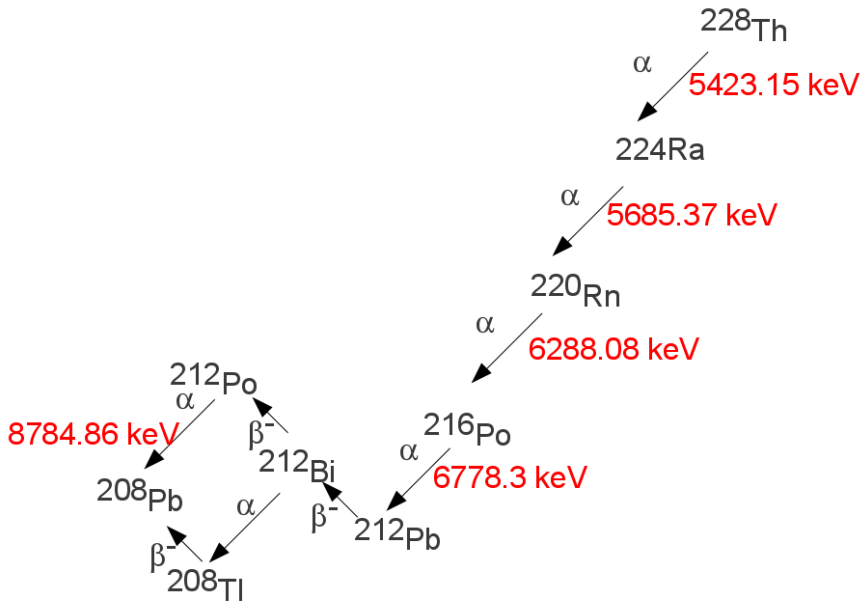

Figure 3.1: Decay chain for ^{228}Th. Energies of prominent α particles are given in red.

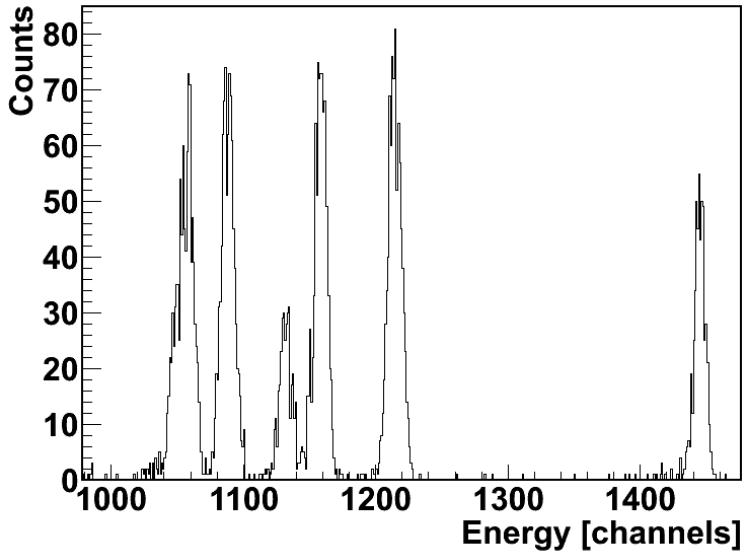

Figure 3.2: Example of a raw α spectra for a single strip.

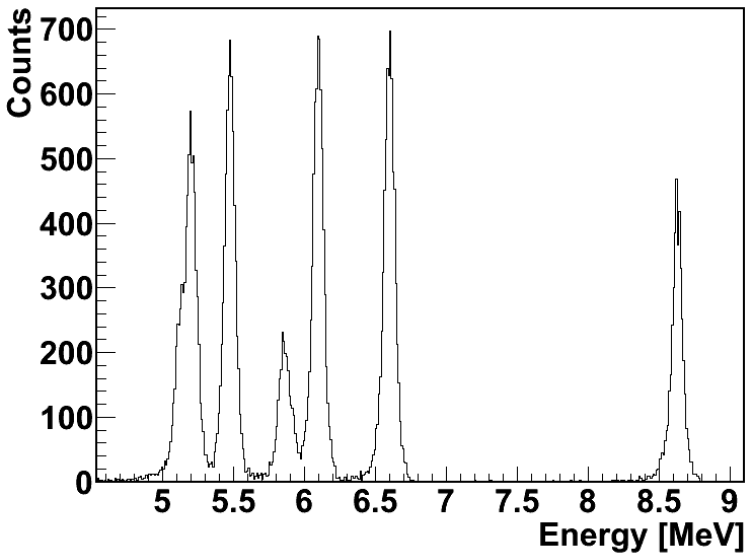

Figure 3.3: Example of a calibrated α spectra for all EF strips in one detector.

A variety of energy losses must be taken into account when using an α source to calibrate silicon strips. The α particles lose energy going through a 50 μg/cm^2 thick gold window seal on the source itself. They then lose energy going through 1.9 μm thick aluminized mylar foil covering each detector. Finally, the α particles lose energy going through an inactive layer of the silicon surface called the dead layer. After these energy losses are taken into account, all strips are calibrated with a linear extrapolation between channel numbers and known energies. The result is a calibrated spectrum such as that shown in Fig. 3.3.

3.1.1.1 Readout Order Corrections

This experiment used the first version of the Application Specific Integrated Circuit (ASIC) electronics developed by collaborators at Washington University in St. Louis. It was noticed during this experiment that the channel number corresponding to a particle with a given energy is dependent upon the order in which the electronics reads out that channel, hence the name "readout order problem." This experiment ran in sparse mode which means only

channels with a signal above threshold are read out. Channels are read out in a specific order each event. In a given motherboard, chipboards are read out from bottom to top. The chipboards for EBs are always lower than those for EFs, so they are always read out first.

The "readout order problem" results from digital-analog cross-talk. The digital signals from control logic of the ASIC during readout add to the amplitudes of the analog signals that are present and sent out from the switched capacitor array to the ADC. The cross-talk actually occurs at the ASIC level, so it could only be removed with a redesign of the ASIC, which was completed after this experiment.

Suppose only one particle enters a HiRA detector for a given event. If the particle deposits 5 MeV in an EB strip, its shaped signal would be digitized in the ADC to provide data in a channel value of 667 in accordance with the approximate energy calibration of 7.5 keV/channel. Now suppose instead, another particle deposits 40 MeV in another EB strip. With the same conversion, a channel of 5333 would be expected. However, such an energetic particle may also induce cross talk on neighboring strips in the same EB detector. Although the cross-talk signal may be small, the electronics for these other strips will often be triggered by these cross-talk signals. Most likely, one of these other strips will also be read out before the strip that measures the 40 MeV particle. Thus, there may be a number of strips with data in the EB chipboard electronics for this event. The value recorded by the data acquisition for each strip will depend both on the charge collected and also the order that this strip is read out during the event. For example, if this strip with the 40 MeV signal is read out later, and is not the first channel read out, it may not register channel 5333, but another value such as 5365. The shift depends on the precise order of the readout. There is a specific shift in channel if the 40 MeV signal is the second channel read out, another if it

is the third read out and so on.

Each face of each detector is connected to two ASICs. Chip 0 reads out the even strips, and chip 1 reads out the odd strips. Chip 0 is read out before chip 1. Depending on how large the signal is, up to 2 strips on each side may be affected, which means the signal, which contains the useful data, may be read out as 1st, 2nd, 3rd, or even 4th strip due to the cross talk between neighboring channels. In addition, there can be real particles in the detector and in the ASIC, doubling the number of nonzero readout channels. The actual digitized channel number recorded is affected by this order, and the readout order shift must be removed during the analysis process. The average correction for the order on the chipboard is listed below:

- 1st channel read out = no shift
- 2nd channel read out = 22-24 channel shift $\sim$ 180 keV
- 3rd channel read out = 11-13 channel shift $\sim$ 80 keV
- 4th channel read out = 8-10 channel shift $\sim$ 70 keV

The shift in the channels due to the readout order on the chipboard is independent of the size of the original signal. It only depends on the order in which that signal is read out.

There is another readout order correction. Up to 8 chipboards with 2 chips each are housed on one motherboard. The order in which the chipboard is readout also affects the corresponding channel number. This correction is only 2-3 channels, however, at 7.5 keV/channel, correcting for this can improve the resolution by 10-20% [55]. The motherboard and chipboard corrections just sum together, although they affect the channel number in opposite directions.

The DEs were not affected by the readout order problem because they used external preamplifiers. This confirms that the cross-talk problem involves coupling the digitized control signals on the ASIC on to the analog signals on the CSA (preamplifier) of the ASIC. In order to properly calibrate the EF and EB using alpha spectra, one must correct for the order in which each strip is read out on the chipboard and within the motherboard. This can affect the calibration by 0.5%. It is important to calibrate the EF and EB as accurately as possible since their energies are used in the calibration of the CsI crystals described in the next section.

3.1.2 CsI Crystal Calibration

The photodiodes produce an electronic signal which is linearly proportional to the light produced by the particle detected in the scintillator. This signal is amplified in the electronics and digitized by the Analog to Digital Converter (ADC). This may result in small non-linearities in the relationship between the signal produced by the photodiode and the channel number calculated by the ADC. There are four possible steps in calibrating proton energies in a single CsI(TI) crystal. First one needs to correct for non-linearities in the electronics. Second, one needs to determine when the particle is a proton. Third, one needs to calculate the offset, which is the channel number corresponding to zero energy. Fourth, one needs to determine the gain, which is the number of channels per MeV.

3.1.2.1 Linearization

As a first step, these non-linearities are checked and corrected for by using a precision electronic pulser. Depending on the charge and mass of the detected particle, the light

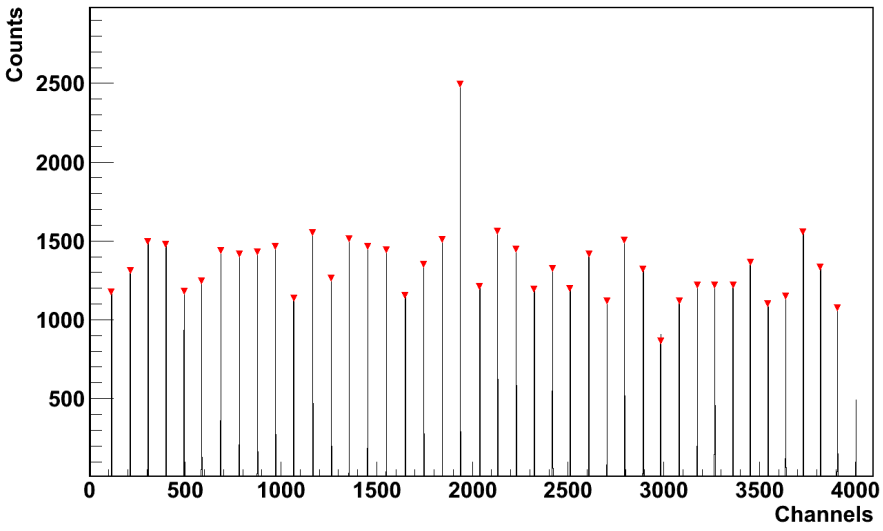

Figure 3.4: Pulser ramp for Telescope 0, crystal 0. The red triangles are the peaks as found by ROOT [7].

output from the crystal can be a non-linear function of the energy deposited by particle in the CsI scintillator. Light output non-linearities have been previously investigated [56]. The results of prior investigations have been used to correct the non-linearities of $A > 1$ particle energies. Such non-linearities are small for protons, but can be much larger for low energy heavy particles.

To determine the non-linearity, a pulser ramp was used. Electronic pulses with evenly spaced voltages with known values were sent into the test input of the CsI pre-amplifiers. Because some pulser amplitudes may be too low or too high to be within the channel range of the ADC, the middle pulse, with half the maximum voltage value, was recorded for twice as long, giving twice as many pulses so that it can be easily seen and identified, as in Fig. 3.4. The middle pulse is then used to identify the voltage values for all channel numbers.

After plotting voltage vs channel number, as shown in Fig. 3.5, each crystal was fit with a 3rd order polynomial in the range of interest. This polynomial function allowed us

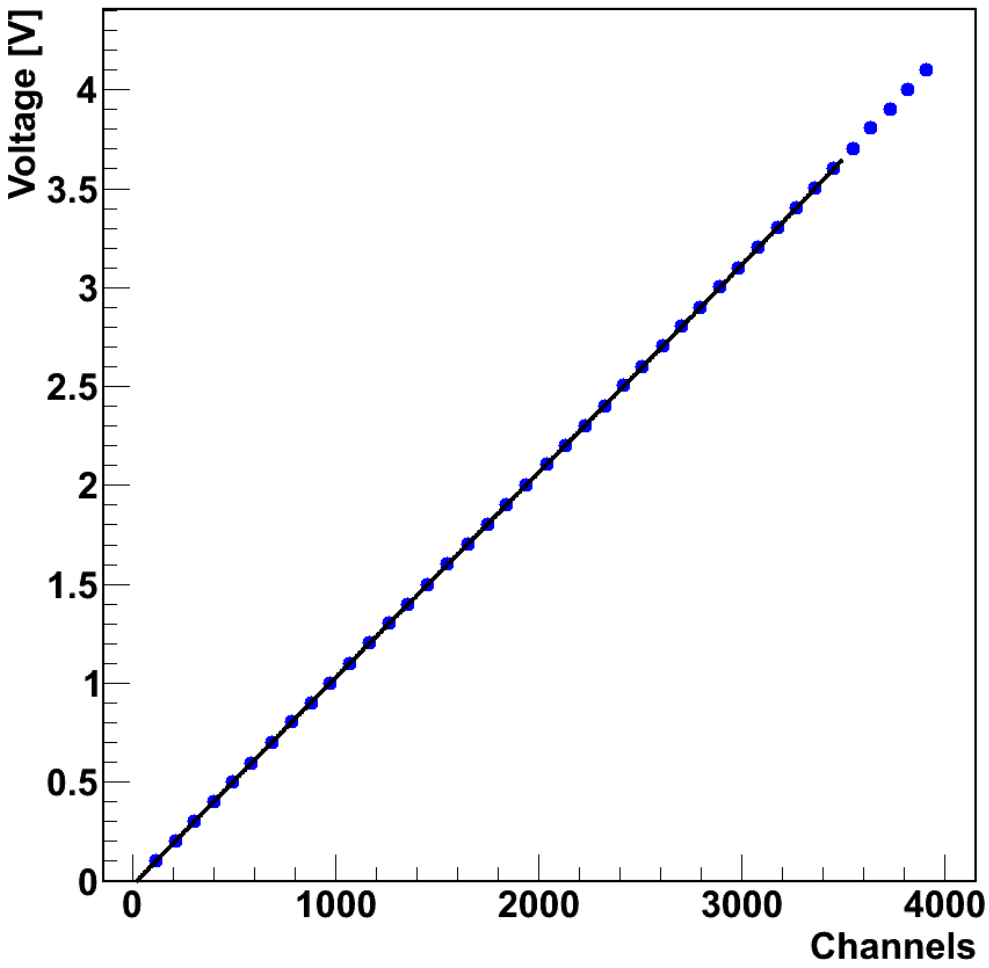

Figure 3.5: A 3rd order polynomial was used to fit the pulser data due to slight non-linearities in the electronics. Shown here are the pulser data and fit for one crystal in telescope 0.

to convert from non-linear channel numbers (up to $\approx$ 3500) to linearized voltages. To ensure the accuracy of the fit, the difference between the input voltage was compared to the reconstructed voltage from the fit with a 3rd order polynomial. This difference is plotted as a function of channel number in Fig. 3.6 for crystal 0 from telescope 0. All differences are smaller than 2 mV. The second stage in the calibration procedure, particle identification is discussed below.

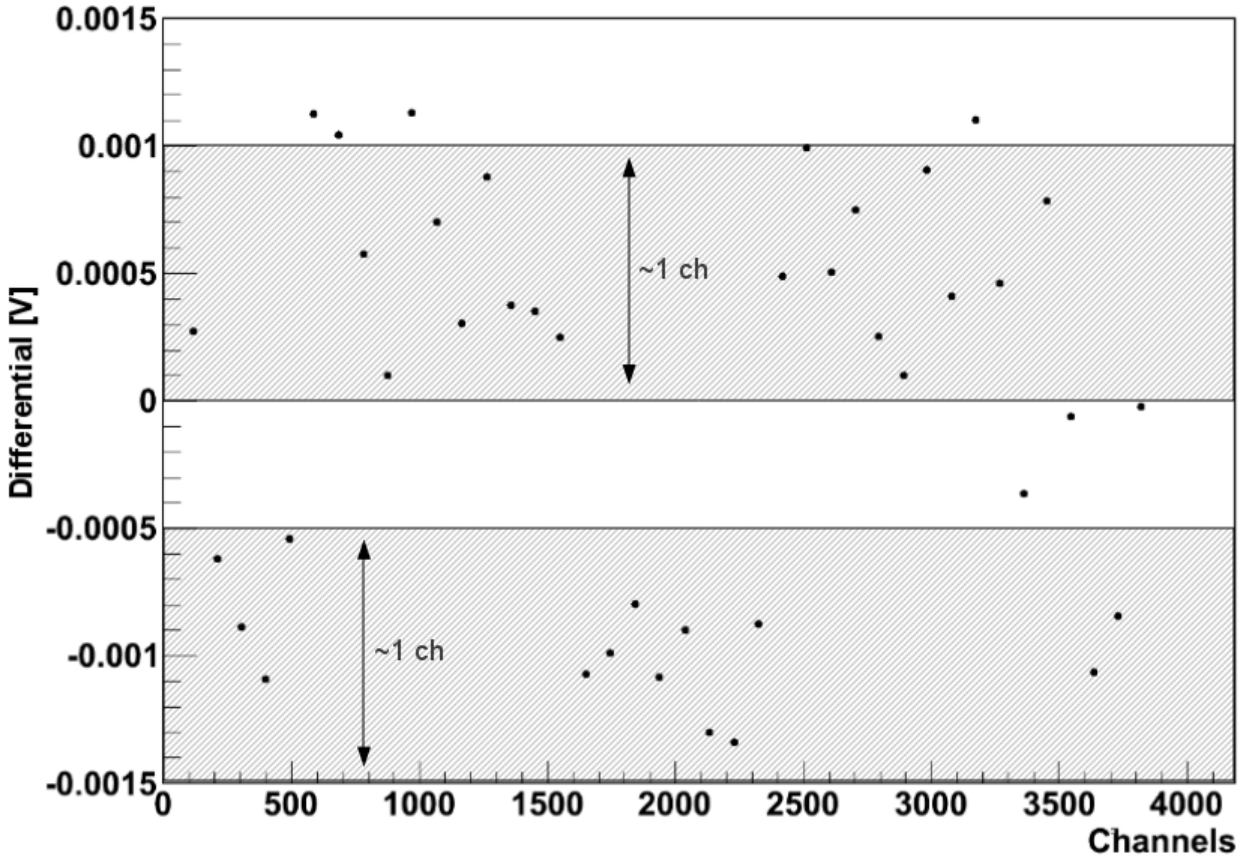

Figure 3.6: The difference between the input voltage and fit voltage is plotted as a function of channel number.

3.1.2.2 Particle Identification (PID)

In order to calibrate the CsI detectors, each species of particle must be accurately identified. Particles can be separated based on their charge and mass by taking advantage of the Bethe Bloch formula

$$-\frac{dE}{dx} = \frac{4\pi}{m_e c^2} \cdot \frac{nZ^2}{\beta^2} \cdot \left(\frac{e^2}{4\pi\epsilon_0}\right)^2 \cdot \left[\ln\left(\frac{2m_e c^2\beta^2}{I \cdot (1-\beta^2)}\right) - \beta^2\right] \tag{3.1}$$

which shows that the energy lost by a particle traversing through a material is proportional to the square of the charge of the incident particle. Other factors in the formula are β, the velocity scaled by the speed of light, n, the electron density of the material, and I, the mean excitation potential of the material. Approximating the kinetic energy by $\frac{1}{2}mc^2\beta^2$, one can show that the Bethe Bloch equation can be approximately reduced to $\frac{dE}{dx} \propto \frac{mz^2}{E} f(v)$ where *f(v)* is a slowly varying function of velocity. Thus, when the energy lost in the silicon is plotted against the energy deposited in the CsI, the data are organized into bands, of which each corresponds to a different isotope. Examples of these particle identification bands can be seen in Fig. 3.7 and 3.8 which are from the collisions ^{40}Ca+^{40}Ca and ^{48}Ca+^{48}Ca respectively.

The bottom three bands are the hydrogen isotopes, starting with protons on the bottom, deuterons in the middle, and tritons on top. The next two bands are the abundant helium isotopes, helions and alphas. While ^{5}He is absent, there is a faint ^{6}He line above the alpha line. ^{6}Li and ^{7}Li can then be seen at the top of the PID. Shown here are fully calibrated PID for all EF strips and CsI crystals in all telescopes. In order to calibrate a CsI crystal, PID must be generated for each crystal separately.

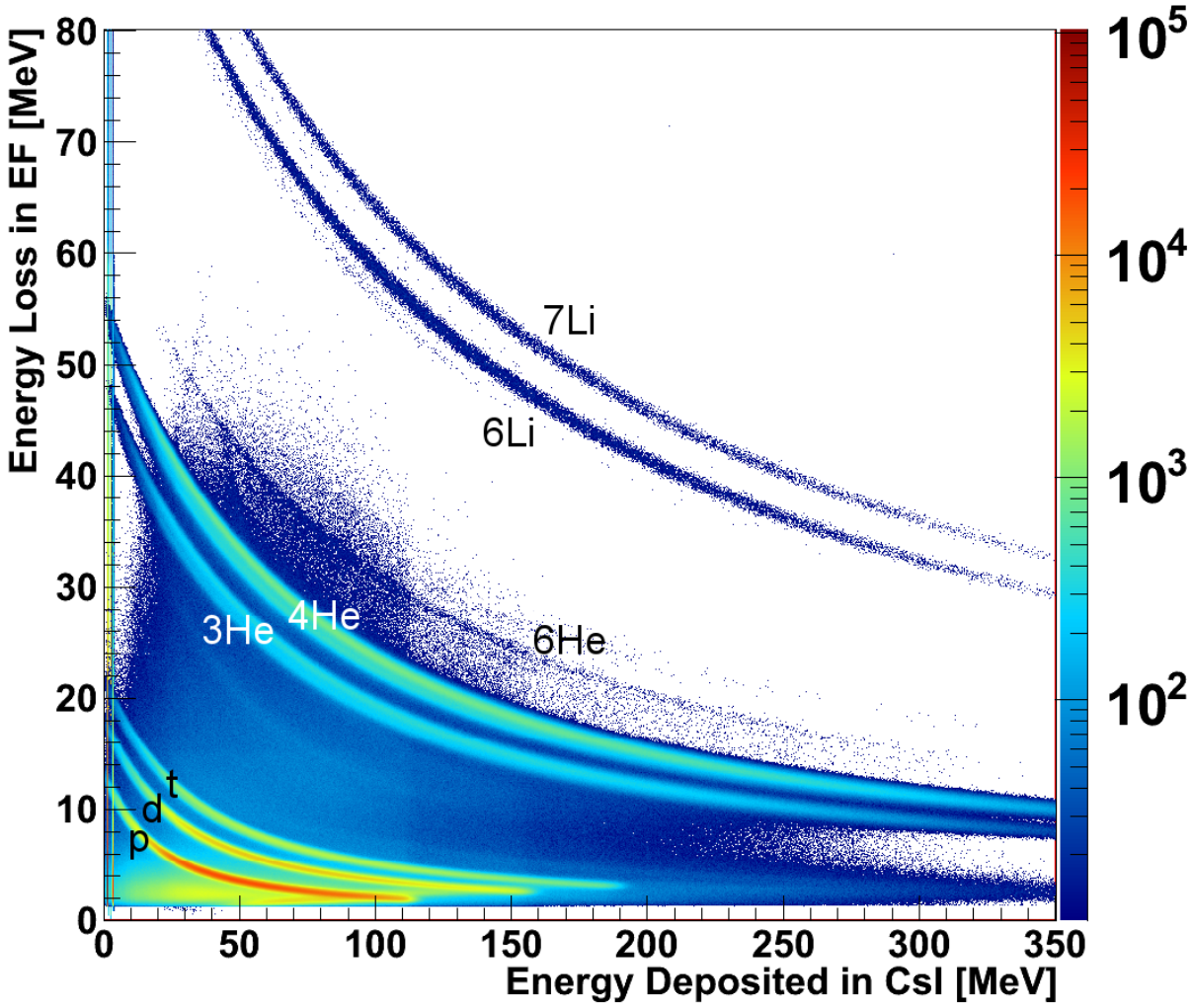

Figure 3.7: Calibrated PID for all ^{40}Ca+^{40}Ca data.

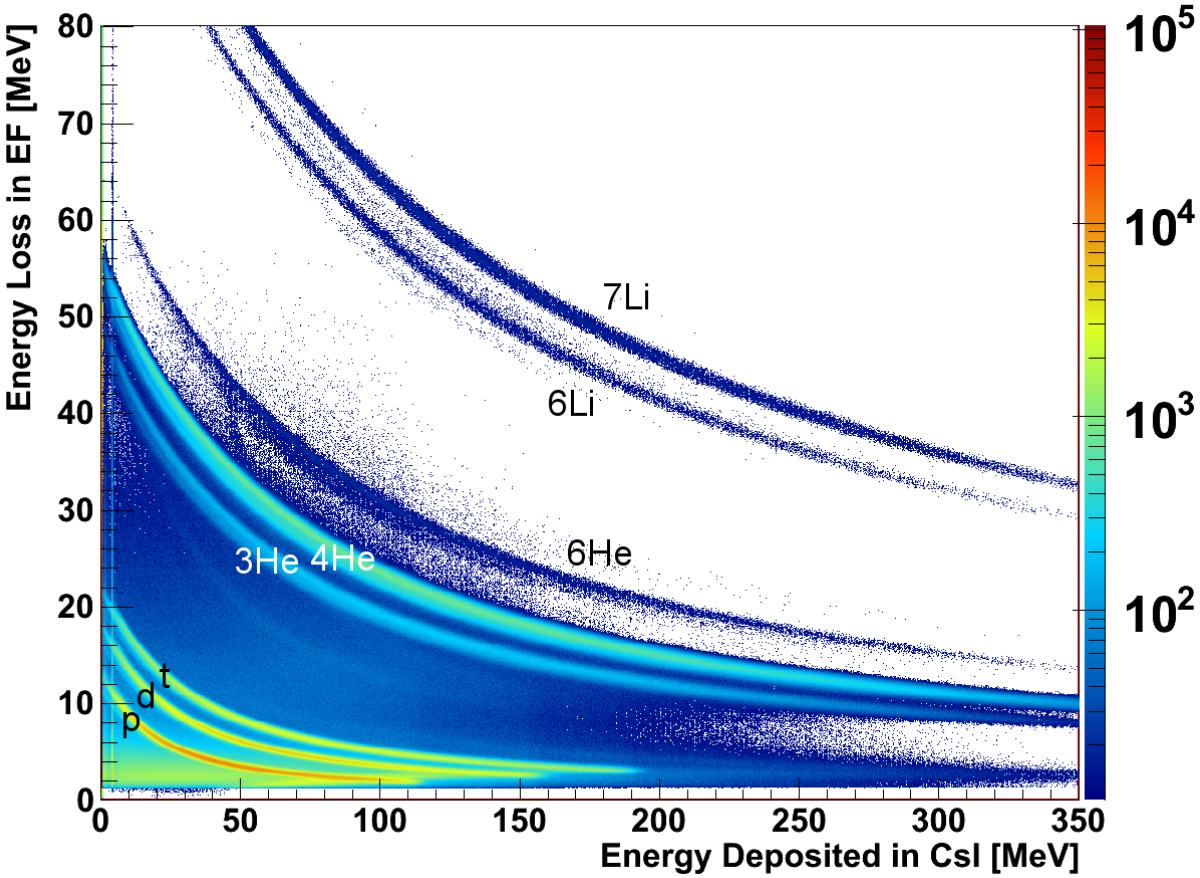

Figure 3.8: Calibrated PID for all ^{48}Ca+^{48}Ca data.

3.1.2.3 Offset Extraction

The second step in the calibration procedure is to extract the offset. Ordinarily, this can be done by running a pulser calibration and finding the channel number corresponding to zero pulse height in the pulser. However, in this experiment, the pulser chopper system had a shift in the zero offset which was undetermined. Therefore we used the energy loss in the telescope to deduce the offset. Partially calibrated PID plots from any reaction system can be used for this purpose. Once the Es are calibrated, it is known how much energy each proton lost in the thick silicon. By plotting calibrated energy from the EF as a function of the raw CsI channels for each crystal, PID are obtained similar to that shown in Fig. 3.9. If the exact thickness of the silicon detectors are known, the energy deposited in the CsI can be calculated for each proton from the energy lost in the EF, using a stopping power program such as LISE++[1]. One such point could be used to deduce the offset. However, the thicknesses of the silicon strip detectors are not known precisely enough to determine the offset from just one point on the E vs CsI plot at low energies. In fact, the thickness is known to only $\approx \pm 50$ μm. However, this is precise enough to extract the offset using several points on a E vs CsI curve for protons such as that shown in Fig. 3.9.

The following procedure was used to extract the offset for the CsI calibration. A few points along the proton PID line, between 6-10 MeV in EF energy, were used to calculate the offset. For each point, the energy lost in the EF was known. By assuming nominal thickness as provided by the manufacturer, the energy deposited in the CsI could be calculated. For each point, the digitized but uncalibrated energy signal in the CsI, in channel number, was known. This channel number was converted into a "pulser" voltage obtained by the

[1] www.nscl.msu.edu/lise

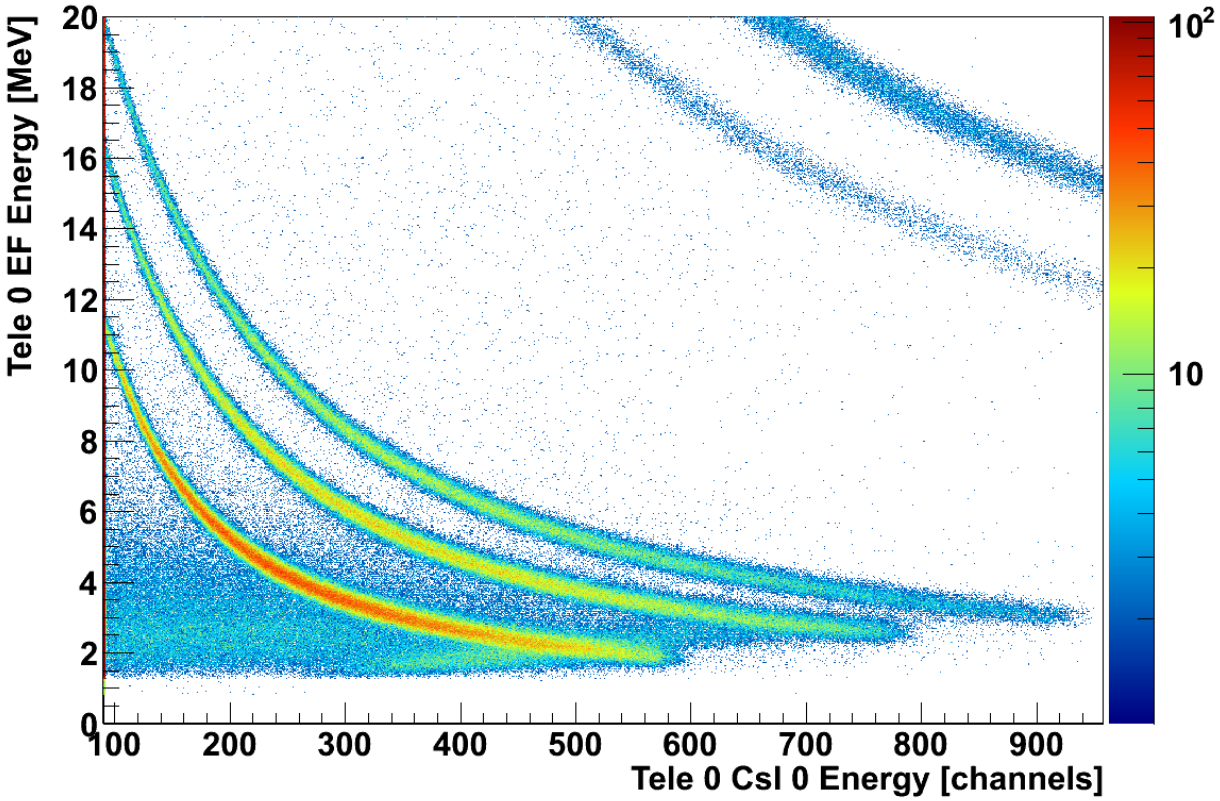

Figure 3.9: Calibrated EF energy vs raw CsI energy.

linearization procedure. This corrected for the non-linearity of the electronics. The energies were then plotted against values in volts for the corresponding signal in the CsI detector. This correlation was used to extrapolate the y-intercept for each crystal.

3.1.2.4 Gain Extraction

To extract the gain in the calibration, one could just use the channel value at which protons punch through the CsI crystal. This energy, $E_{punchthrough} = 114$ MeV can be accurately calculated by energy loss programs using the known thickness of the CsI crystal. However, the average error in this punch through data point would alter the calibration significantly. A better calibration can be obtained by elastically scattering protons into the detectors. This was achieved by degrading a beam of ^{40}Ca to E = 25 MeV and impinging it on a plastic target. Two of the reactions: The elastic and inelastic scattering of ^{40}Ca nuclei on the Hydrogen in the polyethylene target

$$^{40}\mathrm{Ca} + p \rightarrow \ ^{40}\mathrm{Ca} + p \tag{3.2}$$

and

$$^{40}\mathrm{Ca} + p \rightarrow \ ^{40}\mathrm{Ca}^{*} + p \tag{3.3}$$

can be used to calibrate the detector using the beam energy and two-body kinematic relations. The angle of the ^{40}Ca does not deviate significantly from 0 and should not enter any 4π detectors. If we detect a recoil proton in HiRA, no other particles should enter any 4π detectors. To reduce background, we require that only one recoil proton is observed in our proton recoil calibration data.

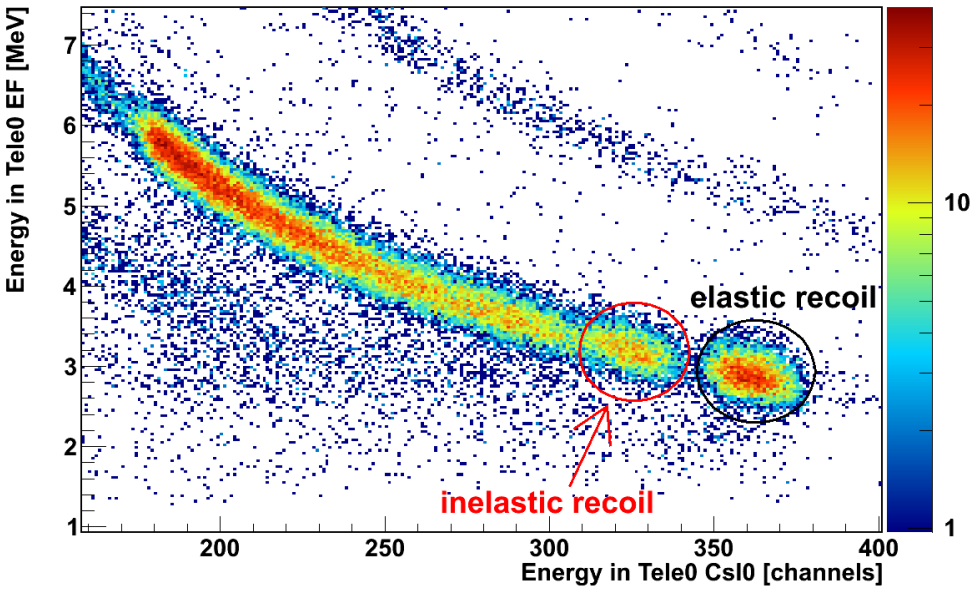

Figure 3.10: PID for ^{40}Ca+CH_2 at E/A = 25 MeV.

From conservation of energy and momentum, protons scattered from the reaction ^{40}Ca+CH_2 will have known energies depending on the proton scattering angle, θ, with respect to the beam-line. Protons scattered from the plastic target can be seen clearly at the high energy end of the PID line in Fig. 3.10. Inelastically scattered protons can also be seen in the figure, however, they cannot always be cleanly separated from protons emitted from other reactions.

In order to cleanly separate not only elastically scattered protons, but also inelastically scattered protons, only protons were selected from the PID and their energy was plotted as a function of θ as shown in Fig. 3.11. Protons with the highest energy at each angle are elastically scattered. Protons that were inelastically scattered have slightly less energy because some energy was transferred to the ^{40}Ca to excite it. Protons with the lowest energies were the result of reactions such as ^{40}Ca+^{12}C that were not completely removed by the requirement of zero charged particle multiplicity in the 4π.

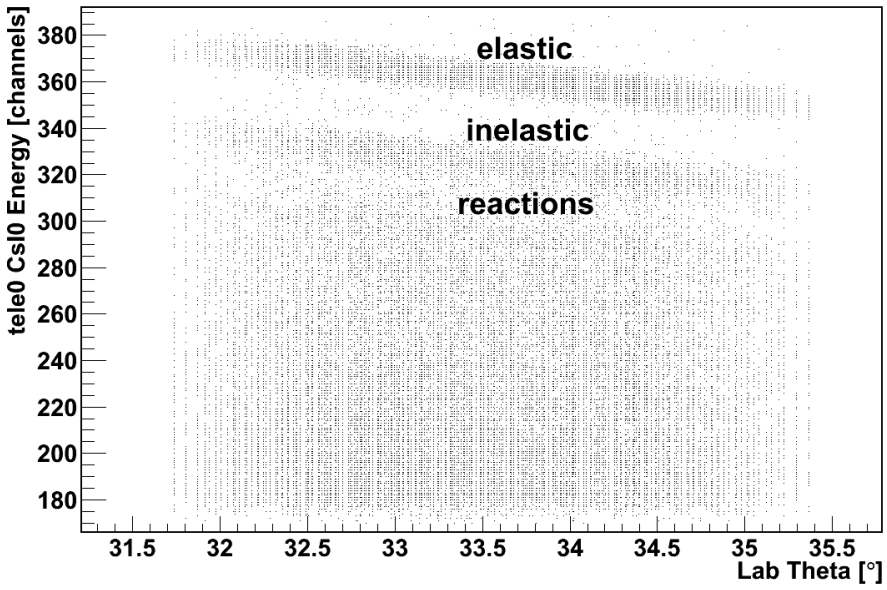

Figure 3.11: The proton energies plotted as a function of θ in the laboratory frame.

After the relevant protons were selected, both the elastic and inelastic groups were divided into 4 angular bins for each crystal. The elastic protons in each bin were assigned an energy based on angle (θ) from Fig. 3.12, which shows energy as a function of angle, minus any energy losses in foils.

The inelastically scattered protons result from ^{40}Ca being in a 3- or 2+ excited state. These states are close in energy and could not be distinguished from one another. Therefore, the energy assigned to a proton was a weighted average of the energies expected from these two states. It was weighted by the expected contribution from each cross section for the given angle. The cross sections are shown in Figs. 3.13 and 3.14 The energy distributions for each inelastically scattered state are shown in Figs. 3.15 and 3.16.

Energy losses through various foils were taken into account to determine the actual energy of a recoil proton entering a CsI crystal. Due to the trajectory, each proton actually traveled through a slightly different amount of material. The effective thickness of each material was

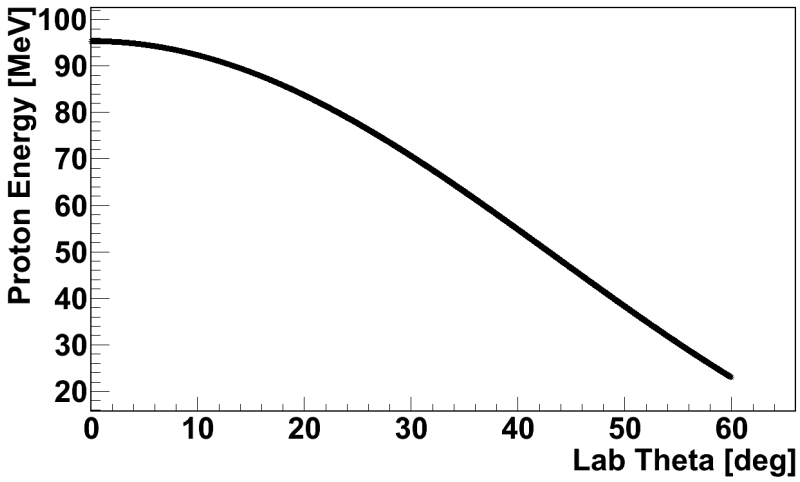

Figure 3.12: Energy as a function of θ (laboratory) for elastically scattered protons.

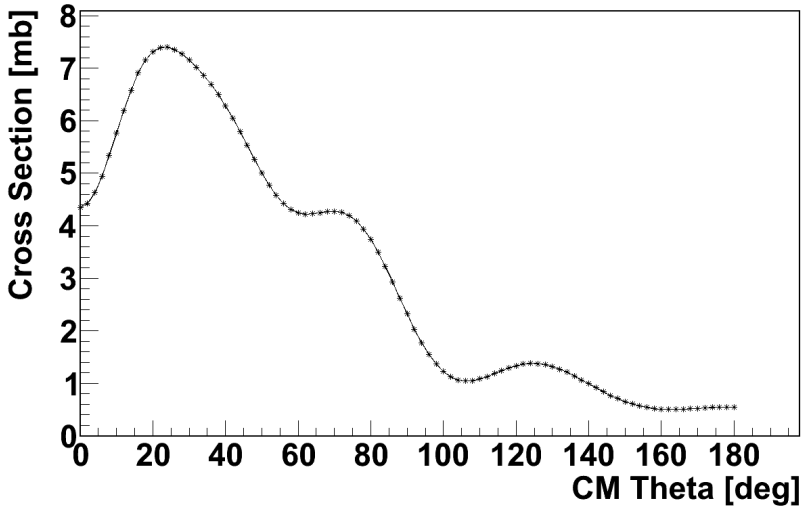

Figure 3.13: Cross sections for the 3- state of ^{40}Ca as a function of θ in the center of mass system.

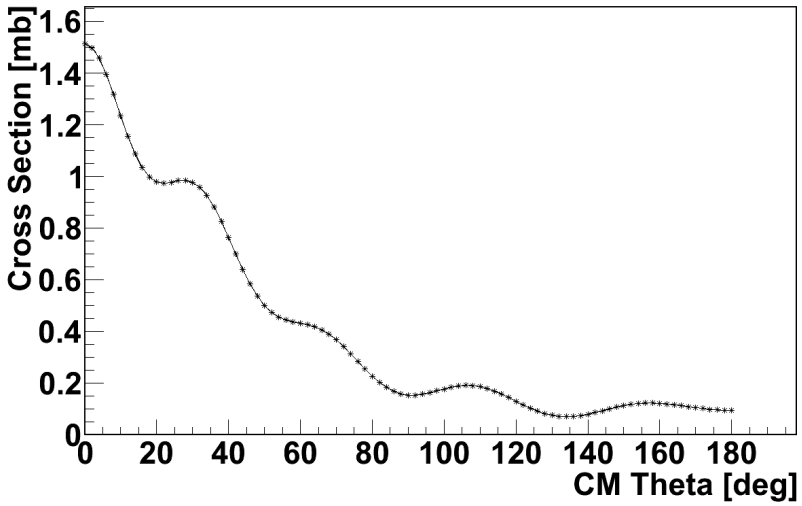

Figure 3.14: Cross sections for the 2+ state of ^{40}Ca as a function of θ in the center of mass system.

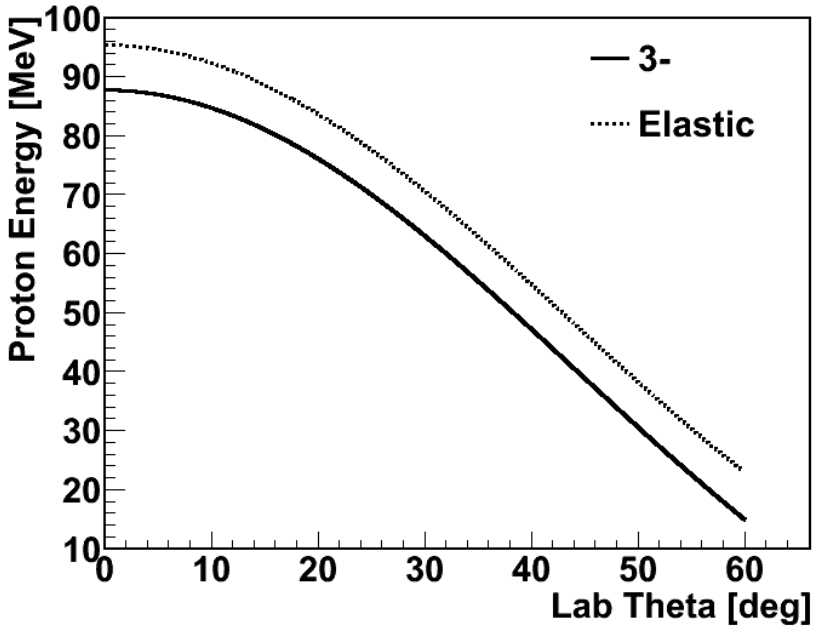

Figure 3.15: Energy as a function of laboratory angle for inelastically scattered protons from the 3- excited state of ^{40}Ca.

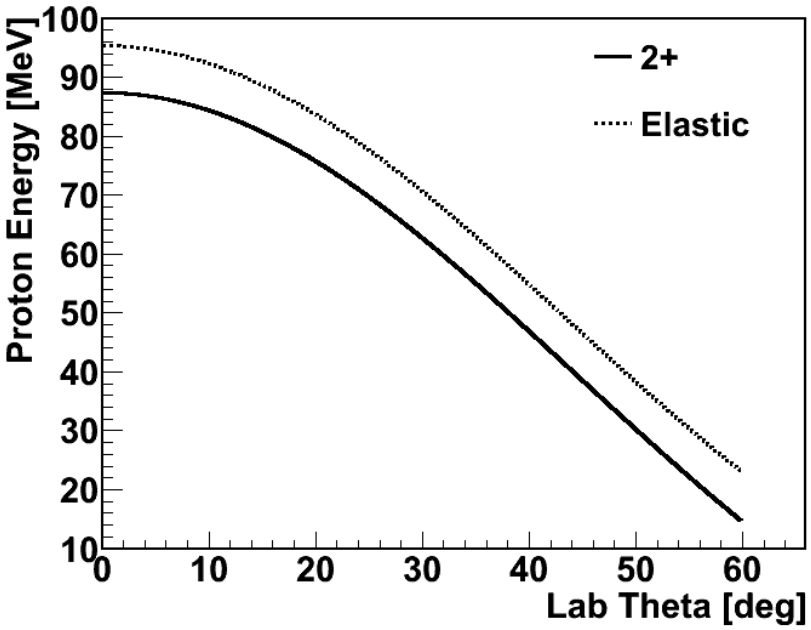

Figure 3.16: Energy as a function of laboratory angle for inelastically scattered protons from the 2+ excited state of ^{40}Ca.

calculated from the angle of the proton, and then the energy loss in Fig. 3.17 was multiplied by this effective thickness for a total energy loss due to the material. Energy losses were calculated sequentially. First, the proton must travel through the second half of the target, assuming that the reaction occurs in the center of the target. Then, the protons travels through Sn-Pb foil. Next, it travels through the mylar foil. Finally, it travels through the dE before entering the thicker silicon.

It was mentioned earlier that the punch through could be utilized to calculate the gain for each crystal. The crystals were 39 mm long on average resulting in a punch through energy of ∼114 MeV. Protons punching through a crystal could have slightly more or less energy due to the angle it went through the crystal, and any scattering that took place. SRIM[2] calculations showed a shoulder in the punch through similar to that seen in Fig. 3.18. The channel value that corresponds to the punch through energy is that at the half-max of the

[2]http://www.srim.org/

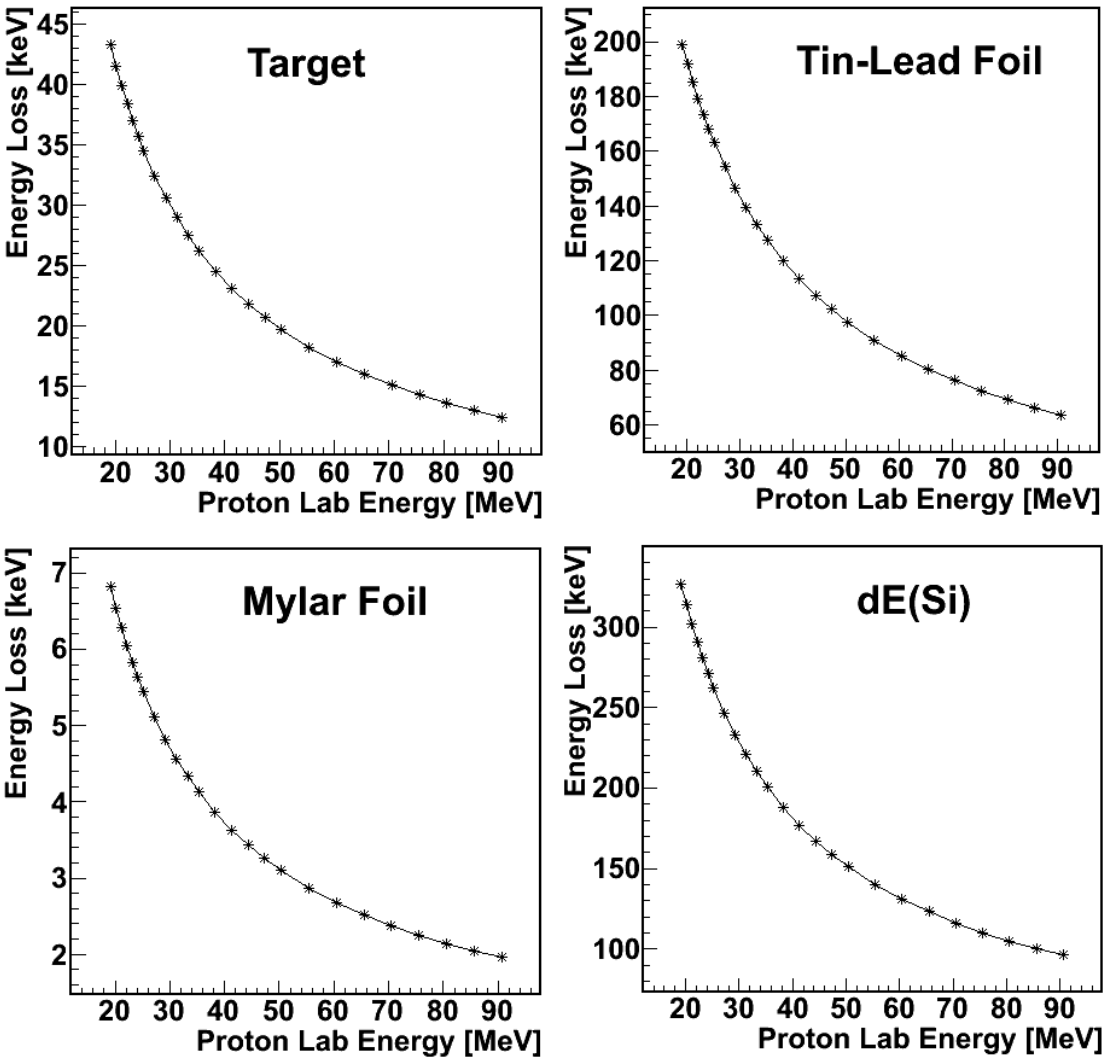

Figure 3.17: Energy loss through relevant foils as a function of proton energy.

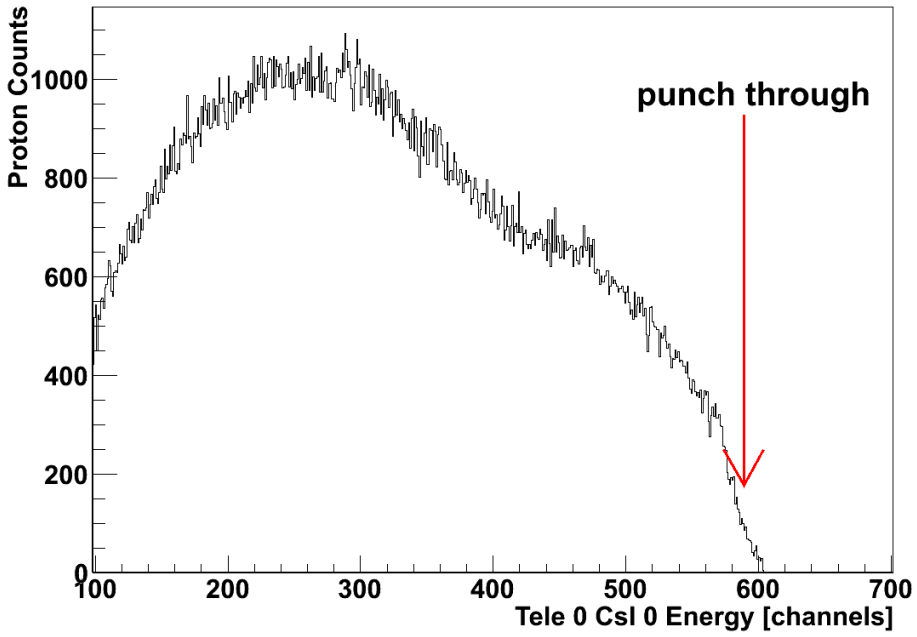

Figure 3.18: Projection of proton PID for selection of the punch through channel.

shoulder.

The last step in the proton calibration is combining all of the information from linearization and the offset to get the gain. This is shown in Fig. 3.19. The offset has been subtracted from all points, so the lowest point is (0,0). The middle points are from elastic and inelastic scattered protons. The highest energy point is the punch through energy.

3.1.2.5 Calibrating $A>1$ Particles

The initial calibration calculates the energy of each particle as if it were a proton, referred to as Ep. Different species of particles interact with the CsI crystal differently, producing different amounts of light for the same energy deposited. Thus, obtaining the correct energy for each isotope requires its own energy calibration. For Z=1 particles, there is a linear

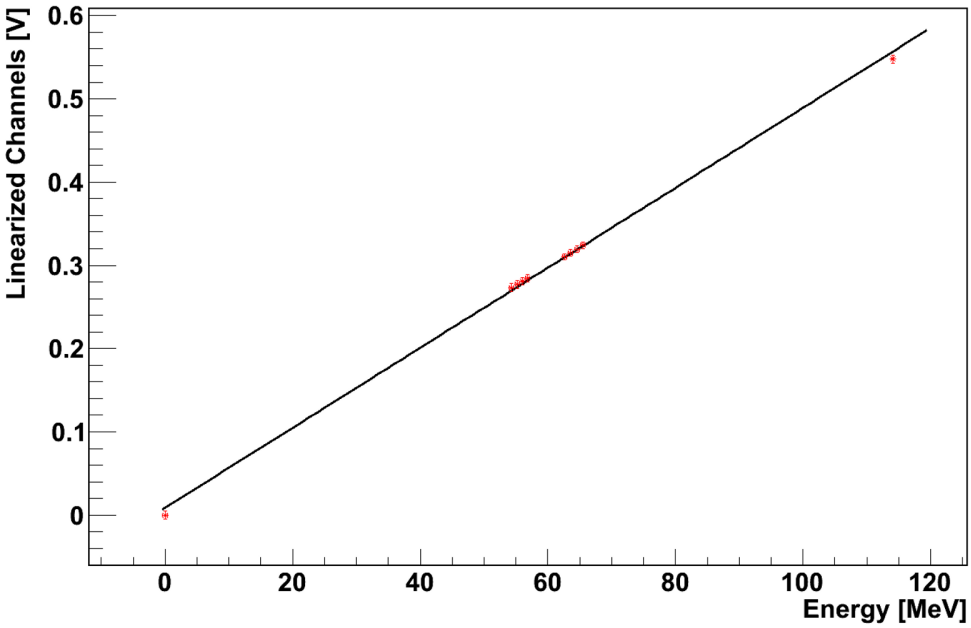

Figure 3.19: Calibration for crystal 0 of telescope 0.

relationship to the proton calibration such that

$$E = aE_p + b \tag{3.4}$$

while the energy calibration for Z=2 particles can be approximated by an exponential term [56]

$$E = aE_p + bA^c(1 - e^{dE_p}). \tag{3.5}$$

In both of these, E_p is the energy that would be assigned if the particle was a proton and a,b,c, and d are fitting parameters. To determine the fitting parameters, LISE++ was used to calculate the energy deposited in the CsI crystal as determined by the energy loss in the E detector. The punch throughs were also used when available as a data point in the fit.

3.2 4π Array

The 4π array provided a support structure for HiRA, a vacuum chamber, and, more importantly, it was also used as a detector to measure the positions and energies of all emitted nuclei which do not enter HiRA. This is essential to determine the impact parameter of each collision, described in Subsec: 3.2.2, which is needed to accurately compare the data to theoretical transport models. In order to calculate impact parameters, the phoswich detectors must be calibrated.

3.2.1 Phoswich Calibration

The fast and slow plastic scintillators have different decay times as was shown in Table 2.3 allowing the signals to be separated. In the following, we designate DE as the signal from the fast plastic and E as the signal from the slow plastic. As in the case of HiRA, DE vs E plots can be used to identify particles due to dE/dx being approximately proportional to AZ^2. Particles which stop in the fast plastic deposit no energy in the slow plastic, but the slow gate still contains a little of the fast signal, resulting in a "punch-in" line with a finite slope. Some particles such as cosmic rays and neutrons deposit energy in the slow plastic without going through the fast. These particles fall in the neutral line which has a slight slope due to the fast signal containing some of the slow rising signal. These lines are shown in Fig. 3.21. The first task in calibrating the phoswiches is to disentangle the fast and the slow signals so that the punch-in line has an infinite slope and the "neutral line" has a slope of 0. The intersection of the lines corresponds to 0 energy, and any difference from 0 is due to offsets in electronics. The electronic offsets are extracted and subtracted to place this intersection at 0.

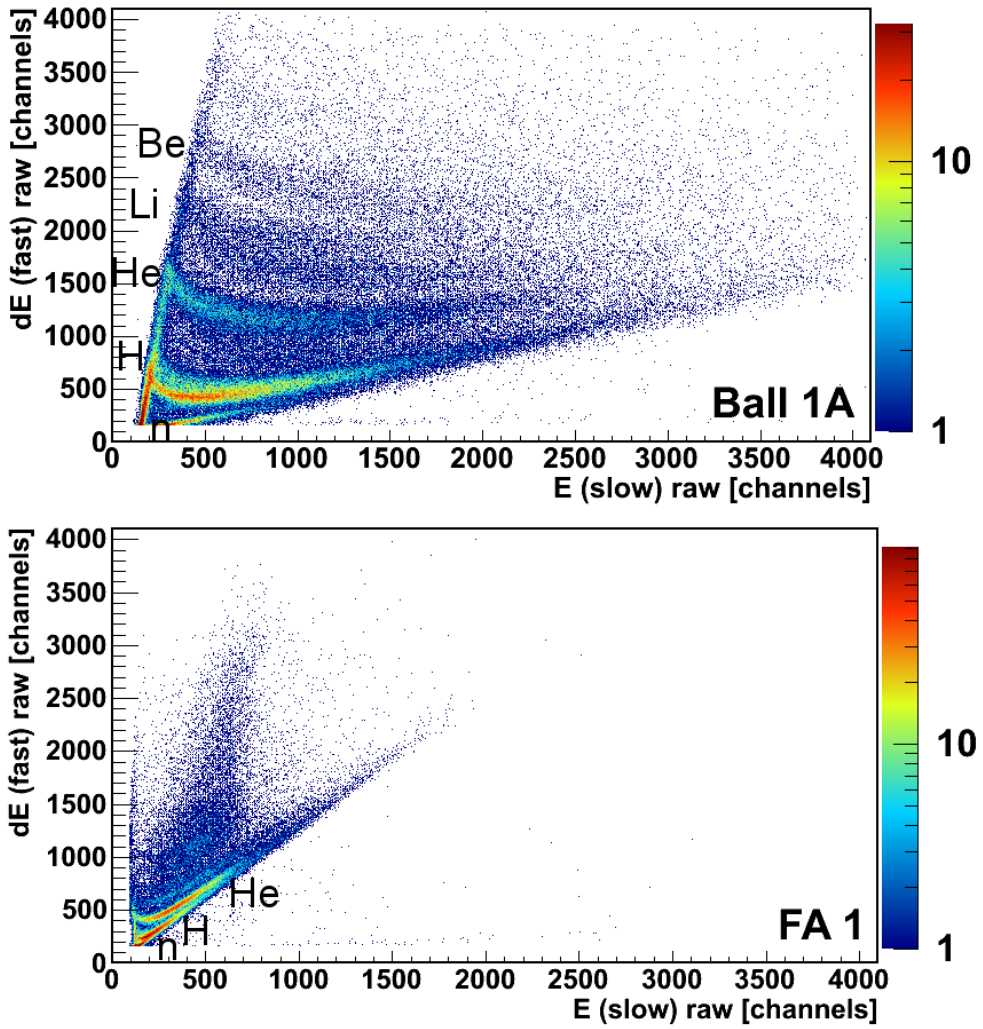

Figure 3.20: Raw PID plots from a ball phoswich (top) and a forward array phoswich (bottom). Axes are in channels.

Calibrating each detector is a three step process. First, PID plots are generated by plotting the fast plastic signals versus the slow plastic signals from the raw uncalibrated data as shown in Fig. 3.20 for one ball phoswich and one FA phoswich. The slope for both the neutral and the punch-in lines are found as well as the intersection point between the two lines as shown in Fig. 3.21. Using Eqs. 3.6 and 3.7, the dE and E signals are disentangled from one another where Mn is the slope of the neutral line, Mp is the slope of

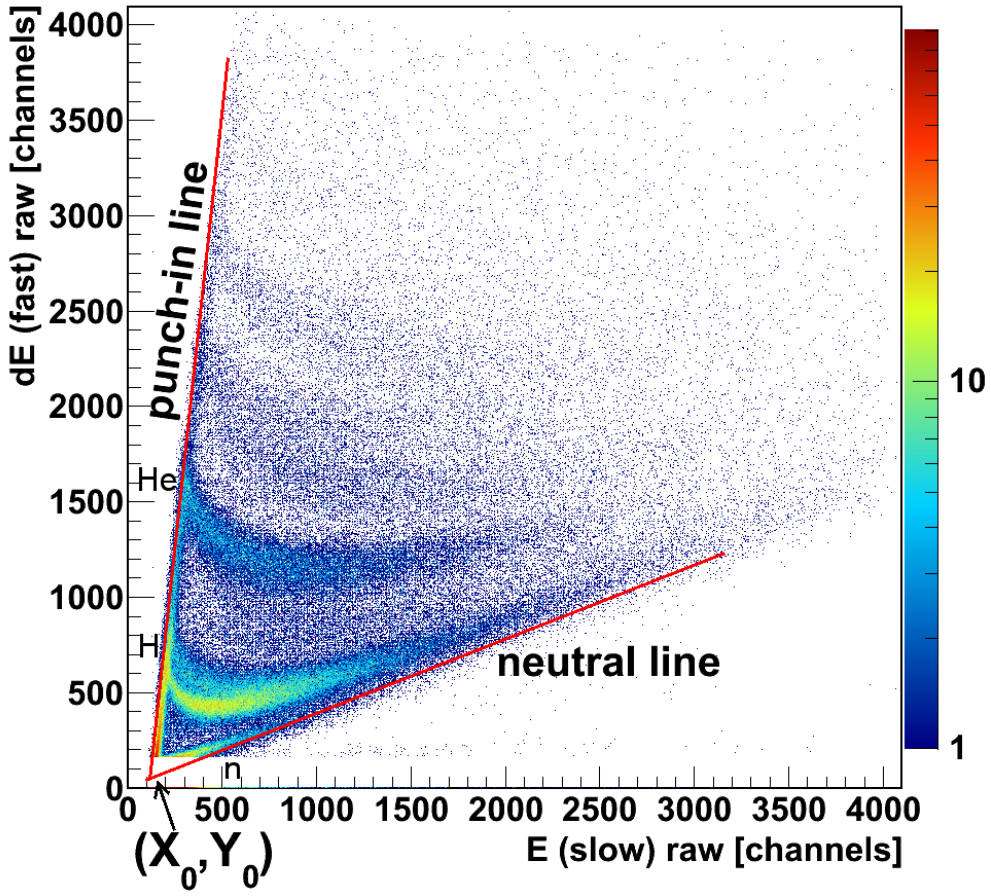

Figure 3.21: Raw PID from a ball phoswich with important calibration features labeled.

the punchthrough line and X_0 and Y_0 are the coordinates of the intersection point.

$$Fast = (dE - Y_0) - (E - X_0) * M_n \tag{3.6}$$

$$Slow = (E - X_0) - (dE - Y_0)/M_p \tag{3.7}$$

Once the fast and slow components are disentangled, as shown in Fig. 3.22, the punch-ins listed in Table 3.1 can be utilized to calibrate the phoswiches. For the ball phoswiches, the

Particle Type	Punch-in Energy [MeV]	Particle Type	Punch-in Energy [MeV]
p	17	Be	214
d	24	B	300
t	28	C	380
He	70	N	483
Li	140	O	593

Table 3.1: Energy punch-ins for ball phoswiches [1].

light response function of the fast plastic is described by Eq. 3.8 while the response of the slow plastic is described by Eq. 3.9 where C_i is a gain factor specific to each detector [57].

$$L_i = C_i\sqrt{dE} \tag{3.8}$$

$$L_i = C_i\frac{E^{1.4}}{Z^{0.8}A^{0.4}} \tag{3.9}$$

The gain factor for the slow plastic, C_i, (for both the ball and the FA) was found by using the energy loss in the fast plastic and LISE++ as in the case of the CsI crystals.

The Forward Array is calibrated similarly with the punch-in energies given in Table 3.2. For the fast phoswich, the energy is still given by the square of the light output, but the

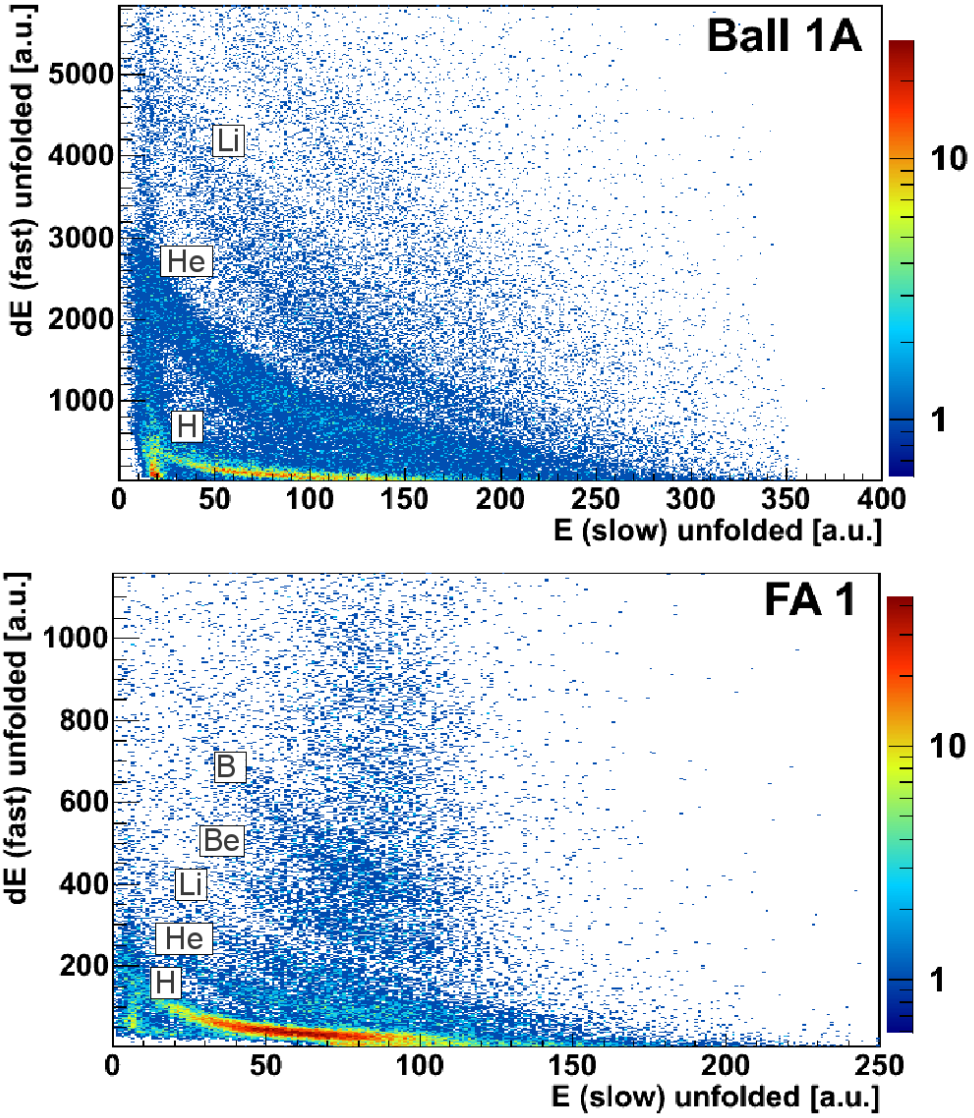

Figure 3.22: Unfolded (disentangled) PID from a ball phoswich (top) and a forward array phoswich (bottom). Axes are in arbitrary units.

Particle Type	Punch-in Energy [MeV]	Particle Type	Punch-in Energy [MeV]
p	13	C	269
d	17	N	341
t	20	O	419
He	50	F	515
Li	99	Ne	591
Be	152	Na	687
B	212	Mg	767

Table 3.2: Energy punch-ins for Forward Array phoswiches.

slow phoswiches have a slightly different calibration given by Eq. 3.10 [5].

$$L_i = C_i \frac{E^{1.35}}{Z^{0.772} A^{0.386}} \tag{3.10}$$

The calibrated spectra for both a ball and a FA detector can be seen in Fig. 3.23.

3.2.2 Impact Parameter Selection

The impact parameter of a nuclear reaction is defined as the distance between straight line trajectories of the centers of the nuclei. If the two nuclei hit head on, the impact parameter is 0 fm and the reaction is classified as central. At the other end of the spectrum, if the nuclei barely graze each other, the reaction is characterized as peripheral. These limits correspond to zero cross section, so ranges of impact parameters must be combined to obtain central collision data. In this dissertation, the impact parameter range of $0 \leq b \leq 4$ fm is defined as central for ^{40}Ca+^{40}Ca and ^{48}Ca+^{48}Ca reactions.

BUU transport simulations show that the size of the source depends on the impact parameter of the nuclear reaction. In the simulation, impact parameter is an input variable. In order to compare between theory and experimental data, it is important to be able to select ranges of impact parameters in the data. This work focuses on central reactions

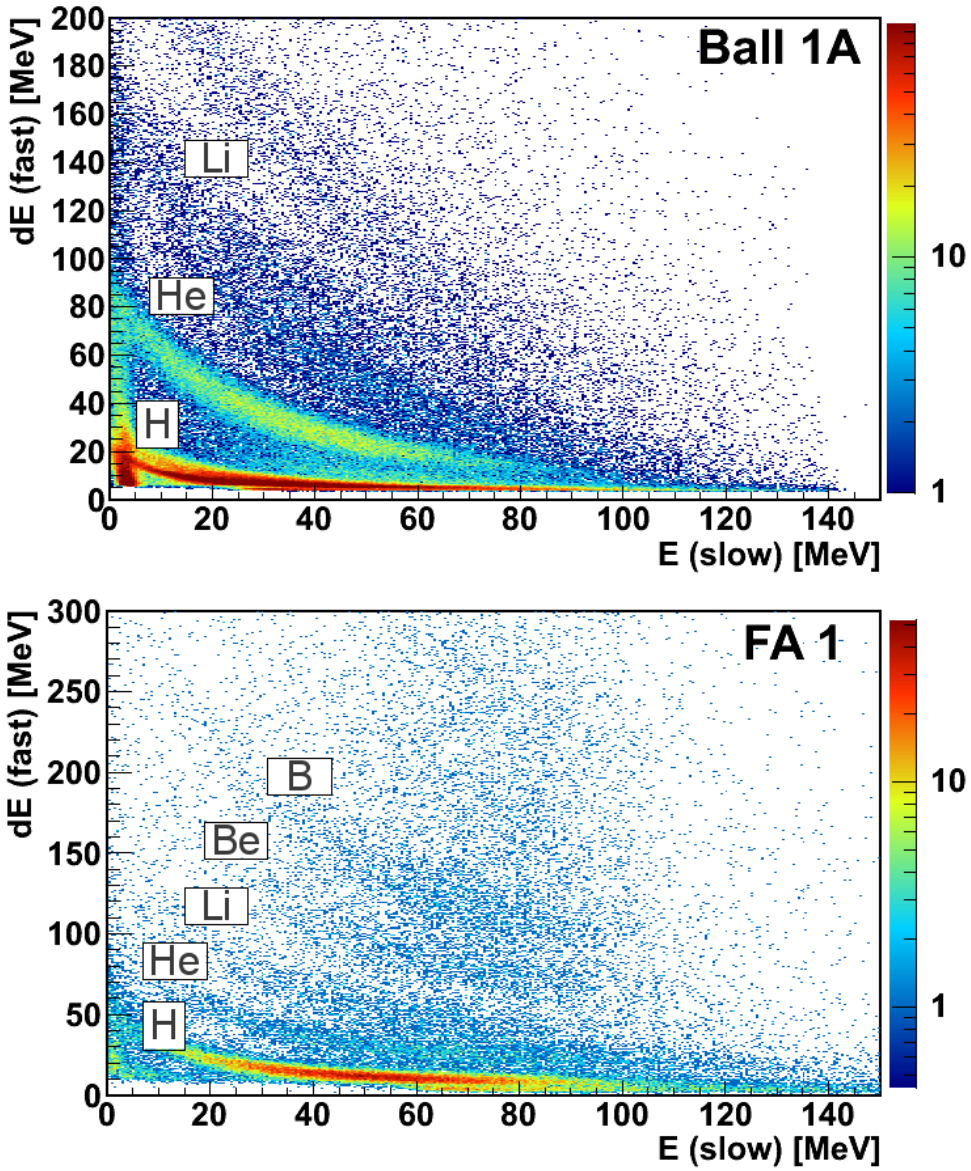

Figure 3.23: Calibrated PID from a ball phoswich (top) and a forward array phoswich (bottom).

because the correlation functions were predicted to be sensitive to the density dependence of the symmetry energy at low impact parameters.

The 4π array was used to extract an experimental impact parameter for each event. Different observables can be used to select ranges of impact parameter in nuclear reactions. Two commonly used observables are charged particle multiplicity, N_C, [24, 58] and transverse energy, E_t [59]. N_C is the number of charged particles detected by the 4π array for a given event. If two particles hit the same detector, they are counted as one. E_t, is defined by

$$E_t = \sum_{i=1}^{N_C} E_i sin^2\theta_i \tag{3.11}$$

where θ is the laboratory angle between the particle's trajectory and the beam axis and E is the measured energy in the laboratory frame.

If one assumes a strictly monotonic relationship between impact parameter and an observable such as N_C or E_t, labeled X, the reduced impact parameter is calculated by

$$\hat{b}(X) = \frac{b(X)}{b_{max}} = \frac{\sqrt{\sum_{X}^{\infty} P(X)}}{\sqrt{\sum_{X(b_{max})}^{\infty} P(X)}} \tag{3.12}$$

following Ref. [58]. Two other assumptions are that X increases as the reaction becomes more central and the fluctuation of the parameter x at a fixed value of b is small compared to the change of x with b. This assumption is only approximately valid and will be addressed in section 5.1.1. In Eq. 3.12, P(X) refers to the probability distribution of observable X, $\hat{b}(X)$ is the reduced impact parameter and b_{max} is the maximum impact parameter consistent

with the experimental setup. b_{max} is estimated from

$$b_{max} = R_1 + R_2 = 1.25A_1^{1/3} + 1.25A_2^{1/3} \tag{3.13}$$

where A is the mass.

From Eq 3.13, the ^{40}Ca+^{40}Ca reaction has a maximum impact parameter of $b_{max} = 8.55$ fm while for the ^{48}Ca+^{48}Ca reaction, the maximum impact parameter was $b_{max} = 9.09$ fm. To the accuracy that the impact parameter was determined in this dissertation, these values are essentially the same. An impact parameter of $b = 4$ fm corresponds roughly to a reduced impact parameter of $\hat{b} = 0.5$, where $\hat{b} = b/b_{max}$. Thus, this value of $\hat{b}$ was used for both reactions when gating on data.

The impact parameter that can be probed in an experimental device such as the 4π detector ranges from 0 up to the largest impact parameter contained in the minimum bias trigger. The minimum bias trigger required a multiplicity of at least two on the 4π array. During the data analysis it was realized that the FA was not triggered during the minimum bias run. Thus the procedure of establishing a relationship between the multiplicity or E_t and impact parameter was first performed using the Ball detectors. Then, a regular data run, in which both the Ball and FA detectors were working, was used to relate the ball multiplicity to the total multiplicity. This total multiplicity was related to the impact parameter selected. The correlation between ball multiplicity and total multiplicity can be seen in Fig. 3.24.

The total multiplicity was extrapolated from this correlation to what it would have been if the FA was working using a second order polynomial. The same procedure was employed

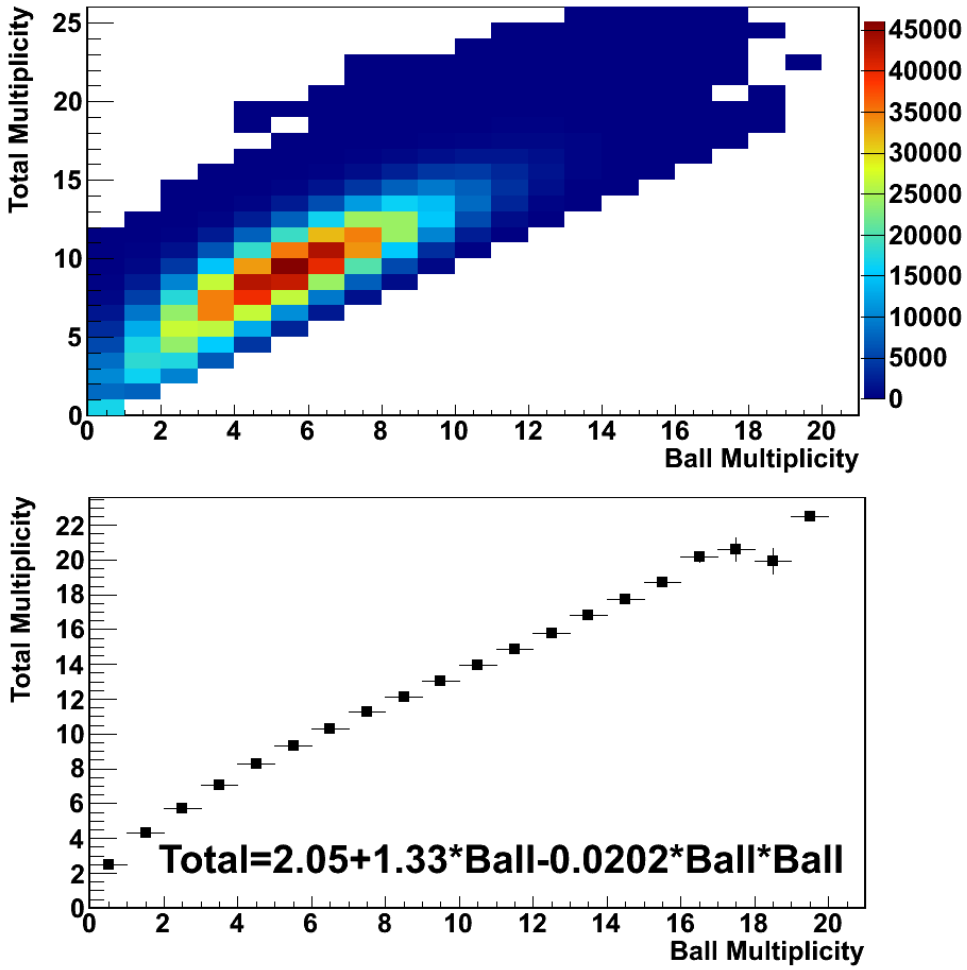

Figure 3.24: The relationship between the total multiplicity in the 4π array and the multiplicity in the ball elements of the array is shown in the upper panel. The lower panel shows the mean total multiplicity as a function of ball multiplicity.

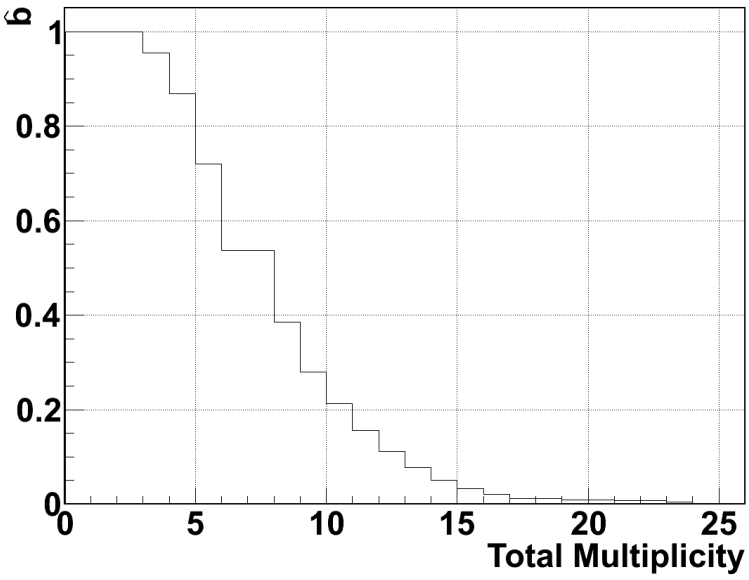

Figure 3.25: Reduced impact parameter as a function of multiplicity.

for E_t which lead to the expression

$$TotalE_t = 10.970 + 1.088 \cdot BallE_t - 4.076e^{-4} \cdot BallE_t^2 + 4.976e^{-7} \cdot BallE_t^3. \quad (3.14)$$

Once E_t and N_c distributions are known from the minimum bias data, a reduced impact parameter, $\hat{b}$, can be calculated for each using Eq. 3.12.

The reduced impact parameter for ^{40}Ca+^{40}Ca as functions of N_c and E_t are shown in Figs. 3.25 and 3.26 respectively. It can be seen that for a centrality condition of $\hat{b} < 0.5$ this corresponds to $N_c \geq 8$ or $E_t \geq 150$ MeV. There was no usable minimum bias data for ^{48}Ca+^{48}Ca, therefore, the same conditions to define centrality are used for both reaction systems. This is a reasonable assumption since E_t is dependent upon charged particles and both reaction systems have the same number of charged particles.

In Fig. 3.27 it can be seen that N_c and E_t are correlated, so both observables should be a good indicator of impact parameter. However, N_c saturates as E_t becomes large. Phair

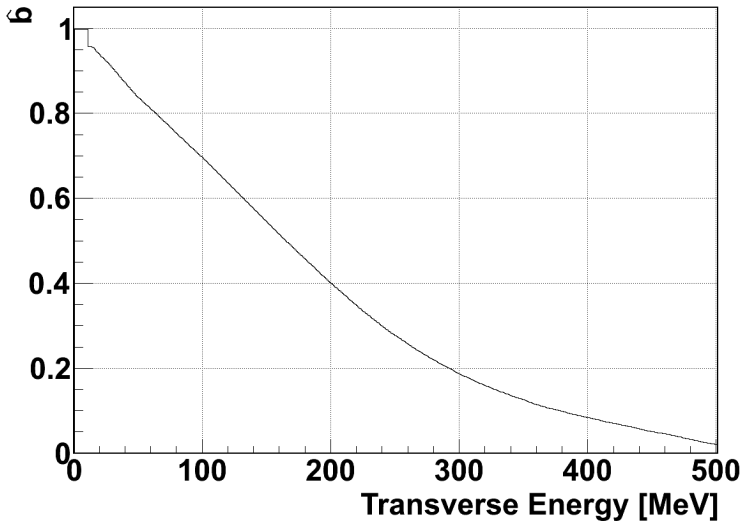

Figure 3.26: Reduced impact parameter as a function of transverse energy.

showed [59] that E_t was a slightly better indicator of centrality than N_C. While N_C was used for some preliminary analysis, E_t was used to select central events for the purpose of this thesis.

There can be a variety of reasons why the multiplicity in the 4π array may change over time. Two explanations are changing thresholds on the detector elements, and oxidation of the Ca target. The latter is explored below.

3.3 Quantification of Calcium Target Oxidation

Calcium is highly reactive with oxygen, forming CaO. The percentage of oxygen (by mass) on a natural calcium target exposed to air is shown in Fig. 3.28 where the percentage was calculated from the increase in weight of the target over time. Fig. 3.28 shows that a target left in air for three hours is nearly 40% oxygen. There was a concern that the targets may oxidize during the experiment since the vacuum in the 4π chamber was only in the range of 10^{-5} Torr. Targets were visually inspected before putting them in the target carousel

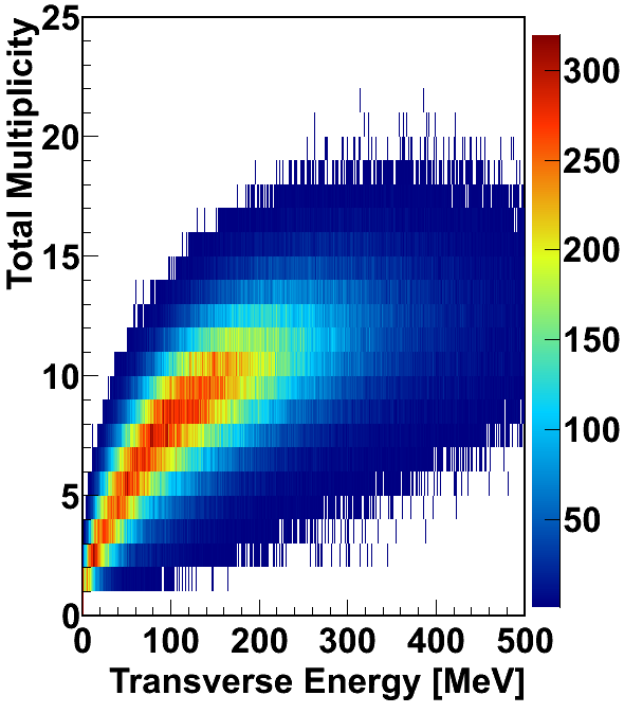

Figure 3.27: Total multiplicity as a function of transverse energy.

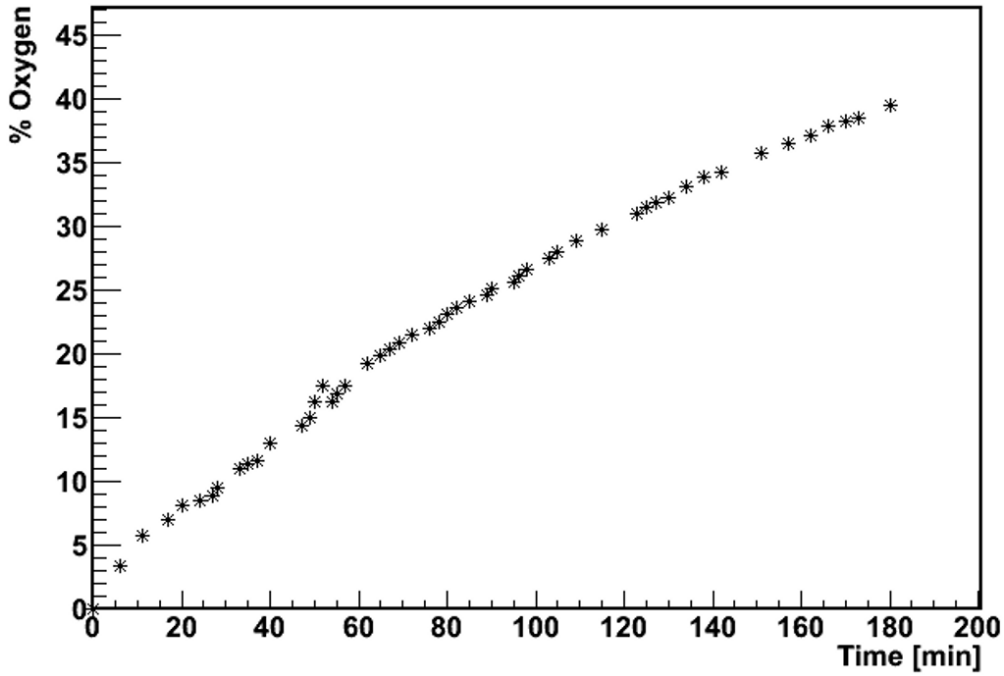

Figure 3.28: Oxidation of natural Ca target as a function of time.

and upon removing them from the carousel. A calcium target will be shiny but an oxidized target will appear duller. The ^{40}Ca target actually appeared more shiny after 226 hours in vacuum, and the ^{48}Ca target did not change in appearance after 63 hours in vacuum.

To monitor target oxidation, the reactions ^{40}Ca+mylar and ^{48}Ca+mylar were studied to observe the effects of the beam reacting with oxygen or carbon instead of calcium. Mylar, (polyethylene terephthalate or PET) has the chemical formula $C_{10}H_8O_4$. Aluminized mylar was chosen to represent an oxygen target due to high carbon and oxygen content, wide availability, and solid form. The thickness of the aluminum layer on the mylar foils was approximately 2-3 μg/cm^2 which is small compared to the 200 μg/cm^2 thickness of the mylar foils, so reactions on the aluminum layer can be neglected.

When calcium reacts with mylar, it is reacting with either carbon, oxygen or hydrogen, all of which have fewer protons than calcium. This results in a lower charged particle multiplicity distribution that peaks at a lower multiplicity for a mylar target than for a calcium target. The average multiplicity in the 4π array for the mylar target is about five, and it does not extend to as high multiplicities as the multiplicity spectra measured on the Ca targets, as shown in Fig. 3.29. If a calcium target is oxidizing, its multiplicity should decrease significantly over time. Fig. 3.29 also shows 4π multiplicity for ^{40}Ca+^{40}Ca (top) and ^{48}Ca+^{48}Ca (bottom) reactions from the early data and later data. There is a slight decrease in 4π multiplicity over time for both reaction systems. However, the decrease is slight for the ^{48}Ca system. The larger decrease observed in the ^{40}Ca system mainly reflects changes in the trigger that were introduced early in the experiment which lead to a small loss of efficiency for charged particle detection.

To be more quantitative, we take the difference between the late and earlier runs and show

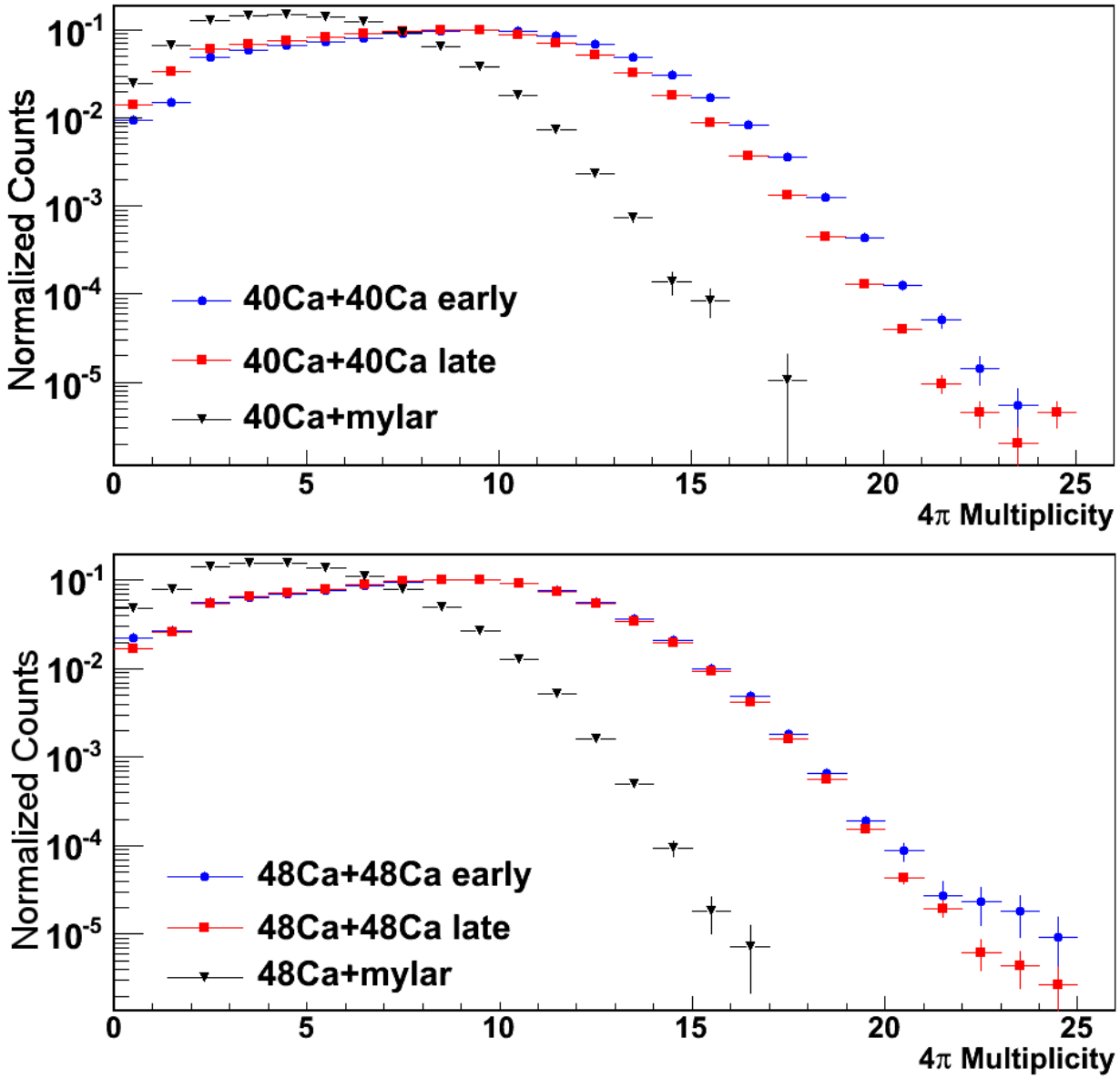

Figure 3.29: Comparison of reactions on Calcium, for early and late data, with reactions on mylar for both Ca beams.

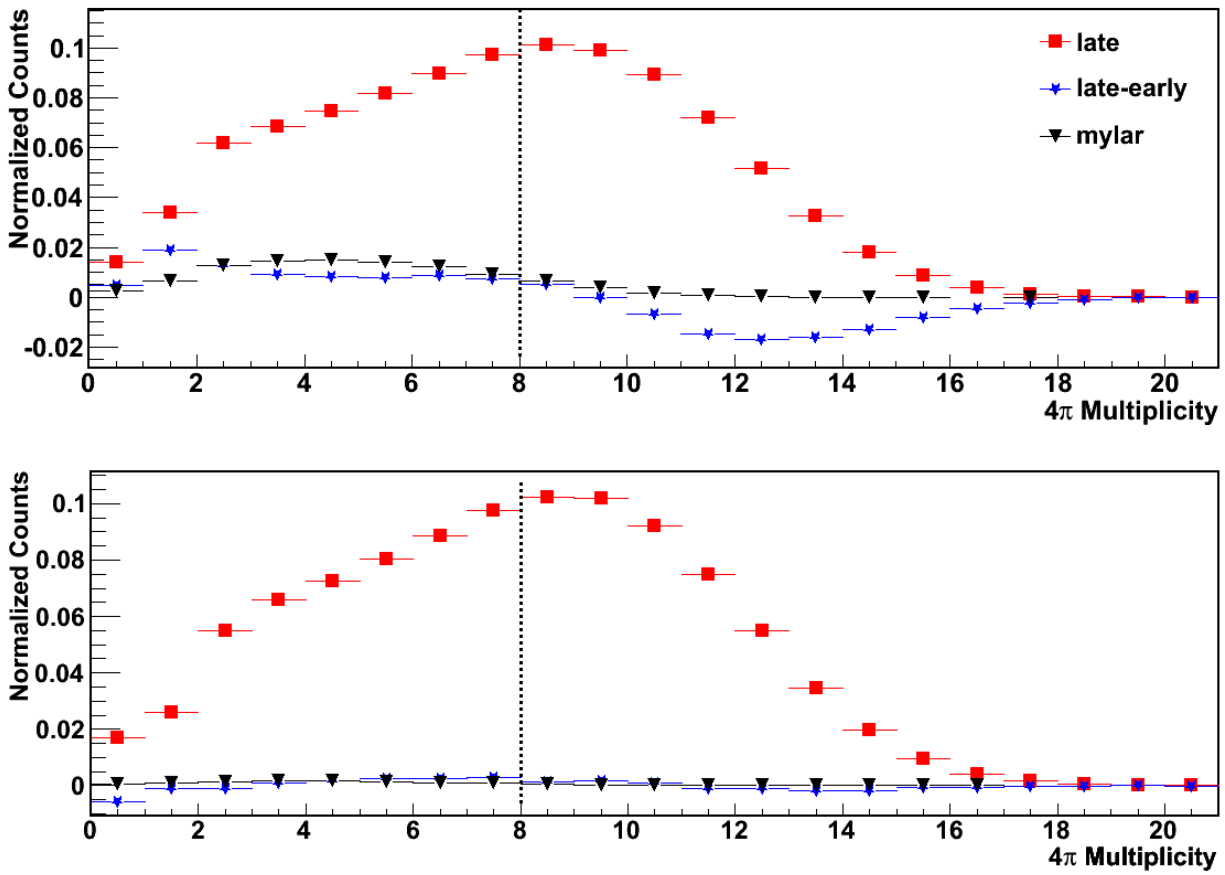

Figure 3.30: Comparison of reactions on Ca, over time, with reactions on mylar for both Ca beams. Details are given in the text.

that with the late run multiplicity in Fig. 3.30. We see that for both targets, there is a few percent increase in this difference at low multiplicity. If we normalize the mylar spectrum to the difference in the calcium spectra at low multiplicity, we see that the correction at higher multiplicities (M>8) consistent with our central collision trigger is negligible.

Chapter 4

Exploration of BUU Physics Inputs

In this chapter, a Boltzmann-Uehling-Uhlenbeck (BUU) transport simulation model, developed by Danielewicz and collaborators [41–43], and introduced in section 1.3, is used to predict the effects of the density dependence of the symmetry energy on source functions for central reactions of ^{40}Ca+^{40}Ca and ^{48}Ca+^{48}Ca at E/A = 80 MeV. Both the size and the shape of the source are explored in this dissertation. When comparing to experimental data, however, the size is more accurately determined than the shape. Appendix C provides details on how this size, $r_{1/2}$, is calculated from sources. In addition to the source size, many observables are explored including lab energy spectra for protons, particle distributions, and average emission time as a function of momentum. The first section outlines the rest of the chapter.

4.1 Description of Parameter Space for Inputs

There are many inputs that can be changed within the BUU transport code, some are basically computational while others are physical. Clearly, observables should be stable against

changes in computational inputs, including the size of the computational grid, duration of reaction, and the number of test particles used. With the exception of section 4.2, the computational grid size was ±30 fm in the x and y directions and ±45 fm in the z direction (beam axis) with a cell size of 0.92 fm in all directions. A time step of .5 fm/c was used with 1000 steps so that each collision took place over 500 fm/c. Either 800 or 1600 test particles per nucleon were used for calculations in this dissertation, although the effect of using only 200 test particles is explored in section 4.3. In addition, each calculation was performed with 20 independent runs with a different random number seed to enhance statistics.

The effects of impact parameter, momentum dependence of the mean field potential, and composite production on observables are also explored. Except in section 4.4, all simulations used an impact parameter of b=1.4 fm. This represents an idealization of what is achievable experimentally. Using a single impact parameter, however, has the advantage of simplicity when comparing the effects of one set of transport inputs to another. In addition, the effects of the symmetry energy are expected to be largest at small impact parameters. Thus, the trends at b=1.4 fm represent close to the maximum sensitivity to the density dependence of the symmetry energy that one might expect. Calculations presented in this chapter reveal that much larger effects are predicted for the NN in-medium cross section than for the density dependence of the symmetry energy. The combined effects of momentum dependence and cluster production are explored in section 4.5. Averaging over impact parameters is discussed later in Ch. 5. This chapter ends with a summary of the predicted sensitivity of the source sizes to various transport inputs.

4.2 Size of Computational Region and Reaction Duration

Two of the first inputs of a numerical simulation that need to be chosen are the computational grid size and the duration of evolution of the reaction. For most calculations, the computational grid size was ±30 fm in X and Y and ±45 fm in the Z direction (beam axis) with a cell size of 0.92 fm in all directions. The calculations ran to 500 fm/c and it was noticed that residues begin to go off of the grid at different times depending on composite production and momentum dependence of the mean field potential. This could make the calculation inaccurate because the mean field goes to zero when the residues go off the grid, influencing some of the experimental observables.

To examine the effect of the grid size, a momentum independent mean field potential and the Rostock in-medium cross section were employed. The grid size was increased to ±45 fm in the X and Y directions and ±90 fm in the Z direction. Figs. 4.1, 4.2, 4.3, and 4.4 show snapshots of the ^{40}Ca+^{40}Ca reaction either at 395 fm/c for the regular grid, or at 495 fm/c for the larger grid. They are all XZ projections of density, summed over all density in the Y dimension. In Figs. 4.1 and 4.2, there is no cluster production, with the latter having a larger grid size. In Figs. 4.3 and 4.4 there is cluster production, with the latter having a larger grid size. The method of cluster production is described in section 4.5.

In the case of the normal sized grid space, Figs. 4.1 and 4.3, the residues start to exit the grid at about 400 fm/c. While in the case of the large grid, Figs. 4.2 and 4.4, the residues remain on the grid until the end of the simulation at 500 fm/c. The figures also show that cluster production has a large effect on the dynamics of the reaction; this is explored further in section 4.5.

For each reaction, energy and baryon number should be conserved. To evaluate the energy

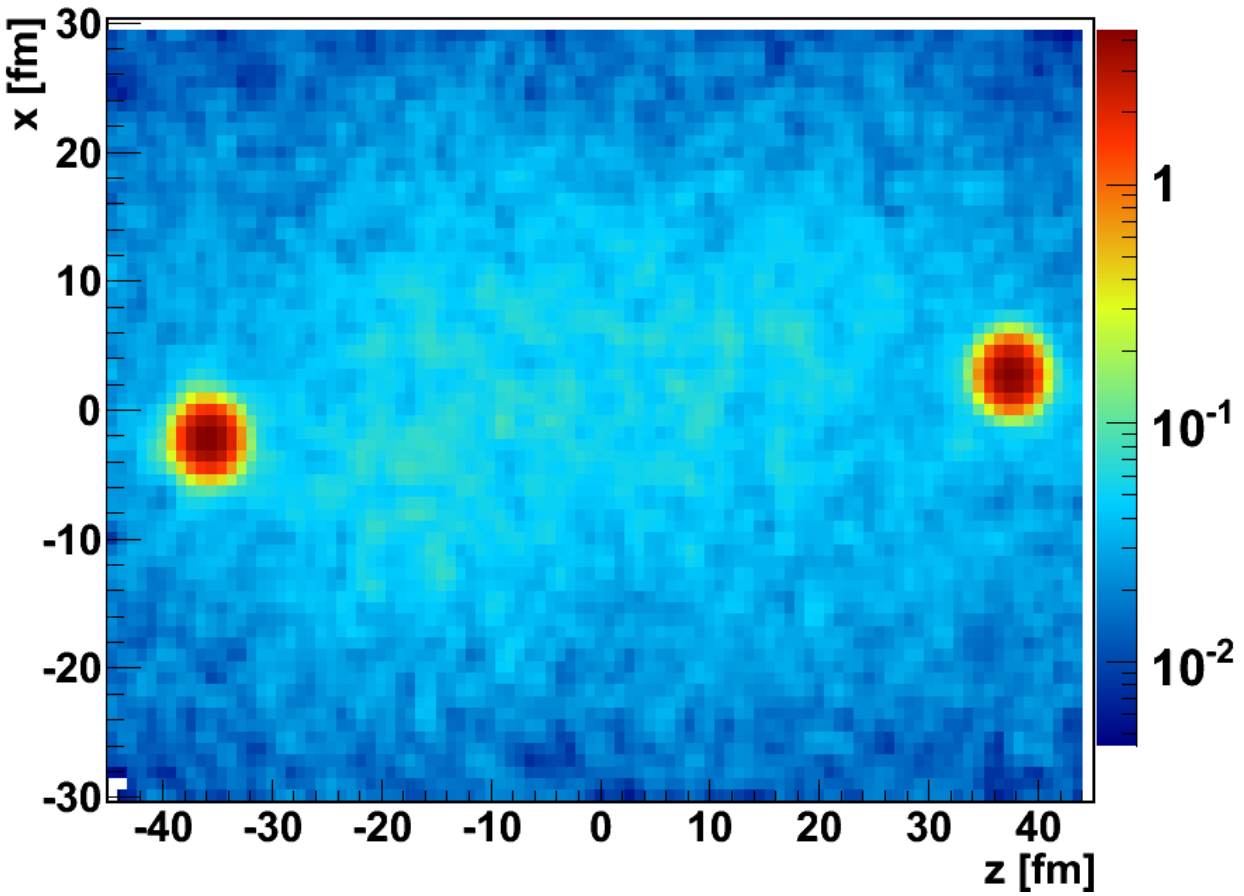

Figure 4.1: XZ plane projection of central ^{40}Ca+^{40}Ca reaction at 395 fm/c without cluster production. The masses of the two large residues were calculated. The sum of the residue masses is displayed in Table 4.1.

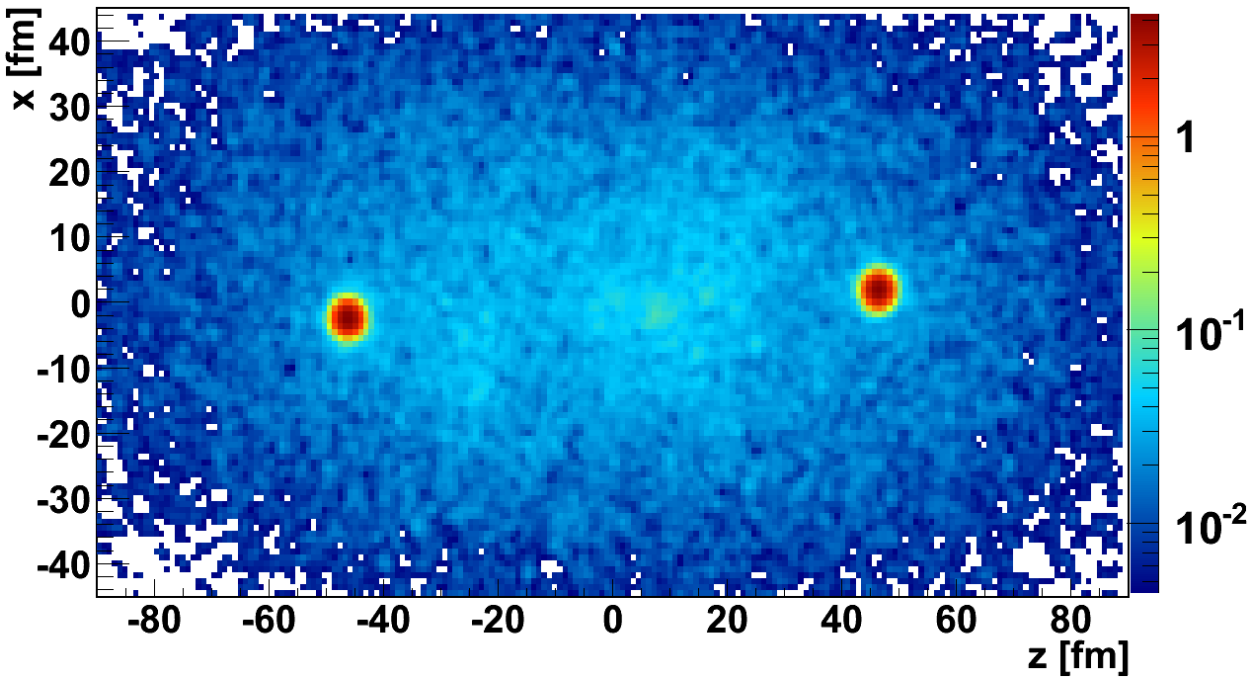

Figure 4.2: XZ plane projection of central ^{40}Ca+^{40}Ca reaction at 495 fm/c without cluster production for a larger computational grid size. The masses of the two large residues were calculated. The sum of the residue masses is displayed in Table 4.1.

conservation, the BUU code outputs the energy per baryon at specified time intervals. For a ^{40}Ca+^{40}Ca reaction at E/A = 80 MeV, the energy per nucleon of the projectile and target in the center of mass is 20 MeV. After taking the binding energy ($\approx$ 8 MeV) into account, the average energy per nucleon is 12 MeV. Fig. 4.5 shows the absolute energy (top) and the change in the average energy per nucleon (bottom) as a function of time, where all values in the bottom plot are with respect to the energy at time=0 fm/c. It is clear that energy is conserved in all cases within approximately E/A = 0.2 MeV. There is a decrease in the case of the normal grid size without clusters, shortly after 300 fm/c, which occurs when the residues exit the grid. That decrease is of the order of 300 keV per nucleon.

Table 4.1 shows how the mass of the system is distributed among the emitted particles. Regardless of cluster production and computational grid size, particle number is conserved.

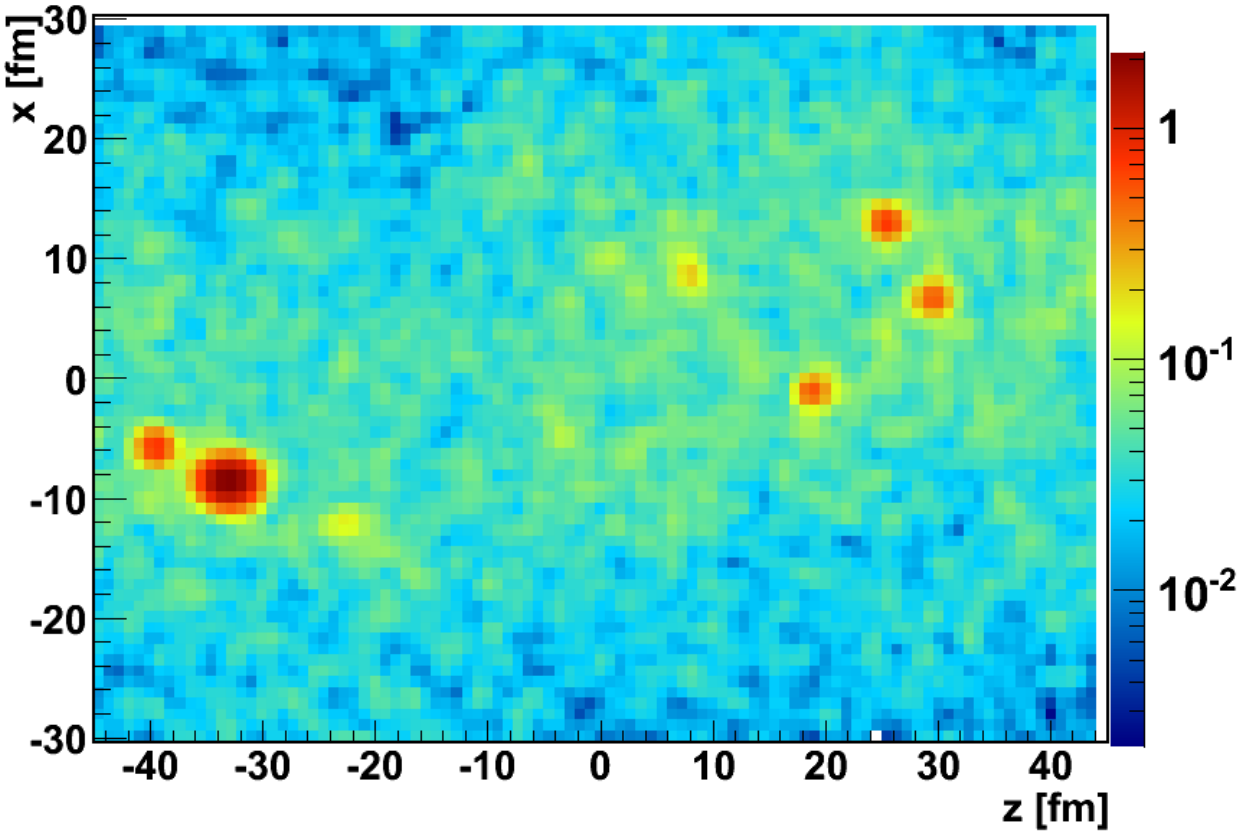

Figure 4.3: XZ plane projection of central ^{40}Ca+^{40}Ca reaction at 395 fm/c with cluster production. The masses of the five largest residues were calculated. The sum of the residue masses is displayed in Table 4.1.

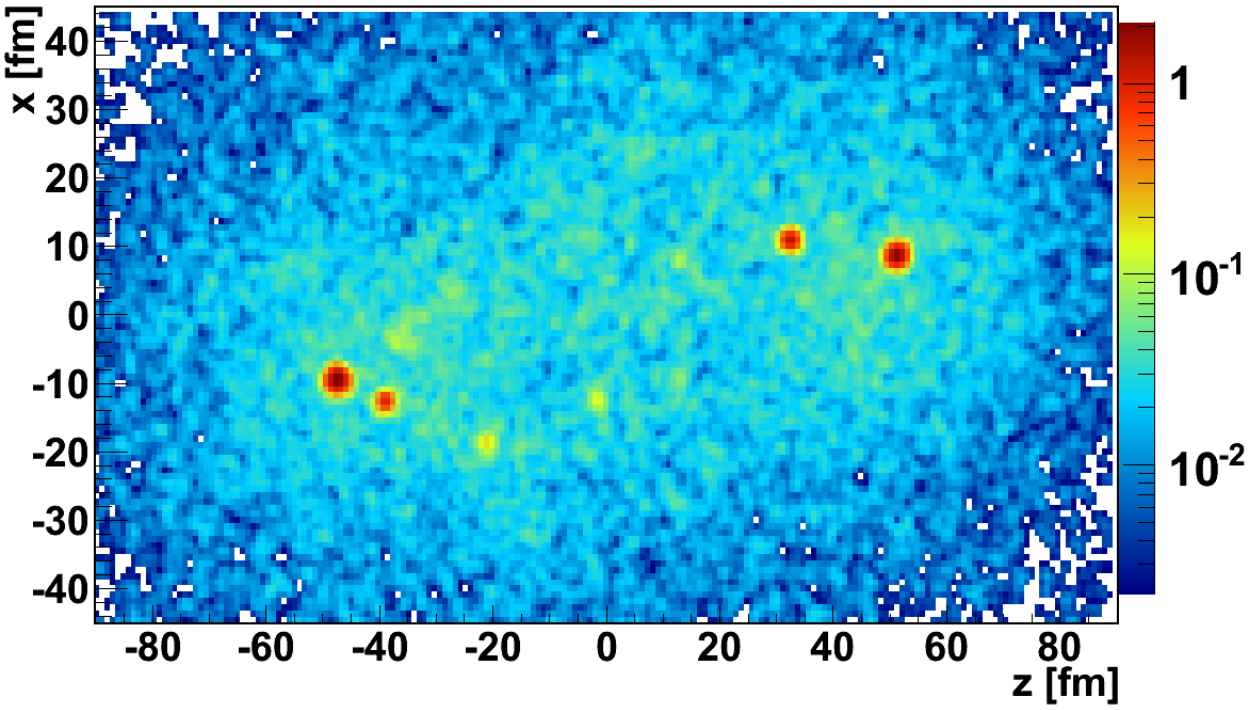

Figure 4.4: XZ plane projection of central ^{40}Ca+^{40}Ca reaction at 495 fm/c with cluster production for a larger computational grid size. The masses of the four largest residues were calculated. The sum of the residue masses is displayed in Table 4.1.

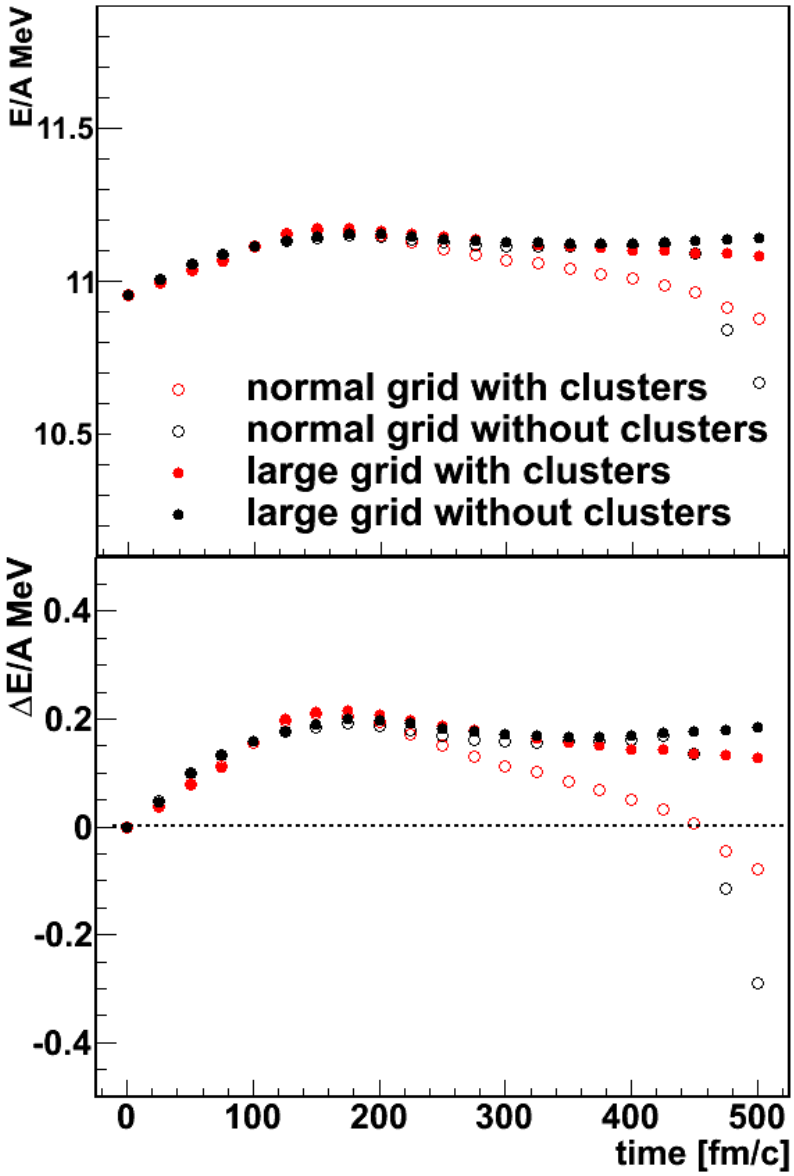

Figure 4.5: Change in average single particle energy as a function of time, illustrating conservation of energy.

It should be noted that the residues are calculated crudely from a density profile and may have been over or under estimated. This explains why the total mass does not sum up to exactly 80.

particle	BG	NG	BGC	NGC
p	30.9	30.9	11.4	11.3
n	30.5	30.5	11.4	11.3
d	0	0	5.1	5.1
3He	0	0	6.8	6.8
t	0	0	6.7	6.8
mass of residues	18.9	18.8	7.1	6.2
total nucleons	80.3	80.2	80.6	79.8

Table 4.1: Results of particle conservation for central ^{40}Ca+^{40}Ca reactions. BG = Big Grid without clusters, NG = Normal Grid without clusters, BGC = Big Grid with Clusters, and NGC = Normal Grid with Clusters.

The source function is the probability of two protons being separated by some distance, r, at the time the second proton is emitted. As a measure of the space-time extent, the source function can depend on the time at which the source is evaluated. Selecting protons emitted before 250 fm/c excludes protons emitted late in the collision. This late emission would increase the size of the source. Thus, the source will be larger when all protons emitted at later times are included.

In general, source functions are calculated by evaluating the separation distance, r, between pairs of protons emitted in BUU simulations at the time when the second of these protons are emitted. Figs. 4.6, 4.7, 4.8, and 4.9 compare sources calculated for two selections of proton transverse momentum, with and without cluster production. They show source functions for high (circles) and low (squares) transverse momentum cuts for four cases: large grid no clusters (upper left), large grid with clusters (upper right), normal grid no clusters (lower left), and normal grid with clusters (lower right). The sources for protons emitted

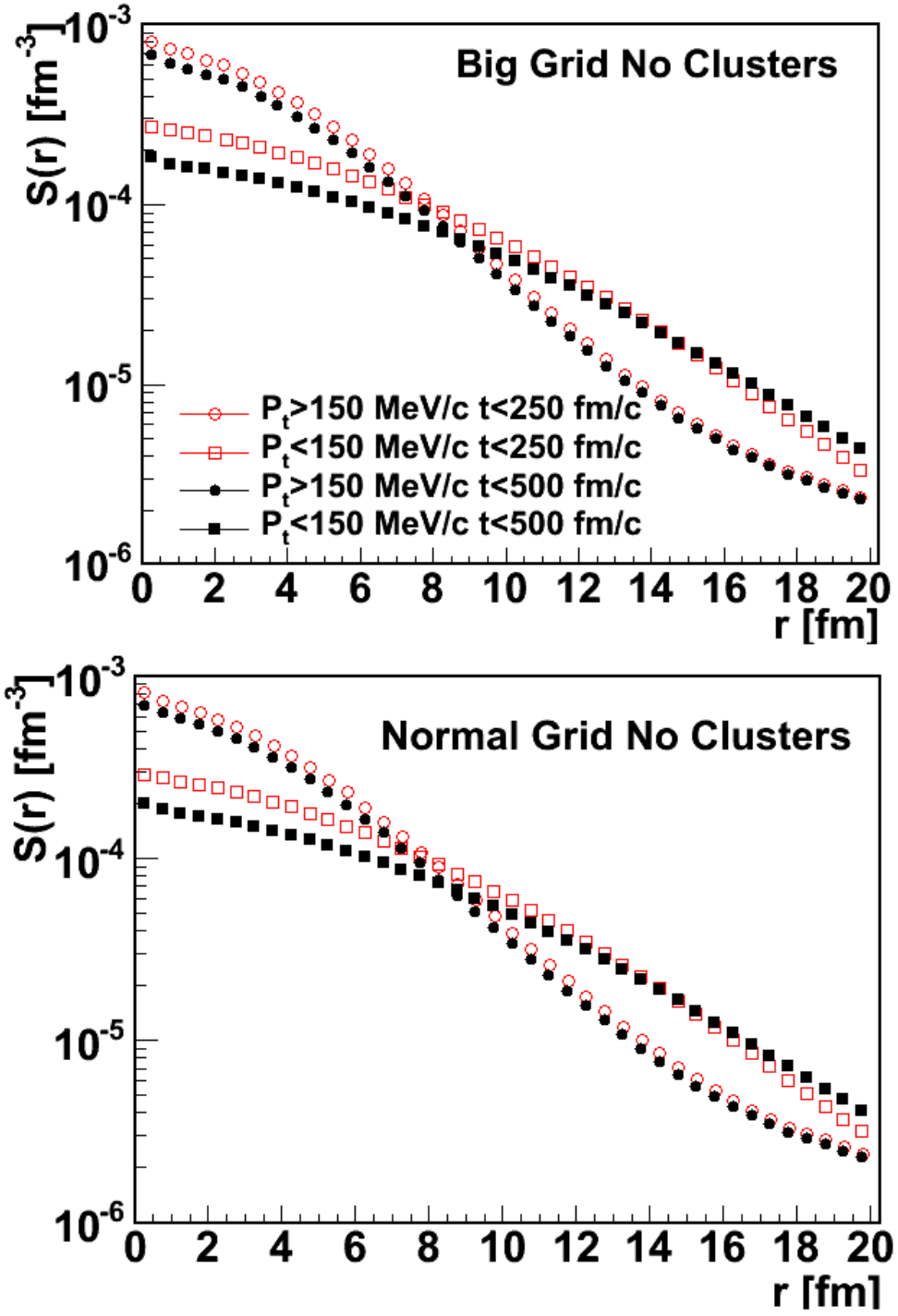

Figure 4.6: Effect of using a time cut on source functions for ^{40}Ca+^{40}Ca without cluster production. $r_{1/2}$ sizes for the sources are given in Table 4.2.

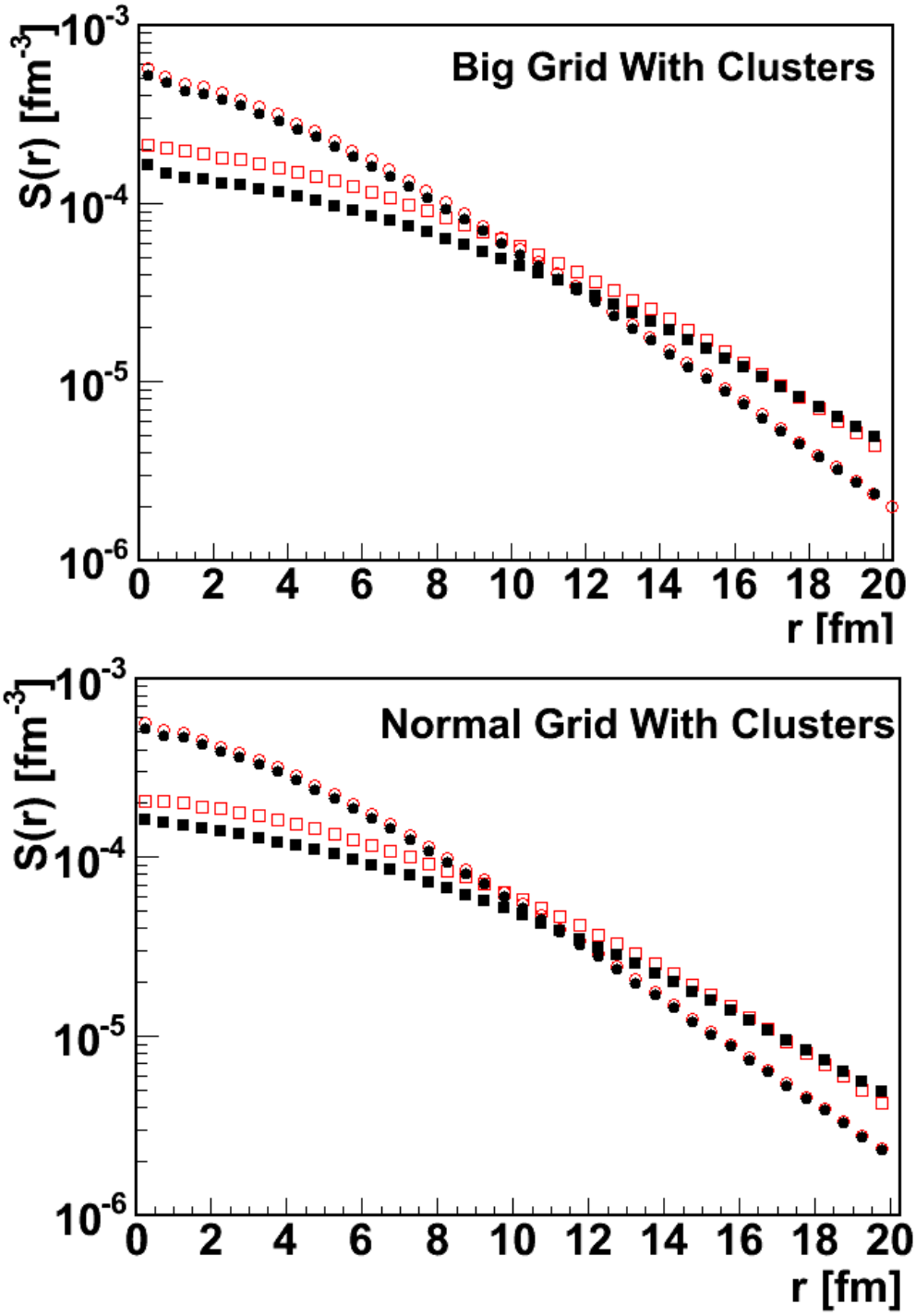

Figure 4.7: Effect of using a time cut on source functions for ^{40}Ca+^{40}Ca with cluster production. The legend is the same as the previous figure. $r_{1/2}$ sizes for the sources are given in Table 4.2.

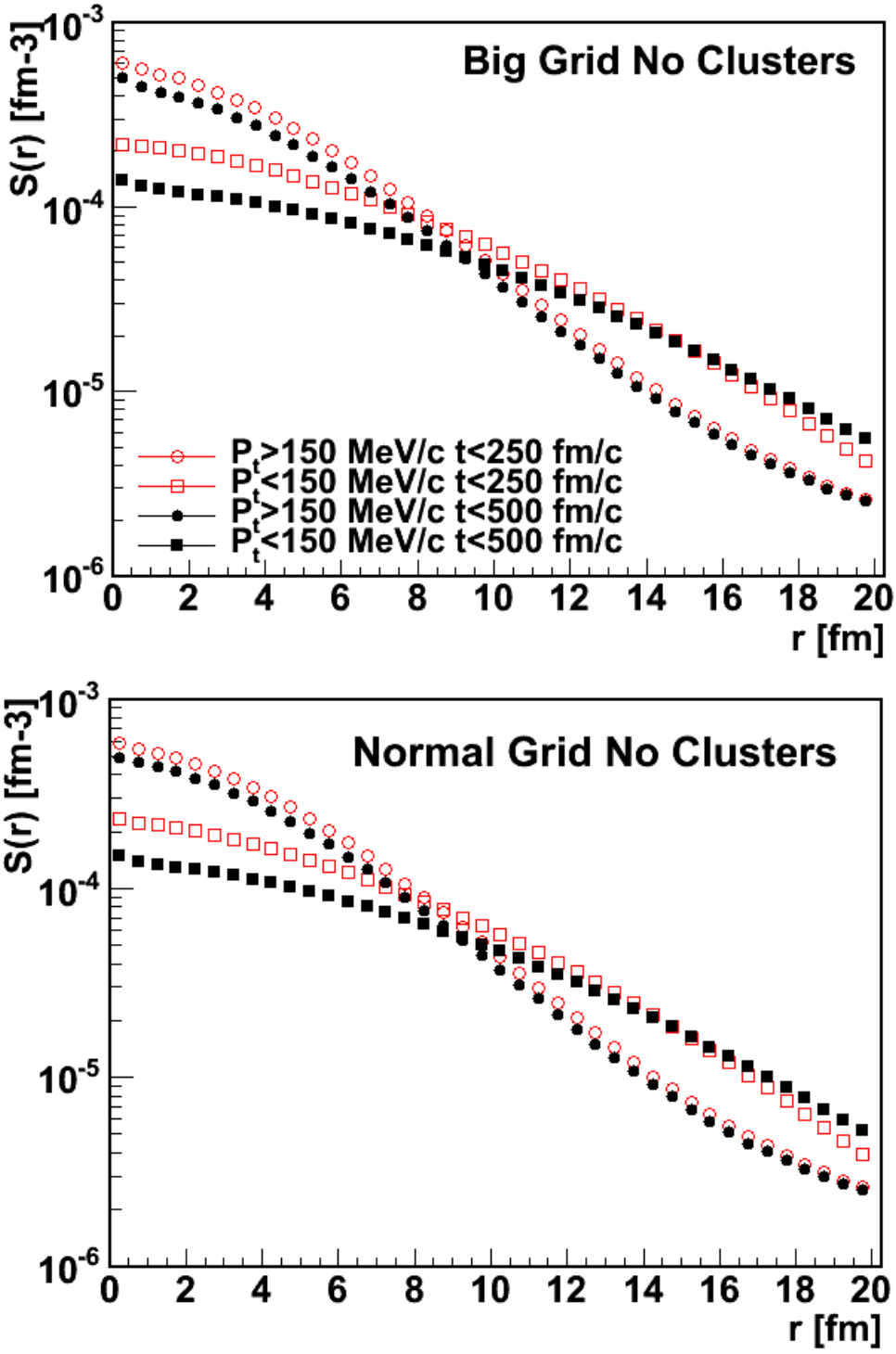

Figure 4.8: Effect of using a time cut on source functions for ^{48}Ca+^{48}Ca without cluster production. $r_{1/2}$ sizes for the sources are given in Table 4.2.

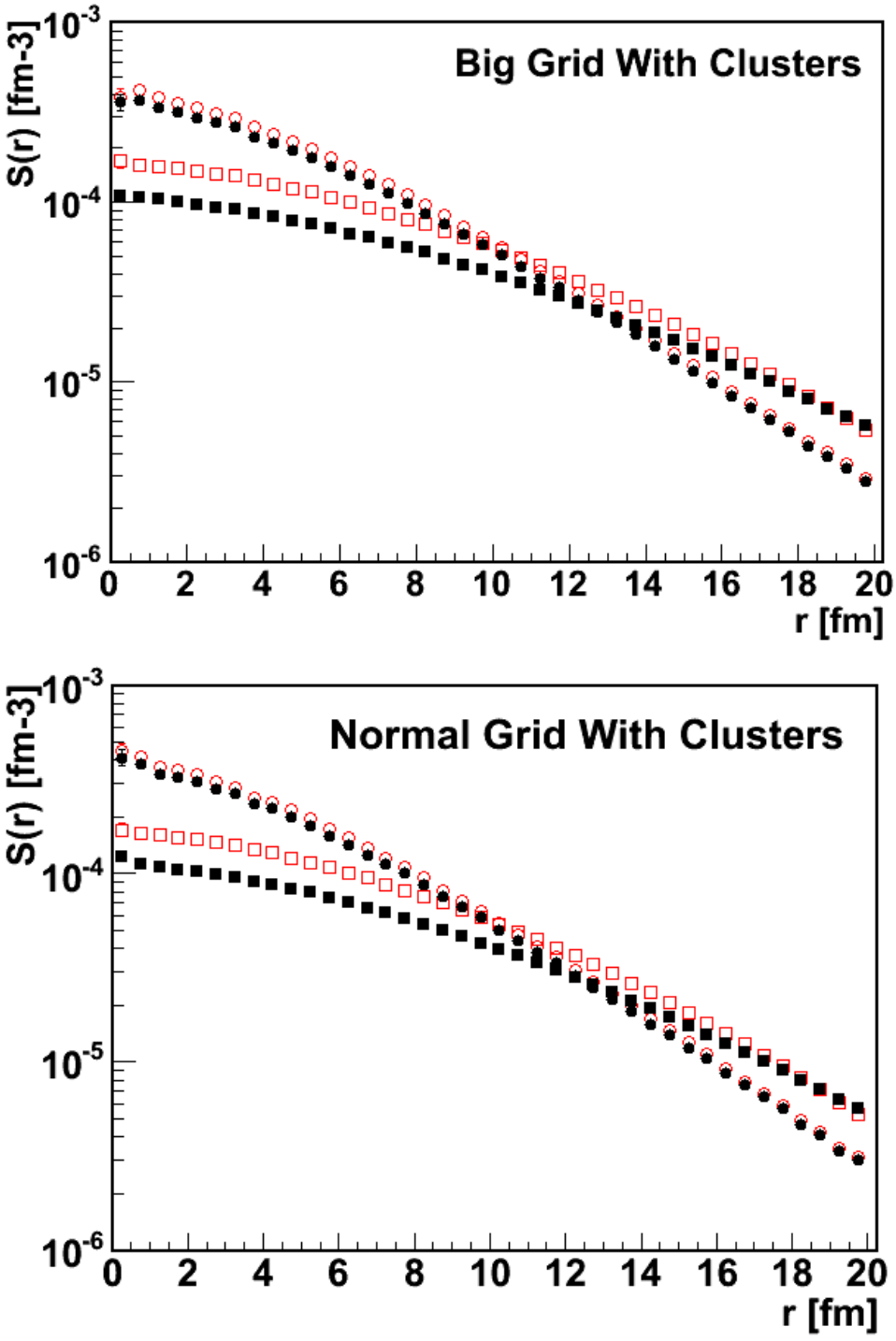

Figure 4.9: Effect of using a time cut on source functions for ^{48}Ca+^{48}Ca with cluster production. The legend is the same as the previous figure. $r_{1/2}$ sizes for the sources are given in Table 4.2.

with t<250 fm/c are in red open symbols and sources for all protons emitted with t<500 fm/c are in black closed symbols. Figs. 4.6 and 4.7 show the results for the ^{40}Ca+^{40}Ca reaction and Figs. 4.8 and 4.9 show the results for the ^{48}Ca+^{48}Ca reaction. The figures show that the source becomes somewhat larger with increased time. The effect is small for high p_T protons, but stronger for low p_T protons which is consistent with the notion that slower protons are often emitted later in time from a cooling, expanding source. The sensitivity to grid size in these figures is very small.

More quantitative information can be obtained by constructing better measures of the space-time extent of these sources. One measure of the space-time extent of the source is the radius at which the source function decreases to 1/2 of its maximum value, $r_{1/2}$, described in Appendix C. The $r_{1/2}$ size for sources in Figs. 4.6, 4.7, 4.8, and 4.9 are given in Table 4.2. For calculations without clusters, 4-5 protons after emitted after 250 fm/c, whereas only 1 proton is emitted after 250 fm/c for calculations with clusters. The source size does not change significantly with changes in the size of the grid. Thus, the normal grid size is adequate for the present purposes.

The total transverse momentum cut has a large effect on the source size, with higher total transverse momentum having a smaller source. This is consistent with the notion that faster protons come from the pre-equilibrium source, early in the reaction, when it is smaller. This larger size for low energy protons can be a reflection of both the physical size of the source, which is expanding with time, and the lifetime for emission, which is longer for lower energy protons. The production of clusters also influences the size of the source, making it larger. If two protons are close together in space after emission, they are more likely to be in a region with a larger density in phase space, making it more likely that a proton will

cluster with other nucleons to form a mass two or three cluster. By depleting the highest density regions, it reduces the number of pairs of protons with a small distance between them and effectively increases the size of the source. Cluster production reduces the relative phase space density. The projection of relative phase space density into coordinate space is the source distribution.

	BG	NG	BGC	NGC
^{40}Ca+^{40}Ca	r[fm]	r[fm]	r[fm]	r[fm]
p_T<150 MeV/c t<250 fm/c	6.39±0.20	6.27±0.25	6.96±0.18	7.12±0.21
p_T>150 MeV/c t<250 fm/c	4.27±0.25	4.25±0.25	4.84±0.23	4.64±0.21
p_T<150 MeV/c t<500 fm/c	7.23±0.25	6.94±0.20	7.30±0.24	7.35±0.23
p_T>150 MeV/c t<500 fm/c	4.30±0.23	4.25±0.25	4.86±0.23	4.65±0.22
^{48}Ca+^{48}Ca				
p_T<150 MeV/c t<250 fm/c	6.86±0.21	6.77±0.24	7.73±0.24	7.70±0.23
p_T>150 MeV/c t<250 fm/c	4.59±0.19	4.63±0.20	5.03±0.23	5.27±0.29
p_T<150 MeV/c t<500 fm/c	8.03±0.19	7.82±0.23	8.13±0.20	8.02±0.20
p_T>150 MeV/c t<500 fm/c	4.65±0.22	4.64±0.21	5.09±0.21	5.29±0.30

Table 4.2: $r_{1/2}$ values for each combination of grid size and cluster production for both reaction systems and two transverse momentum cuts. BG = Big Grid without clusters, NG = Normal Grid without clusters, BGC = Big Grid with Clusters, and NGC = Normal Grid with Clusters.

By comparing calculations with the big grid without clusters (BG) to calculations with the normal grid without clusters (NG) and calculations with the big grid with clusters (BGC) to calculations with the normal grid with clusters (NGC), one can see that the normal grid size of 30 by 30 by 45 fm^3 is sufficient for our purposes. The source size does not change, within uncertainty, if the grid is made larger. The source gets smaller if only protons emitted before

250 fm/c are included because protons emitted at later times are excluded which increases the space-time extent of the source, however, all protons should be included in the source regardless of emission time because emission time is not independently measured. We can only make selections on measurable observables.

4.3 Influence of Number of Test Particles

In BUU calculations, a specified number of test particles are created for each nucleon in the reaction in order to better simulate the continuous phase space distribution corresponding to the Wigner transform of the one body distribution function. These test particles collide with each other and can be emitted from the source. It is important that the calculations are stable with changes in test particle number. Too few test particles per nucleon can cause too large fluctuations in the mean field potential and too large fluctuations in the Wigner transform which is used to calculate the Pauli blocking in the collision term. There is no hard limit on the minimum value of test particles used, but the number of test particles should be greater than about 200 to achieve stability in the mean field and phase space distribution for the Danielewicz version of BUU [60]. Even with 200 test particles per nucleon, there are additional fluctuations not seen with higher numbers of test particles such as 800 or 1600, which is demonstrated below. Calculations with a momentum dependent, soft isoscalar mean field, but without cluster production, were performed to explore the dependence on test particle number. The calculations all used the Rostock in-medium cross sections and a density dependent symmetry energy exponent term, γ=0.7. Calculations shown elsewhere in this dissertation employed 800 or 1600 test particles per nucleon. Here, the calculation with 200 test particles is examined to explore the computational stability against test particle

number.

In Fig. 4.10 snapshots of the ^{40}Ca+^{40}Ca reaction are compared for 3 values of test particle (tp) number, 200, 800, and 1600. The size of the large residue is unchanged when scaled by the number of test particles. Fig. 4.10 shows that the residues are farther apart for 1600 and 800 tp than for 200 tp. In the case of 200 tp, the centers of the residues are separated by about 67 fm. In the case of 800 and 1600 tp, the centers of the residues are separated by about 71 fm. The case of 200 tp was examined with 4 different random seeds to probe whether this difference in separation distance was real, or a result of fluctuations.

The velocities of residues , however, becomes more sensitive to fluctuations when the calculation evolves with fewer test particles. Fig. 4.11 shows how the residue velocities can fluctuate, for a small number of test particles, from collision to collision in the simulation. Different collisions were simulated with different random number seeds, and the variation in the separation of the nuclei at 300 fm/c is consistent with the variation with test particle number. For example, in the case of 200 tp with 4 different random seeds, the separation of the centers of the residues varies from 68-74 fm. This emphasizes the importance of averaging observables over many runs.

Fig. 4.12 shows kinetic energy for protons emitted between 18-58° in θ with respect to the beam axis. The lab energy spectra is nearly identical for 800 or 1600 tp. In the case of 200 tp, there are fewer protons emitted with low energy, and more protons emitted with energies between 40-125 MeV. The low energy regime is dominated by long-lived emission from the residues. Its relative absence for the calculation with 200 tp suggests that the source might be smaller when fewer test particles are used.

In the case of 800 or 1600 tp, the source has a nice smooth shape as seen in Figs. 4.13

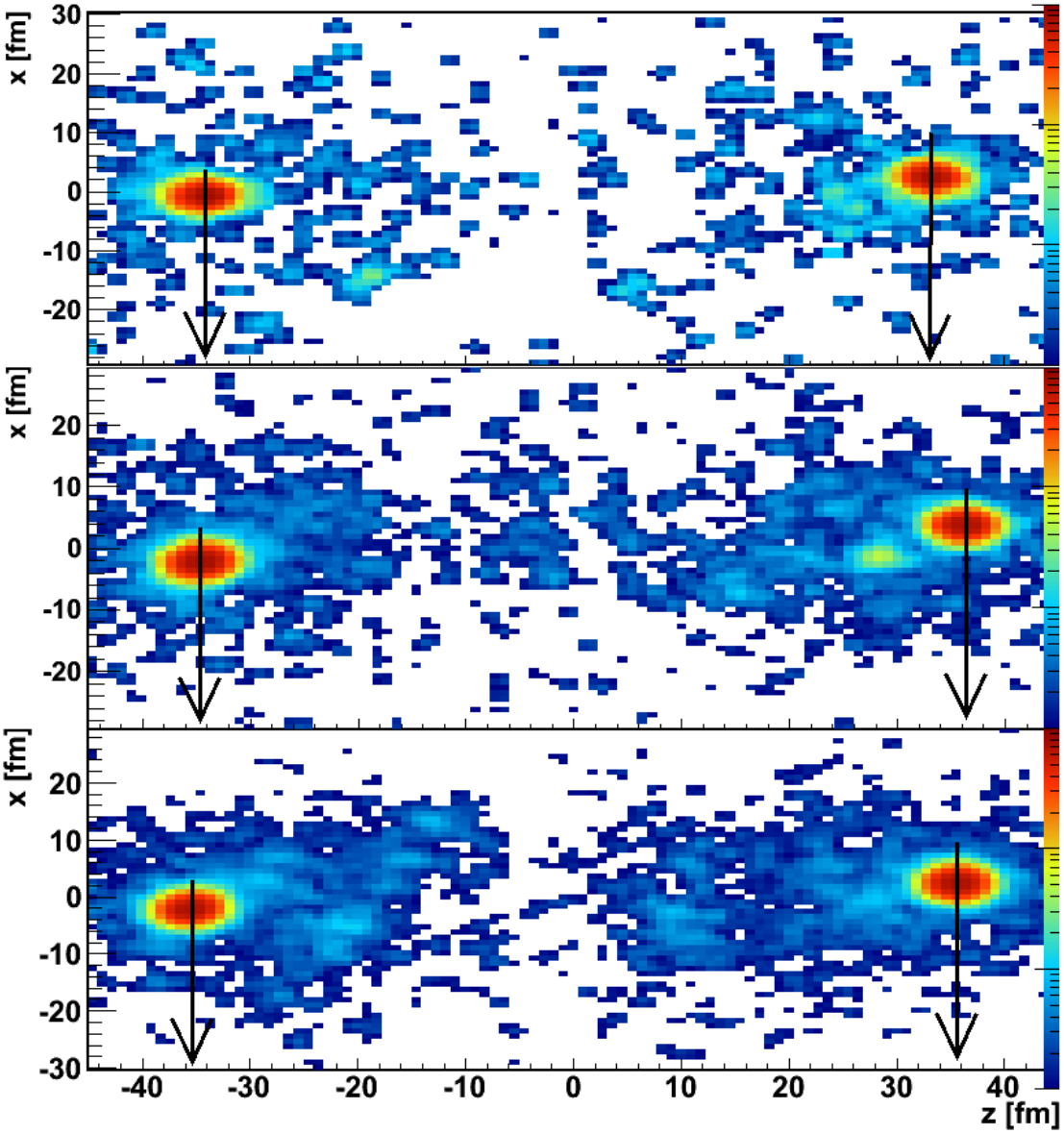

Figure 4.10: Snapshots of the ^{40}Ca+^{40}Ca reaction in the XZ plane at 300 fm/c. These are thin slices in the Y plane centered about $y = 0$. The top panel is for a reaction with 200 test particles, the middle panel is for 800 test particles and the bottom panel is for 1600 test particles.

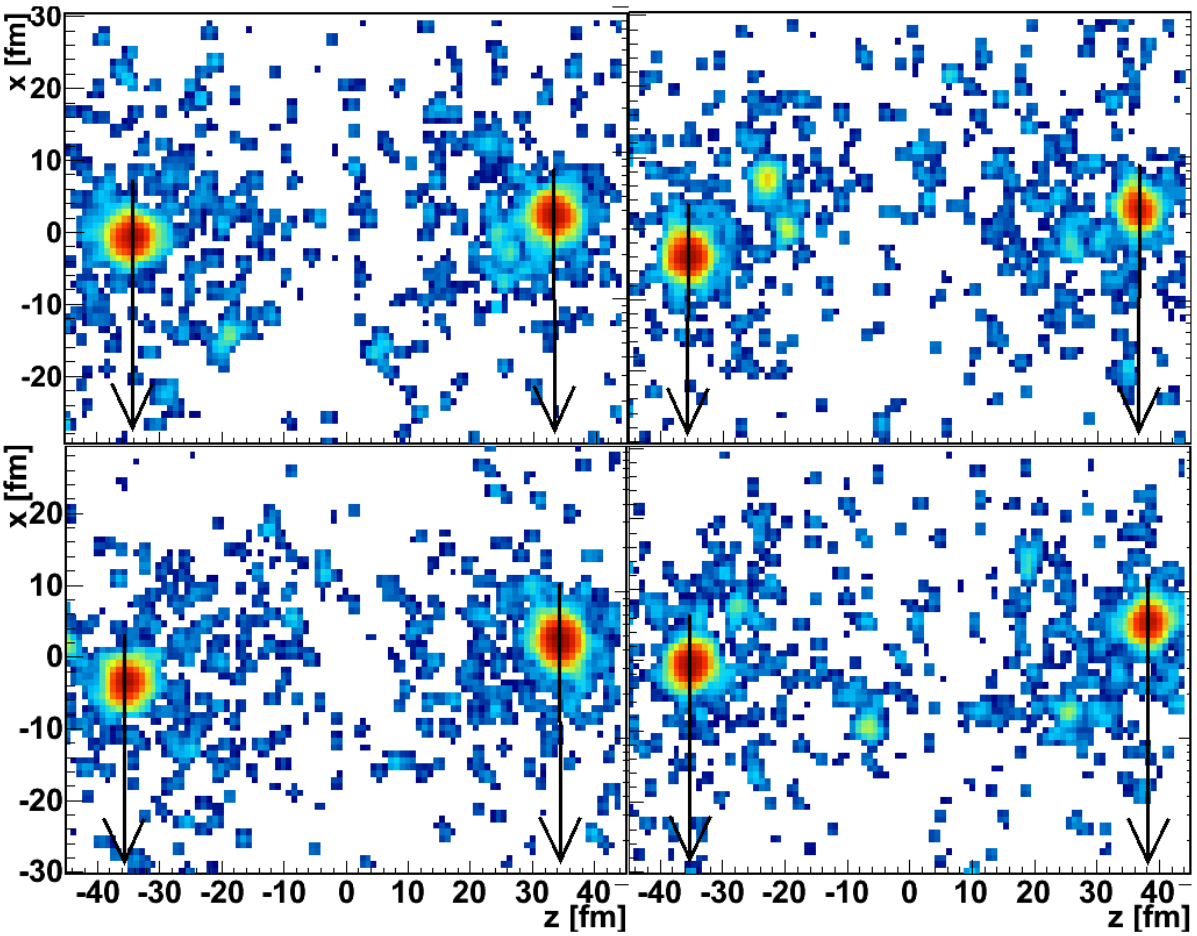

Figure 4.11: Snapshots of the ^{40}Ca+^{40}Ca reaction in the XZ plane at 300 fm/c. Thin slices in the Y plane centered about $y = 0$. All panels are for 200 test particles, with different random number seeds.

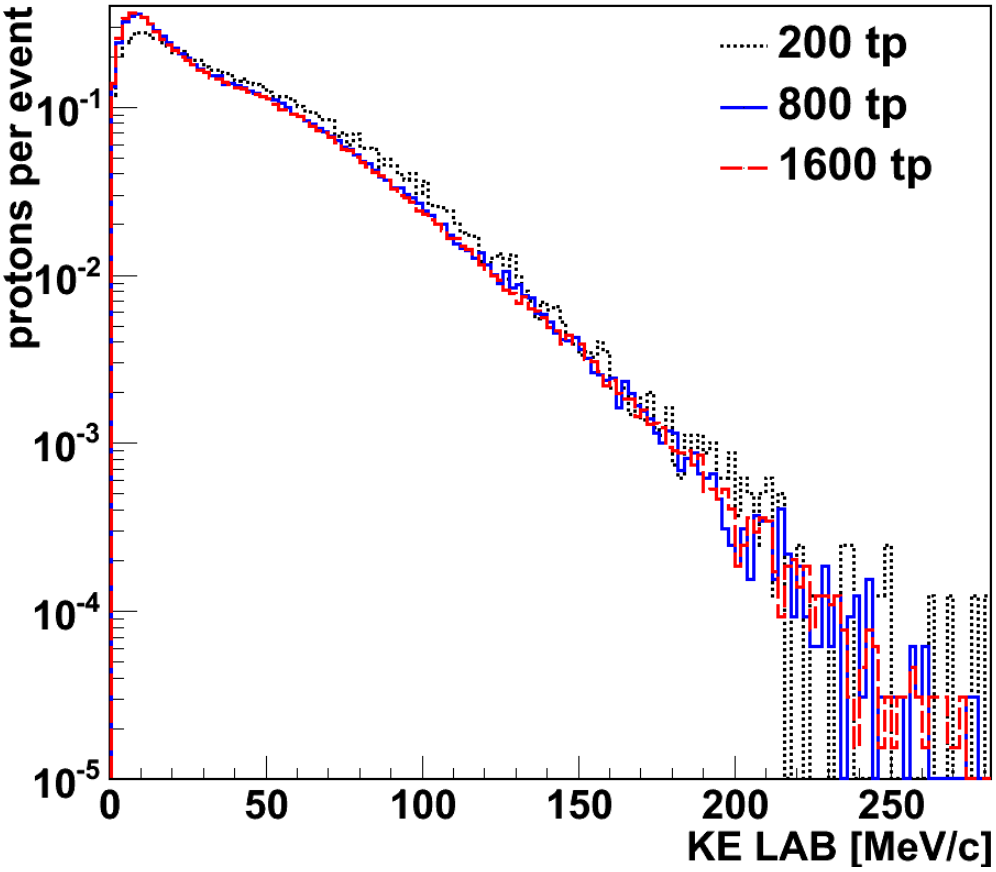

Figure 4.12: Lab energy spectra for protons emitted from ^{40}Ca+^{40}Ca reaction for three different values of test particle number.

and 4.14 and the sources are similar in shape. The source function resulting from protons in the 200 tp case has a somehwat larger tail at large r, especially with high p_T, and a slight peak at low p_T. It is not clear how significant the peak is, as the statistics at low r are small.

Table 4.3 shows $r_{1/2}$ values for simulations with different numbers of test particles. While there may be some differences in dynamics with small test particle number, the differences in $r_{1/2}$ are statistically insignificant.

	200 tp	800 tp	1600 tp
^{40}Ca+^{40}Ca	r[fm]	r[fm]	r[fm]
p_T<150 MeV/c $r_{1/2}$	5.59±0.55	6.10±0.30	6.32±0.25
p_T>150 MeV/c $r_{1/2}$	3.84±0.29	3.95±0.19	4.05±0.19
^{48}Ca+^{48}Ca			
p_T<150 MeV/c $r_{1/2}$	5.99±0.83	6.66±0.30	6.97±0.21
p_T>150 MeV/c $r_{1/2}$	4.57±0.38	4.26±0.25	4.26±0.25

Table 4.3: $r_{1/2}$ values for each value of test particle number for low and high p_T and both reaction systems.

4.4 Sensitivity of Observables to Impact Parameter

This section explores the effects of impact parameter on transverse energy and source size. For the source in these calculations, emitted protons were only included if the laboratory θ was between 18-58°, which corresponds roughly to the acceptance of HiRA. For all values of b explored here, 800 test particles were used with momentum dependent interactions and no cluster production. A somewhat soft symmetry energy exponent of γ=0.7 was used. All three cross sections reduction schemes are explored in this section: free, Rostock, and screened with η=0.7 for all collisions.

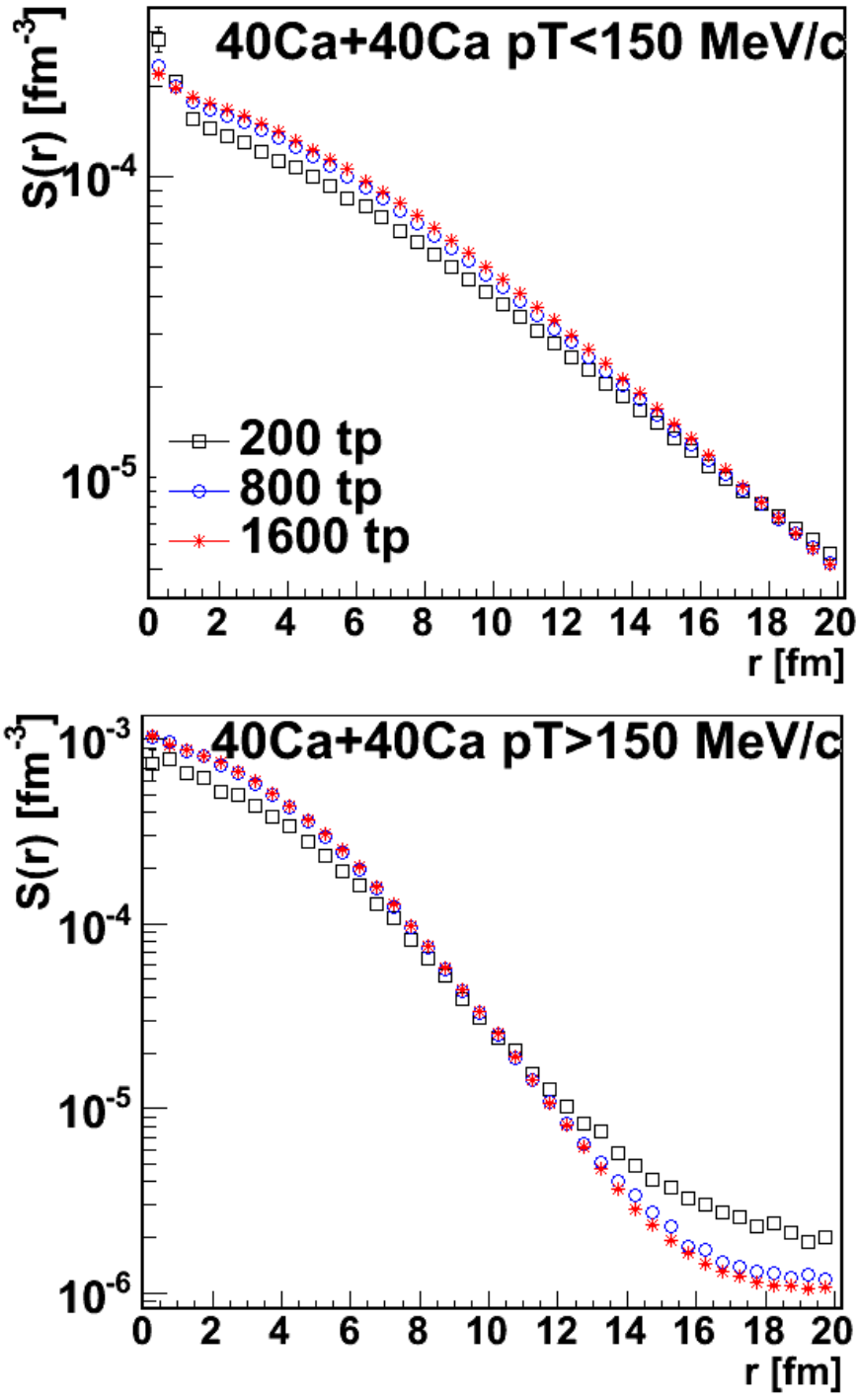

Figure 4.13: A comparison of the shape of source functions for different numbers of test particles used. The upper quadrants are for low p_T for ^{40}Ca+^{40}Ca. The bottom quadrants are for high p_T for the same reaction system.

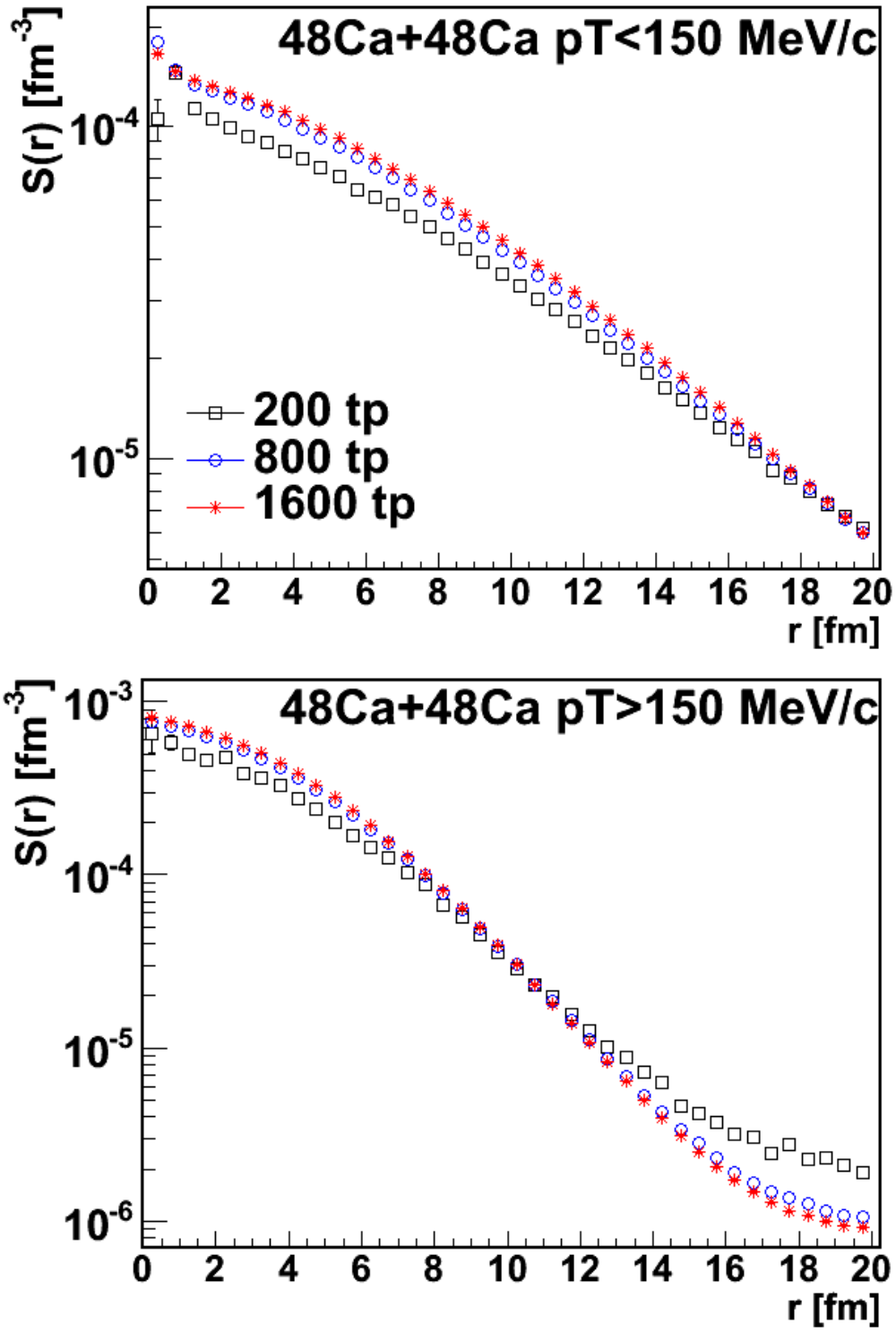

Figure 4.14: A comparison of the shape of source functions for different numbers of test particles used. The upper quadrants are for low p_T for ^{48}Ca+^{48}Ca (right). The bottom quadrants are for high p_T for the same reaction system.

The total transverse energy, E_t, defined by Eq. 3.11, has been shown to be a good candidate for determining the impact parameter [59]. Figs. 4.15, 4.17 and 4.16 show calculated values for E_t as a function of impact parameter for screened, Rostock, and free in-medium NN cross sections respectively. The transverse energy is quite different depending on which NN cross sections are used with larger values for free cross sections than reduced in-medium cross sections. In all cases, however, transverse energy is a monotonic function with respect to impact parameter.

Source functions were constructed as a function of impact parameters for this set of simulations. Figs. 4.18, 4.19, and 4.20 show the impact parameter dependence on source size for screened, Rostock, and free cross sections, respectively. The source radii generally decrease with impact parameter. The size of the source becomes increasingly dependent on impact parameter at larger values of b. Attention must be paid to impact parameter selection when precision comparisons are made between theory and data.

The impact parameter dependence can be understood qualitatively within the participant spectator model. In this picture, most of these protons originate from the participant zone offered by the geometric overlap of the projectile and target nuclei. The collision creates a participant source that expands to the freeze-out density, ρ_f, where the mean free path $\frac{1}{\rho\sigma}$ becomes approximately equal to the volume of the expanding system. At this point, the protons are emitted. The observed source radius, $R \propto (N/\rho_f)^{1/3}$ usually depends on the number of participant nucleons and on the freeze-out density.

In the participant spectator model, the value of $r_{1/2}$ at $b = 0$ fm reflects the freeze-out density when all nucleons are in the participant source. From the value of $r_{1/2}$ at $b = 0$ fm in Figs. 4.18 and 4.20 one can estimate that the freeze-out density is a factor of $(4.5/7)^3 = 0.26$

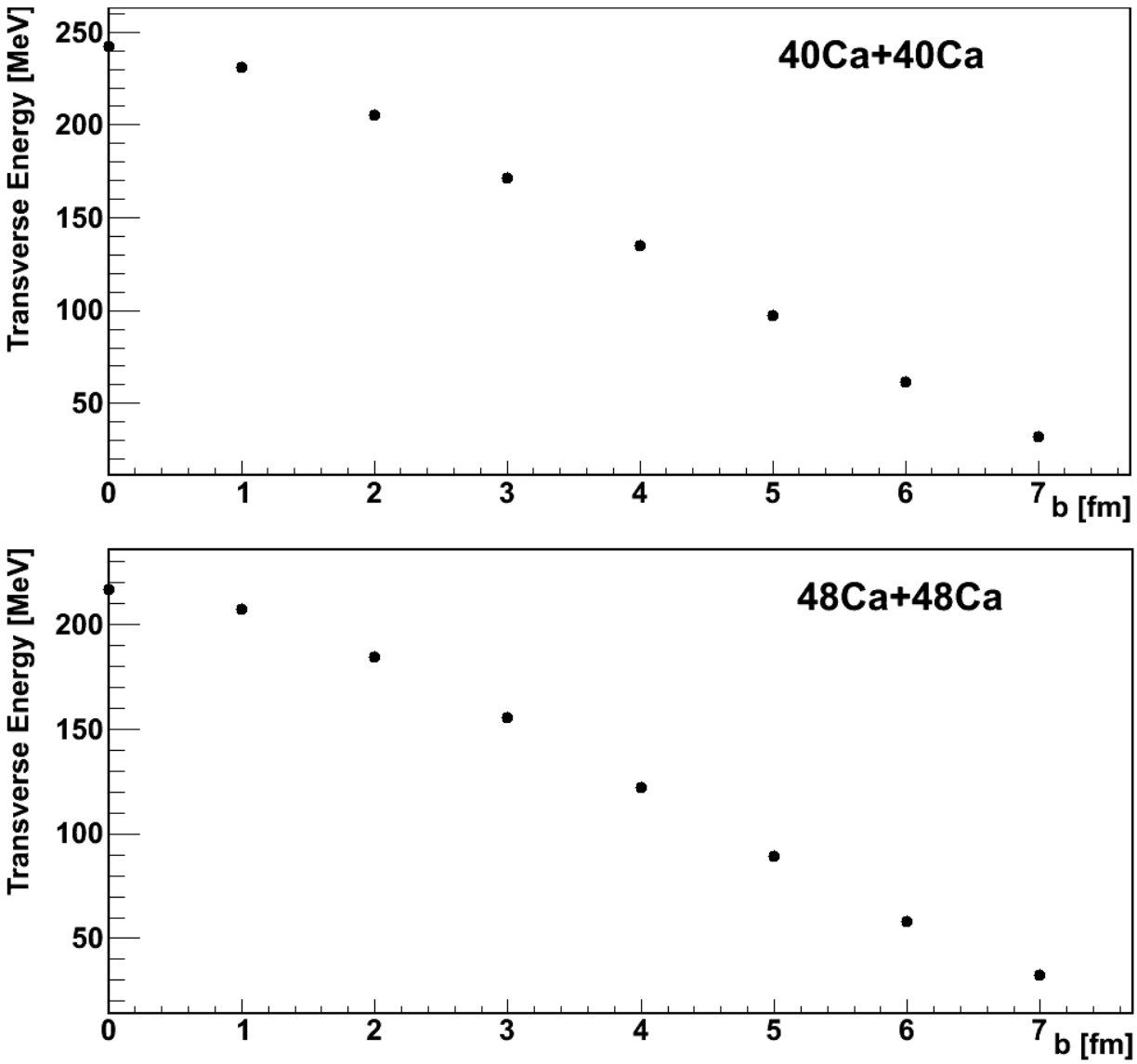

Figure 4.15: Transverse energy as a function of impact parameter for ^{40}Ca+^{40}Ca reaction (top) and ^{48}Ca+^{48}Ca reaction (bottom) for the screened cross section reduction.

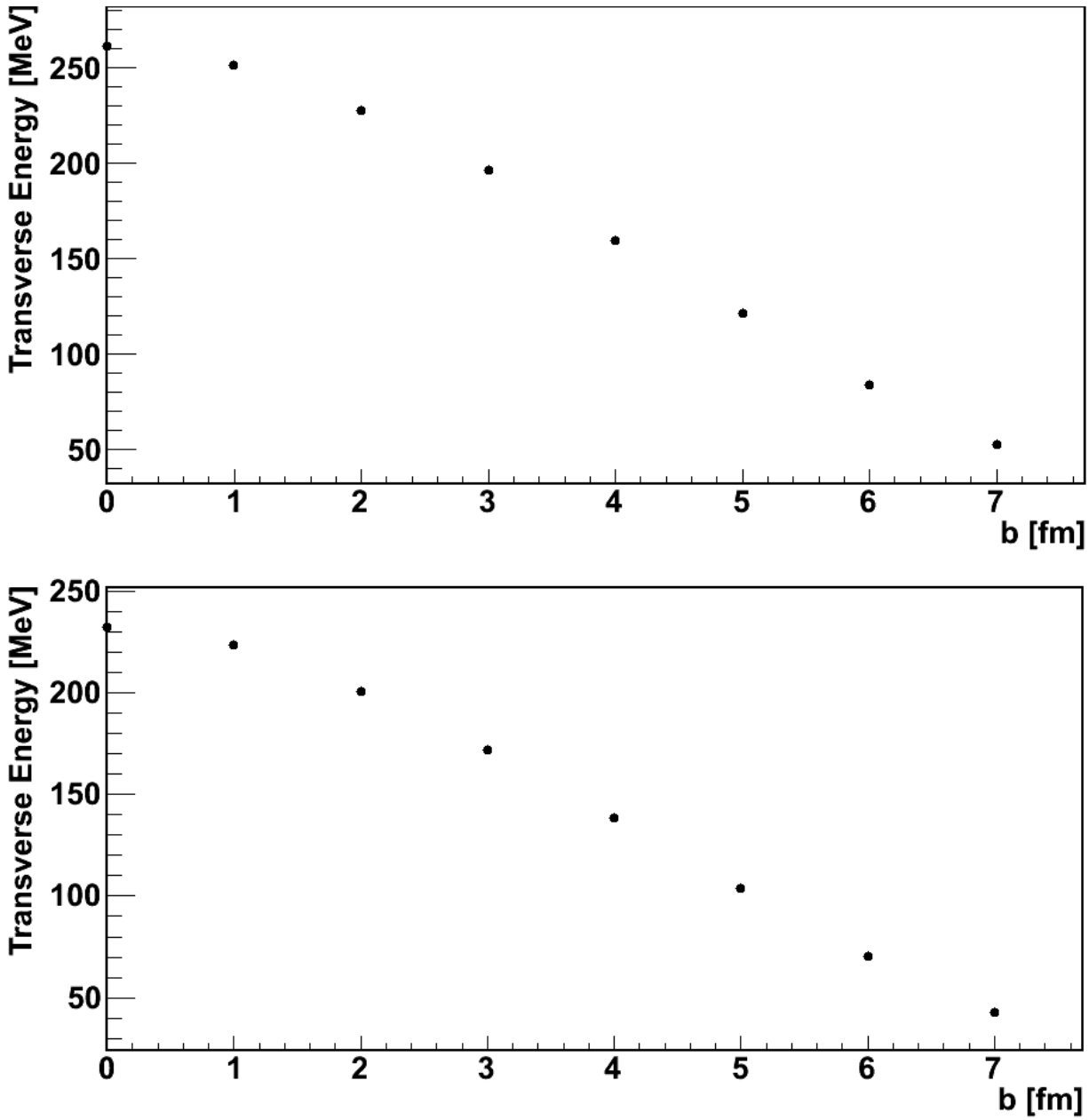

Figure 4.16: Transverse energy as a function of impact parameter for ^{40}Ca+^{40}Ca reaction (top) and ^{48}Ca+^{48}Ca reaction (bottom) for the Rostock cross section reduction.

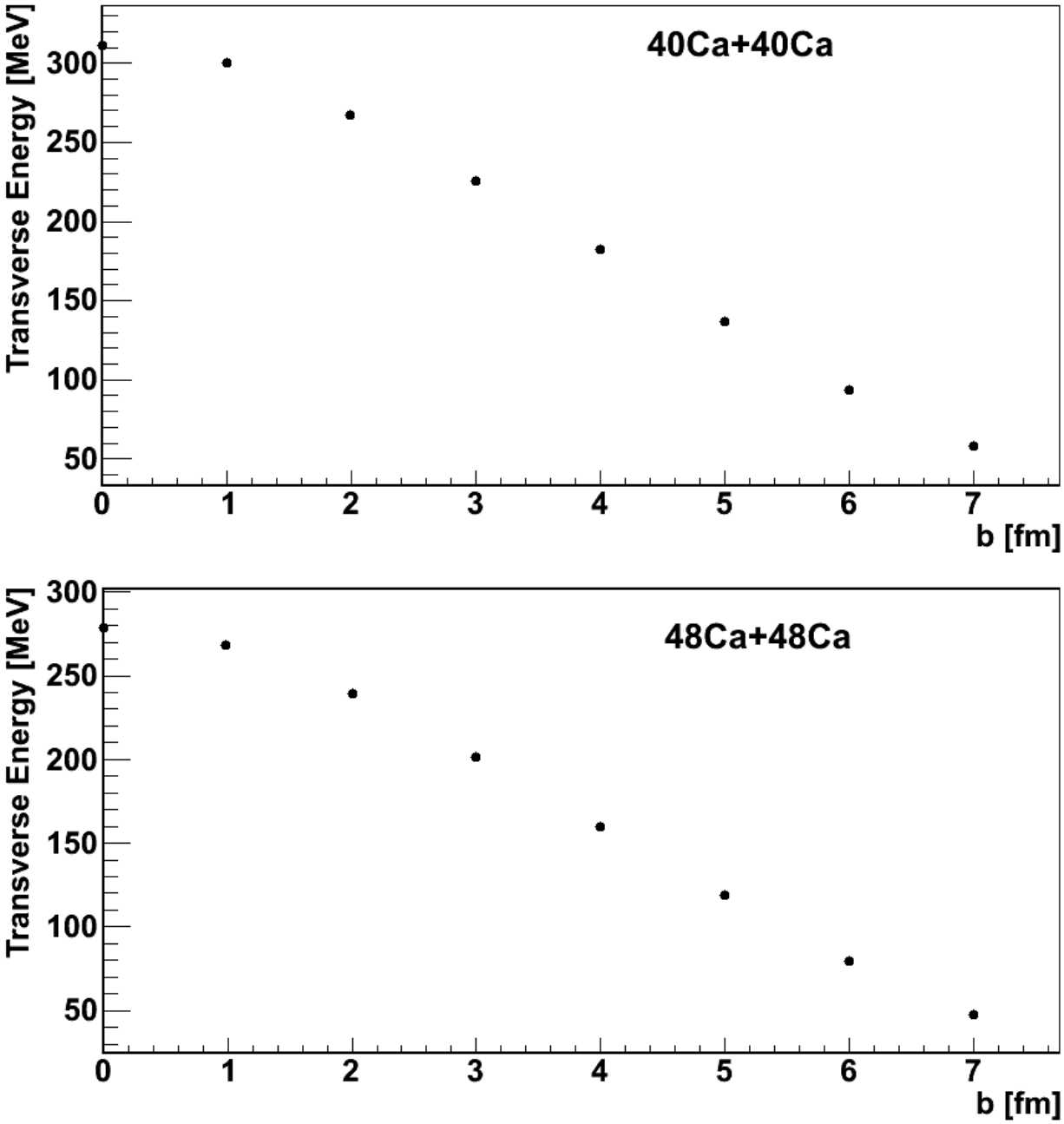

Figure 4.17: Transverse energy as a function of impact parameter for ^{40}Ca+^{40}Ca reaction (top) and ^{48}Ca+^{48}Ca reaction (bottom) for the free cross sections.

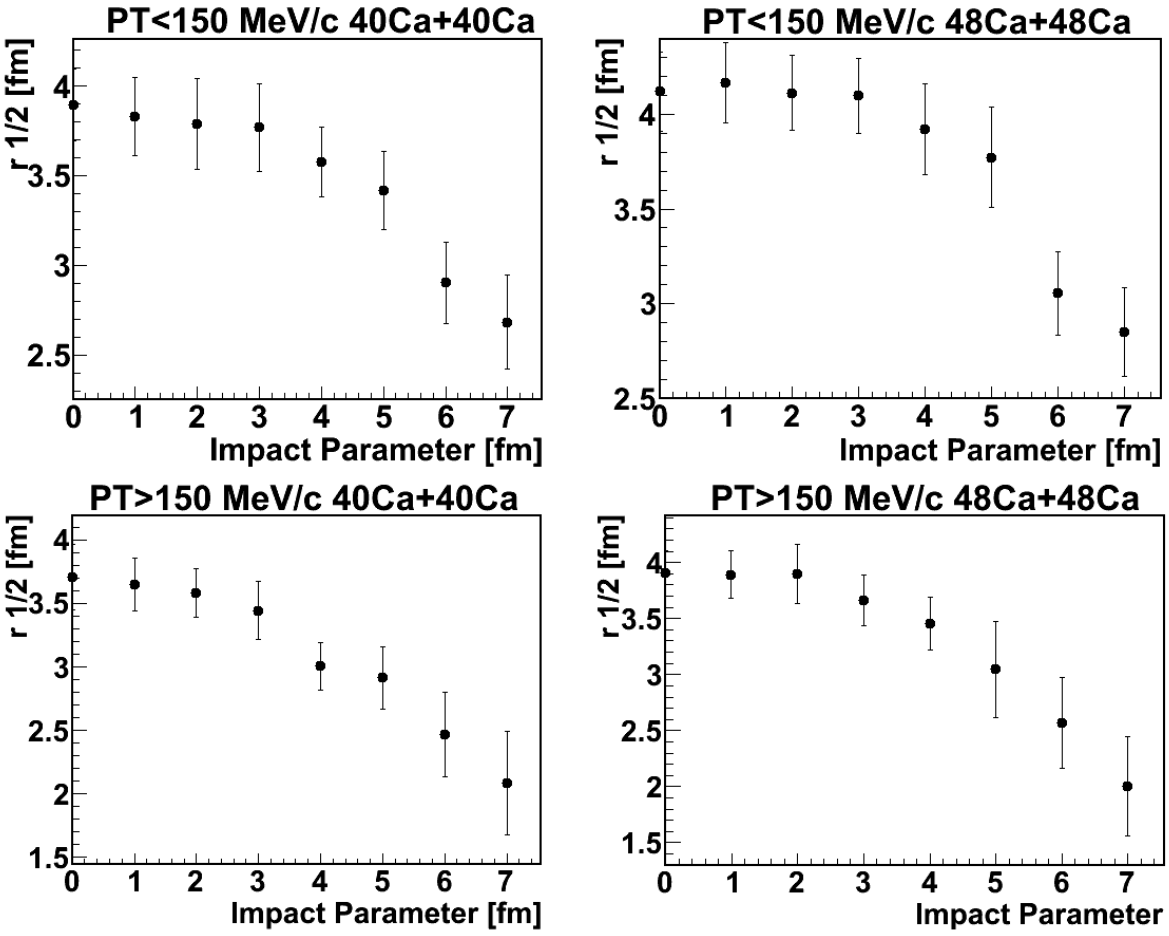

Figure 4.18: $r_{1/2}$ of source functions resulting from screened cross section reductions as a function of impact parameter. The upper quadrants are for a low transverse momentum cut $<$150 MeV/c for ^{40}Ca+^{40}Ca (left) and ^{48}Ca+^{48}Ca (right). The bottom quadrants are for a high transverse momentum cut $>$150 MeV/c for the same reaction systems.

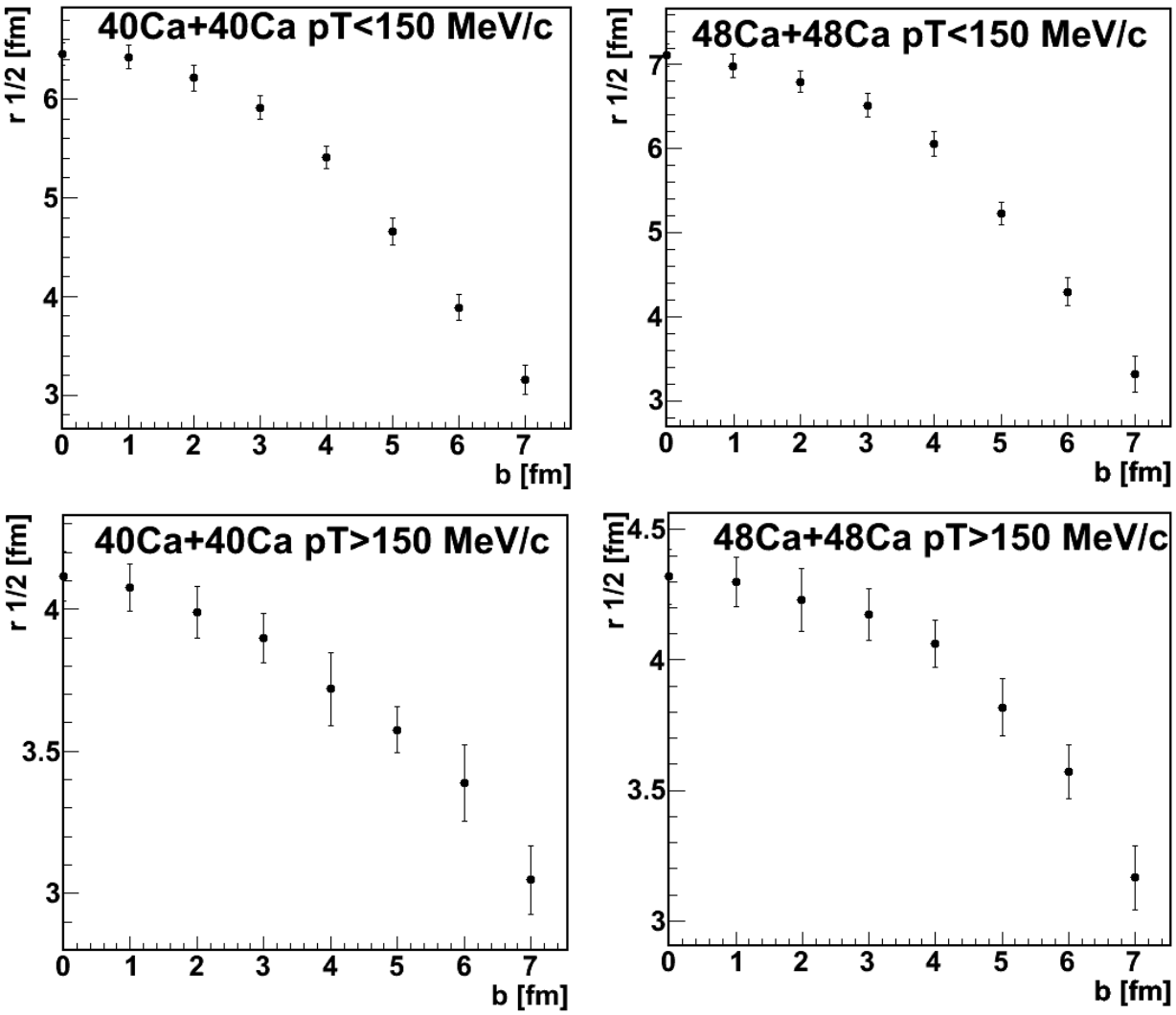

Figure 4.19: $r_{1/2}$ of source functions resulting from Rostock cross section reductions as a function of impact parameter. The upper quadrants are for a low transverse momentum cut $<$150 MeV/c for ^{40}Ca+^{40}Ca (left) and ^{48}Ca+^{48}Ca (right). The bottom quadrants are for a high transverse momentum cut $>$150 MeV/c for the same reaction systems.

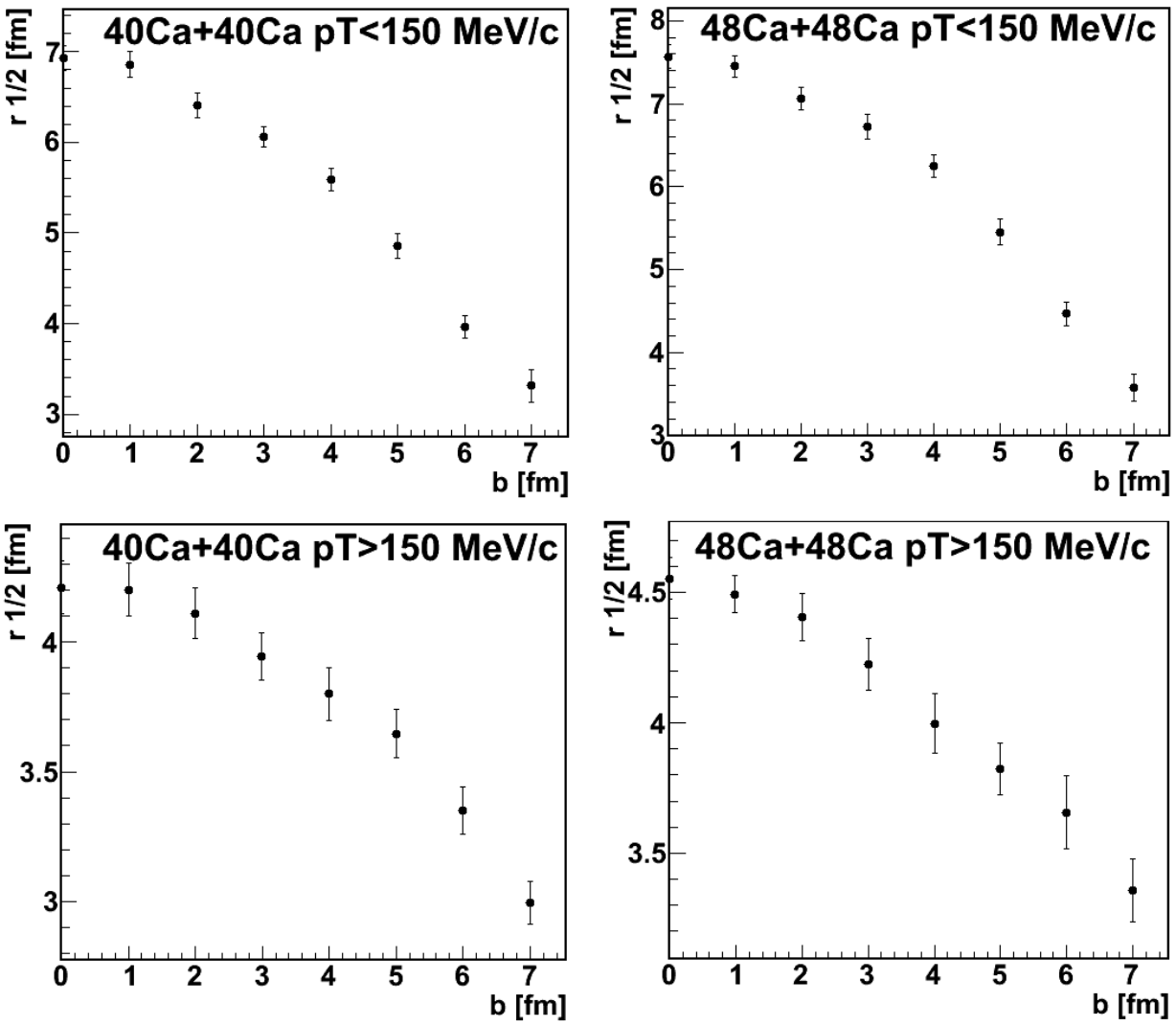

Figure 4.20: $r_{1/2}$ of source functions resulting from free cross sections as a function of impact parameter. The upper quadrants are for a low transverse momentum cut $<$150 MeV/c for ^{40}Ca+^{40}Ca (left) and ^{48}Ca+^{48}Ca (right). The bottom quadrants are for a high transverse momentum cut $>$150 MeV/c for the same reaction systems.

smaller for the free cross sections than for the screened cross section reduction. This is not surprising given that the freeze-out should vary as $\sigma^{-3/2}$. The decrease of the source size with impact parameter varies as the cube root of the number of nucleons contained in the participant volume, which decreases monotonically with impact parameter and vanishes at large impact parameter where the nuclei do not interact.

Figs. 4.18, 4.19, and 4.20 also show that the source is systematically larger for the neutron rich system for both momentum cuts. The source is also larger for proton pairs at low transverse momenta than at high transverse momenta in both reaction systems. The sensitivity to cross section is mainly for low momentum pairs.

4.5 Sensitivity of Observables to Cluster Production and Momentum Dependence

In heavy-ion reactions, clusters and fragments are produced in addition to free nucleons. An option was added to this BUU simulation code [41, 42] such that cluster production could be enabled, producing clusters with $A \leq 3$. When this option is enabled, deuterons are created by three nucleon collisions, and tritons and helions are created by four nucleon collisions, where the extra particle is needed in order to conserve 4-momentum in the formation of the cluster. The formation of clusters is a process which is essentially an inverse to the break-up of an incident cluster that collides with the nucleus. A deuteron is formed if two nucleons collide within an area described by the NN cross section while a third nucleon is within a certain phase-space volume centered about the center of mass of the first two. For the formation of helions (^{3}He) and tritons, two nucleons must be within the approximate

phase-space volume surrounding the two colliding nucleons. *NNd* and *dd* channels are not included in the formation of A=3 clusters.

The mean field potential is attractive when the nucleon has a low relative momentum with respect to the mean field, and repulsive when the nucleon has a high relative momentum. This is due to the different length scales probed in the two cases, giving rise to a momentum dependence of the mean field potential. Microscopically, one can expect a momentum dependence when the exchange potential in the Hartree-Fock mean field is important. To first order in p^2, this momentum dependence can be approximated by replacing the mass in the kinetic energy term with an effective mass for the nucleons. Thus the momentum dependence is sometimes described as an effective mass correction. In the BUU model, the momentum dependence is modeled beyond first order in p^2. Fig. 4.5 showed that using test particles leads to fluctuations in the net energy of the system with energy rising over time due to the diffusive process. This is a larger effect when a momentum dependent mean field is employed because driving terms in both of Hamilton's equations fluctuate instead of just one, as in the case of momentum independent mean field.

The exact momentum dependence is not fully understood, therefore, calculations were performed to determine the sensitivity to the momentum dependence. For the momentum dependent (MD) mean field calculation, a soft isoscaler equation of state (EOS) was used with an incompressibility K=210 MeV, whereas in the momentum independent (MI) case, a stiff isoscalar EOS was used with K=380 MeV. The incompressibility K, given by Eq. 4.1, is the curvature of the isoscalar mean field at ρ_0 and isospin=0 [47].

$$K = 9\rho_0^2 \frac{\partial^2}{\partial \rho^2} \frac{E}{A} |_{\rho=\rho_0,\delta=0,T=0} \tag{4.1}$$

The momentum dependencies were chosen to have a non-relativistic effective mass of 0.7 m_N. Variations in the momentum dependence of the mean field for asymmetric matter were limited to these two options because these two options predict elliptic and transverse flow observables that are consistent with experimental data [45, 61]. However, these two optionsmay not make similar predictions at low energies.

Certain effects of producing A=2 [41] and A=3 clusters [42] in this BUU code have been previously reviewed. It should be noted that inelastic rates for cluster production and breakup are not implemented, which may be important. This section illustrates the sensitivity of the calculations to the combined effects of including or excluding cluster production and the momentum dependence of the mean field. In these calculations, the Rostock in-medium cross section reductions and the density dependent power law dependence γ=0.7 for the symmetry energy are utilized. The reaction dynamics, energy conservation, single particle energy spectra and source functions for four cases are explored: Momentum independent interactions with clusters off (Indep-Off), momentum dependent with clusters off (Dep-Off), momentum independent with clusters on (Indep-On), and momentum dependent with clusters on (Dep-On).

Before quantifying differences between these four cases, it is instructive to look at the dynamics qualitatively. Fig. 4.21 shows that cluster production has a strong impact on the reaction dynamics. Without clusters, there are two large $A \approx 14$ residues. With cluster production there is more fragmentation with smaller residues $A \approx 6$. Momentum dependence has a small influence without cluster production on these figures, but a much stronger effect when clusters are produced. Based on the density snapshots, Dep-Off and Indep-Off should be very similar in single and multi-particle observables while Dep-On and Indep-On should

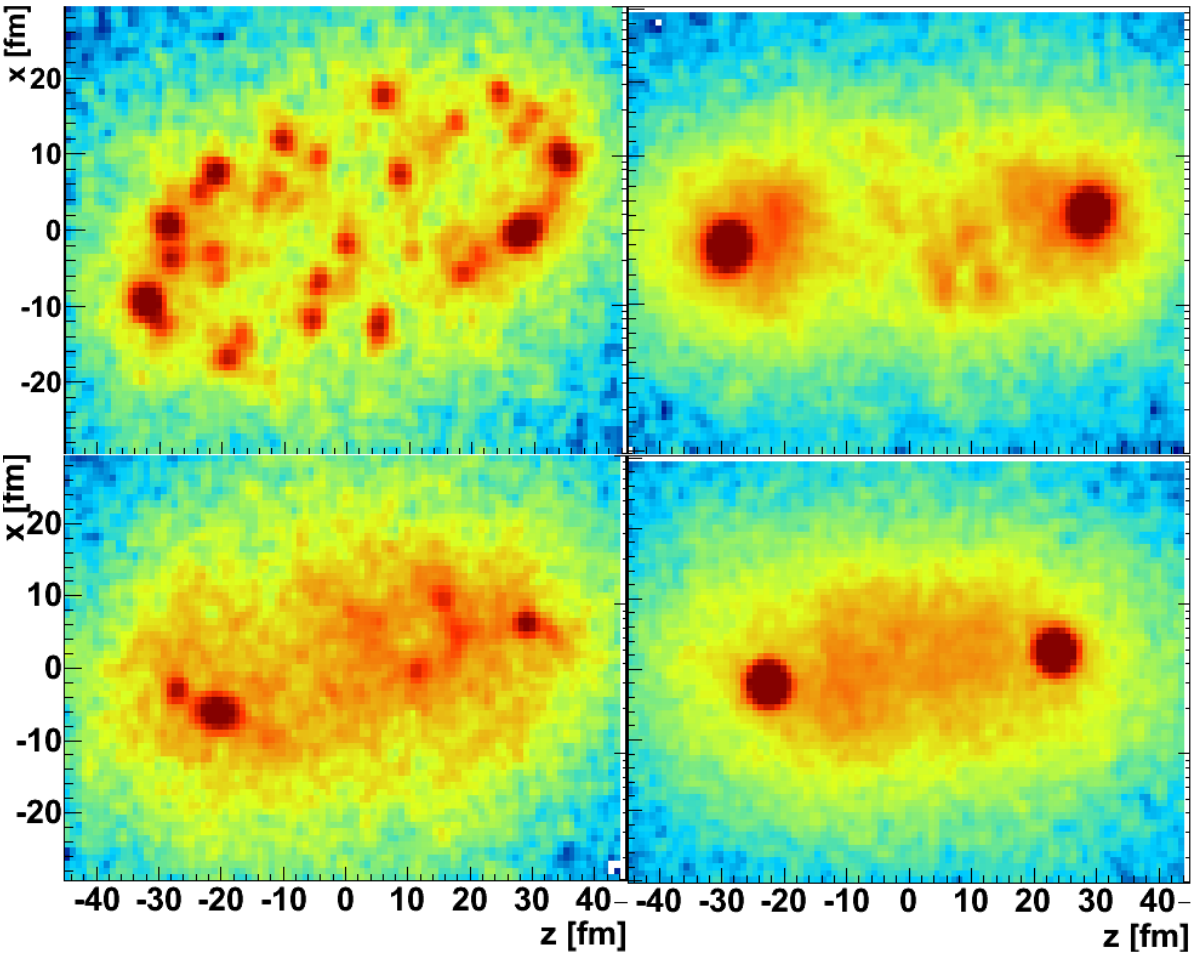

Figure 4.21: Density snapshots in the XZ plane summed over all Y. Top panels show calculations for momentum dependent mean fields. Bottom panels are for momentum independent mean fields. Left panels are with cluster production on, and right panels are without cluster production. All reactions are for ^{40}Ca+^{40}Ca.

be somewhat different and the difference between Dep-Off and Dep-On should be even larger.

The energy conservation is considered in each of the four cases. Fig. 4.22 shows the change in single particle energy as a function of time in the reaction. Momentum independent reactions tend to conserve energy better, but the energy per nucleon in the momentum dependent cases is still conserved to within 1 MeV which is similar to what one expects for this transport code [60]. The valley at early times corresponds to the point at which the nuclei are passing through each other, showing transparency. At this point it is difficult to calculate ΔE precisely. The drop in energy per nucleon at late times, t>300 fm/c, corresponds to a large fragment or residue leaving the computational grid.

As energy is released in creating composite particles, emitted protons not involved in cluster production should get a boost in kinetic energy when cluster production is enabled, which is shown in Fig. 4.23. With clustering on, the number of remaining protons in the interacting system is reduced, and those that remain have a higher average kinetic energy than with clustering off. Also, momentum dependence seems to enhance kinetic energy slightly in the case of clustering. One can see that clustering has a much larger effect in the kinetic energy spectra than making the mean field potential momentum dependent.

With cluster production turned on, protons close together in space are likely to be "eaten up" by clusters, reducing the number of nucleons close together and reducing the magnitude of the source function at small r. This effectively increases the size of the source. The shapes of the sources are shown in Figs. 4.24 and 4.25. For protons with low transverse momentum, momentum dependence and clustering has a small effect on the shape of the source, with cluster production having a larger effect than momentum dependence. For the high transverse momentum selection, both momentum dependence and cluster production

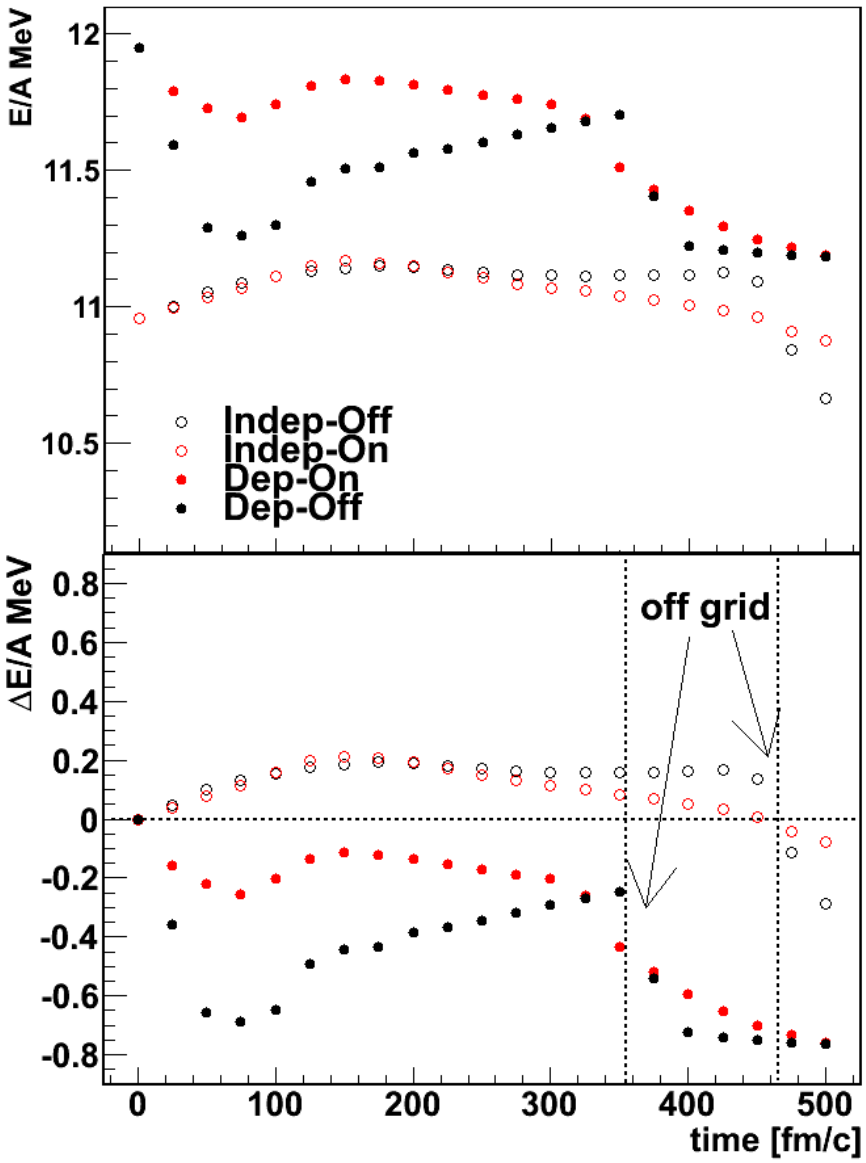

Figure 4.22: Change in average single particle excitation as a function of time, illustrating conservation of energy.

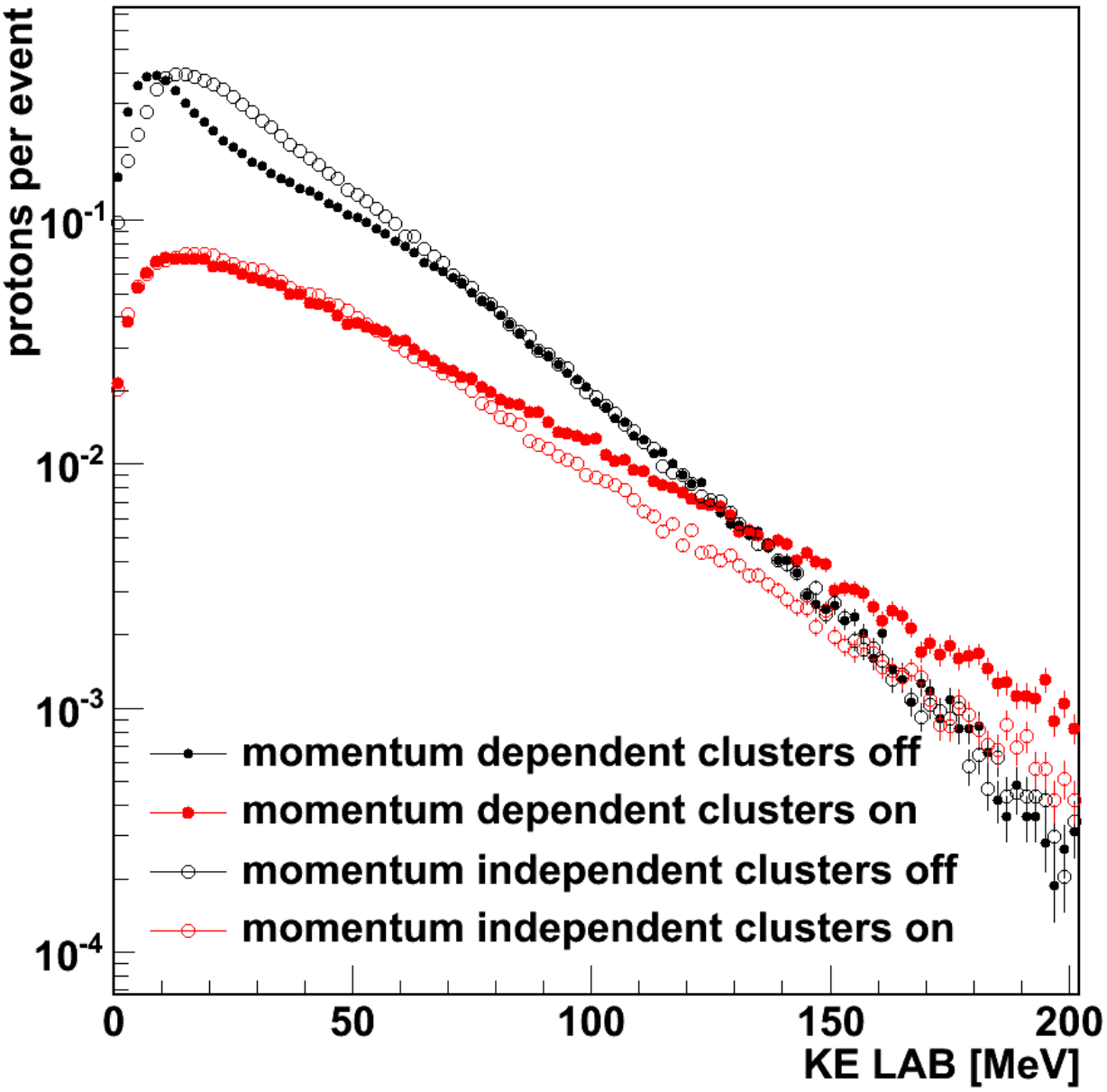

Figure 4.23: Laboratory kinetic energy spectra for protons emitted between 18-58° for Dep-On,Dep-Off,Indep-On, and Indep-Off for the ^{48}Ca+^{48}Ca reaction.

have a significant effect on the shape of the source.

Table 4.4 quantifies the differences in shape by presenting the size of each source. In all cases, enabling cluster production systematically increases the size of the source as expected, although the sources are not always significantly larger. At low transverse momentum, the momentum dependent mean field leads to a smaller source size, but at larger transverse momentum, no clear trend can be seen. Also of interest is that in each case, the neutron rich system has a larger size than the symmetric system, which is expected if the freeze-out density remains roughly constant.

	Dep-Off	Dep-On	Indep-Off	Indep-On
^{40}Ca+^{40}Ca				
p_T<150 MeV/c	6.36±0.23	6.96±0.22	6.94±0.20	7.35±0.23
p_T>150 MeV/c	4.01±0.18	4.81±0.23	4.25±0.25	4.65±0.22
^{48}Ca+^{48}Ca				
p_T<150 MeV/c	6.97±0.20	7.54±0.38	7.82±0.23	8.02±0.20
p_T>150 MeV/c	4.28±0.24	5.29±0.24	4.64±0.21	5.29±0.30

Table 4.4: $r_{1/2}$ values for Dep-On,Dep-Off,Indep-On, and Indep-Off for both reaction systems.

4.6 Effects of Symmetry Energy

The symmetry energy has been predicted to have a strong effect on proton emission rate, average emission time as a function of momentum, and p-p correlation functions [8] calculated using the IBUU transport code for the ^{52}Ca+^{48}Ca reaction at E/A = 80 MeV at $b = 0$ fm impact parameter. A principal motivation for this dissertation was a prediction using the IBUU model that a stiffer symmetry energy would result in a wider correlation function for high total momentum proton pairs, while no difference in source size would be expected for low momentum proton pairs, as seen in Figs. 4.26 and 4.27. Fig. 4.27 is the p-p correlation

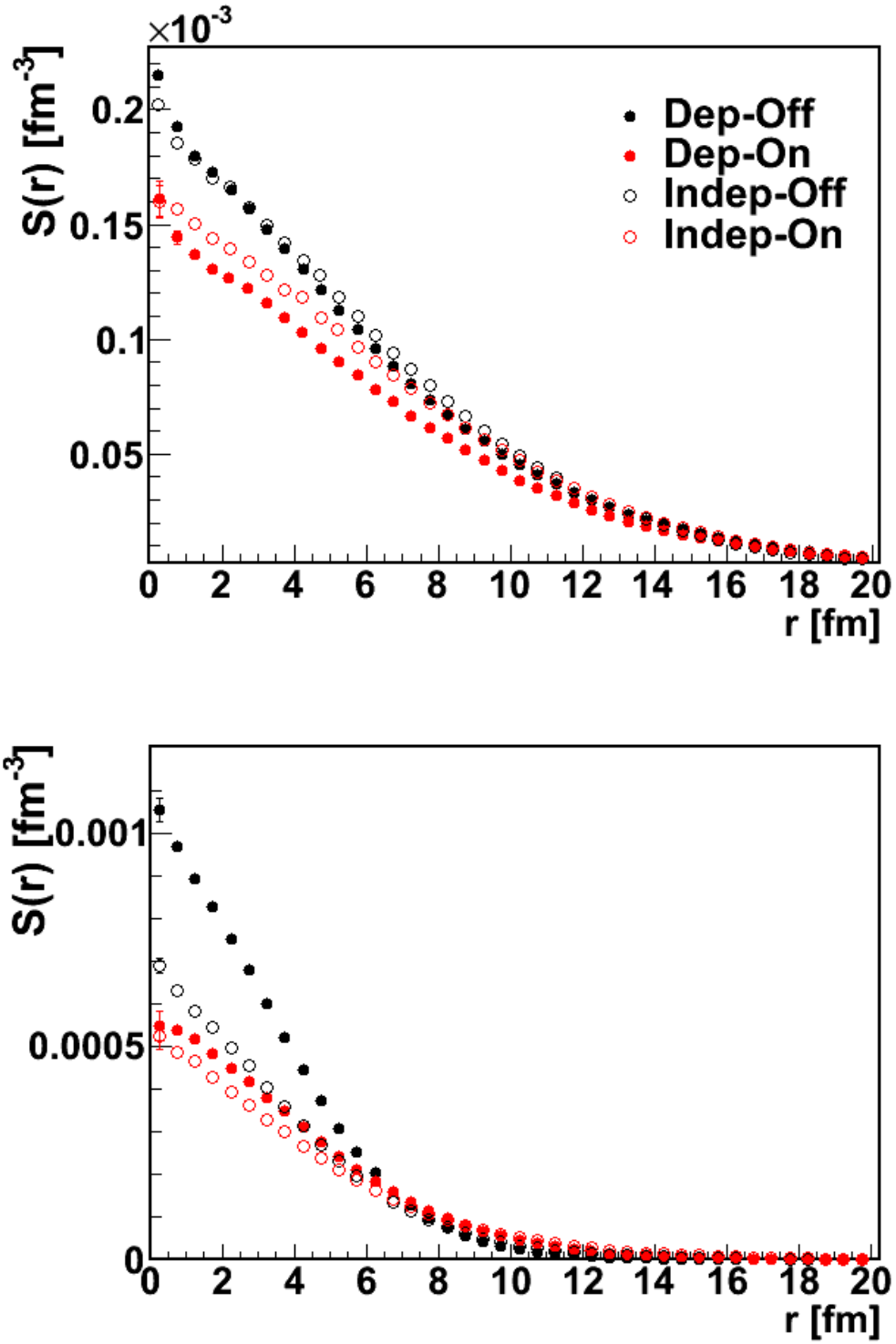

Figure 4.24: Source functions for low p_T (top) and high p_T (bottom) gates for the ^{40}Ca+^{40}Ca reaction system.

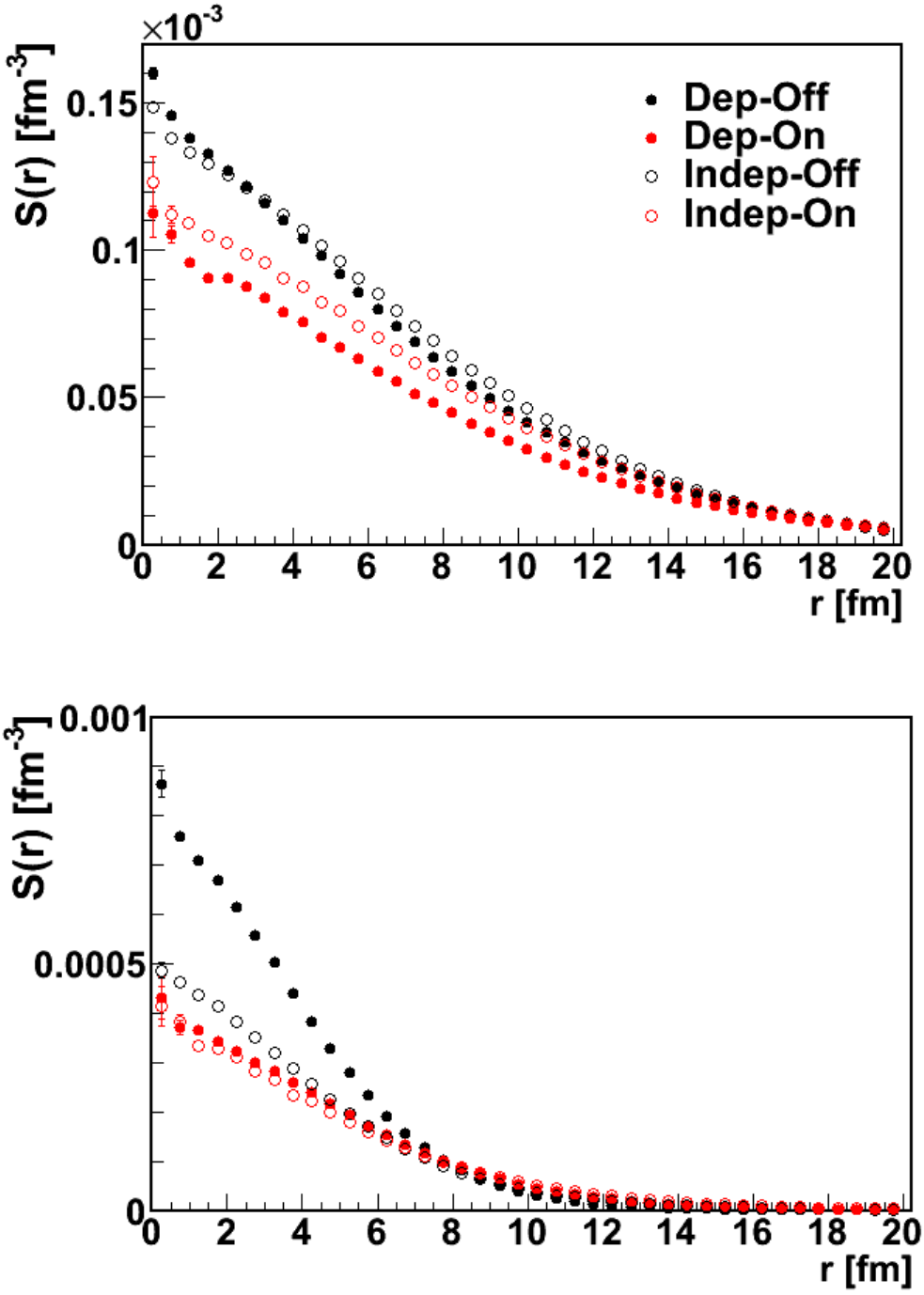

Figure 4.25: Source functions for low p_T (top) and high p_T (bottom) gates for the ^{48}Ca+^{48}Ca reaction system.

function from Fig. 4.26 for high total momentum.

This section explores those observables using a different BUU transport code, developed at MSU by Pawel Danielewicz and collaborators [41], which has been used previously to compare sources to experimental data [38, 48]. Free cross sections and momentum independent interactions were employed to be consistent with Ref. [8]. This section also explores both ^{40}Ca+^{40}Ca and ^{48}Ca+^{48}Ca reactions at E/A = 80 MeV for central collisions (b=1.4 fm). The results should be consistent with those in Ref. [8], as the inputs are similar.

Fig. 4.28 shows average emission rates for protons emitted over all angles from the neutron rich ^{48}Ca+^{48}Ca reaction for soft (γ=1/3) and stiff (γ=2) symmetry energies. It is clear that the stiffer symmetry energy enhances early pre-equilibrium proton emission while in the case of a soft symmetry energy proton emission is delayed. This is consistent with the higher pressures present in the case of the stiff symmetry energy, forcing protons to be emitted early with higher momenta. Fig. 4.29 explores the effect of an angular cut between 18-58°, in the laboratory frame, on the emission rate. Although there are fewer statistics in this angular region, the trends do not change.

Next, Fig. 4.30 shows the average time of emission as a function of momentum. Emission is slightly delayed for the soft symmetry energy as is to be expected. What is striking, is that the difference for protons with different γ values is very subtle, in contrast to previous results with IBUU [8], shown in Fig. 4.31. The trends are also different. In BUU, neutrons are always emitted before protons, on average, regardless of the γ value. In IBUU, for low energy protons, the stiff symmetry energy delays neutron emission such that protons are emitted earlier, on average.

There is a difference in emission times for different density dependencies of the symmetry

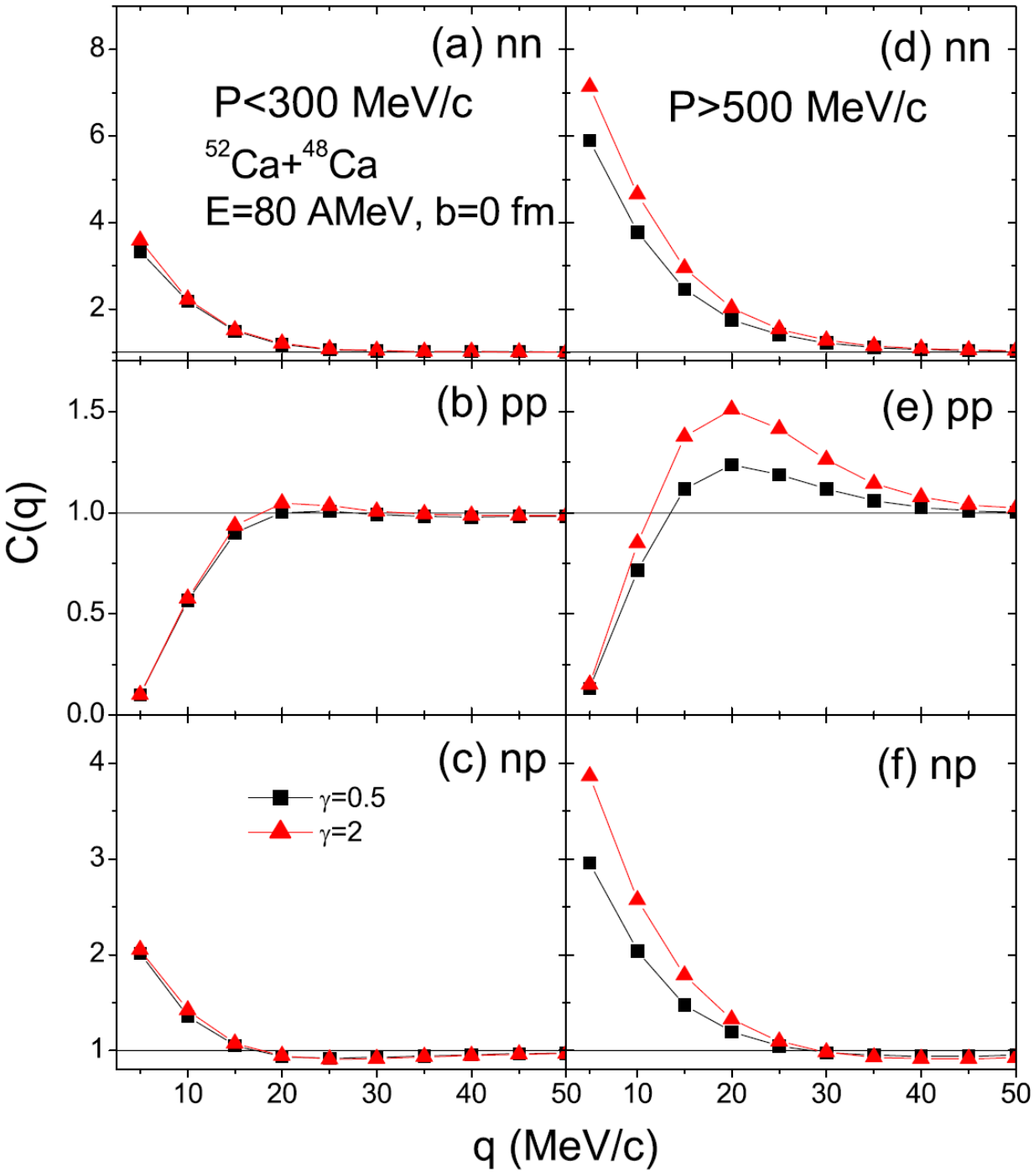

Figure 4.26: Two nucleon correlation functions for a stiff and soft density dependence of the symmetry energy. The left panels are for low total momentum <300 MeV/c while the right panels are for high total momentum >500 MeV/c from Ref. [8].

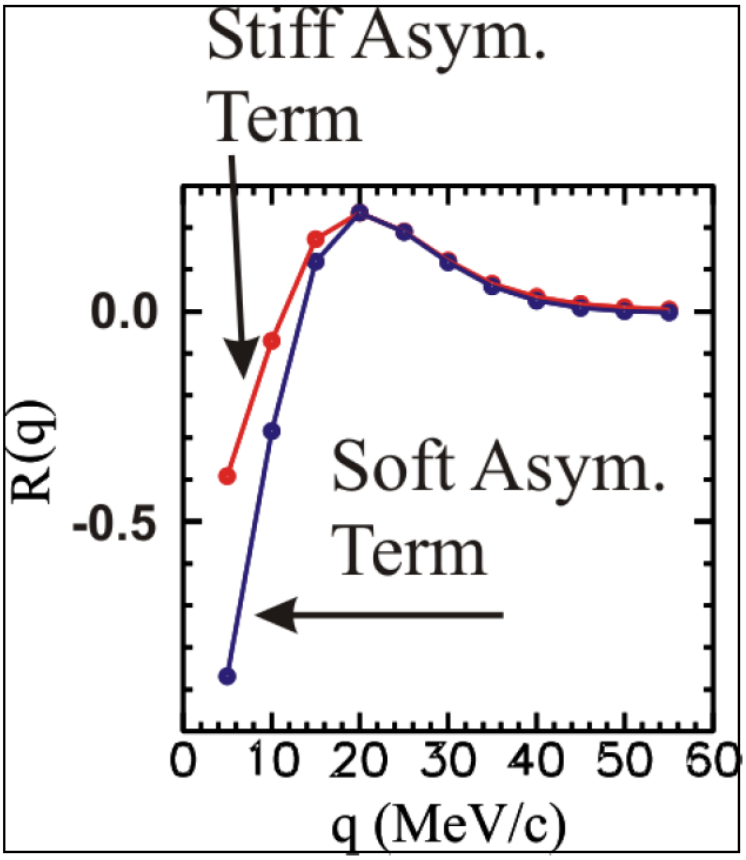

Figure 4.27: p-p correlation function for higher total momentum pairs from Ref. [8] renormalized to match peak heights (by Verde for E03045 proposal) so that the widths can be compared.

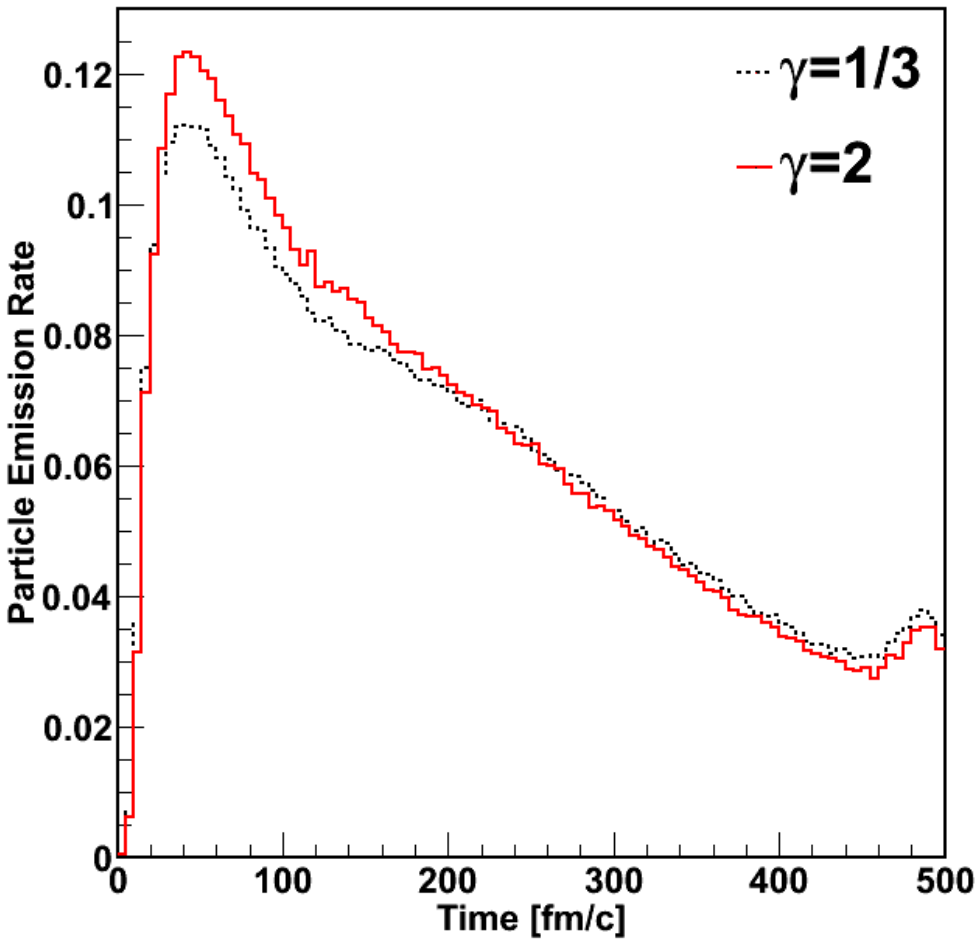

Figure 4.28: Average emission rate for protons with different symmetry energies for the ^{48}Ca+^{48}Ca reaction.

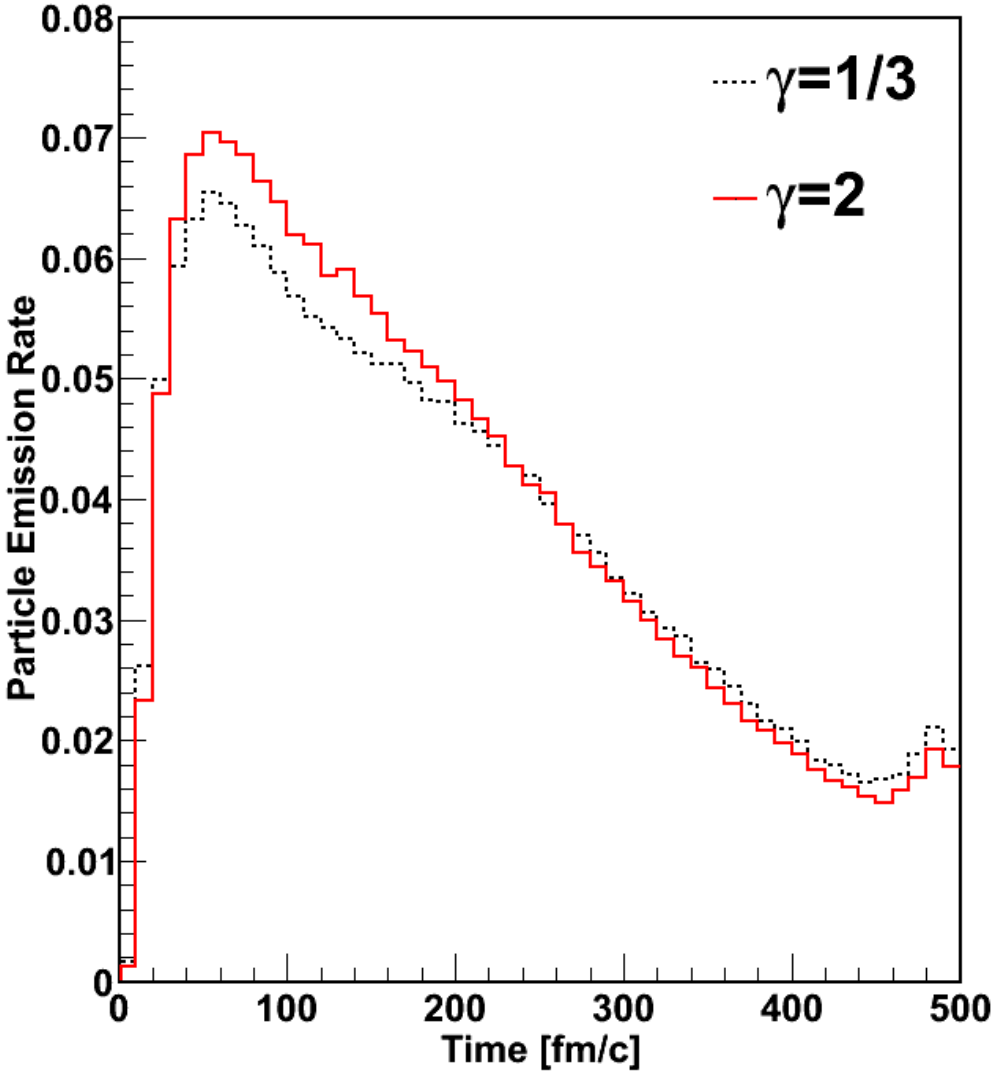

Figure 4.29: Average emission rate for protons emitted between 18-58° with different symmetry energies for the ^{48}Ca+^{48}Ca reaction.

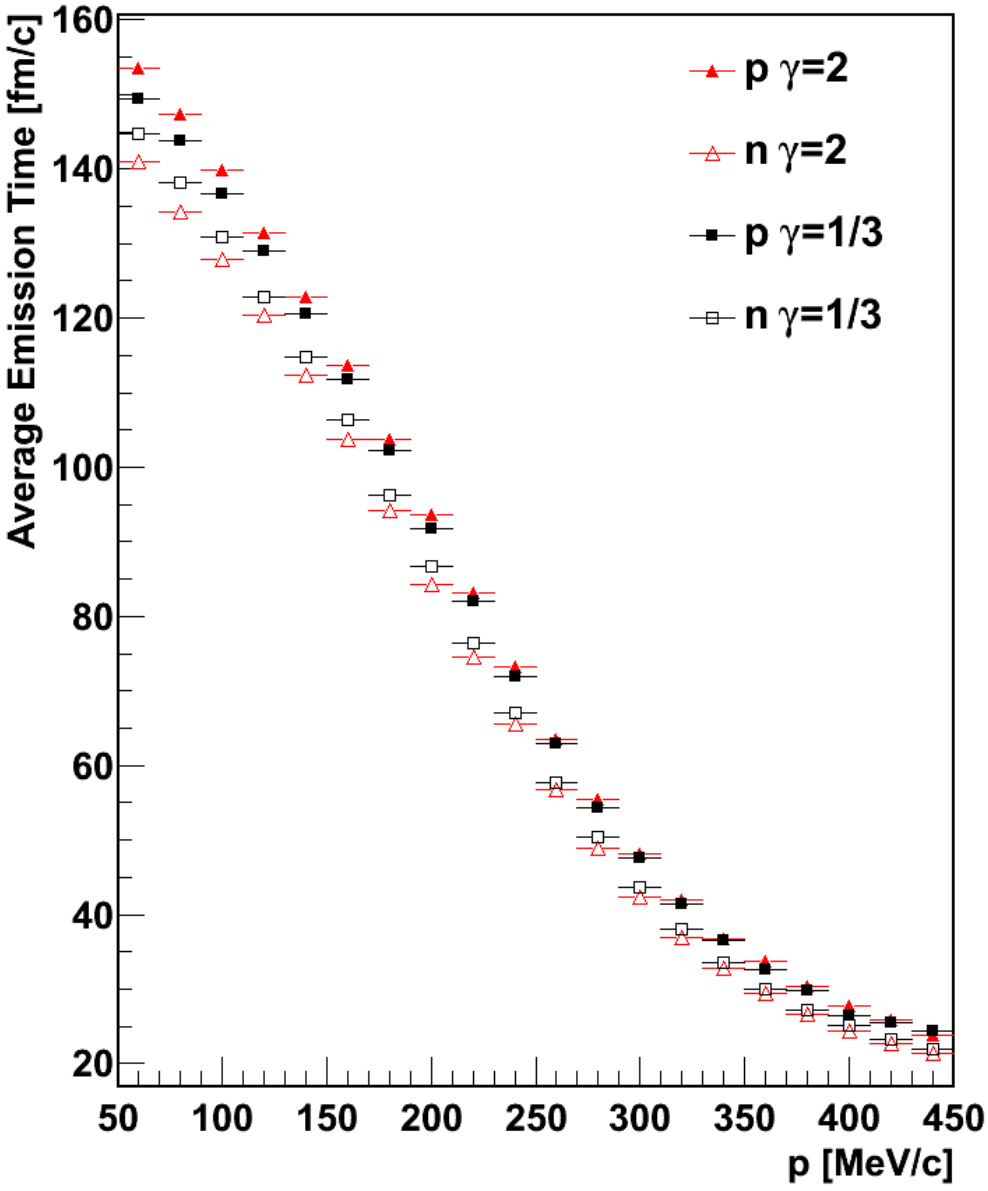

Figure 4.30: Average emission time for protons and neutrons for γ=2 and γ=1/3 for the ^{48}Ca+^{48}Ca reaction.

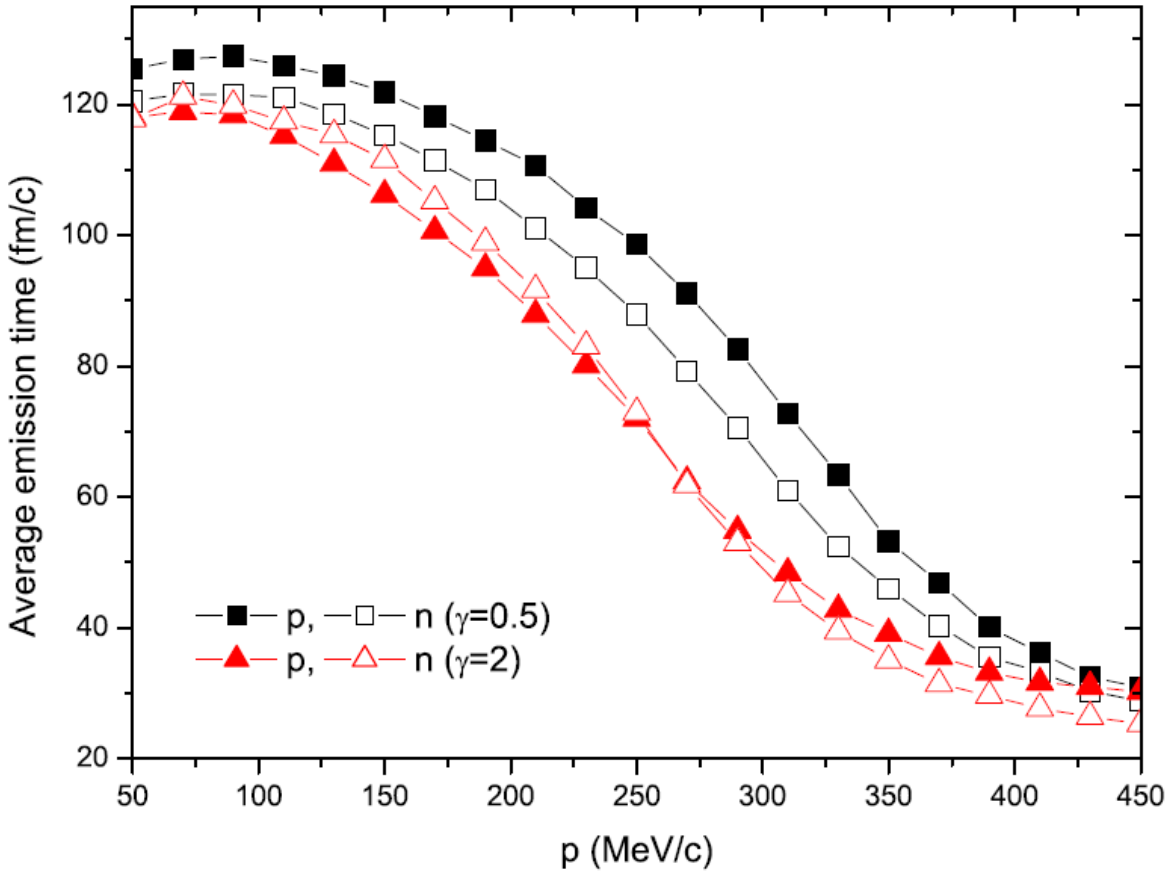

Figure 4.31: Average emission times of nucleons as a function of momentum [8].

energy, and this should be reflected in the size of the source. Figs. 4.32 and 4.33 examine the $r_{1/2}$ size of the source as a function of total momentum of the proton pair for ^{40}Ca+^{40}Ca and ^{48}Ca+^{48}Ca reactions respectively. The gates on total momentum of the pair were 0-300 MeV/c, 500-640 MeV/c, and 740-900 MeV/c. It is clear that the sources are the same size, within error, regardless of momentum cut. It is curious that the strongest difference between source sizes, although not significantly different, occurs at low total momentum.

To be complete, correlation functions were made from the sources for the same momentum gates used in [8] P$<$300 MeV/c and P$>$500 MeV/c for both the symmetric and neutron rich reactions. The p-p correlation functions are shown in Fig. 4.34. There is no discernible difference in magnitude or shape.

Within statistical uncertainties, there is little sensitivity to symmetry energy for source sizes. For all combinations of momentum dependence, clustering, and in-medium cross sections explored in this dissertation, no combinations showed a sensitivity to the symmetry energy. For the remainder of the discussion of BUU, γ =0.7 was used to explore the effects of other parameters in BUU. This value is consistent with recent results [26].

4.7 Comparing Free and In-Medium Cross Sections

The NN cross section is thought to be reduced in nuclear medium, but the exact nature of this reduction is unknown. This section examines the differences between free cross section (no reduction), Rostock (Eq. 1.11) and the screened (Eq. 1.12) NN in-medium cross section reduction. For the screened, a variety of values for η are investigated. The Rostock originated from a parametrization of microscopic calculations, while the screened is geometrical in nature. This section also explores the reduction factor, kinetic energy spectra and sources

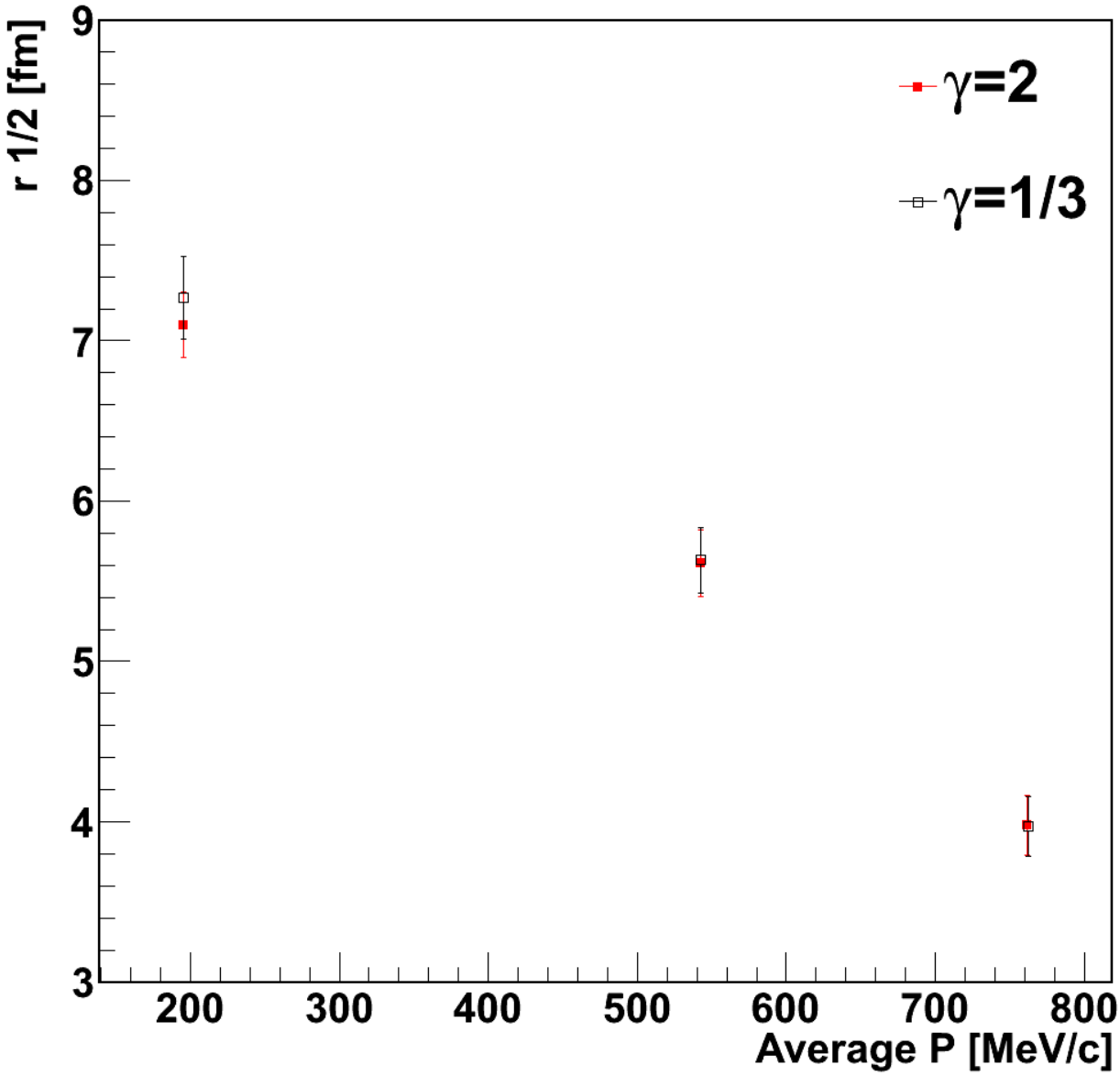

Figure 4.32: $r_{1/2}$ values, obtained from calculations using the code of Danielewicz, as a function of average total momentum of the proton pair for γ=2 and γ=1/3 for the ^{40}Ca+^{40}Ca reaction.

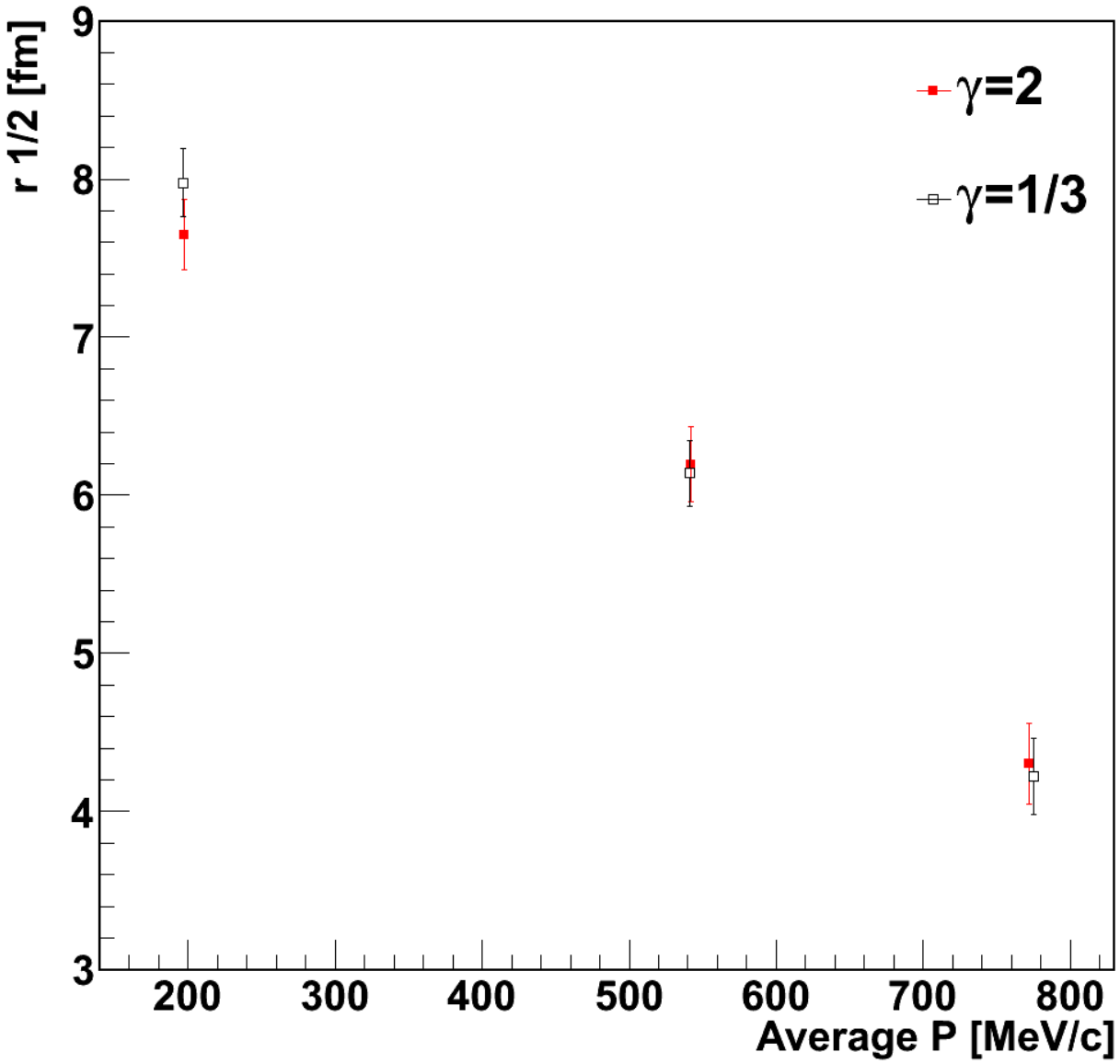

Figure 4.33: $r_{1/2}$ values as a function of average total momentum of the proton pair for γ=2 and γ=1/3 for the ^{48}Ca+^{48}Ca reaction.

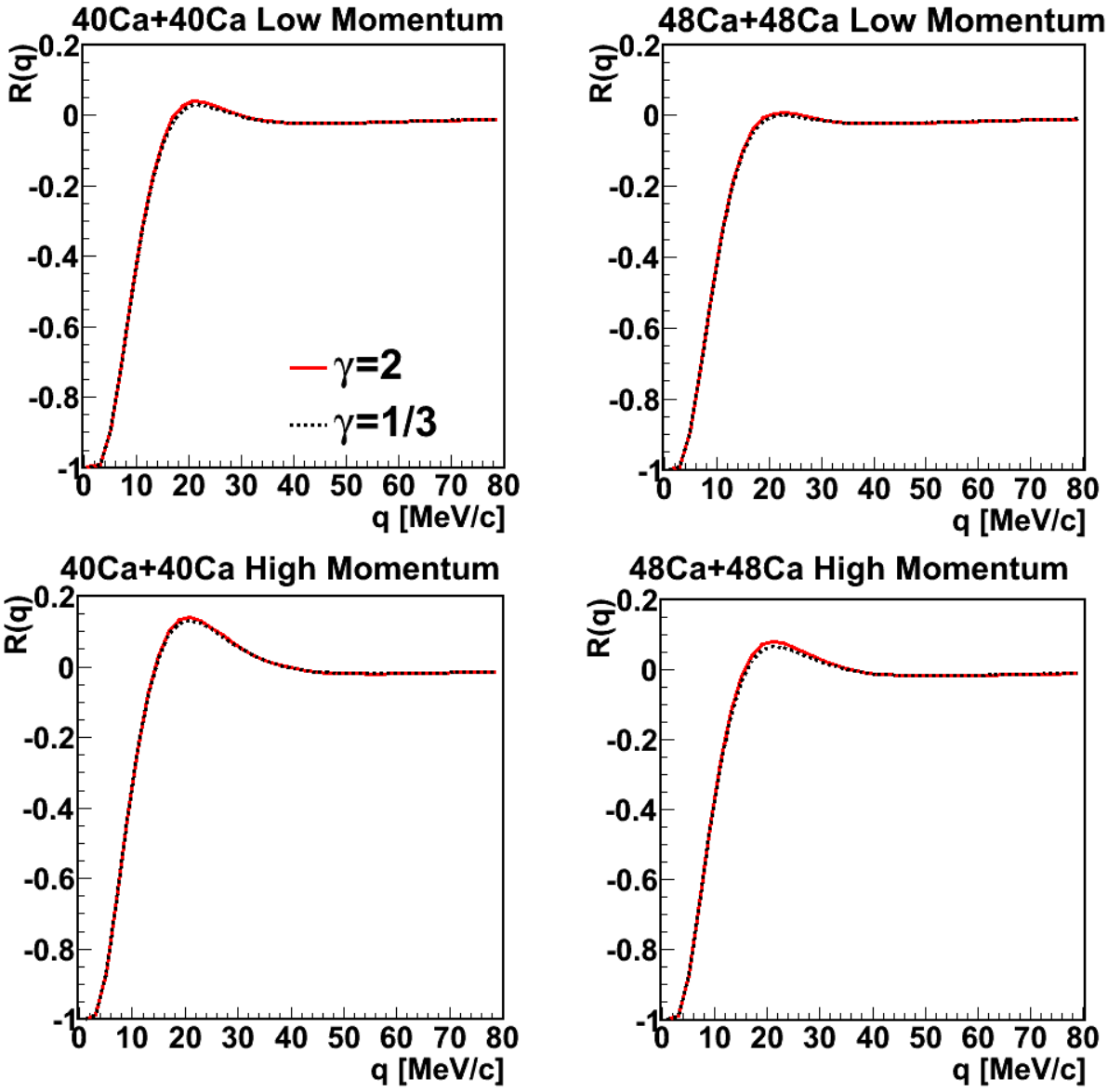

Figure 4.34: Correlation functions for stiff and soft symmetry energy. The upper quadrants are for a low total momentum cut P<300 MeV/c for ^{40}Ca+^{40}Ca (left) and ^{48}Ca+^{48}Ca (right). The bottom quadrants are for a high total momentum cut P>500 MeV/c for the same reaction systems.

for the various cross sections. For all cross sections, momentum dependent interactions are employed with no cluster production and 1600 test particles.

The Rostock and screened in-medium reductions reduce the free cross sections by a factor, which varies from collision to collision. In the case of the screened NN in-medium cross section, it acts to limit the mean free path to be greater than approximately one nuclear mono-layer in the limit of no Pauli blocking. In effect, the larger the free cross section, the more the screened parametrization reduces the free cross section, by construction. The distribution of the values for the reduction factors of a NN collision are plotted in Fig. 4.35 for ^{48}Ca+^{48}Ca. Collisions per test particle are plotted for nn, np, and pp collisions. In this figure, a cross section reduction factor of 0.4 means that the calculated cross section is $0.4\sigma_f$ while a cross section reduction factor of 0.9 means the calculated cross section is $0.9\sigma_f$ where σ_f is the NN cross section in free space.

On average, the reduction in cross section assumed by the Rostock formula is less than that of the screened cross section formula, that is the Rostock cross sections are closer to free cross sections. The Rostock reduction has the same distribution shape for all types of collisions. In regards to the screened reduction, it is clear that np cross sections are reduced more than nn or pp cross sections due to the np cross section being larger than the nn and pp cross section. The screened cross section are generally quite reduced with respect to the Rostock and the free cross sections. The Rostock results in no collisions with reduction factors less than 0.4 while the screened cross section results in very few collisions with reduction factors greater than 0.9.

The more collisions a proton encounters, the greater chance it has of being emitted. This is evident in Fig. 4.36 which shows that the free cross section emits the most protons, and

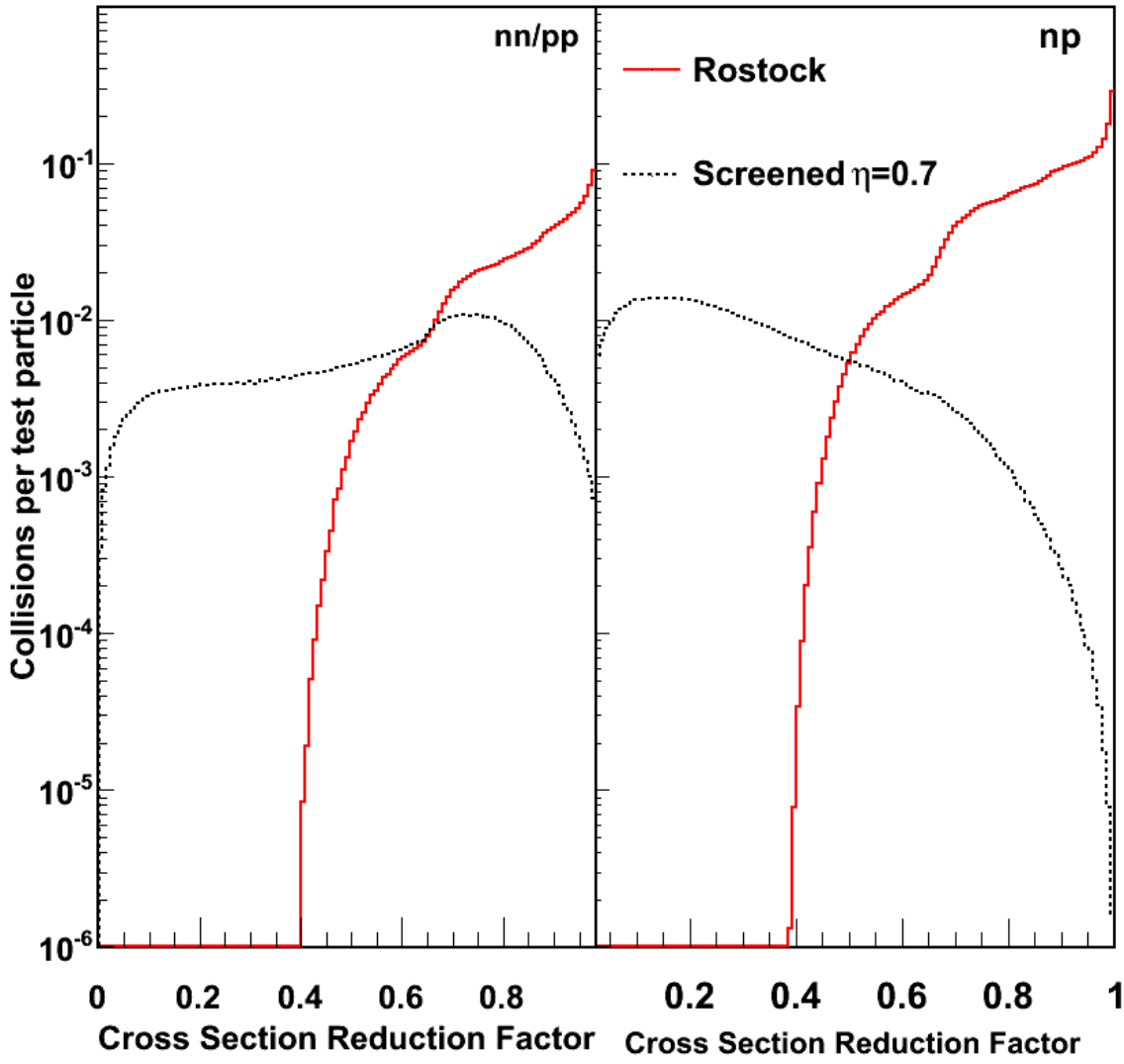

Figure 4.35: In-medium cross section reductions for the screened (η=0.7) and Rostock parametrizations for ^{48}Ca+^{48}Ca reaction. The left panel is for *nn/pp* collisions, and the right panel is for *np* collisions.

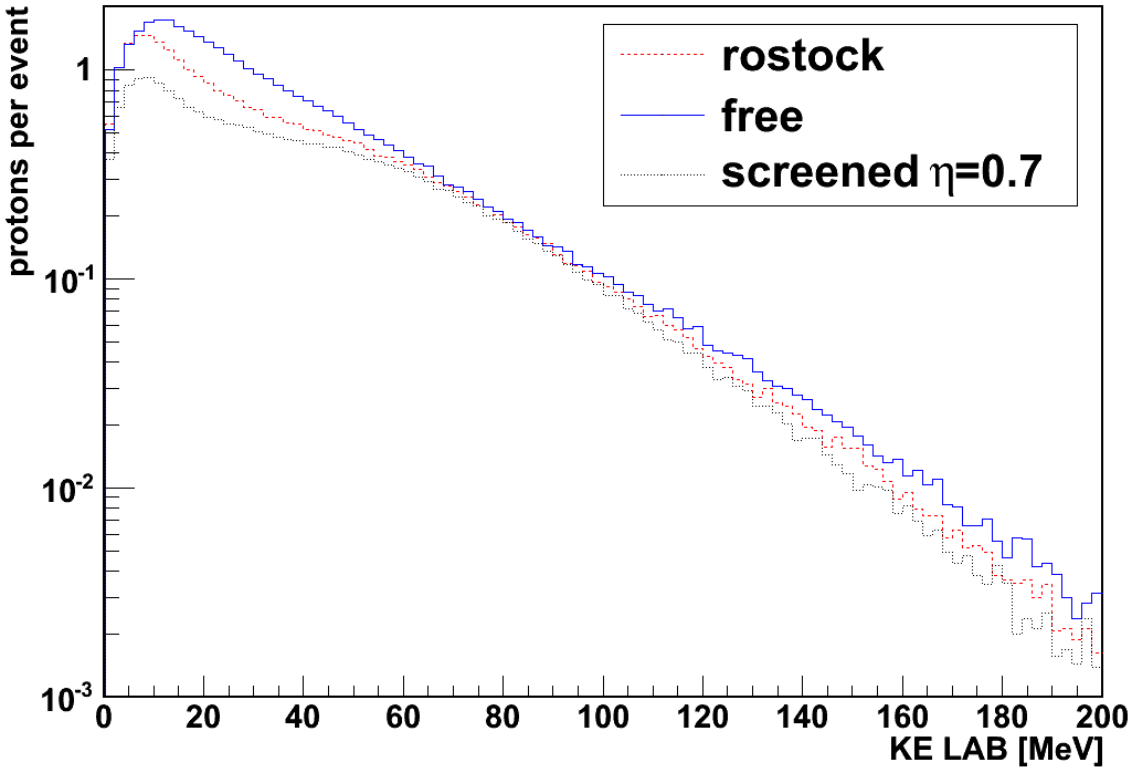

Figure 4.36: Laboratory kinetic energy spectra for the free cross sections and reduced Rostock and screened (η=0.7) cross sections. Only protons emitted between 18-58° are included.

Rostock, having a small reduction, emits more protons than the screened cross section which reduces the cross section more. For free cross sections, the energy spectra fall exponentially, while for reduced cross sections, there is a slight bump in the spectra starting around 50 MeV. Fewer lower energy protons are emitted with reduced cross sections.

The cross section reduction is energy dependent. It is stronger at lower energies than at higher energies. Thus, as the cross section is decreased, the source gets smaller, which is shown qualitatively in Figs. 4.18, 4.19, 4.20, Figs. 4.37 and 4.38 and quantitatively in Table 4.5.

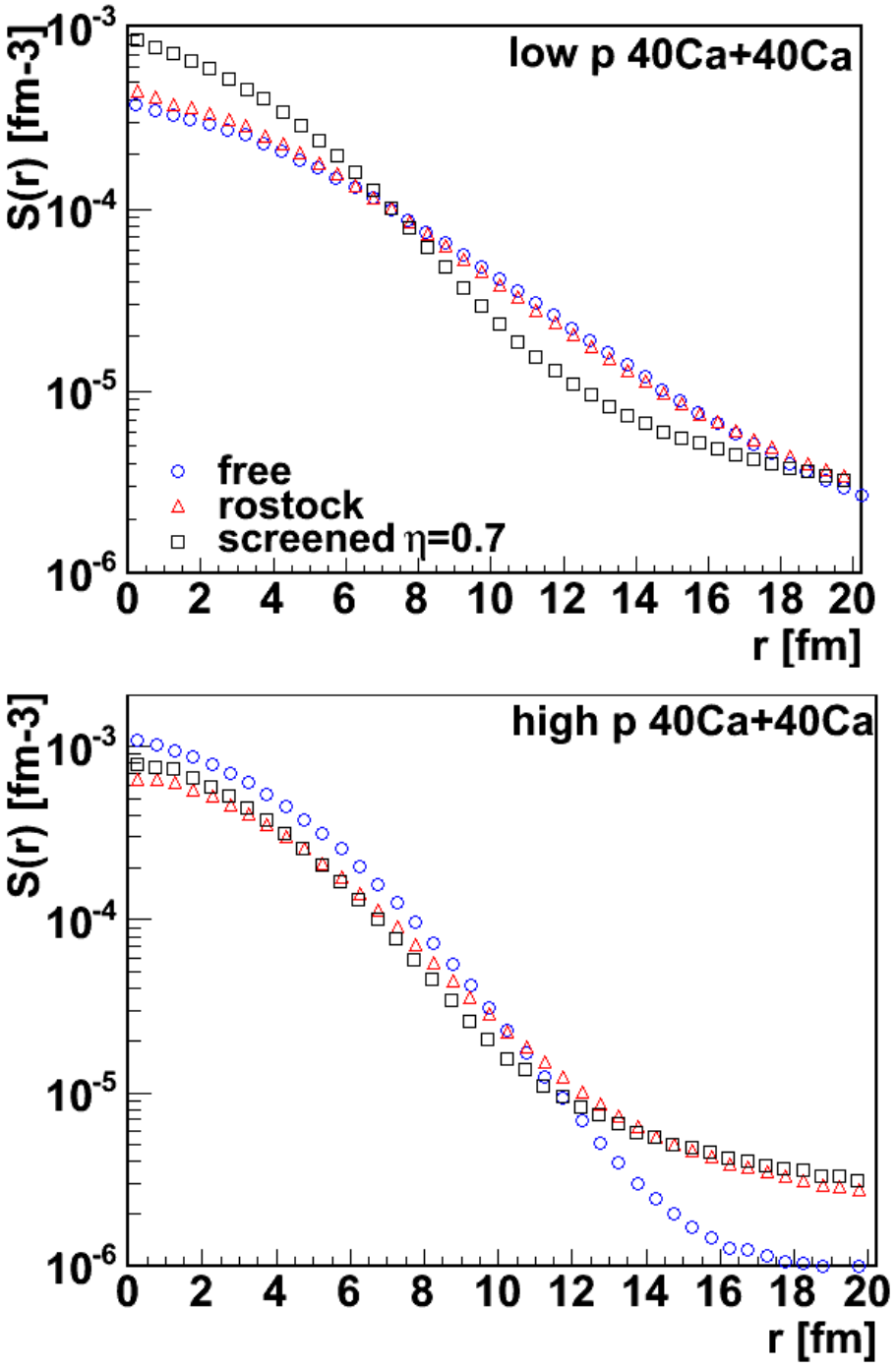

Figure 4.37: Source functions for the free cross sections and reduced Rostock and screened (η=0.7) cross sections. Only protons emitted between 18-58° are included. The ^{40}Ca+^{40}Ca reaction is shown for low total momentum 500-640 MeV/c (top) and high total momentum 740-900 MeV/c (bottom).

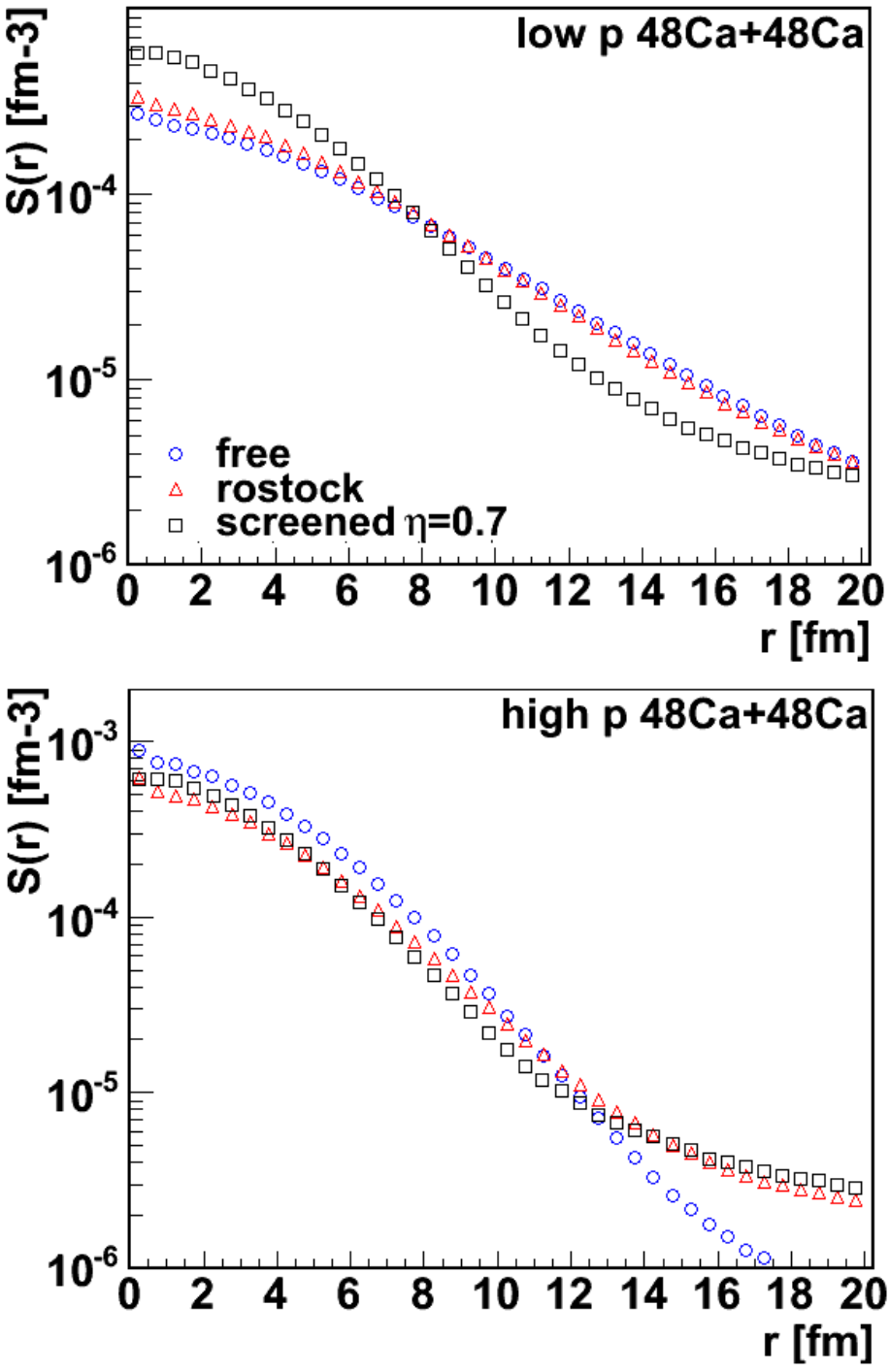

Figure 4.38: Source functions for the free cross sections and reduced Rostock and screened (η=0.7) cross sections. Only protons emitted between 18-58° are included. The ^{48}Ca+^{48}Ca reaction is shown for low total momentum 500-640 MeV/c (top) and high total momentum 740-900 MeV/c (bottom).

	free [fm]	Rostock [fm]	screened [fm]
^{40}Ca+^{40}Ca			
low P $r_{1/2}$	5.12±0.20	4.77±0.25	3.84±0.22
high P $r_{1/2}$	3.90±0.20	3.98±0.18	3.60±0.19
^{48}Ca+^{48}Ca			
low P $r_{1/2}$	5.56±0.21	5.16±0.22	4.13±0.20
high P $r_{1/2}$	4.23±0.25	4.24±0.25	3.80±0.23

Table 4.5: $r_{1/2}$ values for 3 choices of cross section for low and high total momentum cuts and both reaction systems.

4.7.1 Exploring the Density Dependent In-Medium Cross Section

Thus far, the screened in-medium reduction has been set with η=0.7. Although the size of the source is not sensitive to the symmetry energy, perhaps it is sensitive to the in-medium reduction. This section explores all values of η from 0.5 to 0.9 in 0.1 increments for both *nn/pp* and *np* collisions. Momentum dependent interactions were used with no cluster production. The symmetry energy exponent, γ, was set to 0.7.

Fig. 4.39 examines the effect of varying either the *np* or the *nn/pp* cross section. When the *nn/pp* cross section is varied, the source sizes for both ^{40}Ca+^{40}Ca and ^{48}Ca+^{48}Ca show little sensitivity to η. When the *np* cross section is varied, the source size for both systems shows a stronger sensitivity to η, with ^{48}Ca+^{48}Ca showing the strongest effect.

Fig. 4.40 explores the effect of varying both η's at the same time. The *np* cross section is varied along the y-axis and the *nn/pp* cross section is varied along the x-axis. The weight of each cell is the $r_{1/2}$ value of the source. In the case of high momentum (bottom panels) the source varies very little with cross section. However, for low momentum (top panels) the source varies more significantly. Most important are the diagonal lines of nearly equal $r_{1/2}$ values for low momentum for both reaction systems. For a given source size, there are many

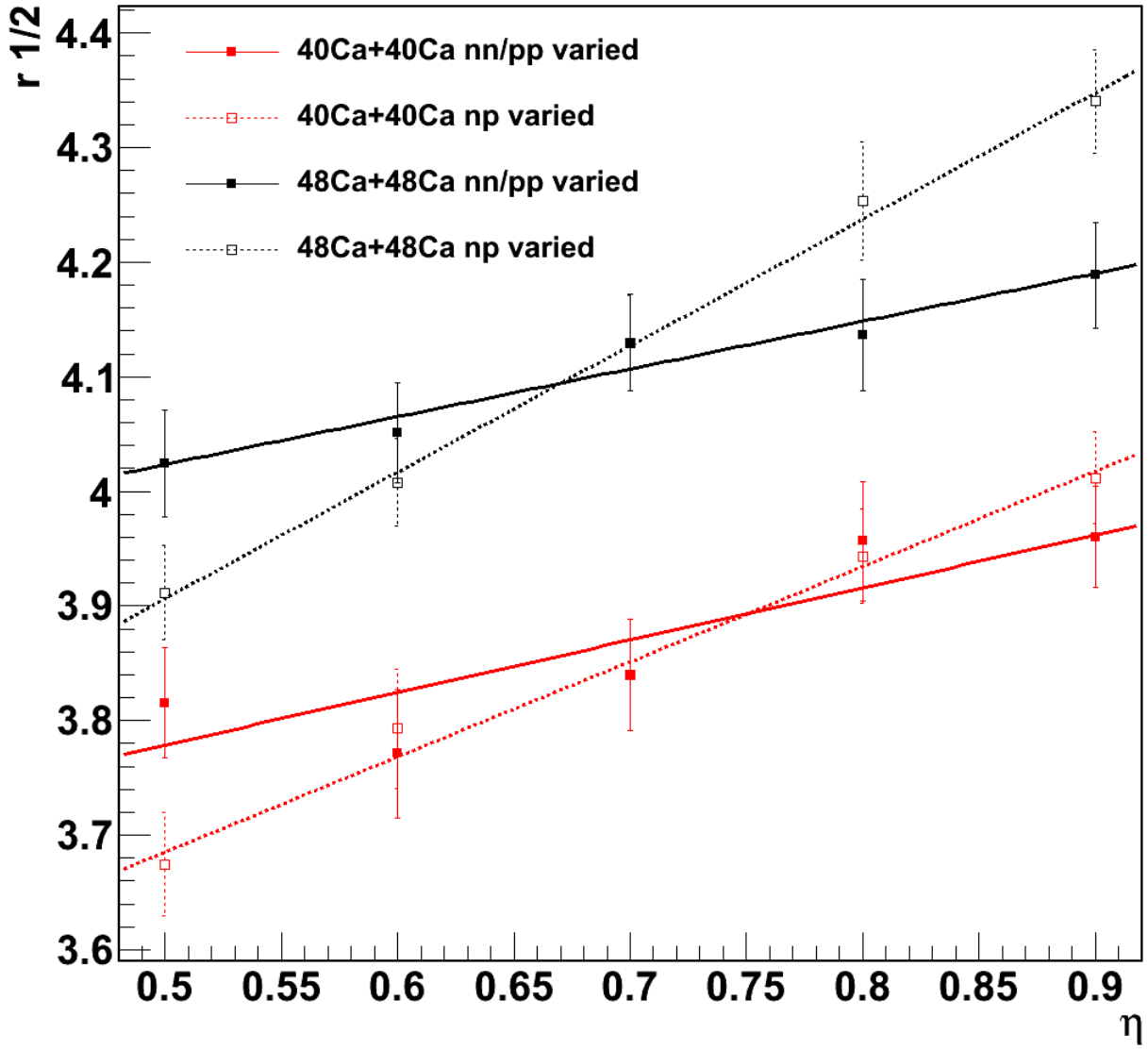

Figure 4.39: Plot of $r_{1/2}$ values for select values of η for both np and nn/pp collisions. When one type of collision cross section is varied, the other η is fixed to 0.7. Only protons between 18-58° in θ were used in calculating the source.

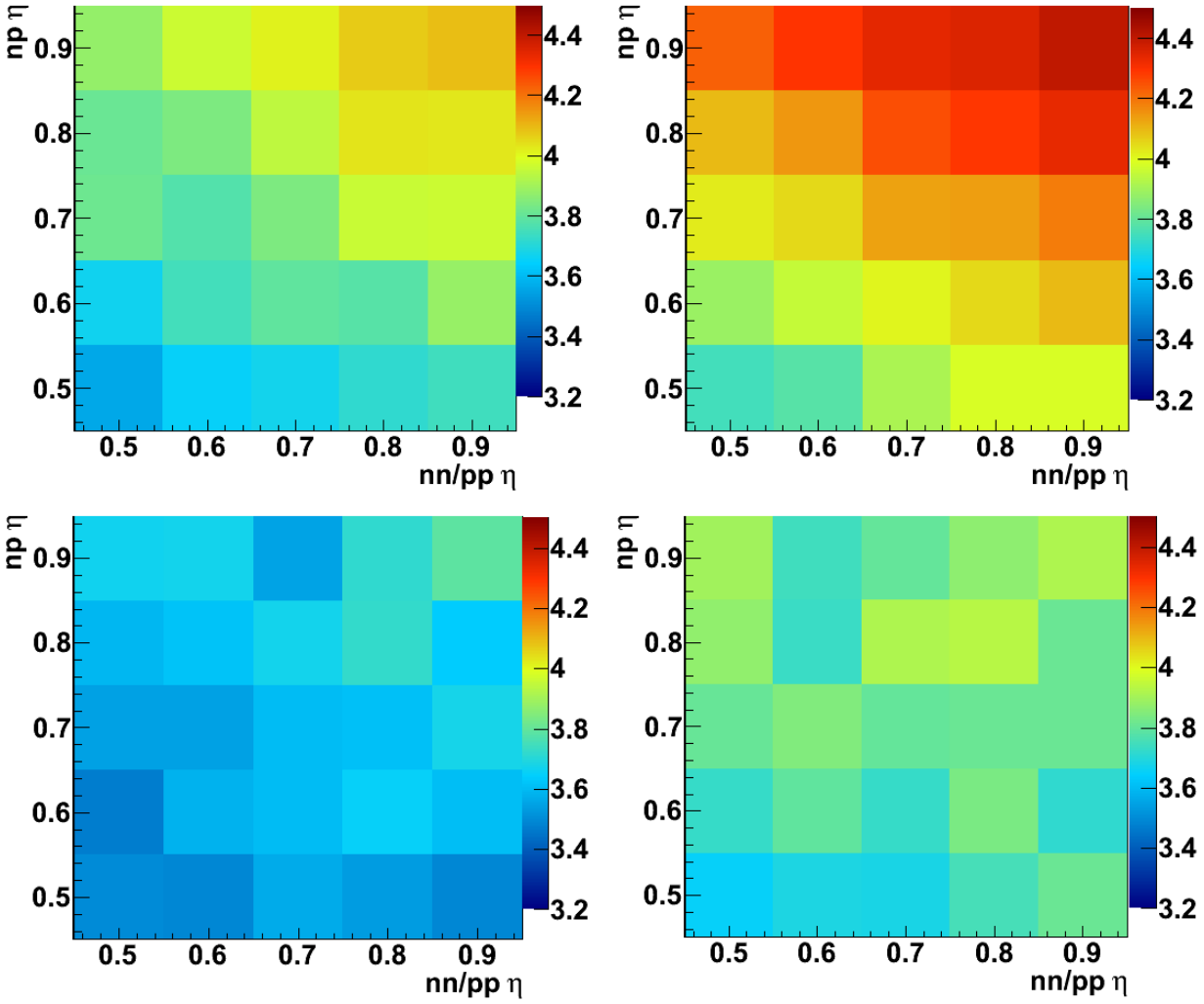

Figure 4.40: 2D plot of $r_{1/2}$ values for all values of η for both np and NN collisions. Only protons between 18-58° were used in calculating the source. The upper quadrants are for low total momentum 500-640 MeV/c for ^{40}Ca+^{40}Ca (left) and ^{48}Ca+^{48}Ca (right). The bottom quadrants are for high total momentum 740-900 MeV/c for the same reaction systems.

combinations of *np* and *nn/pp* cross sections that give the same result.

We note that the sensitivity to the np cross section would be much greater for the Rostock style parametrization of the in-medium cross section. Thus it would be of interest to redo these calculations for the Rostock style cross section or for another one without such extreme reductions in the in-medium *np* cross sections.

4.8 Conclusions

This chapter explored many parameters of the BUU transport simulation code. The collision grid used was of sufficient size even though large fragments or residues may go off the computational grid near the end of the reaction. Increasing the size of the grid did not affect any of the observables. Because residues go off the grid and energy is not conserved as well when this happens, the effect of a time cut was explored. Using a time cut removes a significant amount of low energy protons emitted during late stages when no clusters are produced.

Using the Rostock *NN* in-medium cross section, the effect of the number of test particles was investigated. 200 test particles appear to be too few, as the reaction dynamics are different than when more test particles are used. The code is stable against changes from 800 to 1600 test particles. As long as at least 800 test particles are used, and the collision evolves to 500 fm/c, the results are stable against changes in these computational parameters.

Next, the influence of impact parameter on energy spectra and the size of the source was explored. Both were found to be sensitive to impact parameter, however for $b<3$, the sensitivity to b is relatively small. When comparing to experiment, mixed central impact parameters should be weighted appropriately.

Cluster production had a strong effect on the reaction dynamics of the collision while momentum dependence of the mean field had a weaker effect. Cluster production increases the available kinetic energy to protons and increases the size of the source. Because the source is a probability distribution, removing pairs which are close together during emission increases the overall size of the source. When cluster production is enabled, protons that are close to each other are likely to be "eaten up" by cluster formation, resulting in a larger source size. Without cluster production, the source size is underestimated. The most reasonable physical options appear to be to calculate cluster production and to include momentum dependent mean fields.

Although the symmetry energy shows an effect on proton emission rates, the source size was relatively insensitive to symmetry energy for all gates on momentum and all combinations of cross section, cluster production, and momentum dependence. This is in contrast to previous results using IBUU [8].

The screened in-medium reduction reduces the cross section more than the Rostock and its reduction is considerably greater for the np than for the nn or pp cross sections. Both kinetic energy spectra and source size were dependent upon the cross section reduction. As the cross section is decreased, the number of protons emitted with low kinetic energy is decreased, removing them from the tail of the source and thus decreasing the size of the source. The reduced cross section also decreases the chance of two neighboring protons to collide before being emitted, resulting in more proton pairs with smaller r in the source distribution.

The source size might be used to constrain η in the screened in-medium cross section. However, a given source size can be reproduced by many combinations of nn/pp and np cross

section reductions. Source sizes can constrain the relationship between these reductions but can not fix the individual values for the reductions in σ_{np}, σ_{nn} and σ_{pp}.

Chapter 5

Experimental Results

Nuclear reactions occur over very short timescales on the order of 10^{-21} seconds. For the most part, experimental observables only sample the final stages of the reaction and theoretical models must be used to access the information about the initial stage of the collision as well as the dynamics occurring during the reaction. One exception is intensity interferometry [29, 30], introduced in section 1.2, and known for its sensitivity to the space-time extent of the source from which particles are emitted.

In this chapter, we extract information about the sources for particle emission by fitting the experimental correlation functions with the Koonin-Pratt formula for two different parametrizations of the source. The first involves approximating the source by a Gaussian function of the separation between the two protons at the time of emission. The second involves a more general source function that can be varied to get an "image" of the source. We begin this chapter by introducing these two methods. Then we discuss how to calculate a comparable source using transport theory. We then present the data, extract the sources, and compare measured source sizes to those calculated via the BUU transport model. All

p-p correlation functions are from central events, but different gates on rapidities, transverse momenta and laboratory momenta and angle are explored. The chapter ends with a brief presentation of three-particle correlation functions.

5.1 Imaging and Gaussian Fits

We want to study how shape of the source function for proton emission depends on constraints on quantities such as the centrality of the collisions or the momenta of the emitted protons or both. Recall that the definition of the source function is the probability distribution for the distance between two protons at the time of emission of the second proton. This source function reflects an ensemble average over nucleus-nucleus collisions subject to the aforementioned constraints. From the central limit theorem, one might expect that a reasonable approximation to the ensemble averaged source for particle emission would be Gaussian in form. From the seminal work of Koonin [36], Gaussian sources have been frequently assumed.

If one assumes a Gaussian two particle relative source profile, given by

$$S(r) = \frac{\lambda_G}{(2\sqrt{\pi}R_G)^3} e^{-\frac{r^2}{4R_G^2}}, \tag{5.1}$$

one can obtain a correlation function using the Koonin-Pratt formula (Eq. 1.4). Then the parameters of this Gaussian can be obtained by fitting the experimental correlation function by varying the parameters until the χ^2 per degree of freedom (ndf) is minimized.

There are three free parameters in this fitting procedure; an overall normalization of the correlation function not reflected in the parametrization of the Gaussian source, the λ_G

parameter, and the size of the source R_G, which are parameters of the Gaussian source function. Correlation functions are often normalized such that at large values of q the correlation is nearly 1.

The correlation function has some limits to its sensitivity, particularly when emission involves a superposition of short-lived and long-lived sources [38]. When the λ_G parameter is equal to one, in Eq. 5.2, it assumes that all protons used to construct the experimental correlation function are described by the source. However, if it is Gaussian, it typically neglects very long timescale emissions, which would contribute to the total source whose integral must be unity. In general, however, protons are emitted on both short and long time scales, often described by two different sources, whose combined integral must be unity. In the rest frame of the source, fast protons are often emitted dynamically from collisions over short time scales, while slow protons are often emitted from evaporation and secondary decays which occur over longer time scales. These latter protons still influence the height of the correlation function even though they are uncorrelated with protons emitted earlier from the same collision [38]. They do this by contributing to the uncorrelated background without making a comparable contribution to the correlated peak. The width of the correlation function maximum is mainly sensitive to the fast emitted protons, but the maximum is reduced by the factor λ_G in the presence of a significant contribution from the long time-scale emission. In this case, Eq. 5.2 has a general form that reflects other sources of protons.

$$4\pi \int S(r) r^2 dr = \lambda \tag{5.2}$$

Then, the λ parameter can be related to the fraction of short time scale emitted protons

according to [38]

$$\lambda = f^2. \tag{5.3}$$

The fraction of long time scale emitted protons can be written as $1 - f$.

Previous work [38] has offered the half width half maximum ($r_{1/2}$) of the source function as one way to characterize its size. The relation between $r_{1/2}$ and the size of the Gaussian source distribution (Eq. 5.1) is given by

$$r_{1/2} = 2\sqrt{ln2}R_G. \tag{5.4}$$

In this dissertation, $r_{1/2}$ is used to quantify sizes of sources.

It is possible to relax the assumption of a Gaussian source, provided the correlation function maximum is sufficiently large and measured with sufficiently high statistical accuracy. In the "imaging" approach of Ref. [62–64], the source function inserted in the Koonin-Pratt formula (Eq. 1.4) is not assumed to be Gaussian. Instead, it is parametrized to allow a more general shape, which is then adjusted to optimally reproduce the correlation function data.

Thus, there is a fitting procedure that connects terms in the expansion of the source, indexed by j, to measurements of the correlations function, C_i, measured at relative momenta, q_i. Specifically, the source functions S(r) are expanded in a superposition of polynomial splines,

$$S(r) = \sum_j S_j B_j(r). \tag{5.5}$$

This converts the Koonin-Pratt equation into a matrix equation

$$C_i = 1 + R_i = \sum_j K_{ij} S_j, \tag{5.6}$$

where the terms K_{ij} can be obtained from

$$K_{ij} = \int 4\pi r^2 dr K(q_i, r) B_j(r). \tag{5.7}$$

As in the case of the Gaussian source parametrization, the unknown coefficients S_j in the matrix equation above are obtained minimizing the value of the χ^2 between the experimental and theoretical correlation functions. In the following, we used six 3rd order splines to construct the sources.

When comparing the experimental data to BUU calculations, one can either compare experimental and theoretical correlation functions or experimental and theoretical sources. In practice, it is easier to compare the sources extracted from fits to the experimental data to the theoretical sources provided by the BUU calculations. Since the BUU transport code only describes the protons emitted on a short time scale, it does not describe the later evaporative emission. Thus, the BUU source will need to be normalized so that its integral over r is equal to λ.

5.1.1 Theory Adaptation

Any experimental setup can, in principal, bias the data extracted from it. To avoid this, an experimental filter can be applied to the theoretical results to select only those particles which could have been experimentally measured during the experiment. This includes imposing

energy thresholds and energy maxima on the protons from the simulations. For example, only protons within a certain range are able to stop in the CsI crystal without punching through completely. A more restrictive cut imposed was the requirement that the proton was emitted at angles such that it would enter a working EF/EB pixel in HiRA and yet not slip between two CsI crystals. Multiple simulations were performed with different random seeds to increase the proton statistics after applying the filter. To allow an arbitrary orientation between the HiRA detectors and the total angular momentum vector of each event, the protons in the event were randomly rotated 100 times before applying the HiRA experimental filter, ensuring that all orientations of the reaction plane were sampled.

Most of the BUU simulations in the preceding chapter were done at an impact parameter of $b = 1.414$ fm. However, the centrality of the data is determined by $E_t > 150$ MeV which corresponds approximately to $b < 4$ fm. The transverse energy decreases monotonically with impact parameter on the average. Event by event, however, there is a spread, or fluctuation, in this relationship. This fluctuation was studied by Michael Lisa, who analyzed correlation functions for the ^{36}Ar+^{45}Sc system at E/A=80 MeV [65] and showed that these fluctuations are approximately Gaussian in distribution with a standard deviation of about 1.2 fm.

Depending on the cross section employed, the source size changes differently as a function of b. The impact parameter dependence of the source radii was shown in Figs. 4.18, 4.19, and 4.20 in the preceding chapter for several assumptions about the NN in-medium cross sections. This dependence is approximately described by a second order polynomial,

$$r_{1/2}(b)_{th} = r_{1/2}(b_0)_{th} + a_1 \cdot (b - b_0) + a_2 \cdot (b - b_0)^2 \tag{5.8}$$

Neglecting E_t fluctuations as fixed impact parameter, one needs simply to integrate $r_{1/2}(b)_{th}$

over the impact parameter interval $0 \leq b \leq 4$ fm. This is the main effect, and it reduces the values of $r_{1/2}(b)_{th}$ by about 5%. Impact parameter fluctuations typically reduce $\langle r_{1/2}(b)_{th} \rangle$ by an additional 1% compared to what one calculates without taking them into account. In the following, we consider only the effects of the impact parameter gate and not those of impact parameter fluctuations when making comparisons between BUU calculations and the experimental data for average quantities such as $\langle r_{1/2}(b)_{th} \rangle$. We combine the sources at different impact parameters within the gate, using the correct impact parameter weighting.

5.2 *p-p* Correlation Functions

An experimental correlation function, introduced in section 1.2, is constructed by taking a ratio of yields, as was defined by Eq. 1.2. For two particle correlation functions, such as *p-p* these yields are a function of the relative momentum of the pair in the center of mass of the pair. The numerator is constructed by pairing particles from the same event. In this thesis, the event-mixing method [33] is used to construct the denominator. Particles from different events are paired as if they were from the same event, and the relative momentum is calculated. Any selections on data, such as centrality, are applied to the numerator and denominator equally. To obtain reasonable error bars, the denominator usually had 15 times more statistics than the numerator. When the two yields are divided, the result is a two-particle correlation function.

For this dissertation, *p-p* correlations were measured over a large angular range, wide kinematic range, and with high statistics. As a proof of concept, correlation functions were constructed for ^{40}Ca+^{40}Ca and ^{48}Ca+^{48}Ca at midrapidity, as shown in Fig. 5.1. The isospin symmetric system is shown in red, while the neutron-rich system is shown in blue. At

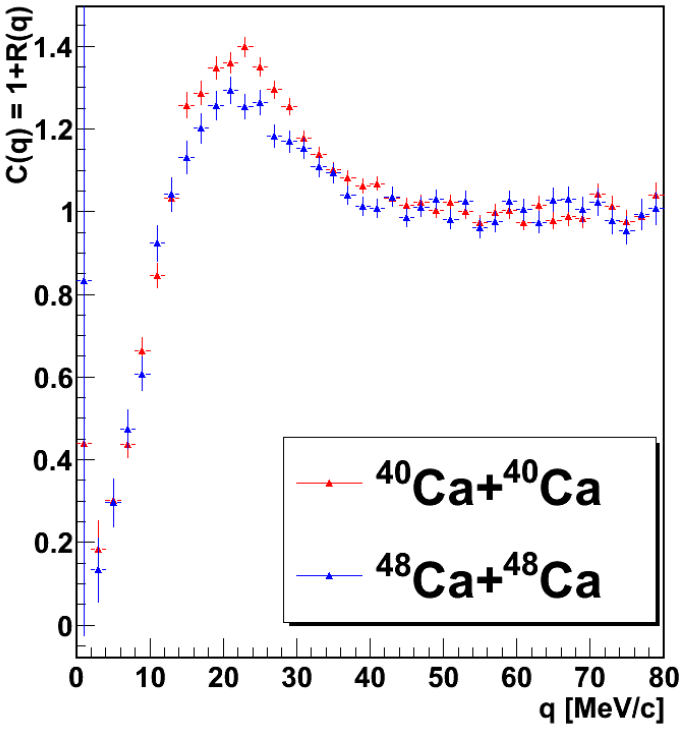

Figure 5.1: p-p correlation functions for both reaction systems at midrapidity, -0.05<y_{cms}<0.05.

first glance, the widths of the correlation functions appear to be very similar, although the width of the correlation function for ^{40}Ca+^{40}Ca is slightly wider than that for ^{48}Ca+^{48}Ca. This corresponds to a larger source for the latter system. This could be a result of the simple fact that the ^{48}Ca+^{48}Ca system is geometrically larger to begin with. Another suggested reason is that the extra neutrons in the ^{48}Ca+^{48}Ca system act to delay or block protons from being emitted. Further study is needed to decide which of the two explanations is more accurate.

5.3 Correlation Functions Selected by Laboratory Angle and Momentum

Experimental measurements at intermediate energies are typically performed with devices of limited solid angle. Selection by laboratory angle and momentum is potentially more easily understood than selection by center of mass angle and momentum or by rapidity and transverse momentum because the experimental efficiency is completely straightforward in the laboratory frame. Many analyses of laboratory correlation functions have been performed [34, 48, 66], which typically exhibit larger and broader proton-proton correlation functions for higher momentum proton pairs consistent with these protons being emitted earlier before the source has had time to expand. Lower momentum protons typically exhibit weaker and narrower correlation functions consistent from the emission of lower energy protons at later times from a cooling, expanding source. Such trends were well documented for the ^{36}Ar+^{45}Sc system at E/A=80 MeV [48, 66], from both Gaussian and imaging analyses, using a device with an angular acceptance that was more limited than HiRA utilized

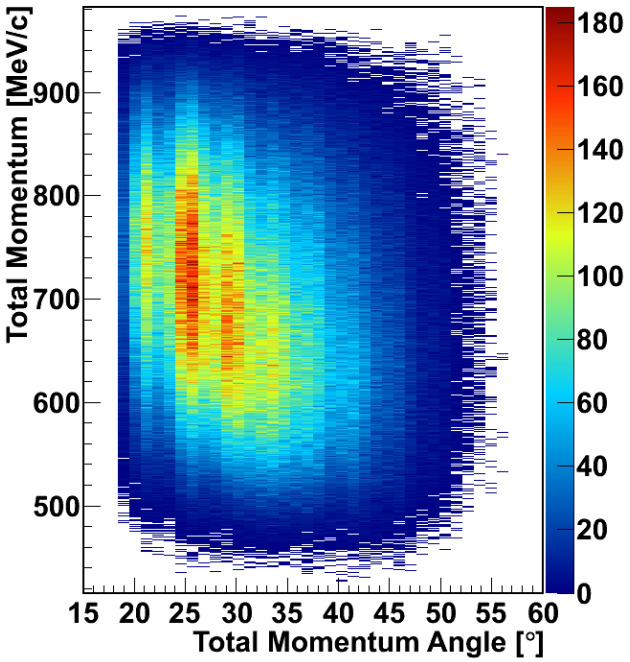

Figure 5.2: Total laboratory momentum of proton pairs as a function of its angle.

in this dissertation.

This section examines the total momentum dependence in the laboratory frame, both in magnitude and angle, on the source size. The phase space covered by HiRA in the total momentum as a function of the laboratory angle is shown in Fig. 5.2. To explore the angular dependence with precision and sensitivity, the lowest and highest third of momentum bins (500-640 MeV/c and 740-900 MeV/c) were subdivided into three angular bins ($18-26^{\circ}$, $26-33^{\circ}$, and $33-58^{\circ}$) with comparable statistics. The correlation functions measured in the experiment for each of these bins are shown in Fig. 5.3. The left panels present results from ^{40}Ca+^{40}Ca and the right panels from ^{48}Ca+^{48}Ca collisions. The upper panels are for protons with low total momentum of the pair in the laboratory frame and the lower panels are for protons with high total momentum. The correlation functions for the most backward angles ($33-58^{\circ}$) in the laboratory frame are represented by black stars, results for intermediate angles ($26-33^{\circ}$) are plotted with red triangles, and results for the forward

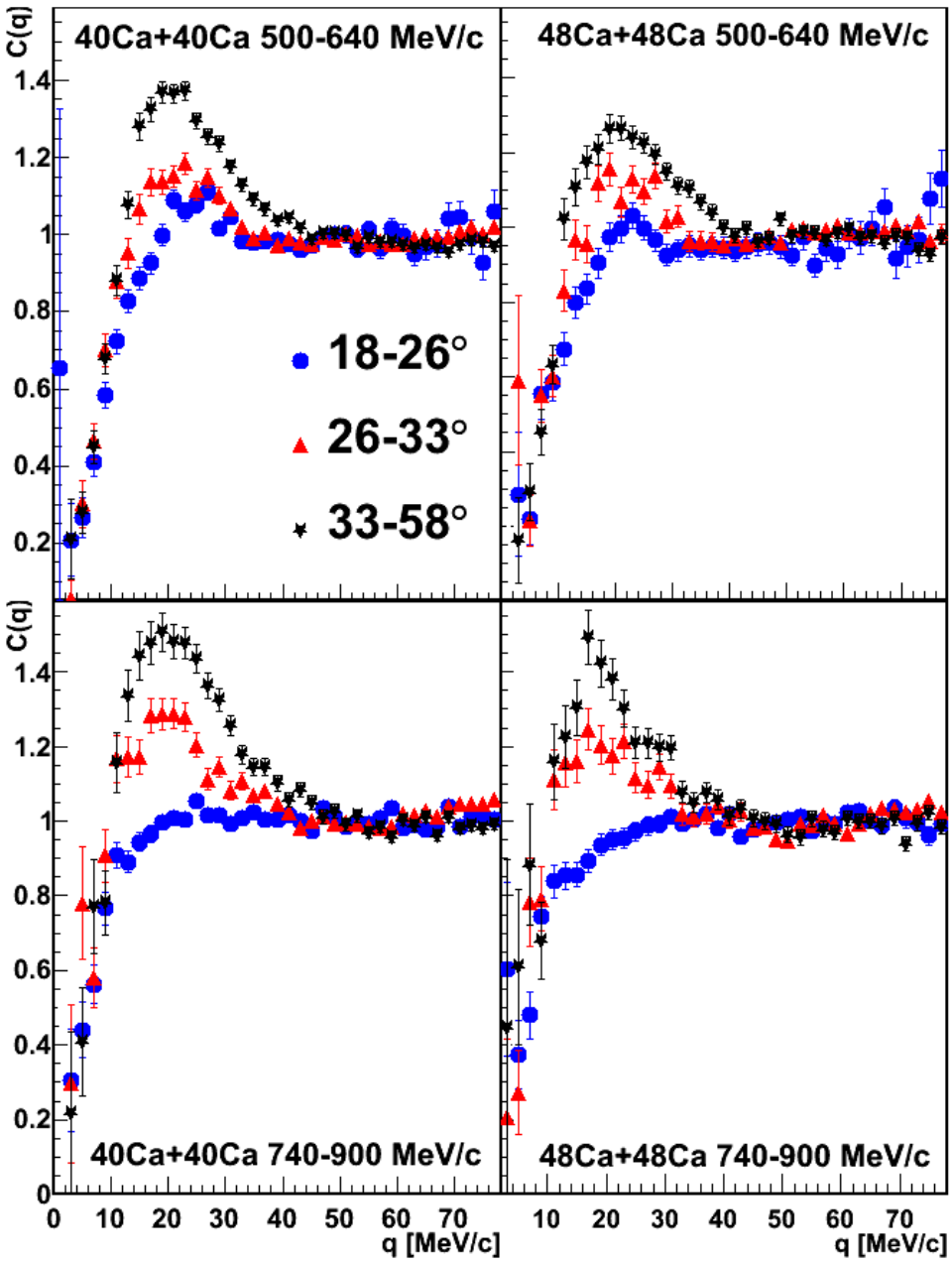

Figure 5.3: Experimental correlation functions from ^{40}Ca+^{40}Ca (left) and ^{48}Ca+^{48}Ca (right). The upper panels include protons with low total momentum (500-640 MeV/c) while the lower panels represent protons with a high total momentum (740-900 MeV/c).

angles ($18-26^{\circ}$) are shown as blue circles. For all, only events with an $E_t > 150$ MeV were used, selecting more central events. This corresponds to a reduced impact parameter $\hat{b} = 0.5$ corresponding approximately to $b < 4$ fm.

Fig. 5.3 shows that at backward and intermediate angle selections, higher momentum protons correspond to a more pronounced correlation function, consistent with prior measurements. However, the trend of the smaller source for high momentum protons is not generally true. Indeed it is false at forward angles of $18-26^{\circ}$. There the correlation functions for faster protons with total momentum $640 \leq P_{Tot} \leq 740$ MeV/c are less pronounced, corresponding to a source that is more extended in space-time. This gate corresponds to proton kinetic energies of $63 \leq$ E/A ≤ 80 MeV, which encompasses much of the expected energy window for nucleons evaporated from an expanding and fragmenting projectile spectator source. The lower momentum gate of 500-640 MeV/c, which corresponds to proton kinetic energies of $22 \leq$ E/A ≤ 43 MeV, contains a mixture of emission from the participant and projectile spectator source, but probably misses most of the contribution from the evaporative emission of excited projectile-like remnants. Based on these observations, we conclude that proton emission from expanding and evaporating projectile remnants is the dominant factor leading to large space-time extent of the source of protons in the high momentum gate for both reactions.

In Fig. 5.4, the data are shown with reconstructed correlation functions from imaging and Gaussian methods. To obtain quantitative information about the emitting source from the correlation functions the imaging technique is employed to construct the source function. Such source distributions from the experimental correlation functions are presented in Fig. 5.5. Also shown are the Gaussian sources which best fit the data. Each panel of

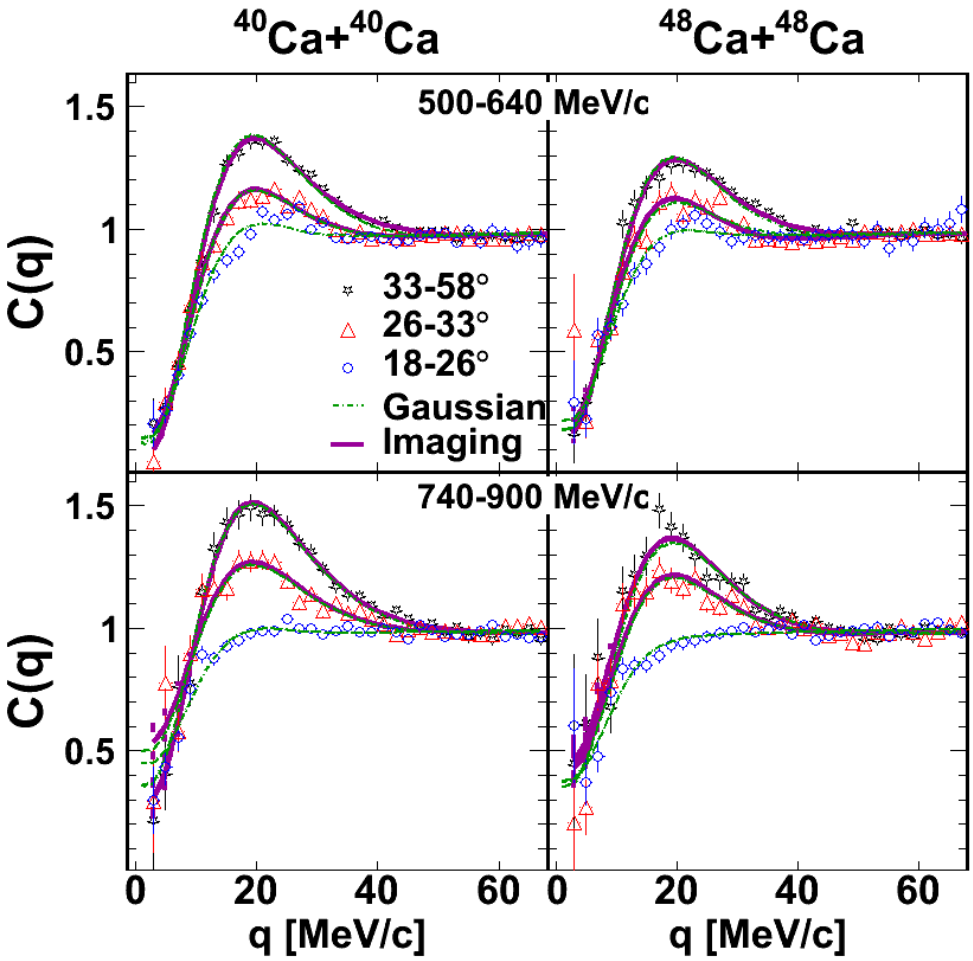

Figure 5.4: Experimental correlation functions from ^{40}Ca+^{40}Ca (left) and ^{48}Ca+^{48}Ca (right). The upper panels include protons with low total momentum (500-640 MeV/c) while the lower panels represent protons with a high total momentum (740-900 MeV/c). The green dotted lines represent the results of the fit assuming a Gaussian source distribution. The purple solid lines are reconstructed correlation functions from imaging.

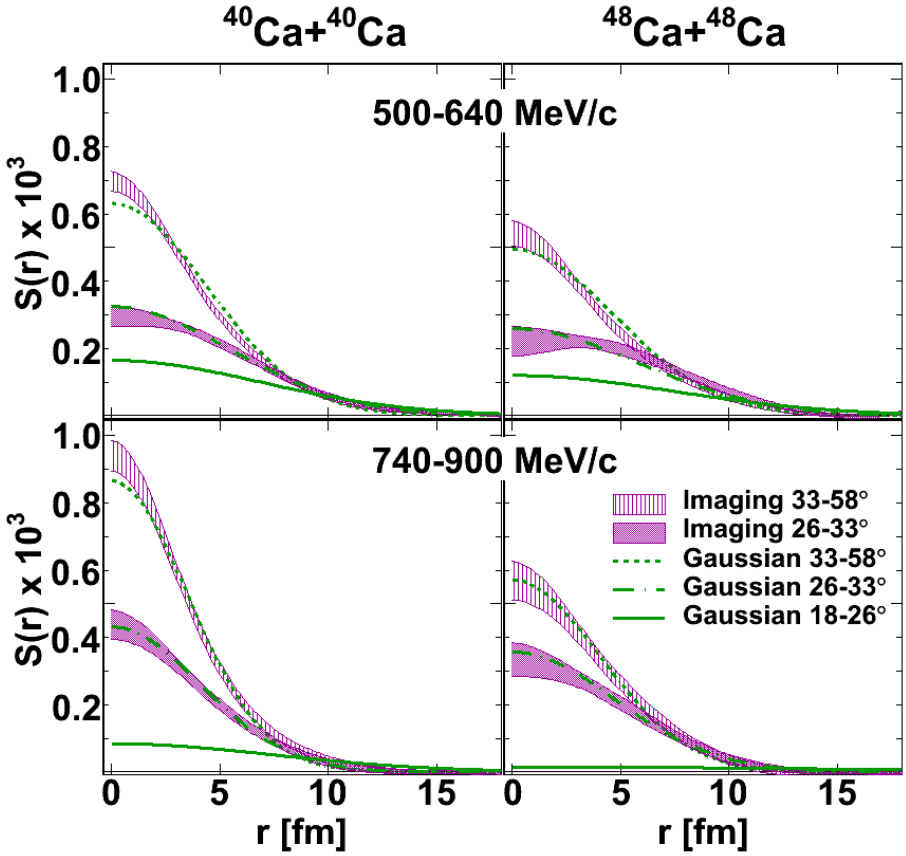

Figure 5.5: Comparison of the imaging fits to the Gaussian fits of p-p correlation functions for ^{40}Ca+^{40}Ca (left) and ^{48}Ca+^{48}Ca (right). The upper panels include protons with low total momentum (500-640 MeV/c) while the lower panels represent protons with a high total momentum (740-900 MeV/c). The green lines are Gaussian source distributions while the purple filled areas are source functions from imaging.

this figure corresponds to the same panel in Fig. 5.4 and the color convention is also the same. The imaging technique was able to construct source distributions for backward and intermediate angles but failed for forward angles.

It is a feature of the imaging technique that it cannot construct the source distribution if the correlation effect at 20 MeV/c is small or is not seen at all (for source sizes larger than 5-6 fm). Larger statistical errors in the correlation function make it even harder for the imaging method to converge.

The fit quality and the λ_I from Eq. 5.2 for imaging, are given in Table 5.1. λ_I is calculated as the scaling factor needed to match the reconstructed correlation function with the correlation function from the data at low q. In general, the imaging method can provide many solutions, source distributions $S(r)$, that will give smaller value of χ^2/ndf than found in Table 5.1. However, solutions with $S(r) < 0$ are not physical, so they were excluded from the analysis. The errors on λ_I parameter were calculated under condition that $S(r) \geq 0$. The imaging method and Gaussian fit method should give roughly the same results for λ since this parameter is related to the fraction of fast emission protons, and this fraction should be independent of the method used to extract it.

The results from the Gaussian fits are presented in Table 5.2. The systematic errors are printed within parentheses next to statistical errors and were estimated by varying the fit range and excluding the first data point of the correlation function from the fit.

Fig. 5.4 shows that the correlation functions reconstructed from imaging and obtained from the Gaussian fit are very similar, and both match the data well. Fig. 5.5 shows that the sources are also consistent between the imaging technique and the Gaussian fitting procedure. Thus, it may not be so problematic that imaging fails at forward angles, because the Gaussian

system	P [MeV/c]	angle θ [°]	λ_I	χ^2/ndf
^{40}Ca+^{40}Ca	[500,640]	$33-58$	$0.93^{+0.13}_{-0.11}$	1.48
^{40}Ca+^{40}Ca	[500,640]	$26-33$	$0.85^{+0.14}_{-0.13}$	1.18
^{40}Ca+^{40}Ca	[740,900]	$33-58$	$0.69^{+0.19}_{-0.12}$	1.06
^{40}Ca+^{40}Ca	[740,900]	$26-33$	$0.52^{+0.17}_{-0.10}$	1.58
^{48}Ca+^{48}Ca	[500,640]	$33-58$	$0.84^{+0.17}_{-0.14}$	1.41
^{48}Ca+^{48}Ca	[500,640]	$26-33$	$0.81^{+0.16}_{-0.12}$	1.17
^{48}Ca+^{48}Ca	[740,900]	$33-58$	$0.60^{+0.16}_{-0.11}$	1.51
^{48}Ca+^{48}Ca	[740,900]	$26-33$	$0.58^{+0.22}_{-0.13}$	1.15

Table 5.1: The normalization of the reconstructed source distribution according to Eq. 5.2 and the χ^2/ndf of the reconstructed correlation function obtained from imaging method.

system	P [MeV/c]	angle θ [°]	λ_G	χ^2/ndf
^{40}Ca+^{40}Ca	[500,640]	$33-58$	$0.86^{+0.03(0.03)}_{-0.03(0.01)}$	1.48
^{40}Ca+^{40}Ca	[500,640]	$26-33$	$0.84^{+0.03(0.01)}_{-0.03(0.01)}$	1.05
^{40}Ca+^{40}Ca	[500,640]	$18-26$	$0.84^{+0.03(0.01)}_{-0.03(0.01)}$	2.12
^{40}Ca+^{40}Ca	[740,900]	$33-58$	$0.61^{+0.06(0.05)}_{-0.06(0.02)}$	0.88
^{40}Ca+^{40}Ca	[740,900]	$26-33$	$0.48^{+0.06(0.06)}_{-0.06(0.01)}$	1.28
^{40}Ca+^{40}Ca	[740,900]	$18-26$	$0.54^{+0.04(0.01)}_{-0.04(0.01)}$	1.52
^{48}Ca+^{48}Ca	[500,640]	$33-58$	$0.81^{+0.05(0.02)}_{-0.05(0.01)}$	1.08
^{48}Ca+^{48}Ca	[500,640]	$26-33$	$0.80^{+0.05(0.01)}_{-0.05(0.01)}$	1.08
^{48}Ca+^{48}Ca	[500,640]	$18-26$	$0.77^{+0.05(0.01)}_{-0.05(0.01)}$	0.97
^{48}Ca+^{48}Ca	[740,900]	$33-58$	$0.59^{+0.09(0.03)}_{-0.09(0.02)}$	1.27
^{48}Ca+^{48}Ca	[740,900]	$26-33$	$0.59^{+0.07(0.01)}_{-0.07(0.02)}$	1.47
^{48}Ca+^{48}Ca	[740,900]	$18-26$	$0.64^{+0.35(0.01)}_{-0.08(0.01)}$	1.04

Table 5.2: Normalization and fit results to the experimental correlation functions assuming Gaussian source distribution.

fitting procedure can be used in this region. From both the shape of the source distributions shown on the Fig. 5.5 and the quality of the reconstructed correlation functions, one can draw the conclusion that the correlation functions at backward angles are for the most part consistent with assumption that the source function has a Gaussian shape.

From λ_G and λ_I,the fraction of fast emission protons can be calculated using Eq 5.3. The results from this are presented in Table 5.3. We note the consistency between the fast fractions extracted by both the imaging and Gaussian fits and that both fast fractions are well above 50%. The fast fractions are similar for both reactions. These values for the fast fraction are much higher than those extracted from correlation functions for slow velocity protons in mass asymmetric ^{14}N+^{197}Au collisions at E/A=75 MeV [38], where values as low as f=0.3 were reported. These values are a little sensitive to the range in r over which the source is evaluated, but the difference also suggests that conventional evaporation may be less relevant for these symmetric collisions as for mass asymmetric collisions at about the same incident energy/nucleon. How to reconcile this with the large radii observed at forward angles in the present work is not clear. To resolve this, it may be useful to analyze directional correlations for the present systems in the forward angular domain [67]. Such directional correlations can distinguish between large spatial sizes, and long lifetimes.

As mentioned before, the imaging method failed to reproduce the source distribution for the most forward angles where the size of the source is large and the correlation effect is not as strong. This emphasizes the need to find a consistent method of determining the size of the source so the results can be compared to each other. The $r_{1/2}$ for each source is presented in Table 5.4 for both reaction systems and both pair momentum ranges in the laboratory frame. Also listed are results from BUU, described in the next section.

system	P [MeV/c]	$\langle P \rangle$ [MeV/c]	angle θ [$^\circ$]	f_G	f_I
^{40}Ca+^{40}Ca	[500,640]	584	$33-58$	$0.93^{+0.02}_{-0.02}$	$0.96^{+0.07}_{-0.06}$
^{40}Ca+^{40}Ca	[500,640]	588	$26-33$	$0.92^{+0.02}_{-0.02}$	$0.92^{+0.08}_{-0.07}$
^{40}Ca+^{40}Ca	[500,640]	594	$18-26$	$0.92^{+0.02}_{-0.02}$	–
^{40}Ca+^{40}Ca	[740,900]	794	$33-58$	$0.78^{+0.04}_{-0.04}$	$0.83^{+0.11}_{-0.08}$
^{40}Ca+^{40}Ca	[740,900]	798	$26-33$	$0.69^{+0.05}_{-0.05}$	$0.72^{+0.12}_{-0.07}$
^{40}Ca+^{40}Ca	[740,900]	802	$18-26$	$0.73^{+0.03}_{-0.03}$	–
^{48}Ca+^{48}Ca	[500,640]	583	$33-58$	$0.90^{+0.03}_{-0.03}$	$0.92^{+0.10}_{-0.08}$
^{48}Ca+^{48}Ca	[500,640]	587	$26-33$	$0.89^{+0.03}_{-0.03}$	$0.90^{+0.09}_{-0.07}$
^{48}Ca+^{48}Ca	[500,640]	594	$18-26$	$0.88^{+0.03}_{-0.03}$	–
^{48}Ca+^{48}Ca	[740,900]	799	$33-58$	$0.77^{+0.06}_{-0.06}$	$0.77^{+0.10}_{-0.07}$
^{48}Ca+^{48}Ca	[740,900]	804	$26-33$	$0.77^{+0.05}_{-0.05}$	$0.76^{+0.14}_{-0.09}$
^{48}Ca+^{48}Ca	[740,900]	805	$18-26$	$0.80^{+0.22}_{-0.05}$	–

Table 5.3: Given are the fractions of fast emission protons from both the imaging technique and from a Gaussian fit routine.

Except for three out of eight selections on momentum and angle where both imaging and the Gaussian fits converge, the resulting values for $r_{1/2}$ are statistically consistent. At the largest angles and the low momentum cut, the imaging fit provides an anomalously small value for $r_{1/2}$. Detailed comparison of the correlation function fits in Fig. 5.4 show that the main difference between the two fits occurs at relative momentum near 40 MeV/c. This small difference in the fits could be an interplay between the background and spline parametrization. The sharp decrease in the radius at small momentum, appears to be inconsistent with the general trend. From that perspective the Gaussian fits appear to be more reasonable.

System	P [MeV/c]	Angle [°]	$r_{1/2}$ [fm]		
			Gaussian fit	imaging	BUU
^{40}Ca+^{40}Ca	[500,640]	33-58	$5.20^{+0.07}_{-0.09}$	$4.49 \pm 0.15^{+0.08}_{-0.36}$	5.04 ± 0.10
^{40}Ca+^{40}Ca	[500,640]	26-33	$6.46^{+0.10}_{-0.10}$	$6.85 \pm 0.33^{+0.07}_{-0.14}$	5.91 ± 0.09
^{40}Ca+^{40}Ca	[500,640]	18-26	$8.11^{+0.22}_{-0.24}$	–	6.68 ± 0.10
^{40}Ca+^{40}Ca	[740,900]	33-58	$4.20^{+0.15}_{-0.17}$	$4.06 \pm 0.13^{+0.10}_{-0.27}$	4.14 ± 0.09
^{40}Ca+^{40}Ca	[740,900]	26-33	$4.85^{+0.22}_{-0.25}$	$4.71 \pm 0.32^{+0.08}_{-0.12}$	4.66 ± 0.09
^{40}Ca+^{40}Ca	[740,900]	18-26	$8.99^{+0.55}_{-0.42}$	–	5.33 ± 0.10
^{48}Ca+^{48}Ca	[500,640]	33-58	$5.62^{+0.12}_{-0.12}$	$4.94 \pm 0.21^{+0.05}_{-0.33}$	5.51 ± 0.11
^{48}Ca+^{48}Ca	[500,640]	26-33	$6.85^{+0.19}_{-0.17}$	$8.35 \pm 0.43^{+0.23}_{-0.30}$	6.58 ± 0.09
^{48}Ca+^{48}Ca	[500,640]	18-26	$8.74^{+0.55}_{-0.42}$	–	7.31 ± 0.11
^{48}Ca+^{48}Ca	[740,900]	33-58	$4.75^{+0.22}_{-0.24}$	$4.69 \pm 0.33^{+0.19}_{-0.10}$	4.50 ± 0.10
^{48}Ca+^{48}Ca	[740,900]	26-33	$5.90^{+0.22}_{-0.24}$	$5.85 \pm 0.56^{+0.14}_{-0.18}$	4.93 ± 0.14
^{48}Ca+^{48}Ca	[740,900]	18-26	$16.37^{+8.46}_{-4.16}$	–	5.80 ± 0.10

Table 5.4: Comparison of systems, angular and momentum dependence of $r_{1/2}$ for imaging, the Gaussian fitting procedure, and BUU.

5.3.1 Comparison to BUU Transport Theory

^{40}Ca+^{40}Ca and ^{48}Ca+^{48}Ca collisions at E/A = 80 MeV were simulated using the BUU transport model. The production of $A \leq 3$ clusters [41, 42] were included, which was found to increase the size of the source, as shown in section 4.5. The Rostock parametrization of NN in-medium cross section reduction was employed [43]. Momentum dependence in the mean field potential was also included, as was a soft equation of state with an incompressibility of K=210 MeV. The density dependence of the symmetry energy was chosen to be $\gamma = 0.7$, which is in agreement with Ref. [26].

From the information provided by the model, source functions were constructed for the same momentum and angular bins in the laboratory as used in the experimental analysis. Then, the quantity $r_{1/2}$ was calculated from the source distribution for protons with the en-

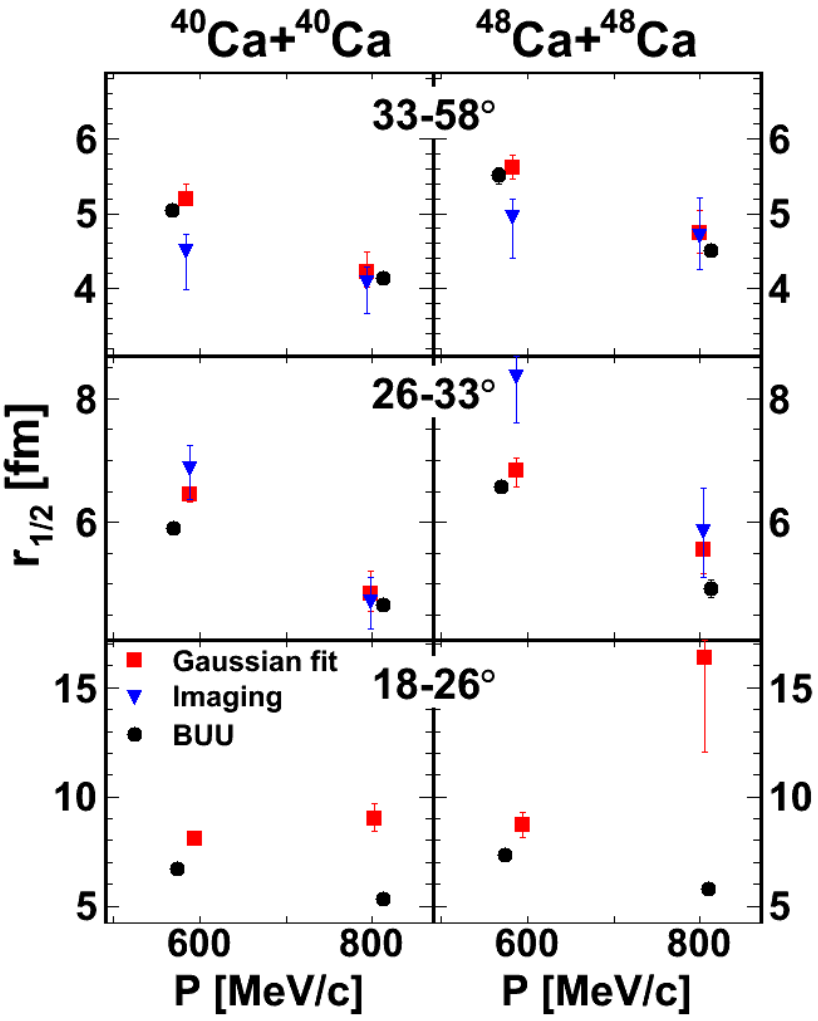

Figure 5.6: $r_{1/2}$ as a function of average total momentum for both reaction systems and all three angular gates. The size of sources from data using the imaging technique is given by blue triangles while that from the Gaussian fit is shown as red squares. Source sizes from BUU are shown as black circles.

ergy and angle gates that are consistent with the acceptance of HiRA during the experiment. This allows the source distributions and the values of $r_{1/2}$ for BUU and the experimental data to be directly compared. Figure 5.6 shows the latter comparison for both Gaussian fits and the imaging technique.

BUU with the specific transport inputs given earlier in this section qualitatively reproduces the measured values for $r_{1/2}$ at backward and intermediate angles for both pair

momentum ranges. It also qualitatively reproduces forward angle source sizes for low momentum but underpredicts the sizes at high momentum. In the laboratory frame, these high momentum protons are moving at the velocity of the projectile-like fragment which is evaporating and fragmenting. BUU does not incorporate evaporation or secondary decay processes into the model so it is not completely unexpected that the source size is smaller than the data for this kinematic region. In the next sections, we present correlation functions gated on rapidity and transverse momentum. Then we vary the transport inputs to see for which values they reproduce the measured values better and which do not.

5.4 Correlation Functions Selected by Rapidity and Transverse Momentum

This section explores dependencies on total transverse momentum, an invariant with respect to the frame of reference, and the pair rapidity in the center of mass reference frame. The phase space in transverse momentum as a function of rapidity as covered by HiRA is shown in Fig. 5.7.

In terms of the velocity, $\beta_{z,cm}$, which is the component of the proton velocity in the center of mass frame parallel to the beam divided by the speed of light, the center of mass rapidity can be defined as

$$y = \ln((1 + \beta_{z,cm})/(1 - \beta_{z,cm}))/2. \tag{5.9}$$

Rapidity is additive under Lorentz transformation and reduces to $\beta_{z,cm}$ in the non-relativistic limit. All rapidities, y, in this dissertation are in the center of mass frame.

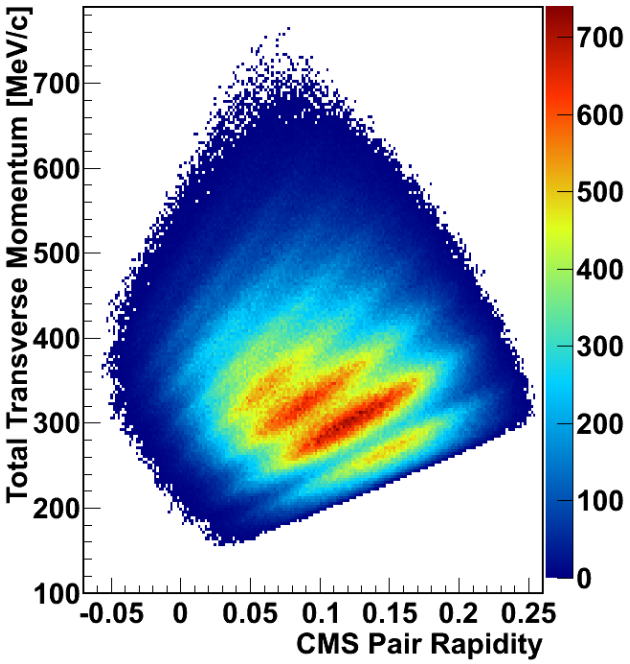

Figure 5.7: Total transverse momentum as a function of pair center of mass rapidity.

This available phase space was divided into six regions with similar statistics. Fig. 5.8 examines the total transverse momentum dependence ($\lesssim 350\text{MeV}/c$) of correlation functions for three rapidity selections and both reaction systems. The left panels present results from ^{40}Ca+^{40}Ca and the right panels from ^{48}Ca+^{48}Ca collisions. For all, an $E_t > 150$ MeV was again used to select more central events. To make a correspondence with the preceding sections, we note that selecting events based on center of mass rapidity, y given by Eq. 5.9, is somewhat similar to selecting events on center of mass angle, with $y = 0$ being similar to $\theta = 90^\circ$.

However, dual gates on rapidity and transverse momentum can select source more precisely than gates on angle and total momentum. Low transverse momentum and high rapidity particles are moving slowly in the rest frame of the projectile remnants. Low transverse momentum and low rapidity is more selective of particles moving in the rest frame of the participant source. The emission to high transverse momentum is characteristic of short

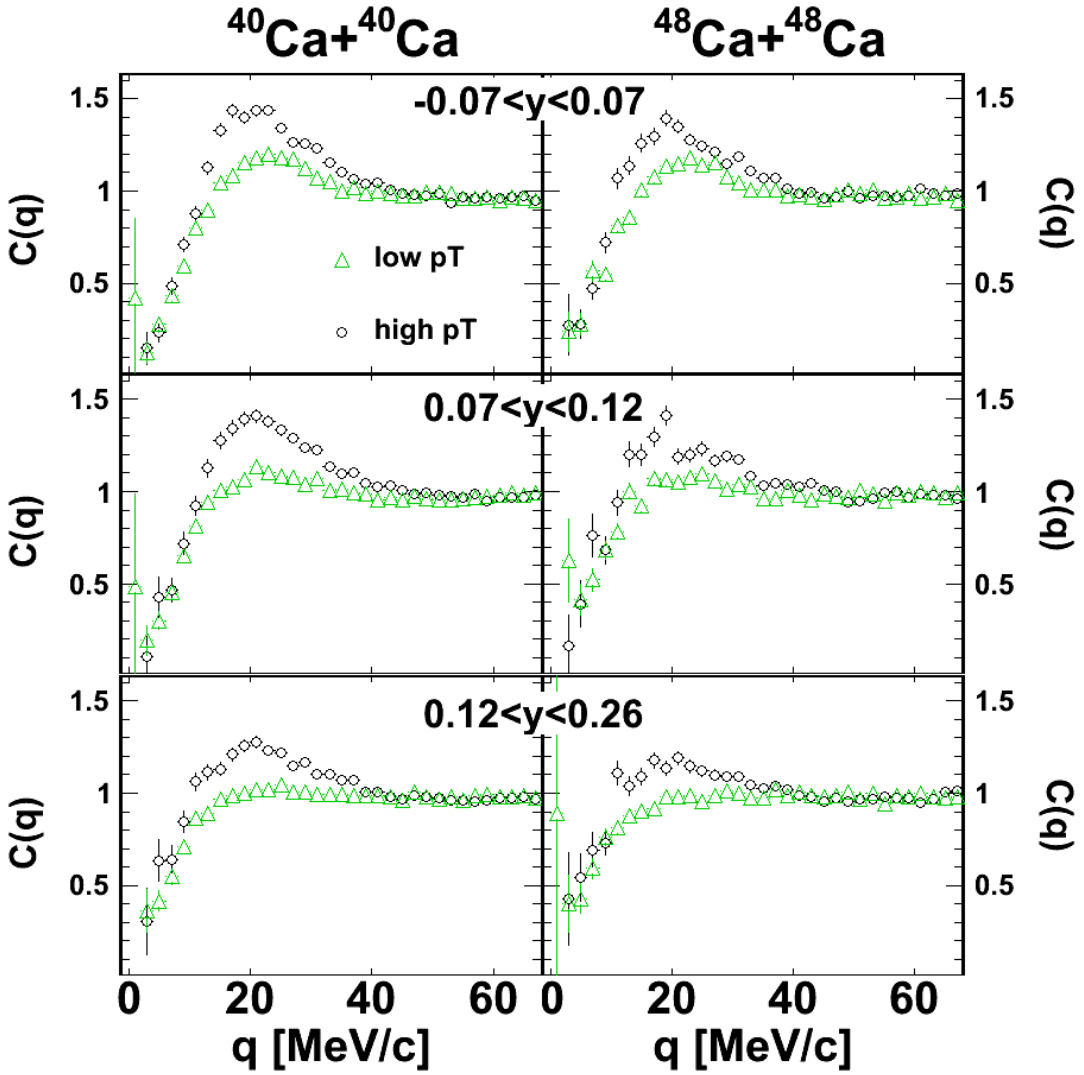

Figure 5.8: Experimental correlation functions from ^{40}Ca+^{40}Ca (left) and ^{48}Ca+^{48}Ca (right). The top panels include protons with low pair rapidity while the middle panels include protons with intermediate pair rapidity and the lowest panels represent protons with a high pair rapidity.

time-scale pre-equilibrium emission.

Fig. 5.8 shows that the highest gates on y leads to the least pronounced correlation functions. However, the lowest and intermediate selections of y give similar correlation functions in most of the cases. In all cases, increasing the total transverse momentum results in a more pronounced peak in the correlation function independent of y.

The correlation functions were fit by both the imaging technique and by assuming a Gaussian source. The reconstructed correlation functions from both methods are shown in Fig. 5.9 with the data. The agreement is good except in the case of low rapidity and low transverse momentum for each reaction system where the data does not peak at 20 MeV/c. This shift in the peak could be due to collective effects not accounted for by the two-particle formalism. Note that the peak for the low transverse momentum and high rapidity selections is nonexistent. This correlation function could not be imaged as in two cases in the previous section.

Fig. 5.10 shows the imaged and Gaussian sources for the same set of data in the same panel structure. The top panels show sources for proton pairs in the lowest rapidity bin. The middle panels show sources for proton pairs in an intermediate rapidity bin. The bottom panels show sources for proton pairs in the highest rapidity bin. Both methods provide similar sources for all rapidity selections, except the case that could not be imaged.

The results for the Gaussian fit method are shown in Table 5.5. The systematic errors are printed within parentheses next to statistical errors and were estimated by varying the fit range and excluding the first data point of the correlation function from the fit.

The source $r_{1/2}$ sizes for both imaging and the Gaussian fit method are shown in Table 5.6. Also shown are sizes from BUU. For this comparison, the mean field potential was

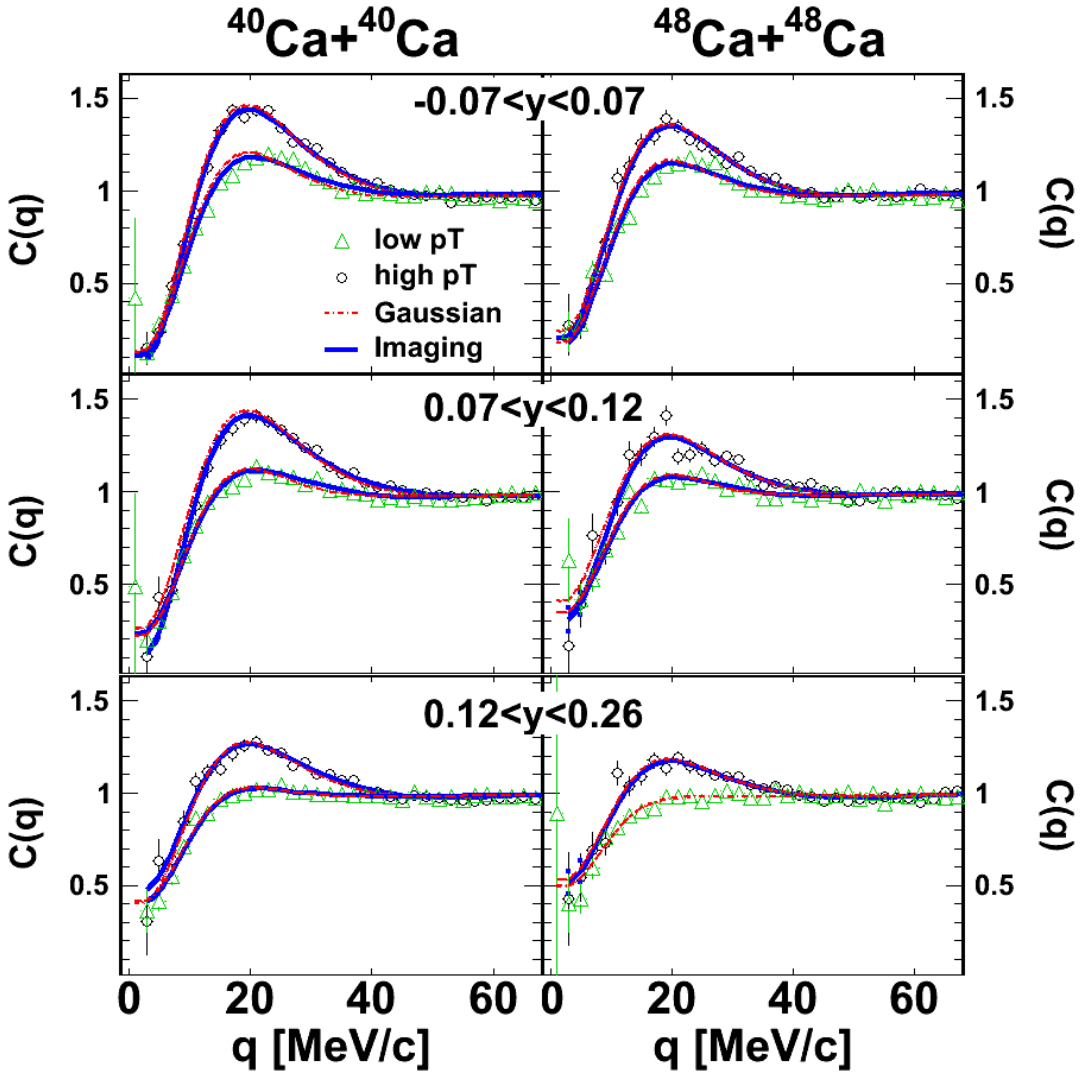

Figure 5.9: Experimental correlation functions from ^{40}Ca+^{40}Ca (left) and ^{48}Ca+^{48}Ca (right). The top panels show correlations for proton pairs in the lowest rapidity bin. The middle panels show correlations for proton pairs in an intermediate rapidity bin. The bottom panels show correlations for proton pairs in the highest rapidity bin.

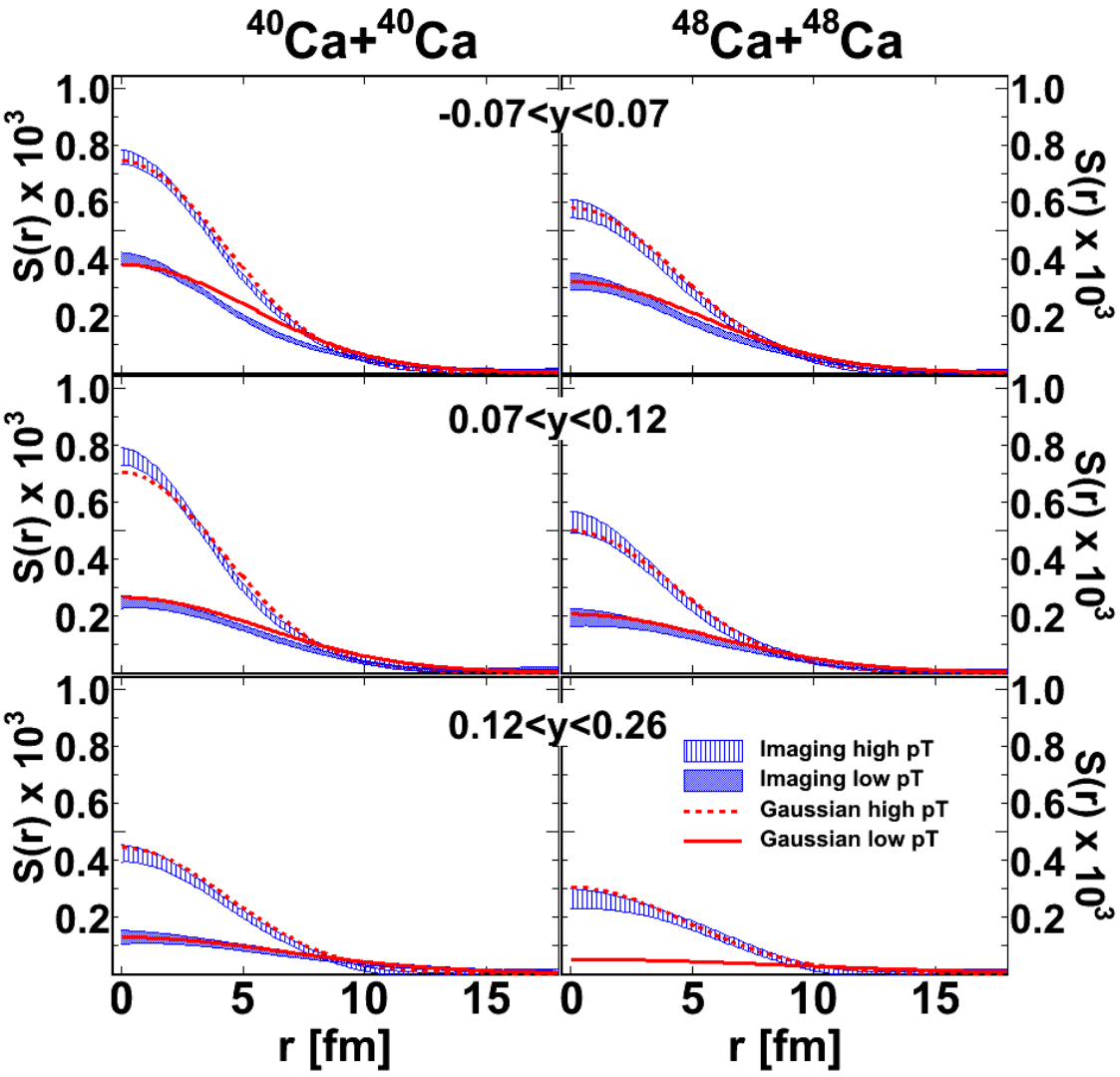

Figure 5.10: Experimental source functions from ^{40}Ca+^{40}Ca (left) and ^{48}Ca+^{48}Ca (right) for both the imaging and Gaussian fit methods.

system	$\langle P_T \rangle$ [MeV/c]	$\langle Y \rangle$	R_G [fm]	λ_G	χ^2/ndf
^{40}Ca+^{40}Ca	294	0.04	$3.79^{+0.04(0.03)}_{-0.04(0.07)}$	$0.88^{+0.02(0.01)}_{-0.02(0.01)}$	3.48
^{40}Ca+^{40}Ca	289	0.10	$4.01^{+0.06(0.05)}_{-0.06(0.02)}$	$0.78^{+0.06(0.01)}_{-0.05(0.01)}$	1.72
^{40}Ca+^{40}Ca	300	0.16	$4.70^{+0.11(0.01)}_{-0.10(0.03)}$	$0.59^{+0.03(0.01)}_{-0.03(0.01)}$	1.01
^{40}Ca+^{40}Ca	417	0.04	$2.99^{+0.04(0.02)}_{-0.04(0.01)}$	$0.89^{+0.04(0.01)}_{-0.03(0.01)}$	1.57
^{40}Ca+^{40}Ca	426	0.10	$2.91^{+0.06(0.08)}_{-0.06(0.01)}$	$0.78^{+0.05(0.03)}_{-0.05(0.01)}$	1.20
^{40}Ca+^{40}Ca	409	0.16	$2.82^{+0.10(0.12)}_{-0.11(0.08)}$	$0.47^{+0.05(0.04)}_{-0.05(0.03)}$	1.07
^{48}Ca+^{48}Ca	295	0.04	$3.88^{+0.06(0.08)}_{-0.06(0.01)}$	$0.83^{+0.04(0.01)}_{-0.04(0.01)}$	2.50
^{48}Ca+^{48}Ca	291	0.09	$4.18^{+0.11(0.04)}_{-0.10(0.01)}$	$0.67^{+0.05(0.01)}_{-0.05(0.01)}$	1.32
^{48}Ca+^{48}Ca	303	0.16	$6.16^{+1.39(0.05)}_{-0.50(0.03)}$	$0.52^{+0.04(0.01)}_{-0.04(0.01)}$	1.08
^{48}Ca+^{48}Ca	419	0.04	$3.12^{+0.07(0.04)}_{-0.07(0.02)}$	$0.78^{+0.05(0.01)}_{-0.05(0.01)}$	1.06
^{48}Ca+^{48}Ca	429	0.09	$3.10^{+0.10(0.01)}_{-0.11(0.06)}$	$0.65^{+0.07(0.01)}_{-0.07(0.02)}$	1.92
^{48}Ca+^{48}Ca	413	0.16	$3.31^{+0.12(0.01)}_{-0.13(0.14)}$	$0.49^{+0.07(0.01)}_{-0.06(0.04)}$	1.21

Table 5.5: Fit results to the experimental correlation functions assuming Gaussian source distribution.

System	P_T [MeV/c]	Y	$r_{1/2}$ [fm]		
			Gaussian fit	imaging	BUU
^{40}Ca+^{40}Ca	[150,350]	[-0.07,0.07]	$6.31^{+0.07(0.05)}_{-0.07(0.12)}$	$5.65 \pm 0.39^{+0.23}_{-0.47}$	5.86 ± 0.08
^{40}Ca+^{40}Ca	[150,350]	[0.07,0.12]	$6.68^{+0.10(0.09)}_{-0.10(0.04)}$	$6.63 \pm 0.54^{+0.33}_{-0.45}$	6.00 ± 0.10
^{40}Ca+^{40}Ca	[150,350]	[0.12,0.26]	$7.83^{+0.19(0.02)}_{-0.17(0.05)}$	$7.80 \pm 0.58^{+0.21}_{-0.43}$	5.52 ± 0.10
^{40}Ca+^{40}Ca	[350,700]	[-0.07,0.07]	$4.98^{+0.07(0.04)}_{-0.07(0.02)}$	$4.70 \pm 0.13^{+0.21}_{-0.32}$	4.64 ± 0.09
^{40}Ca+^{40}Ca	[350,700]	[0.07,0.12]	$4.85^{+0.10(0.14)}_{-0.10(0.02)}$	$4.51 \pm 0.15^{+0.10}_{-0.08}$	4.42 ± 0.09
^{40}Ca+^{40}Ca	[350,700]	[0.12,0.26]	$4.70^{+0.17(0.20)}_{-0.19(0.14)}$	$4.93 \pm 0.24^{+0.12}_{-0.28}$	4.53 ± 0.08
^{48}Ca+^{48}Ca	[150,350]	[-0.07,0.07]	$6.46^{+0.10(0.14)}_{-0.10(0.02)}$	$5.55 \pm 0.28^{+0.12}_{-0.19}$	6.49 ± 0.09
^{48}Ca+^{48}Ca	[150,350]	[0.07,0.12]	$6.96^{+0.19(0.07)}_{-0.17(0.02)}$	$6.78 \pm 0.47^{+0.04}_{-0.32}$	6.52 ± 0.11
^{48}Ca+^{48}Ca	[150,350]	[0.12,0.26]	$10.26^{+2.32(0.09)}_{-0.84(0.05)}$	N/A	6.02 ± 0.10
^{48}Ca+^{48}Ca	[350,700]	[-0.07,0.07]	$5.20^{+0.12(0.07)}_{-0.12(0.04)}$	$5.04 \pm 0.21^{+0.11}_{-0.26}$	5.23 ± 0.09
^{48}Ca+^{48}Ca	[350,700]	[0.07,0.12]	$5.16^{+0.17(0.02)}_{-0.19(0.10)}$	$4.77 \pm 0.15^{+0.18}_{-0.29}$	4.92 ± 0.09
^{48}Ca+^{48}Ca	[350,700]	[0.12,0.26]	$5.51^{+0.20(0.17)}_{-0.22(0.24)}$	$5.55 \pm 0.52^{+0.22}_{-0.39}$	4.79 ± 0.13

Table 5.6: Comparison of system size, angular and momentum dependence of $r_{1/2}$ obtained from reconstructed source distribution with imaging method, Gaussian fitting procedure and BUU transport model simulations.

momentum dependent, $\gamma = 0.7$, clusters were produced, and the Rostock in-medium cross section reductions were used.

5.4.1 Comparison to BUU Transport Theory

Chapter 4 examined source dependencies on a variety of transport inputs. It is worthwhile to revisit the BUU source dependencies when experimental filters are taken into account. In this subsection, BUU is briefly re-examined. For this exploration, the mean field potential is momentum dependent, clusters are being produced, $\gamma = 0.7$, and the Rostock *NN* in-medium cross section reduction is employed, unless otherwise stated.

Fig. 5.11 shows the effect of changing the symmetry energy on the source size for the two reaction systems. In the case of the N=Z symmetric reaction system, the symmetry energy has little effect, which is to be expected. In the neutron-rich reaction system, the stiffer symmetry energy systematically results in a larger source size. The increase is not significant at low transverse momentum, but is significant at higher transverse momentum. The trend is opposite of that predicted by the IBUU model [8] and Fig. 4.33, neither of which included cluster production. This difference may not be experimentally distinguishable. In addition, there are other unconstrained inputs which affect the source size, as we saw in Ch. 4, and is explored again below.

Fig. 5.12 shows that free cross sections lead to a larger source [48] while screened in-medium cross section reductions [43] result in much smaller sources. The energy dependent (Rostock) *NN* in-medium cross section reduction [43] is between free and screened, lying closer to free in terms of reduction and source size. The effect of in-medium cross section on source size is stronger for lower transverse momentum proton pairs than higher transverse

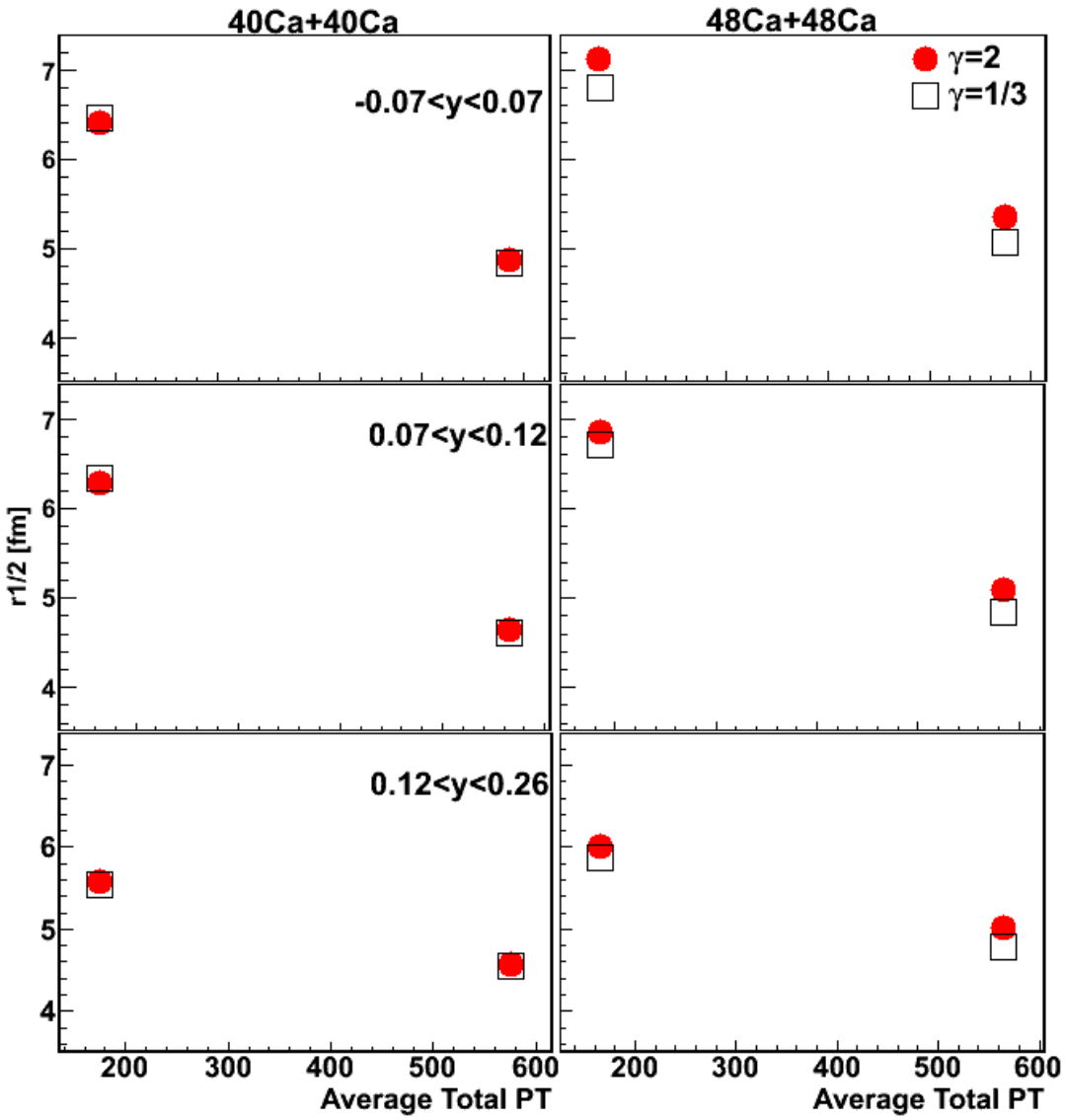

Figure 5.11: $r_{1/2}$ values as a function of average total transverse momentum for low rapidity (top), intermediate rapidity (middle) and high rapidity (bottom). Results using a stiff symmetry energy are shown by red filled circles while those using a soft symmetry energy are shown with black open squares.

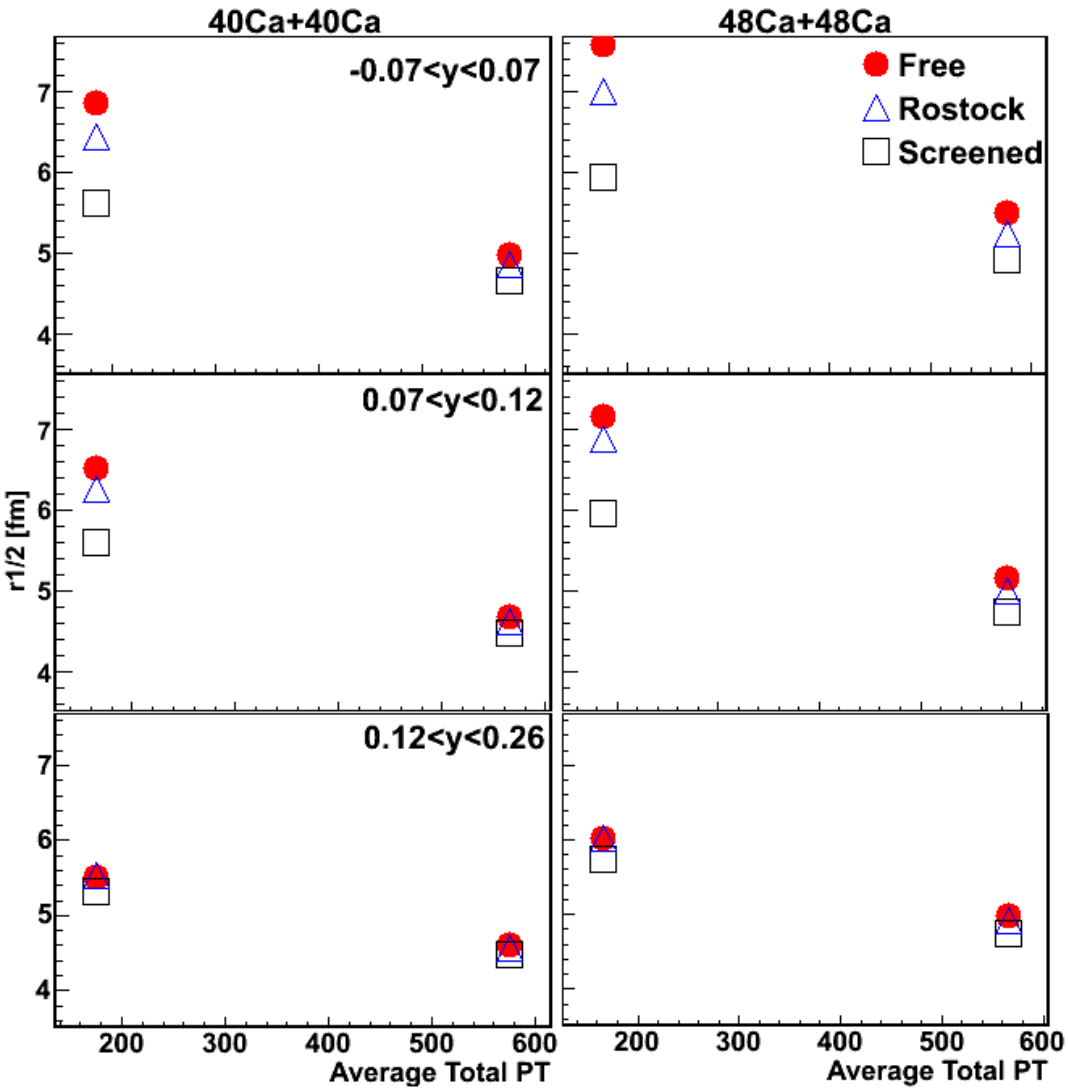

Figure 5.12: $r_{1/2}$ values as a function of average total transverse momentum for low rapidity (top), intermediate rapidity (middle) and high rapidity (bottom). Results using free cross sections are shown as red filled circles while those using a screened in-medium cross section reduction are shown as black open squares.

momentum pairs. In addition, the effect is much stronger at lower rapidity. At the highest rapidity, the effect is subtle.

When colliding nuclei using BUU, one has the option of producing clusters. Fig. 5.13 shows the effect of $A \leq 3$ cluster [41, 42] production. Including clusters in the simulation increases the size of the source significantly and systematically. The effect of cluster production on source size is slightly stronger for lower momentum proton pairs and is mostly independent of rapidity.

Including momentum dependence with a soft EOS (K=210 MeV) gives rise to a slightly different size source, as shown in Fig. 5.14, than using a momentum independent mean field potential with a stiff EOS (K=380 MeV) although the two parametrizations lead to similar elliptic flow observables [45] for high beam energies. The effect of momentum dependence of the mean field is most noticeable for higher transverse momentum proton pairs at the highest rapidity, but is not experimentally distinguishable.

Depending on the choice of momentum dependence in the mean field, cluster production, and cross section reduction, one could imagine that different conclusions could be made about the symmetry energy by comparing p-p correlation functions between theory and data. This dissertation makes no attempt to constrain the symmetry energy while these other inputs are still somewhat unconstrained.

Now that the dependence of various inputs on source size has been re-explored, Fig. 5.15 shows a comparison between data for the three in-medium NN cross sections, one without cluster production. For this comparison, the mean field potential is momentum dependent with a soft EOS and $\gamma = 0.7$.

The agreement between theory and data is reasonable for the free and Rostock cross

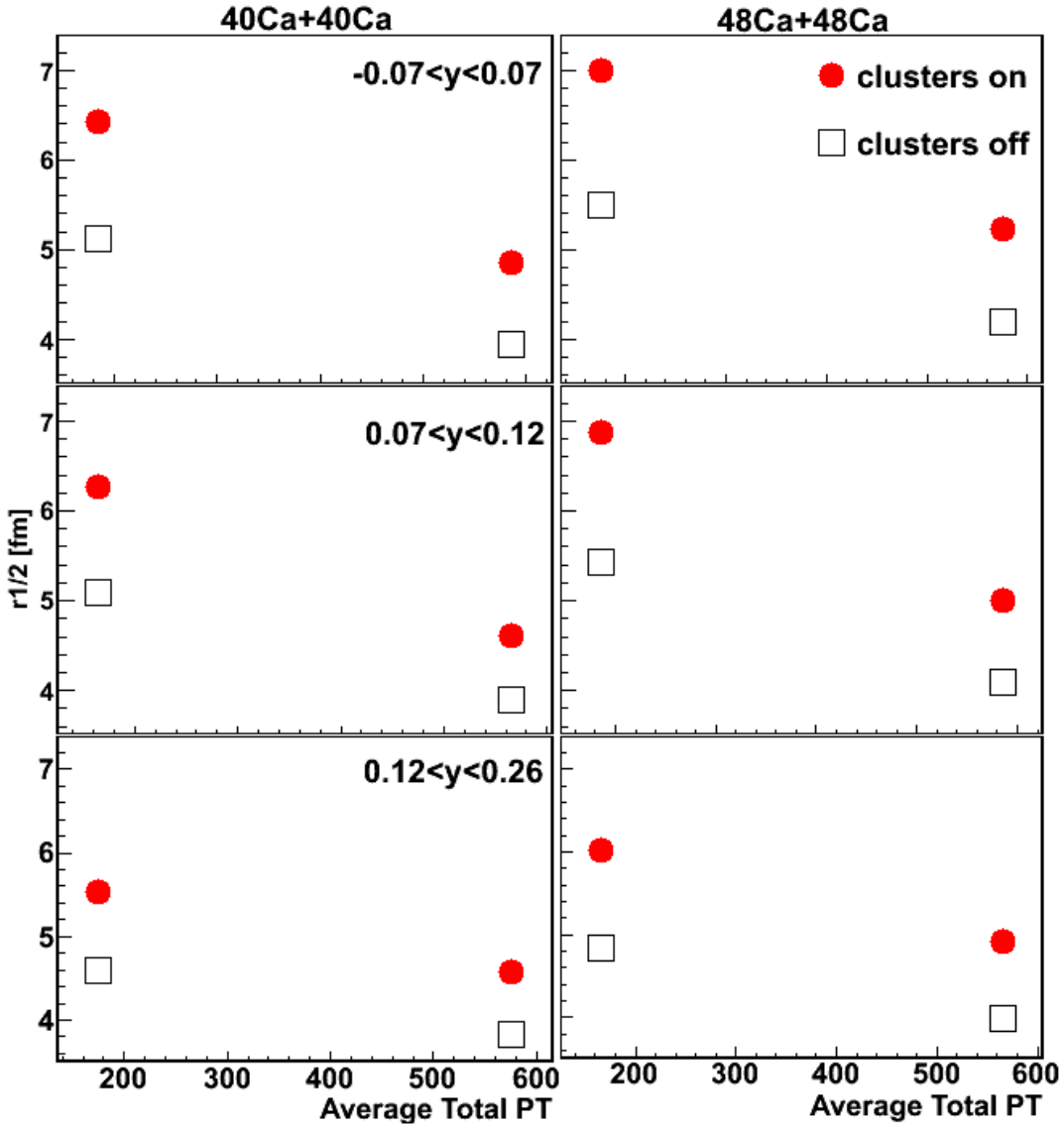

Figure 5.13: $r_{1/2}$ values as a function of average total transverse momentum for low rapidity (top), intermediate rapidity (middle) and high rapidity (bottom). Results with cluster production are given by red filled circles, results without cluster production are given by black open squares.

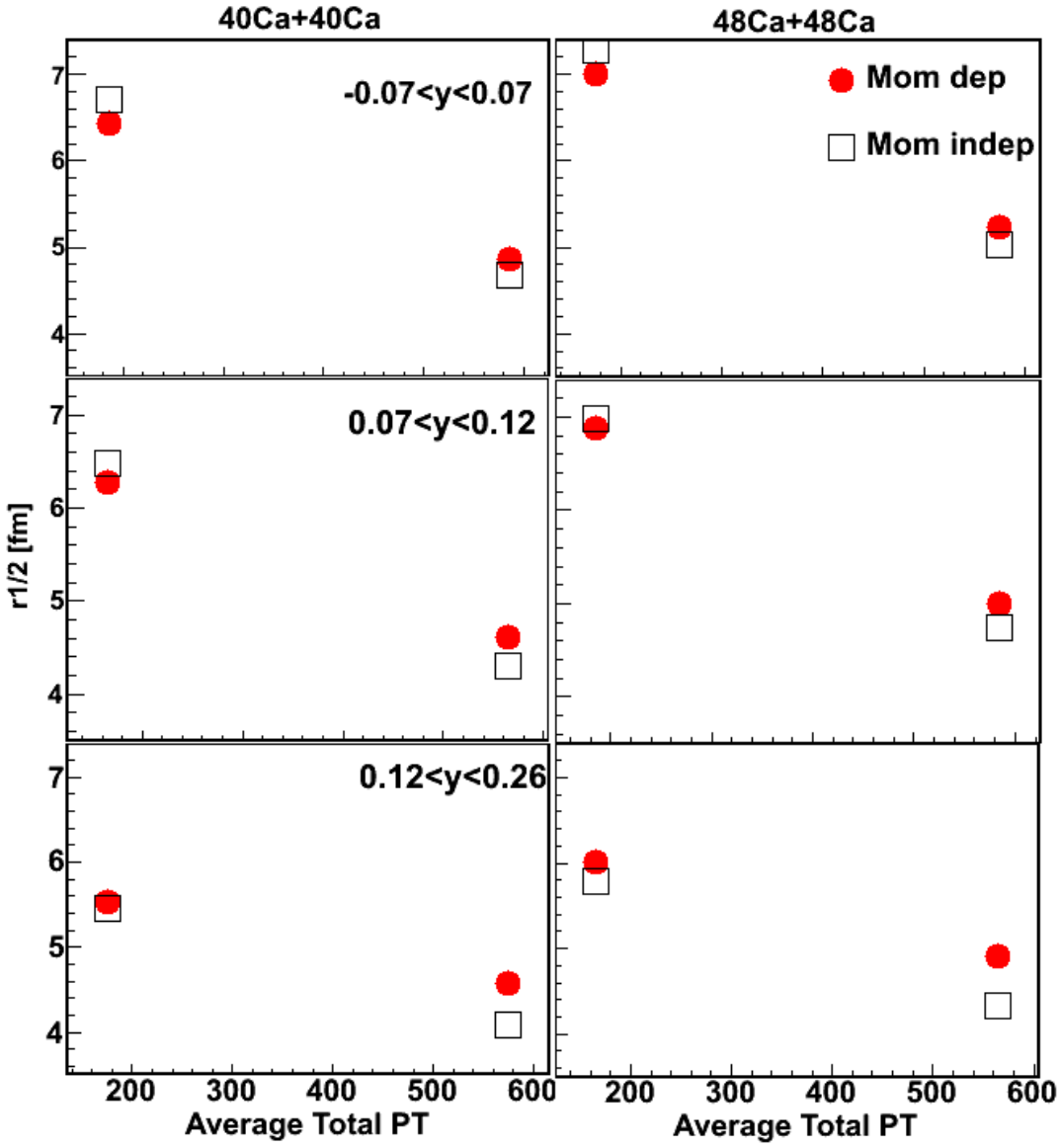

Figure 5.14: $r_{1/2}$ values as a function of average total transverse momentum for low rapidity (top), intermediate rapidity (middle) and high rapidity (bottom). Results from calculations using a momentum dependent mean field potential are shown with red filled circles, while those using a momentum independent potential are shown with black open squares.

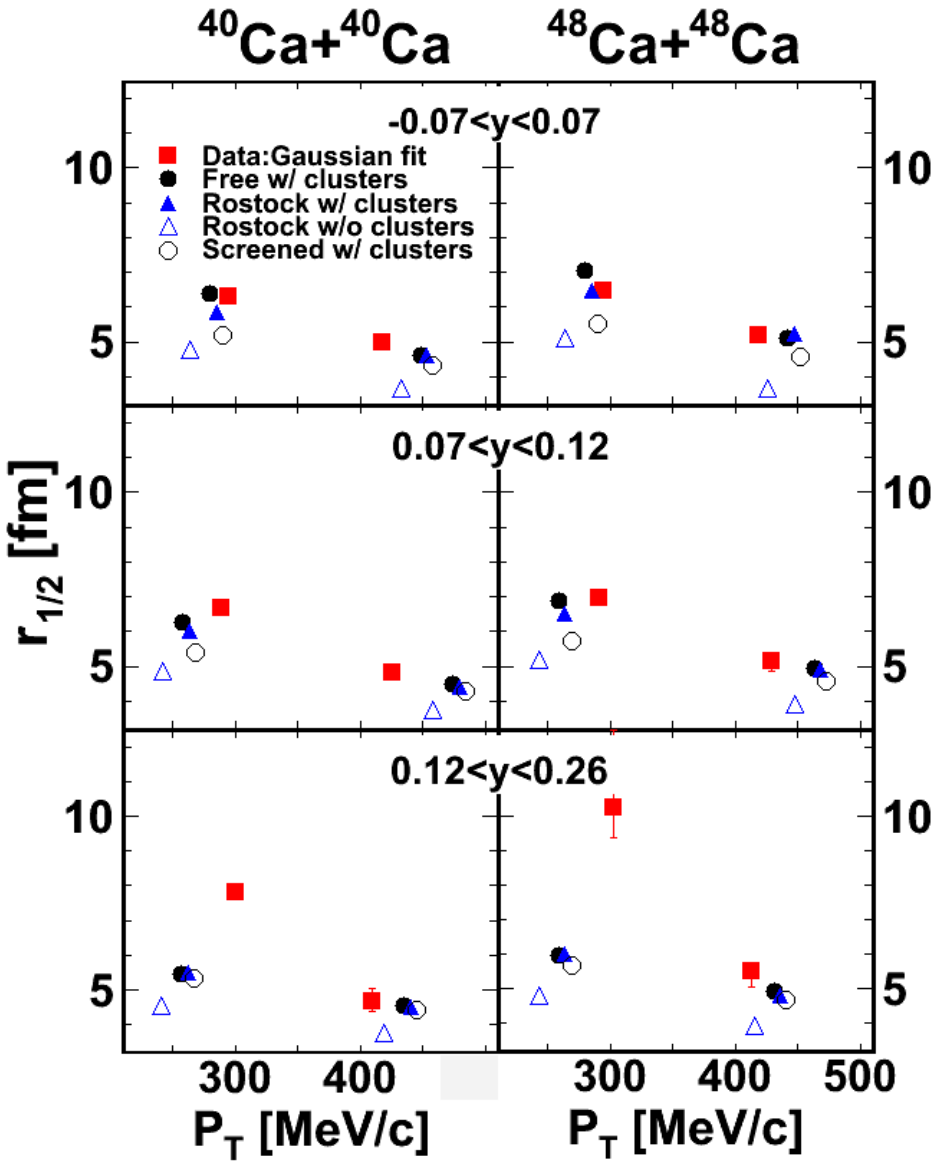

Figure 5.15: Source $r_{1/2}$ values from ^{40}Ca+^{40}Ca (left) and ^{48}Ca+^{48}Ca (right) for data using the Gaussian fit and 4 parametrizations of BUU.

sections with cluster production. Turning cluster production off with the Rostock cross section underpredicts the size of the source. This also occurs when using the screened in-medium cross section reduction. It is clear that cluster production and larger in-medium cross sections are needed to explain the p-p correlation functions from the data. It is not clear whether free cross sections or the Rostock in-medium reduction is in better agreement with the data.

Protons emitted with higher transverse momentum always come from a smaller source than those emitted with lower transverse momentum. At high rapidity, protons are being emitted from an evaporating, fragmenting projectile like source. Such emission occurs over longer timescales resulting in a large source. BUU does not incorporate secondary decays or evaporation so this can be a reason why it fails to reproduce the trend seen in the data. It should be noted that the disagreement between theory and data at high rapidity is not due to the experimental resolution of the detectors, as the correlation functions from data are narrower and not broader than the theory. The correlations are also narrower than what they would be if the cross section was smaller.

5.5 Three Particle Correlations

Just as p-p correlation functions were constructed in the previous sections, 3-particle correlations can also be constructed from heavy-ion reactions which probe the excited state of the parent nucleus. When constructing p-p correlation functions, the ratio of the yields is plotted as a function of relative momentum in the pair's center of mass frame. In the case

of 3-particle correlations, the ratio of yields is plotted as a function of relative kinetic energy

$$E_{rel} = T1 + T2 + T3 \tag{5.10}$$

where T is the kinetic energy of each particle in the center of mass of the system of three particles. The mass excess for the decay is subtracted from the relative kinetic energy to determine the state in the parent nucleus. For this section, there were no selections on centrality of the collisions. The normalization of the correlation function is arbitrary. While these have not been analyzed in detail, four 3-particle correlations are described in this section.

Fig. 5.16 shows the resonant 0+ ground state and 2+ state from the breakup of ^{6}Be. The ground state peak is more pronounced despite the spin degeneracy of the excited state. This is probably due to the increase in the background under the 2+ peak. The background can be seen below and between the peaks. It decreases to zero at small relative energy reflecting the Coulomb repulsion between the ^{6}Be decay products. The background in these multi-particle correlations increase with relative momentum more strongly with each additional particle. This is a phase space effect. The peak appears as a single level, multiplied by the 2J+1 spin degeneracy factor. It appears at the energy of the excited state; its detection efficiency modulates the number of detector events in the peak. The background has the same efficiency factor, so it divides away in the correlation function. The natural strength in the uncorrelated background scales with the semi-classical phase space density. As a function of energy, it has an additional phase space factor of $E^{3/2}$ for each addition particle in the multi-particle final state. As the relative energy is increased, relative contribution of the resonance decays become steadily smaller. The width in the excited state 1.67 MeV is

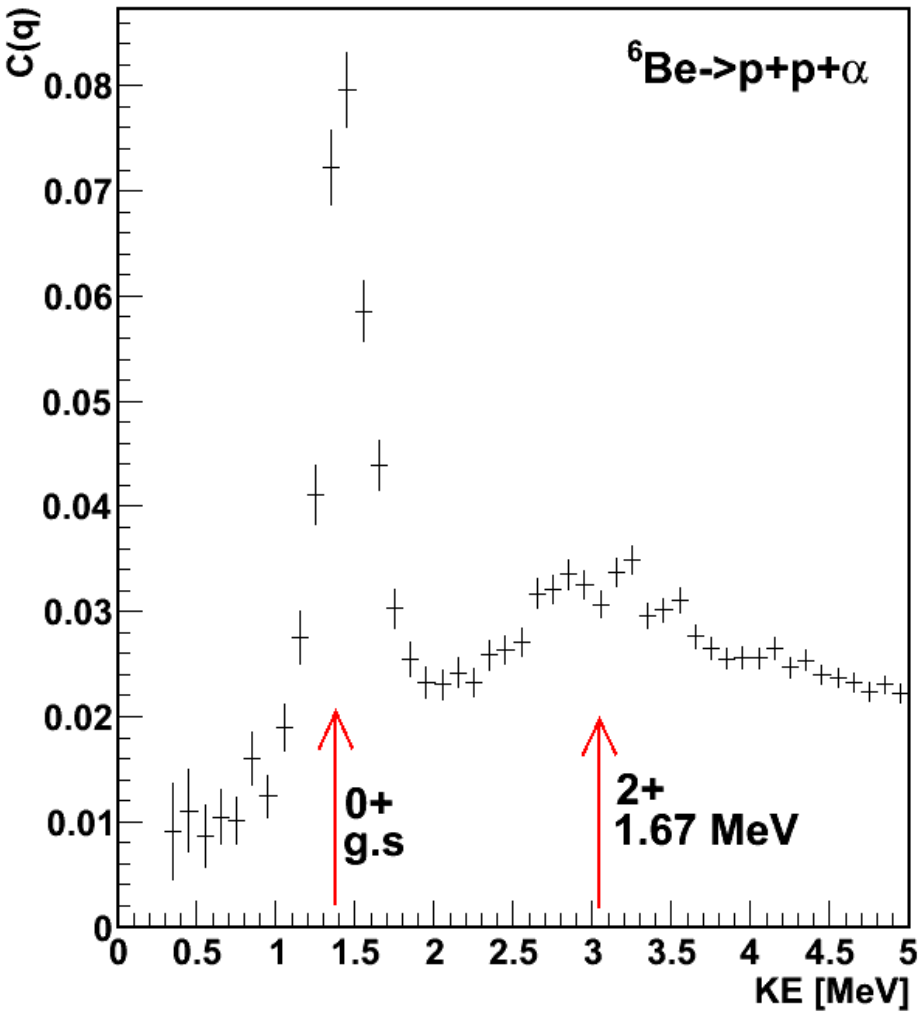

Figure 5.16: 3-particle correlation for ^{6}Be→ p+p+α. Known states are labeled by red arrows.

broad. Its appearance is similar to that observed by Charity *et al.* [68]. More information on the three-body decay of ^{6}Be can be found in Refs. [69, 70].

Fig. 5.17 shows the ground state and 2 excited states of ^{9}B that undergo 3-body breakup into a proton and 2 α particles. The ground state is quite pronounced, while the two excited states are close together so that they appear to form one peak. More information on the low lying states of ^{9}B can be found in Ref. [71]. For a discussion regarding the difference between ^{9}B→ p+α+α and ^{9}B→ p+^{8}Be channels see Ref. [70].

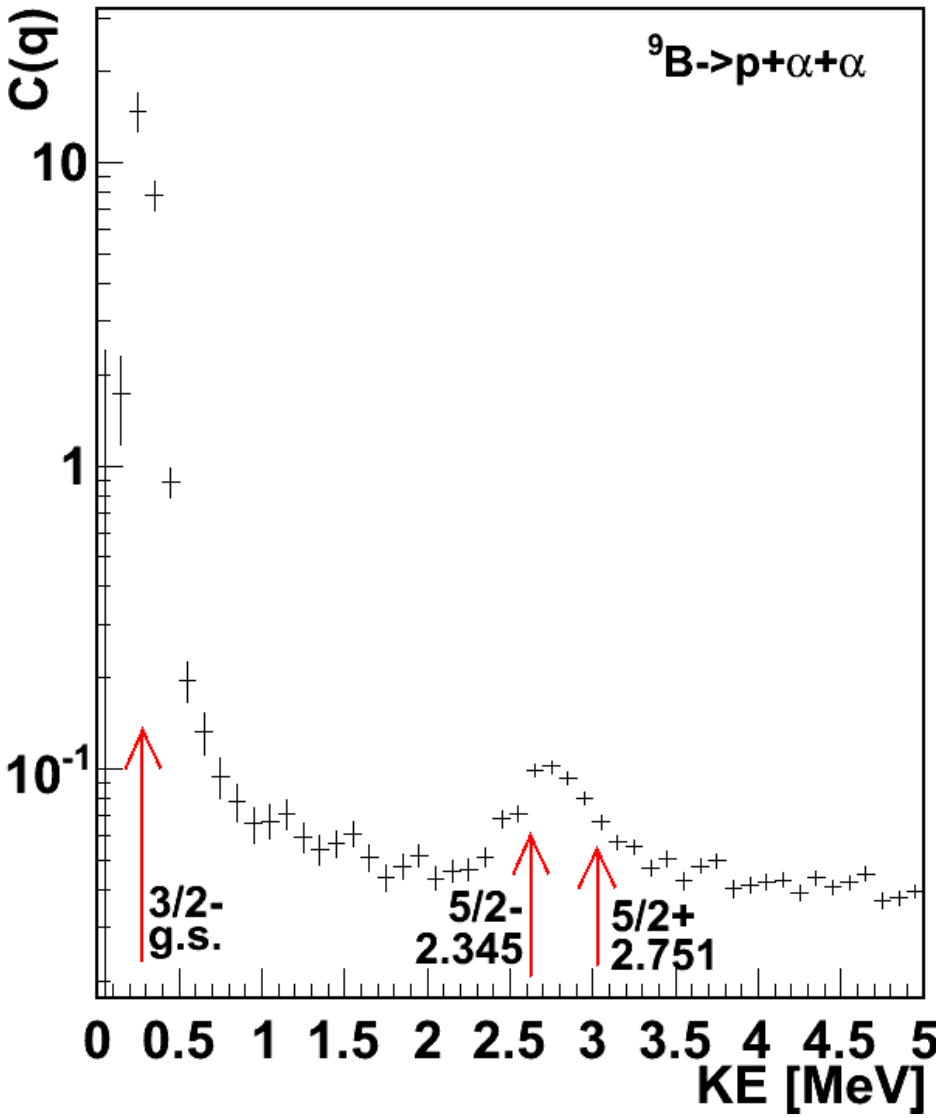

Figure 5.17: 3-particle correlation for ^{9}B$\rightarrow$ p+α+α. Known states (in MeV) are labeled by red arrows.

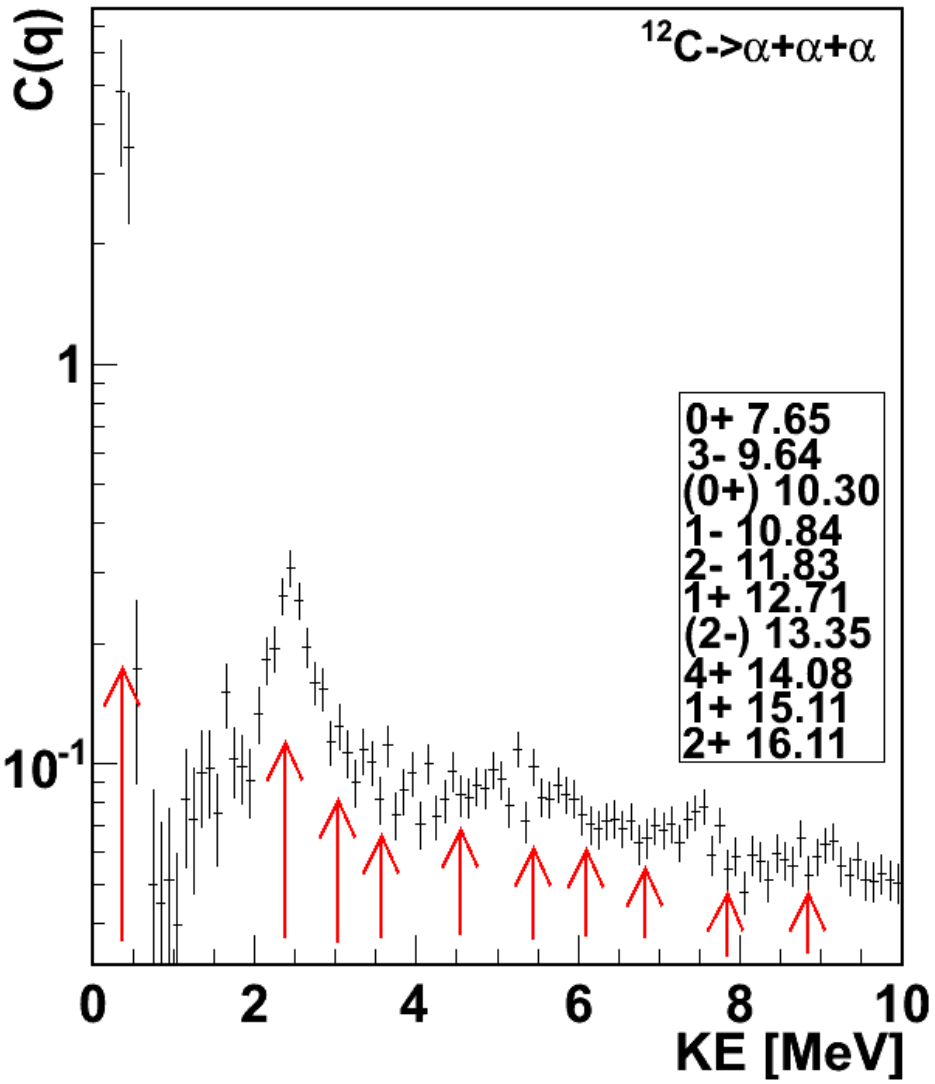

Figure 5.18: 3-particle correlation for $^{12}\mathrm{C} \rightarrow \alpha + \alpha + \alpha$. Known states are labeled by red arrows. States (in MeV) are listed in ascending order.

The Hoyle state was predicted [72], as an excited state in carbon. This state was measured a few years later [73] and thought to make possible a thermal resonance in the Salpeter process, to take place in red giant stars. Fig. 5.18 shows the 0+ Hoyle state at the lowest lying energy, along with many states at higher relative kinetic energies. The second lowest peak corresponds to a 2+ resonance at 9.7 MeV [74, 75], or 2.4 MeV in relative kinetic energy.

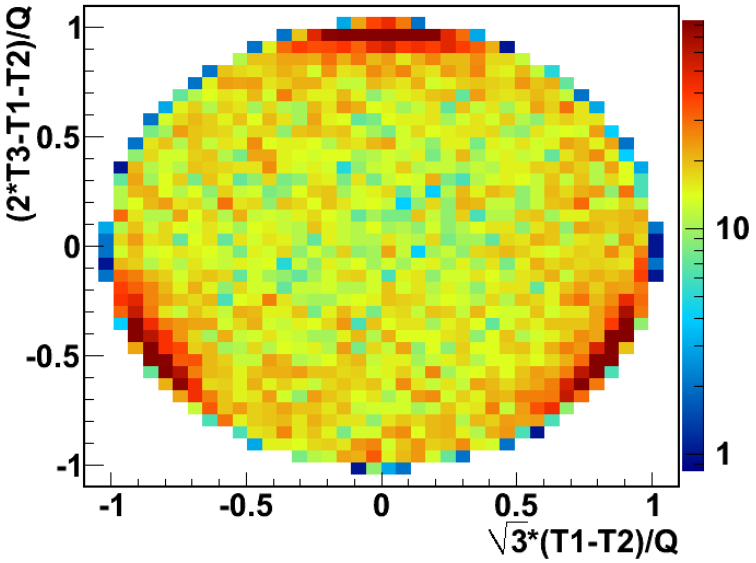

Figure 5.19: Dalitz plot for ^{12}C$\rightarrow \alpha + \alpha + \alpha$ and ^{12}C$\rightarrow$ ^{8}Be$+\alpha$.

A phase space Dalitz plot [76] is also included for the triple α breakup of ^{12}C. Fir. 5.19 shows that nearly all of the ^{12}C breakup goes through the ^{8}Be channel. Significant 3-body breakup would be noticeable in the center of the Dalitz plot, where T1=T2=T3. Instead, there are three "hot spots" which each correspond to one α particle having a higher kinetic energy than the other two, which have nearly equal kinetic energies. It may be possible to extract the three branch ratio for the ground state decay from this Dalitz plot, but additional work is needed to accomplish this.

Chapter 6

Summary

The experiment for this dissertation (the final experiment for the 4π Array) was part of the HiRA group's campaign to constrain the density dependence of the symmetry energy. Although it was found that p-p correlation functions are sensitive to changes in γ with a certain choice of inputs and gates on transverse momentum, no constraints can be placed on γ. There are other unconstrained inputs in the BUU transport theory that are competing effects when comparing- source sizes. Constraining the density dependence of the symmetry energy via transport codes is a multidimensional issue in that it requires a number of constraints on different inputs.

Dependencies of p-p correlations were studied for central ^{40}Ca+^{40}Ca and ^{48}Ca+^{48}Ca nuclear reactions at E/A = 80 MeV. Measurements were performed with the HiRA detector complemented by the 4π Array at NSCL. In this chapter we first summarize the conclusions from a systematic study of the BUU transport simulations. This is followed by a discussion of the data and a summary of the comparison between theory and data for both center of mass and laboratory selections on data. The chapter will end with a discussion of possible

future work to be completed.

6.1 Conclusions from BUU Transport Simulations

Many inputs of the BUU transport simulation code were explored including those which affect the numerical aspects of a transport code. BUU was found to be stable with the choice of grid size and test particle number. The main observable, source size, was stable against changes in these computational inputs.

Many calculations were performed to explore the sensitivity of the calculated source radii to theoretical quantities. These quantities include the density dependence of the symmetry energy, in-medium *NN* cross sections, the production of clusters, and the momentum dependence of the mean field potential. The momentum dependence of the mean field had little effect on the size, although momentum independent mean fields produced slightly larger sources in most cases. The density dependence of the symmetry energy had only a slight effect on the source size. Reducing the *NN* in-medium cross section reduces the size of the source because it increases the free mean path of the protons and increase the freeze-out density. Cluster production increased the size of the source which is consistent with the picture that protons close together in space prefer to be in clusters, and are taken out of the source. Since clusters are produced in nuclear collisions in this energy domain, this suggests that cluster production needs to be considered more carefully in reaction dynamics calculations. Efforts should be made to include and improve the description of cluster production, as it has a significant effect on source size.

Thus one finds that there are significant sensitivities to both the in-medium cross sections and the cluster production. Consequently, *p*-*p* correlation functions, and thus source

sizes, cannot constrain any transport property such as the in-medium cross sections, without making some choice about the implementation of cluster production mechanism. It a multidimensional project. Other observables with different sensitivities to these quantities, such as in-medium cross sections, need to be sought out and explored. Then the various constraints can be combined to provide significant constraints on quantities such as the density dependence of the symmetry energy. More theoretical work is needed in this area.

6.2 Summary of Experimental Results

At midrapidity, *p*-*p* correlation functions show that the ^{48}Ca+^{48}Ca reaction systems results in a larger source size than the ^{40}Ca+^{40}Ca reaction system. Part of this is due to ^{48}Ca+^{48}Ca having a larger geometric size. The observed effect is somewhat larger than what one would get by scaling up by $A^{1/3}$. If extra neutrons act to delay proton emission, through the large *np* cross section or the density dependent symmetry energy, until the source has expanded, the effect is relatively small.

6.2.1 Dependencies in the Laboratory Frame

When selecting on laboratory observables in central reactions, the trend of the smaller source for high momentum protons is not generally true. For backward and intermediate angle selections, higher momentum protons correspond to a more pronounced correlation function, however for forward angle selections, the high momentum protons come from an evaporating, fragmenting projectile spectator source. This source is much larger due to the longer time scales. The trends are the same in both ^{40}Ca+^{40}Ca and ^{48}Ca+^{48}Ca reaction systems.

A strong angular dependence within *p*-*p* correlation functions was found, reflecting the

different space-time extent of the source selected. Sources observed at backward angles, in the laboratory frame, reflect the participant zone of the reaction, while much larger sources are seen at forward angles which reflect the evaporating, fragmenting projectile-like residue. A decrease of the source size was observed with increasing momentum of the proton pair emitted at backward and intermediate angles while an opposite trend is seen at forward angles. In all cases, the ^{48}Ca+^{48}Ca reaction system results in larger sources than the ^{40}Ca+^{40}Ca reaction system. It was also found that BUU transport calculations reproduce the data well at backward and intermediate angles for low momentum protons, but failed to reproduce the data at forward angles. This probably reflects the lack of a suitable description of fragmentations, evaporation and secondary decays in the BUU model.

6.2.2 Dependencies on Transverse Momentum and Rapidity

When selecting on center of mass and frame invariant observables in central reactions, we find that the protons with largest rapidities exhibit the least pronounced correlation functions. In contrast, the protons measured at the lowest and intermediate rapidities exhibit larger correlation functions of similar magnitude. In all cases, correlations at larger total transverse momenta exhibit more pronounced peaks in the correlation function. These correlations at large transverse momenta are relatively independent of rapidity. In BUU, this trend can be approximately reproduced, indicating that the space-time extents of early emitted protons at large transverse momenta may allow quantitative comparisons between theory and experiment.

Both cluster production and larger in-medium cross sections as parametrized by the Rostock formula, are needed in BUU transport simulations to reproduce the source sizes seen

in the data. BUU with a momentum dependent mean field potential, cluster production, $\gamma = 0.7$, and the Rostock in-medium cross section reduction (or free cross sections) reproduced most of the trends seen in the data. This is true for both the neutron deficient ^{40}Ca+^{40}Ca and the neutron-rich ^{48}Ca+^{48}Ca system, indicating no need for unusual reductions of the *np* cross section in the medium. The only place where these comparisons fail is in the low transverse momentum and high rapidity domain, which corresponds to the projectile like spectator source. This source is evaporating and fragmenting which results in protons being emitted over longer time scales and a much larger source. BUU does not incorporate evaporation or secondary decays into the transport of particles. Again, BUU should only be compared to data in kinematic regions where the model adequately describes the relevant physical processes.

6.3 Outlook

A specific set of experiments could distinguish whether the ^{48}Ca+^{48}Ca system results in a larger source than the ^{40}Ca+^{40}Ca system because of initial geometric size, or whether it is isospin dependent. An example of two reactions that could be compared are ^{96}Ru+^{96}Ru and ^{96}Zr+^{96}Zr. While ^{96}Ru and ^{96}Zr have similar geometric sizes, the latter is neutron-rich, while the former is neutron-poor. A comparison of source sizes from these two reactions would examine the role of isospin in *p*-*p* correlation functions.

The most obvious work to be continued in the future is to continue to constrain the density dependence of the symmetry energy by using other experimental observables. Experiments have already been performed as part of the HiRA campaign to constrain γ using n/p ratios and isospin diffusion. In addition, as stated earlier, more work is needed to find observables

which isolate inputs in reaction dynamics.

On the theoretical front, transport models in general need to incorporate cluster production, especially alpha particles. The inclusion of evaporation and secondary decays would alleviate discrepancies between theoretical models and experimental data where these processes are important.

Appendices

Appendix A

Laser Measurements

The Laser Based Alignment System [77] (LBAS) provides accurate positions of detectors and targets. It is a non-contact, high precision, detector alignment tool. LBAS was essential in measuring the location of the target and the detectors in this dissertation experiment. The target would move if touched, so a non-contact method was needed to measure it. Also, the detector faces are too sensitive to touch, therefore a non-contact measurement was again needed. The detector array sagged a little under the weight of the detectors and thus the design specifications were not precise enough to use in the analysis. An optimal position resolution of each pixel in the detector is 0.25 mm for the necessary angular resolution. Better angular resolution allows us to calculate p-p correlation functions at low q more accurately. The discrepancy between the location of the detectors from the mechanical design and the actual location of the detectors can be seen in Fig. A.1. The measuring device also needed to be small enough to fit inside the 4π array to measure the location of the target. LBAS fit all of these requirements.

LBAS is composed of 3 main devices, two OWIS rotary stages [78] and an Acuity Laser

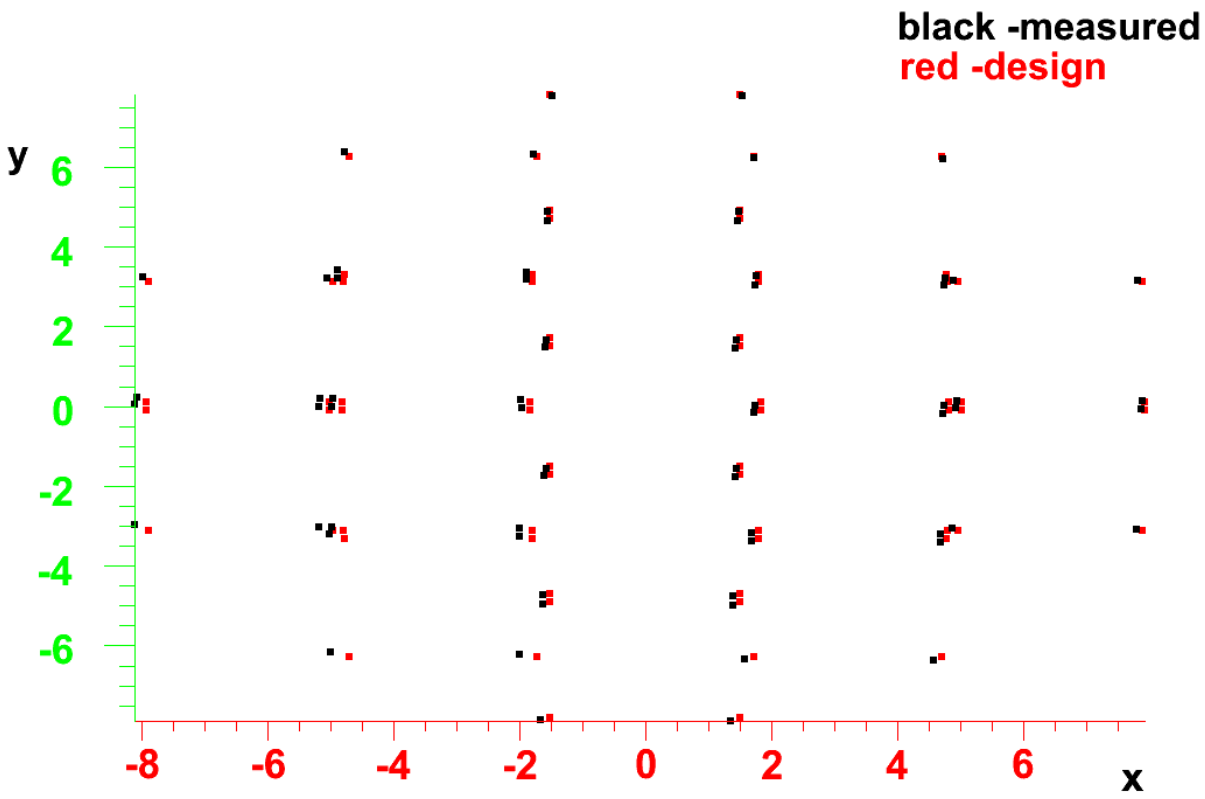

Figure A.1: The black dots are corners of the detectors as measured by LBAS. The red dots are corners of the detectors as given by the design of the mechanical setup for the array. The discrepancy shows the need for such a laser measurement. Units are in inches.

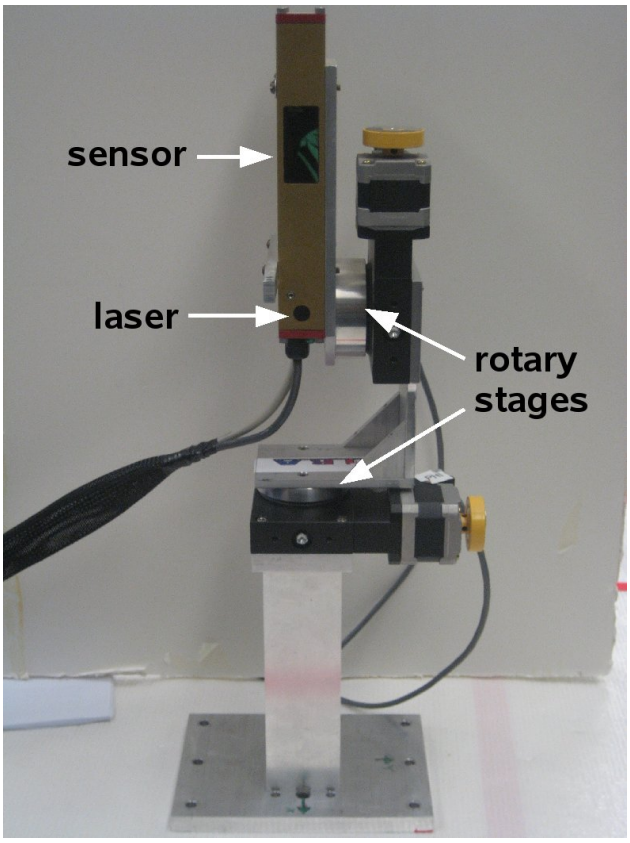

Figure A.2: A photograph of LBAS with components labeled.

Displacement Sensor [79]. The rotary stages provide the theta and phi angles while the laser gives the distance within a range of 25.4-40.6 cm. Light diffusely reflecting off of surfaces is focused by a lens in the sensor onto a CCD which focuses the position of the image. Since the lens is located above the beam, the intensity maxima in the CCD shifts upwards if the object is closer to the sensor and downwards if it is located farther away. A triangulation method is used to compute the distance to the measured object. A photograph of LBAS can be seen in Fig. A.2. The displacements of the rotary stages and the laser itself are taken into account in the final calculations of positions. The distance between the object and LBAS can be measured to within 60 μm. For a 0.010° step in angle, the position resolution is ∼0.2 mm which exceeds the specifications of 0.25 mm.

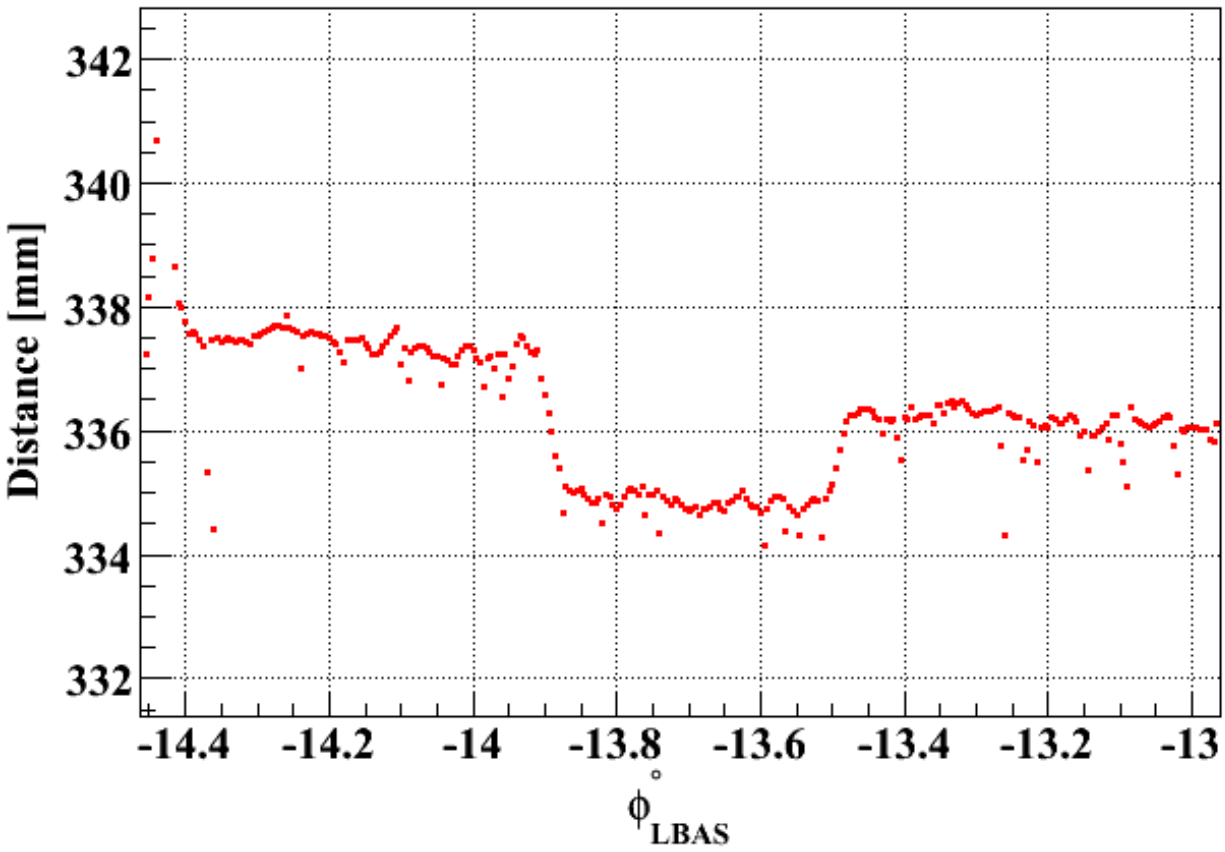

Figure A.3: An example of an edge scanned with LBAS.

Software was developed to control the laser and scan edges of objects with specified step sizes. An example of a scan of the edge of a detector is shown in Fig. A.3. The output from LBAS is distance, theta (horizontal angle), and phi (vertical angle), although the angles are modified from normal spherical coordinates with the z-axis along the laser beam. Under normal operation, the conversion from LBAS angles to spherical angles is given by:.

$$\theta_{spherical} = 90^{\circ} + \theta_{LBAS} \tag{A.1}$$

and

$$\phi_{spherical} = -\phi_{LBAS}. \tag{A.2}$$

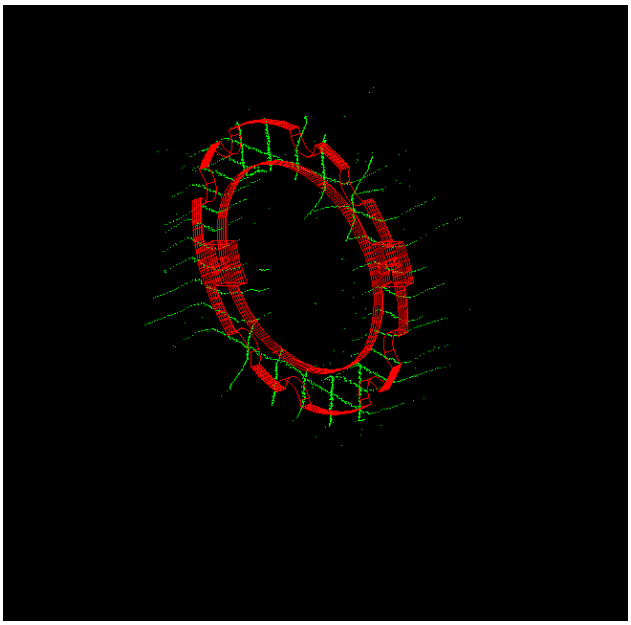

Figure A.4: The red lines are the mechanical drawing of the target frame used to hold a target. The green dots are from the LBAS scans of a target while it was inside the chamber.

Some examples of the LBAS scans are shown in Figs. A.4 and A.5. The green dots are directly from the LBAS scans and the red outline is the mechanical drawing of the target frame and reference block respectively. The block and target together, along with a photograph of the actual positions can be seen in Fig. A.6. LBAS measured:

- The target
- The edges of all HiRA detectors once the array was extracted from the 4π
- The reference block

The reference block was used to link together measurements of positions made by two separate lasers, LBAS and a contact based laser system owned by NSCL.

The NSCL laser was a contact based measuring device. The laser locked on to the position of a ball that touched the surface of the object being measured. By moving the ball around

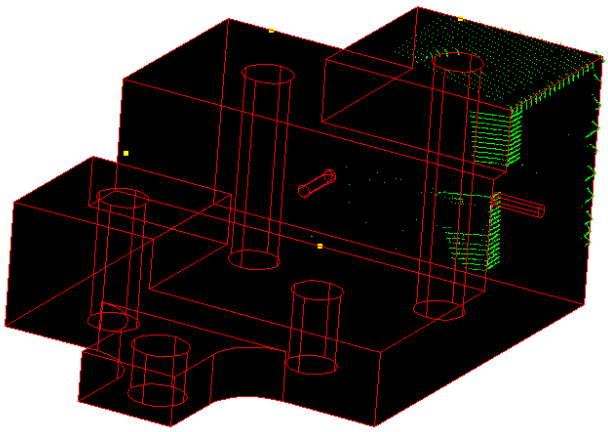

Figure A.5: The red lines are the mechanical drawing of the reference block used to link different measurement reference frames together. The green dots are from LBAS scans of the block.

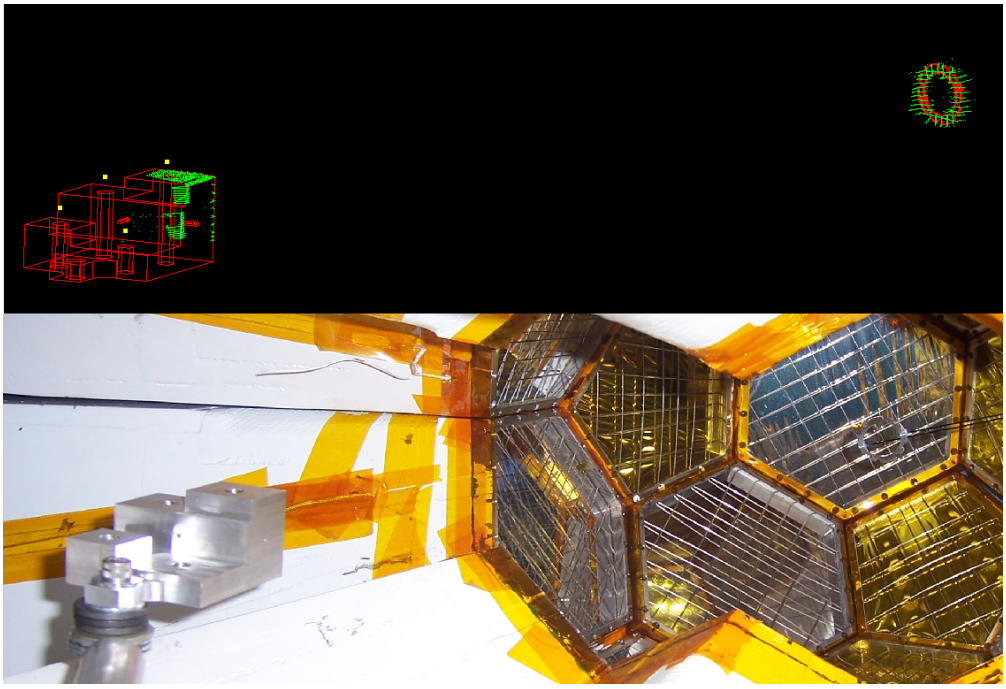

Figure A.6: The LBAS scans with mechanical drawings are shown on top while a photograph of the actual setup is shown below. The target can be seen on the right hand side of the figure, while the reference block can be seen on the left hand side of the figure.

a surface at least three times, the plane of the surface could be determined. The NSCL laser measured:

- 3 reference points within the vault to connect the vault to the rest of the lab
- 3 reference points on the last quadrupole in the beam line before the 4π
- The front and back of the 4π to define the beam axis
- The reference block
- Reachable sides of HiRA

The last two items were the most important for linking together different measurements. The target was measured by LBAS in its place, but HiRA was measured with LBAS outside of the vacuum chamber. To reference the position of HiRA during the experiment, the NSCL laser was necessary, even though it only measured a few sides of one HiRA detector. The reference block was needed to link together the target, the beam line, and HiRA into one reference frame, since it was measured by both lasers. From the measurement of the corners of each HiRA detector, the location of each pixel could be calculated from the precision design of HiRA. From the location of the target, assuming the beam was centered on target, the angle of each particle emitted from the reaction could be calculated.

Appendix B

ROOT Analysis

For the analysis of this experimental data (and some theoretical simulations), the ROOT [7] analysis software package was utilized. First, information from the data acquisition software was mapped onto detector components. With that information, the ROOT tree structure was employed to make a tree for each data file, with branches for each individual detector component. For example, within HiRA, the DEs, EFs, EBs, and CsI crystals each had their own branch which were arrays of 32 (4) for the silicon strips (CsI crystals). The 4π array was also divided into branches, one for each slow and fast scintillator in the phoswich, with additional branches for the FA elements. Initially, the values assigned to each branch was filled with energies in raw channels. After calibrating, a new tree was made with calibrated energies. Total transverse energy from the 4π array was added to this tree.

Each particle was recorded in a particular DE, EF, EB, and CsI for a given telescope. First, the energy loss in each detector was summed to provide a total energy for each particle. Then, from the detector information coupled with position measurements from LBAS, each EF/EB pixel could be assigned a position in θ-ϕ space. From PID plots, each particle could

be identified and labeled with a number corresponding to a certain isotope. For each event, the number of particles recorded in HiRA for that event and the total transverse energy from the 4π were written to a text file. Then the isotope label, energy, and position of each particle in HiRA was written to the same text file. Each data run was transcribed into a text file in this manner.

Physics ROOT trees were then made from these text files for the purpose of making two particle correlation functions. In this tree structure, each "event" was comprised of two particles entering the HiRA detector array. From these particles, the relative momentum for each pair in their center of mass was calculated (Qrel) along with center of mass rapidity (CMSrapid), individual momentum (pLAB/pCMS), total momentum (PpairLAB/PpairCMS), transverse momentum (pT), energy (LAB/CMS) and angle relative to the beam axis (thetaLAB/CMS), azimuthal angle (phiLAB/CMS), telescope number (tscope) in the laboratory (LAB) and center of mass (CMS) frames as shown in Fig. B.1. Here each branch is a different observable for the event. The pairangleLAB was the angle between the pair of particles, while the pairthetaLAB/CMS was the angle of the total momentum vector of the pair. The total transverse energy (Etrans) and 4π multiplicity (multi4pi) for each event were also recorded for selection on impact parameter. In the tree, 1 and 2 refer to particle number. For identical particles, the number was randomized so that the distribution for the particle 1 branch was identical to the corresponding distribution for the particle 2 branch. For different particles, the one with the smallest A (or Z) is particle 1. Any observables without a number are for the pair.

Identical trees were made for the numerator files and the denominator files, although different event files were used. In the case of the numerator, data taken with a minimum CsI

Figure B.1: Tree structure for creating 2 particle correlation functions.

multiplicity of two were used, and protons were mixed from the same event. In the case of the denominator, data files with a minimum CsI multiplicity of one were used, and protons were mixed from different events. Similar trees were made from the text files for constructing 3 particle correlation functions. In this last case, the trees included relative kinetic energy instead of relative momentum.

Appendix C

Calculation of $r_{1/2}$ and Error

When source functions are calculated using an ancillary code to BUU, they are normalized such that the volume integral is 1 (Eq. C.1) which means the height depends on the source at very large separation distance, r.

$$4\pi \int_0^\infty S(r) r^2 dr = 1 \tag{C.1}$$

It is important that the half width half maximum (or $r_{1/2}$) of the source, and its associated error, are calculated in a consistent manner for all sources. Different methods for finding the maximum of the source were explored. The first bin usually has a large error associated with it and was excluded. One method was to regard the height of the second bin (r=0.75 fm) as the maximum. This method was eventually rejected because the second bin was sometimes not consistent with a smooth continuous source due to poor statistics. To avoid discrepancies in the height of the source function, it was thought to use the rms of the source, assume a Gaussian distribution, and then the $r_{1/2}$ is simply $rms \cdot \sqrt{2ln2}$. However, the rms is very sensitive to the maximum radius in the summation, and does not converge.

The best method was to fit bins 2-5 ($0.5<r<2.5$ fm) with $a+bx^2$ and use the y-intercept as the maximum of the source. This averages out any inconsistencies in a single point and forces the derivative of the source to be 0 at $r = 0$. The error in the maximum is the error of the fit scaled by $\sqrt{\chi^2/2}$.

Once the maximum, y_{max}, is found, calculating the $r_{1/2}$ is elementary. The bins with contents just above and below the half maximum give points (x_1,y_1) and (x_2,y_2) respectively where x is r and y is $S(r)$. A linear extrapolation is used to find the x value corresponding to $y = y_{max}/2$ as shown by

$$r_{1/2} = (\frac{y_m}{2} - y_1)(\frac{x_2 - x_1}{y_2 - y_1}) + x_1. \tag{C.2}$$

The error in the $r_{1/2}$ is found by propagation of errors

$$\delta_{r_{1/2}} = \sqrt{(\frac{\partial r_{1/2}}{\partial y_m}\delta_{ym})^2 + (\frac{\partial r_{1/2}}{\partial x_1}\delta_{x1})^2 + (\frac{\partial r_{1/2}}{\partial x_2}\delta_{x2})^2 + (\frac{\partial r_{1/2}}{\partial y_1}\delta_{y1})^2 + (\frac{\partial r_{1/2}}{\partial y_2}\delta_{y2})^2}. \tag{C.3}$$

The error in the height, δ_{ym}, was discussed above, while δ_y is the error of the source function for those points below and above the maximum, and δ_x=0.1 fm (half of the bin size). The partial derivatives are given in Eqs. C.4, C.5, C.6, C.7,and C.8, where $dy = y_2$-y_1. The contributions to the error from the error in the source at y_1 and y_2 are smaller than the contributions from the other three variables.

$$\frac{\partial r_{1/2}}{\partial y_{max}} = \frac{x_2 - x_1}{2dy} \tag{C.4}$$

$$\frac{\partial r_1/_2}{\partial y_1} = \frac{-x_2 + x_1}{dy} + \frac{(ymax - 2y_1)(x_2 - x_1)}{2dy^2} \tag{C.5}$$

$$\frac{\partial r_1/_2}{\partial y_2} = \frac{(ymax - 2y_1)(x_2 - x_1)}{-2dy^2} \tag{C.6}$$

$$\frac{\partial r_1/_2}{\partial x_1} = \frac{-ymax + 2y_1}{2dy} + 1 \tag{C.7}$$

$$\frac{\partial r_1/_2}{\partial x_2} = \frac{ymax - 2y_1}{2dy} \tag{C.8}$$

REFERENCES

References

[1] W. K. Wilson. *Azimuthal Distributions in Intermediate Energy Heavy-Ion Collisions*. PhD thesis, Michigan State University, 1991.

[2] A. M. Rogers. *Study of ^{69}Br Ground State Proton Emission and Effects on the rp-Process ^{68}Se Waiting Point*. PhD thesis, Michigan State University, 2009.

[3] M. S. Wallace. *Experimental and Theoretical Challenges in Understanding the rp-Process on Accreting Neutron Stars*. PhD thesis, Michigan State University, 2005.

[4] J. Lee. *Survey of Neutron Spectroscopic Factors and Asymmetry Dependence of Neutron Correlations in Transfer Reactions*. PhD thesis, Michigan State University, 2010.

[5] R. Pak. *Collective Flow in Intermediate Energy Heavy-Ion Collisions*. PhD thesis, Michigan State University, 1996.

[6] D. Henzlova, 2010. Private communication.

[7] Cern. http://root.cern.ch, 2011.

[8] L. W. Chen, V. Greco, C. M. Ko, and B. A. Li. Isospin effects on two-nucleon correlation functions in heavy-ion collisions at intermediate energies. *Phys. Rev. C*, **68**:014605, 2003. http://dx.doi.org/10.1103/PhysRevC.68.014605.

[9] R. B. Wiringa, V. Fiks, and A. Fabrocini. Equation of state for dense nucleon matter. *Phys. Rev. C*, **38**(2):1010–1037, Aug 1988. http://dx.doi.org/10.1103/PhysRevC.38.1010.

[10] D. Boyanovsky. Phase transitions in the early and the present universe:From the big bang to heavy ion collisions. 2001. hep-ph/0102120.

[11] Matthias Liebendörfer, Anthony Mezzacappa, Friedrich-Karl Thielemann, O. E. Bronson Messer, W. Raphael Hix, and Stephen W. Bruenn. Probing the gravitational well: No supernova explosion in spherical symmetry with general relativistic Boltzmann neutrino transport. *Phys. Rev. D*, **63**(10):103004, Apr 2001. http://dx.doi.org/10.1103/PhysRevD.63.103004.

[12] J. M. Lattimer and M. Prakash. The physics of neutron stars. *Science*, **304**:536, 2004. http://dx.doi.org/10.1126/science.1090720.

[13] P. Danielewicz, R. Lacey, and W. G. Lynch. Determination of the equation of state of dense matter. *Science*, **298**:1592, 2002. http://dx.doi.org/10.1126/science.1078070.

[14] B. A. Brown. Neutron radii in nuclei and the neutron equation of state. *Phys. Rev. Lett.*, **85**:5296, 2000. http://dx.doi.org/10.1103/PhysRevLett.85.5296.

[15] A. Klimkiewicz, N. Paar, P. Adrich, M. Fallot, K. Boretzky, T. Aumann, D. Cortina-Gil, U. Datta Pramanik, Th. W. Elze, H. Emling, H. Geissel, M. Hellström, K. L. Jones, J. V. Kratz, R. Kulessa, C. Nociforo, R. Palit, H. Simon, G. Surówka, K. Sümmerer, D. Vretenar, and W. Waluś. Nuclear symmetry energy and neutron skins derived from pygmy dipole resonances. *Phys. Rev. C*, **76**:051603, 2007. http://dx.doi.org/10.1103/PhysRevC.76.051603.

[16] Andrea Carbone, Gianluca Colò, Angela Bracco, Li-Gang Cao, Pier Francesco Bortignon, Franco Camera, and Oliver Wieland. Constraints on the symmetry energy and neutron skins from pygmy resonances in ^{68}Ni and ^{132}Sn. *Phys. Rev. C*, **81**:041301, 2010. http://dx.doi.org/10.1103/PhysRevC.81.041301.

[17] U. Garg, T. Li, S. Okumura, H. Akimune, M. Fujiwara, M.N. Harakeh, H. Hashimoto, M. Itoh, Y. Iwao, T. Kawabata, K. Kawase, Y. Liu, R. Marks, T. Murakami, K. Nakanishi, B.K. Nayak, P.V. Madhusudhana Rao, H. Sakaguchi, Y. Terashima, M. Uchida, Y. Yasuda, M. Yosoi, and J. Zenihiro. The giant monopole resonance in the Sn isotopes: Why is tin so fluffy? *Nucl. Phys. A*, **788**:36 – 43, 2007. Proceedings of the 2nd International Conference on Collective Motion in Nuclei under Extreme Conditions - COMEX 2 http://www.sciencedirect.com/science/article/B6TVB-4MV74YN-G/2/43398042e042f02c27aaf964d6aa56ba.

[18] P. Danielewicz and J. Lee. Symmetry energy I: Semi-infinite matter. *Nucl. Phys. A*, **818**:36, 2009. http://dx.doi.org/10.1016/j.nuclphysa.2008.11.007.

[19] M. Prakash, T. L. Ainsworth, and J. M. Lattimer. Equation of state and the maximum mass of neutron stars. *Phys. Rev. Lett.*, **61**:2518, 1988. http://dx.doi.org/10.1103/PhysRevLett.61.2518.

[20] J. M. Lattimer and M. Prakash. Neutron star structure and the equation of state. *The Astrophysical Journal*, **550**:426, 2001. http://dx.doi.org/10.1086/319702.

[21] J. M. Lattimer, C. J. Pethick, M. Prakash, and Pawel Haensel. Direct URCA process in neutron stars. *Phys. Rev. Lett.*, **66**:2701, 1991. http://dx.doi.org/10.1103/PhysRevLett.66.2701.

[22] M. A. Faminao, T. Liu, W. G. Lynch, M. Mocko, A. M. Rogers, M. B. Tsang, M. S. Wallace, R. J. Charity, K. Komarov, D. G. Sarantites, L. G. Sobotka, and G. Verde. Neutron and proton transverse emission ratio measurements and the density dependence of the asymmetry term of the nuclear equation of state. *Phys. Rev. Lett.*, **97**:052701, 2006. http://dx.doi.org/10.1103/PhysRevLett.97.052701.

[23] M.B. Tsang, C.K. Gelbke, X.D. Liu, W.G. Lynch, W.P. Tan, G. Verde, H.S. Xu, W. A. Friedman, R. Donangelo, S. R. Souza, C.B. Das, S. Das Gupta, , and D. Zhabinsky. Isoscaling in statistical models. *Phys. Rev. C*, **64**:054615, 2001. http://dx.doi.org/10.1103/PhysRevC.64.054615.

[24] T. Liu. *Isospin Dynamics and the Isospin Dependent EOS*. PhD thesis, Michigan State University, 2005.

[25] M. B. Tsang, T. X. Liu, L. Shi, P. Danielewicz, C. K. Gelbke, X. D. Liu, W. G. Lynch, W. P. Tan, G. Verde, A. Wagner, H. S. Xu, W. A. Friedman, L. Beaulieu, B. Davin, R. T. de Souza, Y. Larochelle, T. Lefort, R. Yanez, V. E. Viola, R. J. Charity, and L. G. Sobotka. Isospin diffusion and the nuclear symmetry energy in heavy ion reactions. *Phys. Rev. Lett.*, **92**:062701, 2004. http://dx.doi.org/10.1103/PhysRevLett.92.062701.

[26] M. B. Tsang, Y. Zhang, P. Danielewicz, M. Famiano, Z. Li, W. G. Lynch, and A. W. Steiner. Constraints on the density dependence of the symmetry energy. *Phys. Rev. Lett.*, **102**:122701, 2009. http://dx.doi.org/10.1103/PhysRevLett.102.122701.

[27] B. A. Li, L. W. Chen, and C. M. Ko. Recent progress and new challenges in isospin physics with heavy-ion reactions. *Phys. Rep.*, **464**:113, 2008. http://www.sciencedirect.com/science/article/B6TVP-4SDGR1C-1/2/0e1d94465e37ec9f9e3342b9120435d7.

[28] M.B. Tsang, Z. Chajecki, D. Coupland, P. Danielewicz, F. Famiano, R. Hodges, M. Kilburn, F. Lu, W.G. Lynch, J. Winkelbauer, M. Youngs, and YingXun Zhang. Constraints on the density dependence of the symmetry energy from heavy ion collisions. *Progress in Particle and Nuclear Physics*, 2011.

[29] R. Hanbury Brown and R. Q. Twiss. A test of a new type of stellar interferometer on sirius. *Nature*, **178**:1046, 1990. http://dx.doi.org/10.1038/1781046a0.

[30] D. H. Boal, C. K. Gelbke, and B. K. Jennings. Intensity interferometry in subatomic physics. *Rev. Mod. Phys.*, **62**:553, 1990. http://dx.doi.org/10.1103/RevModPhys.62.553.

[31] S. J. Gaff, C. K. Gelbke, W. Bauer, F. C. Daffin, T. Glasmacher, E. Gualtieri, K. Haglin, D. O. Handzy, S. Hannuschke, M. J. Huang, G. J. Kunde, R. Lacey, W. G. Lynch, L. Martin, C. P. Montoya, R. Pak, S. Pratt, N. Stone, M. B. Tsang, A. M. Vander Molen, G. D. Westfall, and J. Yee. Two-proton correlations for ^{16}O + ^{197}Au collisions at E/A=200 MeV. *Phys. Rev. C*, **52**:2782, 1995. http://dx.doi.org/10.1103/PhysRevC.52.2782.

[32] D. O. Handzy, M. A. Lisa, C. K. Gelbke, W. Bauer, F. C. Daffin, P. Decowski, W. G. Gong, E. Gualtieri, S. Hannuschke, R. Lacey, T. Li, W. G. Lynch, C. M. Mader, G. F. Peaslee, T. Reposeur, S. Pratt, A. M. Vander Molen, G. D. Westfall, J. Yee, and S. J. Yennello. Two-proton correlation functions for ^{36}Ar+^{45}Sc at E/A=80 MeV. *Phys. Rev. C*, **50**:858, 1994. http://dx.doi.org/10.1103/PhysRevC.50.858.

[33] M.A. Lisa, W.G. Gong, C.K. Gelbke, and W.G. Lynch. Event-mixing analysis of two-proton correlation functions. *Phys. Rev. C*, **44**:2865, 1991. http://dx.doi.org/10.1103/PhysRevC.44.2865.

[34] F. Zhu, W. G. Lynch, T. Murakami, C. K. Gelbke, Y. D. Kim, T. K. Nayak, R. Pelak, M. B. Tsang, H. M. Xu, W. G. Gong, W. Bauer, K. Kwiatkowski, R. Planeta, S. Rose,

Jr. V. E. Viola, L. W. Woo, S. Yennello, and J. Zhang. Light particle correlations for the ^{3}He+Ag reaction at 200 MeV. *Phys. Rev. C*, **44**:R582, 1991. http://dx.doi.org/10.1103/PhysRevC.44.R582.

[35] Z. Chen, C. K. Gelbke, W. G. Gong, Y. D. Kim, W. G. Lynch, M. R. Maier, J. Pochodzalla, M. B. Tsang, F. Saint-Laurent, D. Ardouin, H. Delagrange, H. Doubre, J. Kasagi, A. Kyanowski, A. Péghaire, J. Péter, E. Rosato, G. Bizard, F. Lefèbvres, B. Tamain, J. Québert, and Y. P. Viyogi. Inclusive two-particle correlations for ^{16}O induced reactions on ^{197}Au at E/A=94 MeV. *Phys. Rev. C*, **36**:2297, 1987. http://dx.doi.org/10.1103/PhysRevC.36.2297.

[36] S. E. Koonin. Proton pictures of high-energy nuclear collisions. *Phys. Lett. B*, **70**:43, 1977. http://www.sciencedirect.com/science/article/B6TVN-47284FF-43/2/f60f4d817f619c15ad5692892a47493c.

[37] S. Pratt, T. Csörgő, and J. Zimányi. Detailed predictions for two-pion correlations in ultrarelativistic heavy-ion collisions. *Phys. Rev. C*, **42**:2646, 1990. http://dx.doi.org/10.1103/PhysRevC.42.2646.

[38] G. Verde, D. A. Brown, P. Danielewicz, C. K. Gelbke, W. G. Lynch, and M. B. Tsang. Imaging sources with fast and slow emission components. *Phys. Rev. C*, **65**:054609, 2002. http://dx.doi.org/10.1103/PhysRevC.65.054609.

[39] G. F. Bertsch, H. Kruse, and S. D. Gupta. Boltzman equation for heavy ion collisions. *Phys. Rev. C*, **29**:673, 1984. http://dx.doi.org/10.1103/PhysRevC.29.673.

[40] G. F. Bertsch and S. Das Gupta. A guide to microscopic models for intermediate energy heavy ion collisions. *Phys. Rep.*, **160**:189 – 233, 1988. http://dx.doi.org/10.1016/0370-1573(88)90170-6.

[41] P. Danielewicz and G. F. Bertsch. Production of deuterons and pions in a transport model of energetic heavy-ion reactions. *Nucl. Phys. A*, **533**:712, 1991. http://dx.doi.org/10.1016/0375-9474(91)90541-D.

[42] P. Danielewicz. Formation of composites emitted at large angles in intermediate and high energy reactions. *Nucl. Phys. A*, **545**:21c, 1992. http://dx.doi.org/10.1016/0375-9474(92)90443-N.

[43] P. Danielewicz. Hadronic transport models. *Acta. Phys. Pol. B*, **33**:45, 2002. http://arXiv:nucl-th/0201032v1.

[44] E. A. Uehling and G. E. Uhlenbeck. Transport Phenomena in Einstein-Bose and Fermi-Dirac Gases. I. *Phys. Rev.*, **43**:552, 1933. http://dx.doi.org/10.1103/PhysRev.43.552.

[45] P. Danielewicz. Determination of the mean-field momentum-dependence using elliptic flow. *Nucl. Phys. A*, **673**:375, 2000. http://dx.doi.org/10.1016/S0375-9474(00)00083-X.

[46] R. J. Lenk and V. R. Pandharipande. Nuclear mean field dynamics in the lattice Hamiltonian Vlasov method. *Phys. Rev. C*, **39**:2242, 1989. http://dx.doi.org/10.1103/PhysRevC.39.2242.

[47] L. Shi. *Transport Phenomena in Heavy-Ion Reactions*. PhD thesis, Michigan State University, 2003.

[48] G. Verde, P. Danielewicz, W. G. Lynch, D. A. Brown, C. K. Gelbke, and M. B. Tsang. Probing transport theories via two-proton source imaging. *Phys. Rev. C*, **67**:034606, 2003. http://dx.doi.org/10.1103/PhysRevC.67.034606.

[49] B. A. Li and L. W. Chen. Nucleon-nucleon cross sections in neutron-rich matter and isospin transport in heavy-ion reactions at intermidiate energies. *Phys. Rev. C*, **72**:064611, 2005. http://dx.doi.org/10.1103/PhysRevC.72.064611.

[50] H.-J. Schulze, A. Schnell, G. Röpke, and U. Lombardo. Nucleon-nucleon cross sections in nuclear matter. *Phys. Rev. C*, **55**(6):3006–3014, 1997. http://dx.doi.org/10.1103/PhysRevC.55.3006.

[51] NSCL. http://www.nscl.msu.edu/experiments#PAC27, 2003.

[52] A.M. Vander Molen, J.S. Winfield, and N.T.B. Stone. L'user's guide to the MSU 4π Array. 3rd Edition, 1996.

[53] HiRA. http://groups.nscl.msu.edu/hira/, 2011.

[54] M. S. Wallace, M. A. Famiano, M. J. van Goethem, A. M. Rogers, W. G. Lynch, J. Clifford, F. Delaunay, J. Lee, S. Labostov, M. Mocko, , L. Morris, A. Moroni, B. E. Nett, D. J. Oostdyk, R. Krishnasamy, M. B. Tsang, R. T. de Souza, S. Hudan, L. G. Sobotka, R. J. Charity, J. Elson, and G. L. Engel. The high resolution array (HiRA) for rare isotope beam experiments. *Nucl. Instr. and Meth. A*, **583**:302–311, 2007. http://dx.doi.org/10.1016/j.nima.2007.08.248.

[55] V. Henzl, 2009. Private communication.

[56] W. Tan. *Probing the Freezeout Mechanisms and Isospin Effects in Multifragmentation*. PhD thesis, Michigan State University, 2002.

[57] D. A. Cebra. *Charged-Particle Correlations from Intermediate Energy Nuclear Reactions*. PhD thesis, Michigan State University, 1990.

[58] C. Cavata, M. Demoulins, J. Gosset, M. C. Lemaire, D. L'Hôte, J. Poitou, and O. Valette. Determination of the impact parameter in relativistic nucleus-nucleus collsions. *Phys. Rev. C*, **42**:1760, 1990. http://dx.doi.org/10.1103/PhysRevC.42.1760.

[59] L. Phair, D. R. Bowman, C. K. Gelbke, W. G. Gong, Y. D. Kim, M. A. Lisa, W. G. Lynch, G. F. Peaslee, R. T. de Souza, M. B. Tsang, and F. Zhu. Impact-parameter filters for ^{36}Ar+^{197}Au collisions at E/A = 50, 80 and 110 MeV. *Nucl. Phys. A*, **548**:489, 1992. http://dx.doi.org/10.1016/0375-9474(92)90697-I.

[60] P. Danielewicz, 2009. Private communication.

[61] P. Danielewicz, R. A. Lacey, P.-B. Gossiaux, C. Pinkenburg, P. Chung, J. M. Alexander, and R. L. McGrath. Disappearance of elliptic flow: A new probe for the nuclear equation of state. *Phys. Rev. Lett.*, **81**:2438, 1998. http://dx.doi.org/10.1103/PhysRevLett.81.2438.

[62] D. A. Brown and P. Danielewicz. Imaging of sources in heavy-ion reactions. *Phys. Lett. B*, **398**:252, 1997. http://www.sciencedirect.com/science/article/B6TVN-3SPGXP4-72/2/edac150984f33fa44917287b2afec651.

[63] D. A. Brown and P. Danielewicz. Optimized discretization of sources imaged in heavy-ion reactions. *Phys. Rev. C*, **57**:2474, 1998. http://dx.doi.org/10.1103/PhysRevC.57.2474.

[64] D. A. Brown and P. Danielewicz. Observing non-gaussian sources in heavy-ion reactions. *Phys. Rev. C*, **64**:014902, 2001. http://dx.doi.org/10.1103/PhysRevC.64.014902.

[65] M. A. Lisa. *Impact Parameter-Gated Two-Proton Intensity Interferometry in Intermediate Energy Heavy-Ion Collisions*. PhD thesis, Michigan State University, 1993.

[66] M. A. Lisa, C. K. Gelbke, W. Bauer, P. Decowski, W. G. Gong, E. Gualtieri, S. Hannuschke, R. Lacey, T. Li, W. G. Lynch, C. M. Mader, G. F. Peaslee, T. Reposeur, A. M. Vander Molen, G. D. Westfall, J. Yee, and S. J. Yennello. Impact-parameter-selected two-proton intensity interferometry for ^{36}Ar+^{45}Sc at E/A=80 MeV. *Phys. Rev. Lett.*, **70**(24):3709, 1993. http://dx.doi.org/10.1103/PhysRevLett.70.3709.

[67] T. Glasmacher, L. Phair, D. R. Bowman, C. K. Gelbke, W. G. Gong, Y. D. Kim, M. A. Lisa, W. G. Lynch, G. F. Peaslee, R. T. de Souza, M. B. Tsang, and F. Zhu. Two-fragment correlation functions with directional cuts for central ^{36}Ar+^{197}Au collisions at E/A=50 MeV. *Phys. Rev. C*, **50**:952, 1994. http://dx.doi.org/10.1103/PhysRevC.50.952.

[68] R.J. Charity and *et al.* Investigations of three, four, and five-particle exit channels of levels in light nuclei created using a ^{9}C beam. 2011. http://arxiv.org/abs/1105.1144v1.

[69] L. V. Grigorenko, T. D. Wiser, K. Mercurio, R. J. Charity, R. Shane, L. G. Sobotka, J. M. Elson, A. H. Wuosmaa, A. Banu, M. McCleskey, L. Trache, R. E. Tribble, and

M. V. Zhukov. Three-body decay of ^{6}Be. *Phys. Rev. C*, **80**(3):034602, Sep 2009. http://dx.doi.org/10.1103/PhysRevC.80.034602.

[70] R. J. Charity, T. D. Wiser, K. Mercurio, R. Shane, L. G. Sobotka, A. H. Wuosmaa, A. Banu, L. Trache, and R. E. Tribble. Continuum spectroscopy with a ^{10}C beam: Cluster structure and three-body decay. *Phys. Rev. C*, **80**:024306, 2009. http://dx.doi.org/10.1103/PhysRevC.80.024306.

[71] R. Sherr and H. T. Fortune. Low-lying levels of ^{9}B. *Phys. Rev. C*, **70**(5):054312, 2004. http://dx.doi.org/10.1103/PhysRevC.70.054312.

[72] F. Hoyle. On Nuclear Reactions Occuring in Very Hot STARS.I. the Synthesis of Elements from Carbon to Nickel. *Astrophysical Journal Supplement*, **1**:121, 1954. http://adsabs.harvard.edu/abs/1954ApJS....1..121H.

[73] C. W. Cook, W. A. Fowler, C. C. Lauritsen, and T. Lauritsen. ^{12}B, ^{12}C, and the red giants. *Phys. Rev.*, **107**(2):508–515, Jul 1957. http://dx.doi.org/10.1103/PhysRev.107.508.

[74] M. Freer, H. Fujita, Z. Buthelezi, J. Carter, R. W. Fearick, S. V. Förtsch, R. Neveling, S. M. Perez, P. Papka, F. D. Smit, J. A. Swartz, and I. Usman. 2^{+} excitation of the ^{12}C hoyle state. *Phys. Rev. C*, **80**:041303, Oct 2009. http://dx.doi.org/10.1103/PhysRevC.80.041303.

[75] T Munoz-Britton, M Freer, N I Ashwood, T A D Brown, W N Catford, N Curtis, S P Fox, B R Fulton, C W Harlin, A M Laird, P Mumby-Croft, A St J Murphy, P Papka, D L Price, K Vaughan, D L Watson, and D C Weisser. Search for the 2 + excitation of the Hoyle state in ^{12}C using the ^{12}C(^{12}C,3α)^{12}C reaction. *J. Phys. G*, **37**(10):105104, 2010. http://stacks.iop.org/0954-3899/37/i=10/a=105104.

[76] R. H. Dalitz. Decay of τ mesons of known charge. *Phys. Rev.*, **94**(4):1046–1051, May 1954. http://dx.doi.org/10.1103/PhysRev.94.1046.

[77] A. M. Rogers et al. in preparation.

[78] OWIS. http://www.owis-staufen.de, 2011.

[79] Acuity Laser. http://www.acuitylaser.com/, 2011.